

Bio-Inspired Hydro-Acoustic Sensor for Sensing Directivity of Sound

Jin-Hyuk Lee

A dissertation  
submitted in partial fulfillment of the  
requirements for the degree of

Doctor of Philosophy

University of Washington  
2013

Reading Committee:  
Per G. Reinhall, Chair  
Brian C. Fabien  
James C. Hermanson

Program Authorized to Offer Degree:  
Mechanical Engineering

©Copyright 2013

Jin-Hyuk Lee

University of Washington

**Abstract**

Bio-Inspired Hydro-Acoustic Sensor for Sensing Directivity of Sound

Jin-Hyuk Lee

Chair of Supervisory Committee:  
Professor Per G. Reinhall  
Mechanical Engineering

The aim of this research is to develop a biomimetic miniature underwater acoustic sensor for the measurement of the directivity of underwater sound. In contrast to a hydrophone array which detects direction by the arrival time of the sound waves this novel sensor is based on a mechanically coupled mechanism which amplifies the time delay by an order of two. In this research and design effort we develop a comprehensive mathematical model of the sensor in order to understand and optimize its performance characteristics. Fluid mass load and fluid-structure radiation are evaluated using both finite element analysis (FEA) and models obtained from the literature. It shows that the bio-inspired sensor can be designed to be directionally sensitive and operational at around up to 2 kHz within the current design limitation (2-D) and the micro range. This is because there is a tradeoff between the time delay amplification and the bandwidth of the sensor. This tradeoff and parametric study lead us to a design optimization of the sensor. For the design optimization, two independent optimization problems are solved: Amplification

optimization of the time delay of the sensor and phase difference varying optimization with respect to the angle of incidence of the incoming sound. As an example, the results of the several different design optimizations are presented. Based on the design optimization, it is compared to the FEA simulation and shows a good agreement.

# TABLE OF CONTENTS

<b>LIST OF FIGURES .....</b>	<b>iii</b>
<b>LIST OF TABLES .....</b>	<b>x</b>
<b>CHAPTER 1. INTRODUCTION .....</b>	<b>1</b>
<b>1.1</b> MOTIVATION AND INTRODUCTION .....	1
<b>1.2</b> ACOUSTIC VECTOR SENSOR (AVS) .....	3
<b>1.3</b> Background to Directivity Detection .....	5
<b>1.4</b> RESEARCH OBJECTIVES .....	6
<b>1.5</b> OUTLINE .....	9
<b>CHAPTER 2. MODELING AND CHARACTERISTICS OF THE SENSOR.....</b>	<b>11</b>
<b>2.1</b> MATHEMATICAL MODELING OF THE ACOUSTIC SENSOR .....	11
<b>2.2</b> CHARACTERISTICS OF THE SENSOR MODEL .....	14
<b>2.3</b> IDEALIZATION OF THE SENSOR.....	18
<b>2.3.1</b> Mode-Summation Model of the Sensor .....	18
<b>2.3.2</b> Lumped Parameter Five DOF Discrete Model .....	27
<b>2.4</b> CAPACITIVE SENSING.....	37
<b>CHAPTER 3. DETECTION OF DIRECTION OF THE SOUND SOURCE.....</b>	<b>43</b>
<b>3.1</b> INTRODUCTION .....	43
<b>3.2</b> DIGITAL SIGNAL ANALYSIS FOR DIRECTIVITY .....	45
<b>3.2.1</b> Single Source with One Frequency.....	45
<b>3.2.2</b> Multiple Sources with Multiple Frequencies.....	47
<b>3.2.3</b> Single Band-Limited White Noise Source.....	49
<b>CHAPTER 4. PARAMETRIC STUDY OF UNDERWATER SENSOR FOR DIRECTIVITY .....</b>	<b>52</b>
<b>4.1</b> Added Mass due to Fluid Loading.....	52
<b>4.1.1</b> Added Mass for a Translating Rigid Plate .....	57
<b>4.1.2</b> Added Mass for a Rotating Rigid Plate .....	58
<b>4.1.3</b> Added Mass Effect on Higher Frequency of a Vibrating Cantilever Beam/Sensor.....	62
<b>4.2</b> MODELING OF VARIABLE FLUID LOADED MASS FOR THE HYDRO-SENSOR.....	68
<b>4.3</b> PARAMETRIC STUDY .....	71
<b>4.3.1</b> Spring constants $k_1$ , $k_2$ , and $k_3$ .....	74
<b>4.3.2</b> Area.....	75
<b>4.3.3</b> Angle of Incidence $\theta$ .....	75
<b>4.3.4</b> Thickness $t$ .....	76
<b>4.3.5</b> Damping constants $d_1$ , $d_2$ , and $d_3$ .....	77
<b>4.4</b> Sensitivity Analysis .....	84

<b>CHAPTER 5. FINITE ELEMENT ANALYSIS.....</b>	<b>88</b>
<b>5.1 INTRODUCTION .....</b>	<b>88</b>
<b>5.2 MODAL ANALYSIS .....</b>	<b>88</b>
<b>5.2.1 FEM model and mesh sensitivity analysis.....</b>	<b>89</b>
<b>5.3 2-D PARAMETRIC ANALYSIS OF THE SENSOR IN FLUID-STRUCTURE INTERACTION.....</b>	<b>91</b>
<b>5.4 VALIDATION OF FEA SIMULATION .....</b>	<b>95</b>
<b>CHAPTER 6. DESIGN OPTIMIZATION OF THE SENSOR.....</b>	<b>99</b>
<b>6.1 DESIGN CONSIDERATION OF ACOUSTIC SENSOR.....</b>	<b>99</b>
<b>6.1.1 Design Consideration with Spring Constants and Natural Frequencies .</b>	<b>101</b>
<b>6.2 Directional Sensitivity and the Location of Natural Frequencies.....</b>	<b>104</b>
<b>6.3 Location of the Second Natural Frequency and the Need for Design Optimization .....</b>	<b>108</b>
<b>6.3.1 Case 1.....</b>	<b>109</b>
<b>6.3.2 Case 2.....</b>	<b>111</b>
<b>6.3.3 Case 3.....</b>	<b>111</b>
<b>6.3.4 Case 4.....</b>	<b>111</b>
<b>6.4 DESIGN OPTIMIZATION OF THE SENSOR.....</b>	<b>118</b>
<b>6.4.1 Design Optimization Problem.....</b>	<b>118</b>
<b>6.4.2 Design Optimization Results .....</b>	<b>121</b>
<b>6.4.3 Rayleigh Damping for the 5 DOF Lumped Parameter Sensor Model....</b>	<b>129</b>
<b>CHAPTER 7. DISCUSSION .....</b>	<b>133</b>
<b>7.1 SIGNAL NOISE.....</b>	<b>133</b>
<b>7.1.1 Case 1: Input Signal Frequency is Different from Band-Limited Noise</b>	<b>135</b>
<b>7.1.2 Case 2: Input signal frequency is embedded in the band limited white noise. ....</b>	<b>136</b>
<b>7.1.3 Case 3: Input Signal is Smaller than White Noise.....</b>	<b>138</b>
<b>7.2 EFFECT OF RIGID BODY MOTION OF THE SENSOR.....</b>	<b>138</b>
<b>7.3 DIFFICULTIES WITH SOUND SIGNAL DETECTION.....</b>	<b>142</b>
<b>7.4 Design Optimization (Multiple local min).....</b>	<b>142</b>
<b>CHAPTER 8. CONCLUSIONS AND FUTURE RESEARCH .....</b>	<b>143</b>
<b>8.1 CONCLUSION.....</b>	<b>143</b>
<b>8.2 FUTURE RESEARCH.....</b>	<b>144</b>
<b>BIBLIOGRAPHY.....</b>	<b>146</b>
<b>APPENDIX A: MATHEMATICA® FILE.....</b>	<b>149</b>
<b>APPENDIX B: SENSITIVITY ANALYSIS.....</b>	<b>160</b>
<b>APPENDIX C: SENSOR SIZE SELECTION .....</b>	<b>166</b>

## LIST OF FIGURES

Figure 1.1: Wilcoxon TV-001 vector sensor [7].....	4
Figure 1.2: The directional beam patterns of the microelectromechanical-based Hydroflown and examples of time and frequency domain plots [8].....	5
Figure 2.1: Mechanical model of ears of Ormia ochracea [10]. .....	12
Figure 2.2: Left: Response plot of $x_1$ and magnitude for input frequency at 2000 Hz. Right: Frequency response of the transfer function 1 (Ipsilateral). .....	14
Figure 2.3: Mechanical responses obtained from the transfer functions in amplitude, phase, and time delay: Blue solid line and red dotted line represent responses of the transfer function 1 and 2 .....	16
Figure 2.4: The Predicted time delays between the mechanical response of $x_1$ and $x_2$ depending on the angle of incidence at various frequencies (2000, 6000, 15000 Hz). .....	16
Figure 2.5: The simple model of the sensor and two vibrational modes. ....	17
Figure 2.6: Representation of the sensor as beam sections 1, 2, and 3 with their coordinates. ....	19
Figure 2.7: First and second mode shapes of Mode-Summation Sensor model. ....	27
Figure 2.8: Representation of the sensor system composed of 4 beam elements. ....	28
Figure 2.9: First and second mode shapes of the 5 DOF lumped parameter sensor model. .....	34
Figure 2.10: A parallel-plate capacitance with an overlapping area $A$ and a spacing $d$ ...	38
Figure 2.11: Image of typical comb fingers [18] .....	39
Figure 2.12: Left: Harmonic response of the sensor for ambient noise of 0.001 Pa. Right: Displacement of the sensor. ....	40
Figure 2.13: Left: Capacitance vs. time plot based on Figure 2.12. Right: Capacitance and Displacement show a linear relationship. ....	41
Figure 3.1: Sound field description.....	43
Figure 3.2: Left: Time response at 15000 Hz with 45° incidence angle. Right: Zoom-in plot in which the time-delay is measured.....	46
Figure 3.3: Left: Comparison plot of $\tau$ vs. $\theta$ at 2000 Hz. Right: at 6000 Hz.....	47

Figure 3.4: Left: Time domain representation of $x_1$ with a modulation signal composed of three sinusoids. Right: Frequency domain representation of $x_1$ signal composed of three sinusoids.....	48
Figure 3.5: Time delay by xcross on broadband noise of 1000 ~ 5000 Hz. ....	50
Figure 3.6: Comparison plot of $\tau$ vs. $\theta$ between frequency analysis and wide-band noise Left: at 2500 Hz. Right: at 4600 Hz.....	51
Figure 4.1: Added mass of 20 by 20 mm plate vs. 2kHz and frequency.....	54
Figure 4.2: Plot of added mass vs. frequency up to critical frequency.....	57
Figure 4.3: Comparison between FEA simulation of cantilever beam in air (upper row) and in water (lower row). ....	63
Figure 4.4: Top: Natural frequencies in air and in water based on FEA simulation, Bottom: Comparison of frequency reduction ratio by simulation. ....	64
Figure 4.5: Comparison of simulation between in water, in air, and in vacuo mode (top to bottom order). ....	66
Figure 4.6: Top: Natural frequencies in air and in water based on FEA simulation, Bottom: Comparison of frequency reduction ratio by simulation of the sensor.....	67
Figure 4.7: Beam element with nodal degrees of freedom. ....	69
Figure 4.8: Left: Frequency response of 1mm by 1 mm sensor with 6e-6 m thickness in water, Right: Fluid loaded mass vs. frequency based on Eq. 4.1 and Eq. 4.2. ....	70
Figure 4.9: Comparison of frequency responses between in air (Top) and in water (Bottom). ....	72
Figure 4.10: Comparison of time delay between in air (Left) and in water (Right). ....	72
Figure 4.11: Response of the sensor in water of frequencies at 2400 Hz (Top), and 3500 Hz (Bottom) .....	73
Figure 4.12: Time delay $\tau$ vs. Frequency $f$ with variable coupling spring constant $k_3$ (5 ~ 50 N/m). ....	74
Figure 4.13: Time delay $\tau$ vs. Frequency $f$ with variable area. ....	75
Figure 4.14: Time delay $\tau$ vs. Frequency $f$ in water for variable angle of incidence $\theta$ .....	76
Figure 4.15: Time delay $\tau$ vs. Frequency $f$ in water for variable thickness, $t$ . ....	77
Figure 4.16: Damping effect between air and water based on FEA: Left: Air, Right: Water. ....	78

Figure 4.17: Harmonic responses showing half-power points and bandwidth for the first natural frequency of the sensor in air (Top) and in water (Bottom). .....	79
Figure 4.18: Harmonic responses showing half-power points and bandwidth for the second natural frequency of the sensor in air (Top) and in water (Bottom). .....	80
Figure 4.19: Time delay $\tau$ vs. Frequency $f$ in water for different damping constant $c_3$ ...	81
Figure 4.20: Time delay vs. frequency with varying damping constant $d$ for smaller sensor (i). .....	83
Figure 4.21: Time delay vs. frequency for varying damping constant $d$ for bigger sensor (ii). .....	83
Figure 4.22: Magnitude vs. frequency in water with the spacing $d = 1.2$ mm, and 1mm by 1 mm diaphragm .....	85
Figure 4.23: Phases vs. frequency in water with the spacing $d = 1.2$ mm, and 1mm by 1 mm diaphragm .....	85
Figure 4.24: Predicted Sensitivity of 1 mm by 1mm Plate of the Sensor in Water and in Air .....	87
Figure 5.1: Three dimensional FE model with axes. ....	88
Figure 5.2: Left: Rocking, out-of-phase mode. Right: Bending (translational), in-phase mode. ....	89
Figure 5.3: Geometry of the 2-D sensor model in discretized finite element mesh with quadrilateral element (all dimensions are in meters) .....	90
Figure 5.4: Results of the mesh sensitivity analysis. ....	91
Figure 5.5: Mesh Mode in FEA .....	94
Figure 6.1: (a) Time delay vs. frequency plot of case 1 with $k_3 = 51.8$ N/m, (b) Time delay vs. angle of incidence at 100, 200, and 300 Hz, (c) Time delay vs. angle of incidence at 350, 400, and 450 Hz (d) Time delay vs. angle of incidence at 500, 1000, 2000, and 3000 Hz. ....	100
Figure 6.2: Time delay amplification vs. angle of incidence in water at various frequencies. ....	101
Figure 6.3: Time delay vs. angle of incidence in water at $20^\circ$ incidence angle ( $k_3: 5 \rightarrow 50$ N/m). ....	101

Figure 6.4: Time delay vs. Frequency progression as the coupling spring constant $k_3$ varies. ....	102
Figure 6.5: Top: Time delay vs. Frequency plot, Bottom: Time delay vs. Angle of Incidence plot. ....	103
Figure 6.6: Time delay vs. frequency: Left: 1 mm by 1 mm, Right: 3.5 mm by 3.5 mm sensor .....	104
Figure 6.7: Time delay vs. angle of incidence for 1 mm by 1 mm sensor.....	105
Figure 6.8: Time delay vs. angle of incidence for 3.5 mm by 3.5 mm sensor.....	106
Figure 6.9: Directional sensitivity polar plot for 1 mm by 1 mm: (a) 500 Hz (b) 1000 Hz (c) 2000 Hz, and for 3.5 mm by 3.5 mm: (d) 500 Hz (e) 1000 Hz (f) 2000 Hz. ....	107
Figure 6.10: Time delay vs. Frequency plot: varying coupling spring constant $k_3$ .....	109
Figure 6.11: (a) Time delay vs. frequency plot of case 1 with $k_3 = 51.8$ N/m, (b) Time delay vs. angle of incidence at 100, 200, and 300 Hz, (c) Time delay vs. angle of incidence at 350, 400, and 450 Hz (d) Time delay vs. angle of incidence at 500, 1000, 2000, and 3000 Hz. ....	112
Figure 6.12: (a) Time delay vs. frequency plot of case 1 with $k_3 = 103.6$ N/m, (b) Time delay vs. angle of incidence at 100, 200, and 300 Hz, (c) Time delay vs. angle of incidence at 350, 400, and 450 Hz (d) Time delay vs. angle of incidence at 500, 1000, 2000, and 3000 Hz. ....	113
Figure 6.13: (a) Time delay vs. frequency plot of case 1 with $k_3 = 3.45$ N/m, (b) Time delay vs. angle of incidence at 100, 200, and 300 Hz, (c) Time delay vs. angle of incidence at 350, 400, and 450 Hz (d) Time delay vs. angle of incidence at 500, 1000, and 2000 Hz. ....	114
Figure 6.14: Left: Time delay vs. frequency plot of case 2 with $k_3 = 4.9$ N/m, Right: Time delay vs. angle of incidence at 100, 500, and 750 Hz. ....	115
Figure 6.15: Left: Time delay vs. frequency plot of case 2 with $k_3 = 100$ N/m, Right: Time delay vs. angle of incidence at 100, 300, and 500 Hz. ....	115
Figure 6.16: Left: Time delay vs. frequency plot of case 2 with $k_3 = 4.8$ N/m, Right: Time delay vs. angle of incidence at 100, 300, and 500 Hz. ....	115
Figure 6.17: Left: Time delay vs. frequency plot of case 3 with $k_3 = 7$ N/m, Right: Time delay vs. angle of incidence at 500, 1000, and 1500 Hz.....	116

Figure 6.18: Left: Time delay vs. frequency plot of case 3 with $k_3 = 6$ N/m, Right: Time delay vs. angle of incidence at 500, 1000, and 1500 Hz.....	116
Figure 6.19: Left: Time delay vs. frequency plot of case 4 with $k_3 = 13$ N/m, Right: Time delay vs. angle of incidence at 500, 1000, and 1500 Hz.....	116
Figure 6.20: Left: Time delay vs. frequency plot of case 4 with $k_3 = 50$ N/m, Right: Time delay vs. angle of incidence at 500, 1000, and 1500 Hz.....	117
Figure 6.21: Left: Time delay vs. frequency plot of case 4 with $k_3 = 12$ N/m, Right: Time delay vs. angle of incidence at 500, 1000, and 1500 Hz.....	117
Figure 6.22: Left: Time delay vs. frequency plot of case 4 with $k_3 = 3.5$ N/m, Right: Time delay vs. angle of incidence at 500, 1000, and 1500 Hz.....	117
Figure 6.23: Left: Time delay vs. frequency plot of case 4 with $k_3 = 3.5$ N/m, Right: Time delay vs. angle of incidence at 500, 1000, and 1500 Hz.....	118
Figure 6.24: Time delay vs. Incidence angle.....	121
Figure 6.25: Left: Polar plot at 75 Hz. Right: Time delay vs. Incidence angle at 75 Hz.	122
Figure 6.26: Left: Polar plot at 100 Hz. Right: Time delay vs. Incidence angle at 100 Hz. .....	122
Figure 6.27: Left: Polar plot at 125 Hz. Right: Time delay vs. Incidence angle at 125 Hz. .....	122
Figure 6.28: Left: Polar plot at 135 Hz. Right: Time delay vs. Incidence angle at 135 Hz .....	123
Figure 6.29: Left: Polar plot at 155 Hz. Right: Time delay vs. Incidence angle at 155 Hz .....	123
Figure 6.30: Left: Frequency response based on the 5 DOF lumped parameter model. Right: Frequency response based on FEA harmonic analysis.....	123
Figure 6.31: Variable fluid loaded mass.....	124
Figure 6.32: Left: Phase difference between $x_1$ and $x_2$ based on the 5 DOF lumped parameter model. Right: Phase difference based on FEA harmonic analysis.....	125
Figure 6.33: Left: Output time delay based on the 5 DOF lumped parameter model. Right: Output time delay based on FEA harmonic analysis.....	125
Figure 6.34: Output time delay for the cutoff frequency of 360 Hz.....	126

Figure 6.35: Left: Polar plot at 100 Hz. Right: Output time delay vs. angle of incidence at 100 Hz.....	126
Figure 6.36: Left: Polar plot at 200 Hz. Right: Output time delay vs. angle of incidence at 200 Hz.....	126
Figure 6.37: Left: Polar plot at 300 Hz. Right: Output time delay vs. angle of incidence at 300 Hz.....	127
Figure 6.38: Left: Polar plot at 315 Hz. Right: Output time delay vs. angle of incidence at 315 Hz.....	127
Figure 6.39: Left: Polar plot at 400 Hz. Right: Output time delay vs. angle of incidence at 400 Hz.....	127
Figure 6.40: Left: Frequency response based on the 5 DOF lumped parameter model. Right: Variable fluid loaded mass.....	128
Figure 6.41: Left: Polar plot. Right: Output time delay vs. angle of incidence at 1590 Hz. .....	128
Figure.6.42: Output time delay for cutoff frequency at 1600 Hz. ....	129
Figure 6.43: Left: Time domain representation of a modulation signal x1 with band-limited white noise. Right: Frequency domain representation of a modulation signal x1 with band-limited white noise.....	130
Figure 6.44: Left: Time domain representation of a modulation signal x1 with band-limited white noise. Right: Frequency domain representation of a modulation signal x1 with band-limited white noise.....	130
Figure 6.45: Directional sensitivity at 75 and 100 Hz from left to right plot based on the 5 DOF lumped sensor model without damping ( $\beta = 0$ ). ....	131
Figure 6.46: Directional sensitivity at 75 and 100 Hz from left to right plot based on the 5 DOF lumped sensor model with damping ( $\beta = 8.54e-6$ ). ....	131
Figure 6.47: Example of Rayleigh damping ratio which varies with frequency. ....	132
Figure 7.1: FEA Simulated Sensitivity of the Acoustic Sensor in Water.....	134
Figure 7.2: Left: Time domain representation of a modulation signal x1 with band-limited white noise. Right: Frequency domain representation of a modulation signal x1 with band-limited white noise.....	135

Figure 7.3: Left: Time domain representation of a signal $x_1$ with white noise processed by high pass filter. Right: Frequency domain representation of a signal $x_1$ with white noise processed by high pass filter.....	135
Figure 7.4: Left: Time domain representation of a signal $x_1$ in the presence of white noise. Right: Frequency domain representation of a signal $x_1$ in the presence of white noise..	137
Figure 7.5: Left: Phase difference of signals $x_1$ and $x_2$ in the presence of white noise. Right: Time delay calculated from the phase difference at 3000 Hz.....	137
Figure 7.6: FEA simulation of the sensor in water solving weakly compressible Navier-Stokes equation. ....	140
Figure 7.7: x-axis velocity at 5 vertical lines shown in Figure 7.6 from left to right order. ....	141
Figure 7.8: Y-displacement of the cantilever beam under normal inflow velocity of 0.1 m/s.....	141

## LIST OF TABLES

Table 2-1: Properties of silicon and selected other materials .....	13
Table 2-2: Natural frequencies of the baseline mechanically coupled sensor .....	17
Table 2-3: Comparison for natural frequencies of the mechanically coupled sensor .....	26
Table 2-4: Comparison for natural frequencies of between 5 DOF and FEA model .....	34
Table 4-1: Comparison of added mass at 18,115 Hz for 20 by 20 mm plate (Translational). .....	59
Table 4-2: Comparison of added mass for 1 by 1 mm plate (Translational). .....	60
Table 4-3: Comparison of added mass at 18,115 Hz for 20 by 20 mm (Rotational).....	60
Table 4-4: Comparison of added mass for 1 by 1 mm (Rotational) .....	60
Table 4-5: Comparison table of added mass for 10 by 10 mm (Rotational).....	61
Table 4-6: Comparison table of added mass for 25 by 25 mm (Rotational).....	61
Table 4-7: Natural frequencies of the sensor in water (Hz): Simulation results.....	65
Table 4-8: Comparison of first two natural frequencies for 6e-6 m thickness sensor. ....	70
Table 4-9: Comparison table of the damping effect based on FEA simulation.....	78
Table 4-10: Table of dominant terms for each frequency of interests .....	85
Table 5-1: Number of elements and nodes for three meshes of each element type.....	90
Table 5-2: Natural frequencies of the cantilever beam in various medium (kHz): Experimental and Simulation results .....	96
Table 5-3: Fundamental resonant frequencies in vacuo and air: FEM and Sader [29].....	97
Table 6-1: Sensor sizes for the second natural frequency study.....	109
Table 6-2: Comparison between simulation results.....	128

## **ACKNOWLEDGEMENTS**

I would like to thank my parents Hyunsook Yoo and Sunwon Lee who have always given me support throughout my years of schooling. Without which, I never would have done it.

I am very grateful to my advisor, Professor Per G. Reinhall, who is such a gentleman for his patient guidance, continued encouragement, suggestions, and giving me a chance to pursue my dream of teaching. Through the opportunities given by him, I've gained invaluable experience in terms of research as well as teaching.

I would also like to thank Professor Brian Fabien, who is my role model as a teacher, for letting me learn from his class and suggestions and guidance.

I would also like to thank all the graduate students and staff members in the Department of Mechanical Engineering as well as all the students who have taken my classes. From them, I've learned a lot.

I would like to express my appreciation to the Department of Mechanical Engineering at the University of Washington for providing teaching assistantships and pre-doctoral lecturer position for many years.

Finally, I wish to thank my wife, Jihyun, and two sons, Jeff and Jimmy, for their endless encouragement, support and love through my long years of study.

# Chapter 1. Introduction

## 1.1 Motivation and Introduction

Nature has fantastic designs, and engineers often copy them to make new inventions and/or the existing product better. The mimicry of ideas from nature is called biomimetics. Biomimetic sensors are mainstream research areas alongside with nanotechnology and micro-fabrication. A sensory system of a living creature provides input to the central nervous system about their environment and the muscles are commanded to function upon the analysis of the received information. Pressure, optical, and acoustical sensors are ubiquitous and are continuously being redesigned to improve their sensing capability and reduce their size as well as the required power. Biomimetics is mimicking ideas from biology and includes adapting principles from the eyes to camera, the sensing hairs of crickets as flow-sensors as well as the ciliar-based lateral line system of fish for detecting flow patterns in air and water [1]. Even though not all biomimetic sensors function based on the biological principle being copied, the engineer can decide the best course of action once the biological system is fully comprehended.

While there are an ample number of underwater sensors and underwater sensor network systems available, miniature underwater sensors for directivity based on biomimetics are rather scarce. Francois Guillot from the Georgia Institute of Technology has created an optical fiber sensor that detects the direction from which a sound is coming under water, which is inspired by how fish hear under water. Inside a fish's ear, there are thousands of tiny hairs that move when a sound wave passes through the fish. A. D. Pierce from Boston University investigated the MEMS hydrophone in order to find mines in littoral waters, which operates under a frequency range of 1 to 3 MHz. Many researchers [2] have been working on MEMS based hair flow sensors inspired by the hairs found on the cerci of crickets. Directional sensitivity measurements are successfully carried out on fabricated hair flow sensor arrays on frequency ranges of 85 to 500 Hz [3]. Whereas hair length greatly influences a hair's mechanical sensitivity in water, hair diameter is of only minor importance [2]. MEMS hydrophone and hair sensors both utilize fiber optic sensing techniques to displace traditional sensors. The advantages of fiber optic sensors include lightweight, very small size, passive, lower power, resistant to electromagnetic interference, and

high sensitivity. On the other hand, the disadvantages are high cost and that the technology is unfamiliar to the end user.

Hydrophones are the basic acoustic sensing elements in an underwater acoustic system and are usually piezoelectric or magnetostrictive type. In order for a hydrophone to detect the directivity, two or more hydrophones have to be used as an array to give a sense of direction since a single hydrophone is omni-directional, in other words direction insensitive. The number of hydrophones needed varies with application. Hence, this kind of direction sensing can be expensive if a large number of hydrophones are involved, and the large computational power needed. In addition, Unmanned Underwater Vehicles (UUVs) currently cannot autonomously turn to investigate an explosion occurring on its right or left side for further analysis. Existing sensors cannot determine the angle the sound came from in order for the autonomous system to decide which way to turn the vehicle. Unfortunately, an explosion is too short in duration to use the Doppler Effect to determine the bearing to the explosion; so current searches must involve a system with less than full autonomy. This practice could be eliminated if an array of directional microphones, small enough with low power consumption, could be developed and perfected. Vector sensors can have an important advantage in towed-line arrays by resolving the right-left ambiguity inherent in single-line arrays of hydrophones without requiring a time consuming course change by the towing ship.

A common method of sensing directivity of sound underwater is to use a four channel intensity vector sensor. It consists of a hydrophone and three directional underwater sensors that directly measure each orthogonal component of a particle's acoustic acceleration. One current state of the art sensor of this type is Wilcoxon VS-301 which is a low frequency vector sensor. This vector sensor, which uses separate single crystals to measure acceleration and a hydrophone to measure pressure, can fit in a housing of 0.8 inches in diameter and 3.124 inches in length thanks to the new, single-crystal piezoelectric material [4]. The greatest limitation of existing vector sensors is that they are all too large to be considered as a Micro Electro-Mechanical System (MEMS) sensor application such as for a miniaturized submersible explorer [5]. The sensitivity of the sensor is decreased as the size is reduced. For the reason, it is advantageous to design an underwater acoustic sensor which is small enough and capable of detecting the directivity of the sound accurately for micro scale applications.

Mechanically generated sound waves can travel very far under water. On the other hand, electromagnetic waves at frequencies in the frequency range (3 ~ 30 kHz) can't penetrate more

than 40 meter maximum [6]. Machinery makes characteristic mechanical sounds that can be used for the detection, localization, and classification of vessels.

With the proposed acoustic sensor in this work, we present a methodology and feasibility of a miniature sensor that detects the sound as well as its direction from which a sound is coming under water. Through analysis of the sensor, we will explore the capability of fabricating the sensor with the help of standard micro-fabrication technology.

## 1.2 Acoustic Vector Sensor (AVS)

During the past decades, scalar type sensor such as hydrophone that only measures pressure component of acoustic field is utilized extensively, in field of oceanography. Recently, vector type sensor starts to replace conventional scalar sensor in various sonar applications even though the first particle-velocity sensor for underwater use was developed in 1965 by Leslie *et al.* It has not been until recently that they have attracted much attention. It measures both scalar (pressure) and vector (wave velocity) components of acoustic field. Currently, there are two types of vector sensor namely inertial and gradient vector acoustic sensor. Gradient sensors measure the gradient of the acoustic pressure in one direction to obtain the velocity or acceleration by employing finite difference approximation and acceleration, whereas inertial sensors directly measure the acoustic medium's motion in a specific direction. As the result, four channel vector acoustic sensors not only are smaller in dimension, but also allow narrower beams to be generated with a smaller number of sensors can be obtained from a scalar acoustic sensor. Latest application of vector type acoustic sensor is Wilcoxon TV-001 vector sensor [7].

Figure 1.1 shows the Wilcoxon TV-001 vector sensor which is made highly sensitive, and low-noise in a small, neutrally buoyant package. It was not possible using existing piezoelectric materials, however, a new piezo-material, lead magnesium niobate/lead titanate ( $\text{Pb}(\text{Mg}_{1/3}\text{Nb}_{2/3})\text{O}_3\text{-PbTiO}_3$ ), known as PMN-PT crystals, has made it possible to develop such a sensor. This material has 7~10 times greater piezoelectric properties than conventional piezoelectric ceramic materials, such as lead zirconate titanate (PZT). This allows the sensor to be light and small while maintain a specific sensitivity and signal-to-noise ratio. In the class of acoustic velocity sensors, a number of different types transducers have been constructed, such as those based on the change in inductance of a metallic glass strip, highly sensitive moving-coil geophones, piezoceramics, and fiber optics.

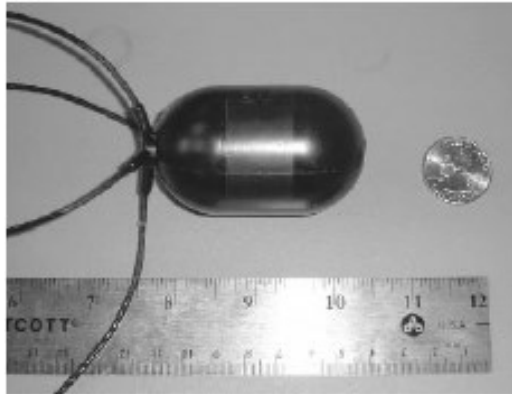


Figure 1.1: Wilcoxon TV-001 vector sensor [7]

As for the vector sensor based upon MEMS technology, the Microflown sensor uses the temperature difference in the cross section of two extremely sensitive heated wires to determine the acoustic particle velocity. Assembling a sound pressure transducer and three orthogonally placed Microflown sensors in one single point, a very compact (5 x 5 x 5 mm) acoustic vector sensor (AVS) has been made. Collaborating with SUASIS Underwater Systems Technology R&D Ltd., Microflown Technologies are working on the Hydroflown which is underwater Microflown sensor. The Hydroflown, a MEMS based AVS, measures particle velocity and its direction in nanoscales. The Hydroflown is able to measure the particle velocity in a bandwidth of one hertz to 20 kHz. The Microflown measures particle velocity using two parallel platinum wire resistances. When voltage is applied across the wire terminals, the wires heat up to 300° C. An acoustic wave propagating perpendicular to the wires results in a temperature difference between the wires. To adapt the Microflown sensors for underwater use, the MEMS design and packaging have been modified, and the prototypes is going through tests for static applications [8].

Hawkes presents some issues with the gradient type sensors which estimate the velocity by differencing the measurements from two nominally identical pressure sensors then integrating the result. Hawkes considered those sensors not suitable for vector-sensor processing for a number of reasons: (1) at low frequency the differencing is susceptible to mismatch; (2) at high frequency the sensor pair is not point-like and their linearized estimate of the gradient is inaccurate; (3) the noise is typically non-white due to the integration time [9].

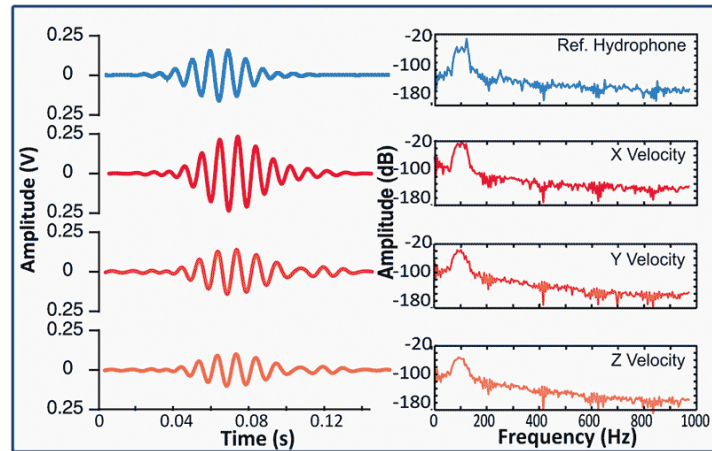


Figure 1.2: The directional beam patterns of the microelectromechanical-based Hydroflown and examples of time and frequency domain plots [8].

When smaller and compact vector sensor is not small enough to fit several applications, a lot of efforts needed to take place to shrink the size down to micro-level. Owing to microelectronics technology and advanced computer aided design, both capacitive type and piezoelectric type acoustic sensors have been successfully miniaturized for underwater applications. In comparison however, development of micro-acoustic sensor for underwater used is relatively slow compared to airborne applications.

Our hydro-sensor, which is based on MEMS technology, will suit for light weight platforms such as portable diver device, remotely operated vehicles (ROV) and unmanned underwater vehicles (UUV) as well as many underwater applications where micro-level is necessary.

### 1.3 Background to Directivity Detection

It is well known that the direction of sound propagation can be detected using an array of microphones. A sound wave, which is a mechanical wave, moves through a medium at a constant velocity. Knowing the signal phase of the measured sound wave and the position of each microphone, it is possible to calculate the angle of the incoming plane wave in relation to the axis of the array.

However, the angular resolution of such array becomes an issue as the spacing of the microphone array gets smaller. Angular resolution describes the resolving power of an array of microphones. Since the resolving power is the ability of the components of the device to measure

the angular separation of the location of a sound, the term resolution refers to the minimum angle between distinguishable sound sources. The resolving power of a pair of microphones is ultimately limited by the ability to measure the time delay of the sound between each microphone face. Since the time delay  $\tau$  is a function of the distance of the microphone  $d$ , speed of sound  $c$ , phase difference  $\phi$ , or frequency of sound wave  $f$ , the minimum time delay of the sound wave to be resolved is dependent on those factors where they are interrelated each other. These relationships will be dealt with more in detail in a later section. In general, as the spacing of the microphones becomes smaller, it gets harder for the incoming sound wave to be resolved; meaning that directivity of the sound becomes incoherent.

Due to the physics of sound propagation, decreasing the distance between the sound receivers results ultimately in vanishingly small amplitude difference and time cues. As the separation of two microphones is decreased, the time difference between them becomes too small to detect with standard methods. This is demonstrated by the remarkable feat of measurement by the ear of the parasitoid fly *Ormia ochracea*. From the fly's small size and the resulting minute interaural distance, the largest interaural time difference (ITD) generated by a passing sound wave does not exceed  $2 \mu\text{s}$  [10]. Such a time difference is clearly too small to be encoded by the nervous system of the fly. For humans, interaural time differences at such an angle of incidence are much larger, varying from  $500 \mu\text{s}$  to  $700 \mu\text{s}$ , depending on head size, the sound path considered, and the frequency considered. Thus, it becomes apparent that microsecond-range interaural time differences, and possibly smaller ones, would cause a major difficulty for the auditory system of the fly, both at the mechanical and neural coding point of view. Another difficulty arises when the second directional cue, the interaural intensity difference (IID), is considered. The behaviorally relevant frequency range is that of the cricket's calling song, which spans from 4.6 to 5.2 kHz – since *Ormia ochracea* is a parasitoid fly meaning that gravid female have to locate and deposit her parasitic larvae on a live field cricket [11]. Since at such frequencies the ratio of wavelength (66 mm at 5.2 kHz) to interaural distance ( $520 \mu\text{s}$ ) is larger than 100, diffraction is very unlikely to occur around the fly's body, or at her ears [12].

## 1.4 Research Objectives

The objective of the research is to analyze and to test the feasibility, as well as to optimize the design, of a MEMS (Micro Electro-Mechanical System) underwater differential sensor for

directivity. Inherent in this work is the exploitation of digital signal processing (DSP) analysis to see how the sensor work in the far field (Fraunhofer zone) where the sound wave becomes planar and the investigation of interaction of the sensor components with fluid medium. It has been shown that this novel hearing sensing ability of parasitoid fly *Ormea Ochracea* has potential in air through the work of Miles and *et al* (1995). The way the sensor works is that it can amplify the phase difference at each end of the sensor using the mechanical coupling mechanism. The direction of the sound can be found through the relationship between the phase difference and the angle of incidence through the time delay. When a sound signal is applied to a sensor, a DSP program can manipulate the output of the sensor and generate a corresponding phase difference of the sensor as an output; hence we can calculate the angle of incidence through the time delay calculation; detailed information on the operation of the sensor system will be discussed in Chapter 3. However, its possibility as a sensor has only been studied in air where the density of the medium is not significant.

Finding a direction of the sound source from the sensor is possible by comparing with mapping information in frequency domain which best approximates the directivity of the source of the sound. From the frequency response of the sensor, we have full range of relationship between the incidence angle and the time delay whereas only the time delay and the frequency information is known from the direct measurement of the sensor. We need to read the angle of incidence from the frequency response based on the measurements; frequency and time delay. Therefore, two independent analyses must be defined and solved: Time domain and frequency domain analyses. The former analysis is used to simulate the actual process and the latter is used to verify the results of that of time domain.

In both analyses, the directivity, hence the directivity of the sound source or sources, should be calculated and compared to find the location of the source, where frequency analysis data is mapped to be used as baseline information and time domain analysis is used to simulate the physical data collection of the sensor at each end. From the direct measurements in the time domain, we can collect the data as  $x_1$  and  $x_2$ ; displacements at each end of the sensor. Using the fast fourier transformation (FFT), we can calculate each phase  $\phi$ 's of  $x_1$  and  $x_2$ . They can be used to calculate the time delay  $\tau$  based on the relationship between the phase difference and the time delay;  $\tau = \Delta\phi/\omega$ , where  $\omega$  is the angular frequency. With this, we can extract an angle of incidence of the sound by reading the mapping plot of the incidence angle vs. time delay from the frequency

domain and this is used as the design parameter toward the values corresponding to the sensor's characteristic performance.

The complexity of the structure-fluid interaction calculations and the large number of design parameters make the finite element method (FEM) the best choice for the analysis and evaluation tool due to its ability to encompass all the methods for connecting many simple element equations over many subdomains to approximate a solution over multi-domain problems. COMSOL® Multiphysics has been chosen as the finite element package for this work.

In order to design our novel directional sensor, this research is subdivided into five objectives:

1. **Develop various models to study the characteristics' of the sensor inspired by parasitoid fly *Ormea Ochracea* in water.** Taking into consideration the effects of water, various analyses/idealizations will be performed and implemented for further study. This will be done – via the use of lumped parameter, continuous, and FEM models. Time and frequency domain analyses as well as sensitivity analyses of the sensor will be incorporated in to the design process and feasibility evaluation. The modeling of the sensor is done considering a frequency dependent fluid loading.
2. **DSP analysis of the sensor output.** In this stage, a DSP program will be written and tested through various simulations with the model developed to find the directivity of the sound wave impinging on the sensor. Based on the simulation result, the process of calculating the phase difference hence the output time delay will be introduced. Performance of the sensor under the noise such as thermal noise is further discussed in chapter 7.
3. **Develop design method through the sensor characteristics study.** The design method of the sensor is to be sought based on the analyses in this study to fall within a specific design goal of the bandwidth and the time delay amplification in terms of frequency through simulation. This can incorporate the FEM (Finite Element Method) and works to find the better sensor design depending on the designer's objective.
4. **Expand the feasibility analysis by incorporating FEM analysis.** This will enable the part of the design process to be accomplished in one software package since COMSOL® has a built-in module to deal with the structure-fluid interaction along with an acoustic module. This will also help in the evaluation of the accuracy of the discrete model. Weakly compressible Navier-Stokes analysis based on COMSOL® is also discussed for the effect of rigid body motion of the sensor under water.

5. **Design optimization of the sensor.** Incorporating the first two modes of the sensor, design optimization is to be performed in order to increase the ability of the sensor to sense direction.

After it is designed and its operation methodology is developed, the mechanically coupled sensor will be simulated and compared to each other using Matlab and Simulink, and COMSOL®.

## 1.5 Outline

The remainder of the dissertation follows the outline below.

In chapter 2, we will present a review of Miles' work regarding the modeling of mechanically coupled differential sensor for directivity in terms of time domain as well as frequency domain. Governing equations for the analysis are derived and shown in this section. The lumped parameter approach, continuous, and FEM based lumped parameter models are presented. Miles model takes into consideration of torsional spring at the coupling joint, which was modeled as the spring constant  $k_3$  without any detailed physical relation. His model can be used for our case, however, his model does not have any detailed way to design the sensor such as type of torsional spring and how to specify the spring constant with design changes. Considering our sensor as a 2-D model sensor, it is beneficial for us to analyze it assuming as 2-D plane strain, which can save time and computing memory when it comes to FEM multi-physics simulation.

After thorough and comprehensive analysis using both time and frequency based DSP, the methodology of how the sensor will be used to detect the directivity is presented. Chapter 3 shows the DSP simulation of the sensor in air. The sensor system as well as DSP code is tested in this chapter since the operation method and DSP code works the same way regardless of the fluid medium. Performance of the sensor under water is presented throughout the Chapters 4, 5, and 6 and its performance in noisy environments is discussed in Chapter 7.

In Chapters 4 and 5, we will investigate the directional sensitivity of the sensor in water and show the feasibility of the sensor through rigorous simulation based on the ordinary differential equations as well as the finite element analyses. The model of the sensor developed in Chapter 2 is integrated with the fluid loaded mass which is a function of frequency. Acoustic fluid structure interaction is studied using COMSOL®. The Navier-Stokes equation for a weakly compressible medium is incorporated to study the rigid body motion of a cantilever plate in water and it is discussed in Chapter 7. Our sensor is simply the two plates/beams coupled together and

symmetrical with respect to the coupling point. Hence if we take advantage of symmetry, it becomes a simple plate or a beam. The need for the design optimization is presented with examples in Chapter 6. Based on the design methodology through parametric analyses, the design optimization is presented in Chapter 6. It is done based on a nonlinear optimization strategy using Matlab. Lastly the general design methodology will be discussed based on previous analyses. Chapter 7 is a discussion about the performance of the sensor in noisy environments and the effect of fluid flow over the sensor.

Finally, Chapter 8 presents the challenges of the current research as well as future work.

## Chapter 2. Modeling and Characteristics of the Sensor

### 2.1 Mathematical Modeling of the Acoustic Sensor

In this chapter, characteristics of the sensor are investigated via modeling of the mechanically coupled sensor which can be used for DSP analysis, design methodology, and design optimization. Figure 2.1 shows a mechanical model of the coupled ears of a fly based on considering those elements which are expected to contain the most kinetic and potential energy during vibration [11]. Miles *et al.* represents that the response  $x_1(t)$  and  $x_2(t)$  of the two ends of the intertympanal bridge shown in the idealization in Figure 2.1 can be obtained by solving the following second order ordinary differential equation.

$$\begin{bmatrix} m & 0 \\ 0 & m \end{bmatrix} \ddot{x} + \begin{bmatrix} c_1 + c_3 & c_3 \\ c_3 & c_2 + c_3 \end{bmatrix} \dot{x} + \begin{bmatrix} k_1 + k_3 & k_3 \\ k_3 & k_2 + k_3 \end{bmatrix} x = f \quad (2-1)$$

where  $x = \begin{pmatrix} x_1(t) \\ x_2(t) \end{pmatrix}$  represents the unknown response vector, and  $f = \begin{pmatrix} f_1(t) \\ f_2(t) \end{pmatrix}$  represents the

applied force of the far field sound wave at each end of the bar respectively. In this mechanical model, the intertympanal bridge is assumed to consist of two rigid bars connected at the pivot through a coupling spring  $k_3$  and a damper  $c_3$ . Springs and dampers shown in Figure 2.1 at the far end of the bridge (① and ②) represent the dynamical properties of the tympanal membranes, and surrounding structures. The constant  $m$  accounts for the effective mass of all moving elements of the system and is assumed to be concentrated at each end of the intertympanal bridge. Solving Eq. 2.1, the transfer functions of  $H_{x_1,p}(\omega)$  and  $H_{x_2,p}(\omega)$  are obtained between the responses and the input pressure by the transfer function of forces relative to the acoustic pressure,  $H_{f_1,p}(\omega) = se^{i\omega\tau/2}$  and  $H_{f_2,p}(\omega) = se^{-i\omega\tau}$  where  $\tau$  is the time for incident sound and  $s$  is the membrane's surface area.

Previous mechanical studies on this acoustic sensor inspired by *Ormia ochracea* by Miles *et al.* (1995) largely focused on the steady-state sensory response to harmonic sounds in frequency domain, mostly evaluating the data through conventional Fourier transforms. Here, however, we

report on the time-resolved mechanical behavior of the sensor by using state space model based simulation in the time domain with digital signal processing and analysis.

$$H_{x_1p}(\omega) = \frac{s(k_3 + i\omega c_3) \times (e^{i\omega\tau/2} - e^{-i\omega\tau/2}) + s(k + i\omega c - m\omega^2)e^{i\omega\tau/2}}{(k + i\omega c + k_3 + i\omega c_3 - m\omega^2)^2 - (k_3 + i\omega c_3)^2} \quad (2-2)$$

$$H_{x_2p}(\omega) = \frac{s(k_3 + i\omega c_3) \times (e^{-i\omega\tau/2} - e^{i\omega\tau/2}) + s(k + i\omega c - m\omega^2)e^{-i\omega\tau/2}}{(k + i\omega c + k_3 + i\omega c_3 - m\omega^2)^2 - (k_3 + i\omega c_3)^2}$$

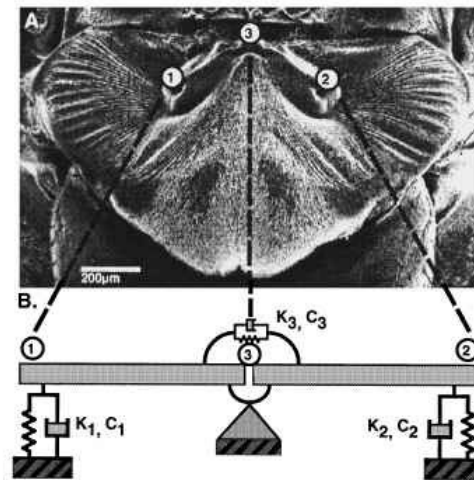


Figure 2.1: Mechanical model of ears of *Ormia ochracea* [10]

As a baseline sensor inspired by the parasitoid fly, its specification has to be chosen prior to modeling. The specifications of the sensor were taken from the ears of *Ormia ochracea* which has been extracted by measurement and the parameters of the model have been found by minimizing the least-square-error between the predicted and measured frequency responses [10]. The size of each sensor is 1 mm by 1 mm with 1  $\mu$ m thickness with an effective mass is estimated to be  $2.88 \times 10^{-10}$  kg. The remaining parameters used in the model in Eq. 2.1, Eq. 2.2, and Eq. 2.3 are  $k_1 = k_2 = 0.576$  N/m,  $k_3 = 5.18$  N/m,  $c_1 = c_2 = 1.15 \times 10^{-5}$  N s/m,  $c_3 = 2.88 \times 10^{-5}$  N s/m, and  $s = 0.288 \times 10^{-6}$  m<sup>2</sup>. The value of  $s$  has been taken from Robert *et al.* (1994). These design parameters are to be modified when it is submerged in water. The materials being considered for the sensor are silicon and PDMS (polydimethylsiloxane). Considering the buoyancy stiffness, due to being placed in water and impedance matching, PDMS has an advantage since it has almost the same density as

water. In addition, silicon is desirable for mechanical micro sensors due to its wide use within the microelectronic integrated circuit industry, well understood and controllable electrical properties, availability of existing design tools, economical to produce single crystal substrates, vast knowledge of the material exists, and its desirable mechanical properties [13]. It is elastic up to its fracture point, is lighter than aluminum, and has a modulus of elasticity similar to stainless steel. Besides, it has a lower density than other well-known materials as shown in Table 2-1.

Table 2-1: Properties of silicon and selected other materials [13]

<i>Property</i>	<i>Si {111}</i>	<i>Stainless Steel</i>	<i>Al</i>	<i>Al<sub>2</sub>O<sub>3</sub> (96%)</i>	<i>SiO<sub>2</sub></i>	<i>Quartz</i>
Young's modulus (GPa)	190	200	70	303	73	107
Poisson's ratio	0.22	0.3	0.33	0.21	0.17	0.16
Density (g/cm <sup>3</sup> )	2.3	8	2.7	3.8	2.3	2.6
Yield strength (GPa)	7	3.0	0.17	9	8.4	9
Thermal coefficient of expansion (10/K)	2.3	16	24	6	0.55	0.55
Thermal conductivity at 300K (W/cm·K)	1.48	0.2	2.37	0.25	0.014	0.015
Melting temperature (°C)	1,414	1,500	660	2,000	1,700	1,600

In order to simulate the sensor model in the time domain, Matlab & Simulink are used as a modeling tool. It is known that the forced response of a damped system to a harmonic disturbance is of the same frequency as the driving force but with a different amplitude and phase. The state space model of the sensor shown in Eq. 2-3 can be derived based on Eq. 2.1. Eq. 2.3 contains the four governing first order ordinary differential equations for the sensor model.

To validate the model, Eq. 2-3 is numerically solved in the time domain and compared to the Bode plots corresponding to the transfer function shown in Eq. 2.2. One of the extreme cases along with two in the middle of the range have been tested based on the fact that the range of hearing for a healthy young person is 20 to 20,000 hertz (Hz) or 15 to 15,000 Hz. The response plot of an input at 2000 Hz for  $x_1$  is shown in Figure 2.2 and its magnitude,  $M$ , is  $2.89 \times 10^{-8}$ . Using  $\text{dB} = 20 \times \log_{10}(M)$ , the magnitude of this graph reaches -150.7 decibels (dB), which corresponds to the Bode diagram from the steady state section. By repeating these steps with a frequency of 6000 Hz and 15000 Hz, and comparing them with the Bode plot, it is validated that simulation results from both domains show a very good agreement to each other.

$$\begin{aligned}
\bullet \\
x_1 &= x_3 \\
\bullet \\
x_2 &= x_4 \\
\bullet \\
x_3 &= \frac{f_1}{m} - \frac{(k_1 + k_3)}{m} \cdot x_1 - \frac{k_3}{m} \cdot x_2 - \frac{(c_1 + c_3)}{m} \cdot x_3 - \frac{c_3}{m} \cdot x_4 \\
\bullet \\
x_4 &= \frac{f_2}{m} - \frac{k_3}{m} \cdot x_1 - \frac{(k_2 + k_3)}{m} \cdot x_2 - \frac{c_3}{m} \cdot x_3 - \frac{(c_2 + c_3)}{m} \cdot x_4
\end{aligned} \tag{2-3}$$

where  $\begin{cases} f_1 = P \cdot \sin(\omega \cdot t + \omega \cdot \tau/2) \\ f_2 = P \cdot \sin(\omega \cdot t - \omega \cdot \tau/2) \end{cases}$  and  $x_1$  and  $x_2$  are the displacements of ① and ② of the sensor in Figure 2.1

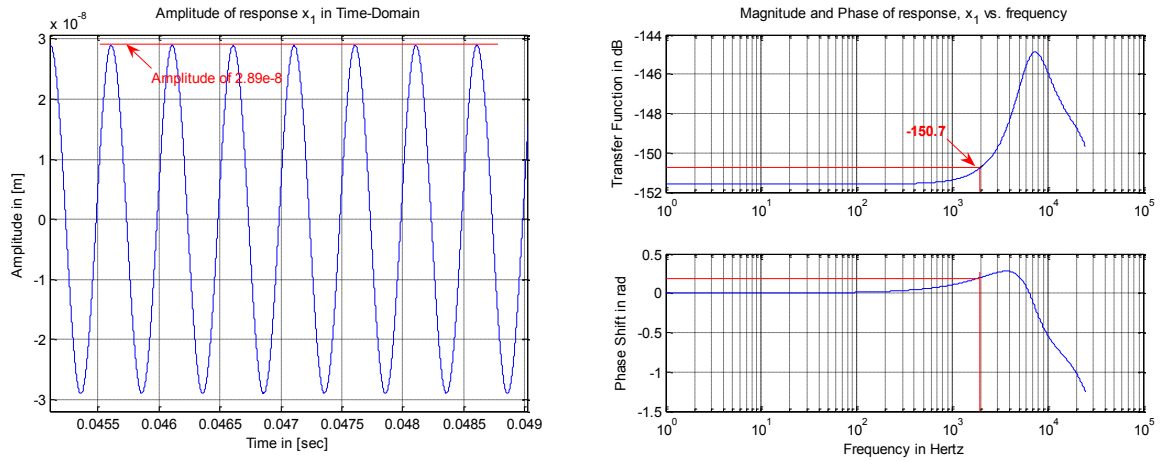


Figure 2.2: Left: Response plot of  $x_1$  and magnitude for input frequency at 2000 Hz. Right: Frequency response of the transfer function 1 (Ipsilateral).

## 2.2 Characteristics of the Sensor Model

In Eq. 2.2, input time delay of the sensor represents  $\tau = d \sin(\theta)/c$ , where  $d$  is the distance between the effective points of application where the displacements ( $x_1$  and  $x_2$ ) are measured and  $c$  is the speed of sound which is about 344 m/s for air, and the direction of propagation of the incident wave is at an angle  $\theta$ , is relative to the sensor's longitudinal axis. The input time delay is easily found to be  $\tau = 2.5 \mu\text{s}$  assuming  $d \approx 1.2$  mm and  $\phi \approx 45^\circ$ . Due to the mechanical coupling of the sensor, this input time delay is enhanced as output time delay by a factor of 40 at 5 kHz. Without this mechanical coupling, it becomes just a bar with a pair of microphone on each end. Then, it would have provided no level difference as a rigidly coupled pivot system. Physically for the sensor this means that the coupling spring constant  $k_3$  of the sensor becomes infinite. It is shown in

Figure 2.3 that the output time delay has been amplified by the sensor's coupling mechanism for frequencies near zero to 25 kHz where low frequencies are usually most useful for underwater sound detection and communication.

The difference in mechanical responses,  $x_1$  and  $x_2$ , of the sensor depends on the angle of incidence of the sound since the transfer functions of  $H_{x_1p}(\omega)$  and  $H_{x_2p}(\omega)$  are a function of the input time delay  $\tau_i$ , which is also a function of incident angle  $\theta$ . The analytical model predicts the output time delays between the mechanical responses which depend on the angle of incidence relative to the forward direction  $\theta$ . The dependency of the output time delay which the analytical model accounts for is shown in Figure 2.4.

Considering the undamped system, we can first solve the eigenvalue problem and use the modal matrix to decouple the system into modal equations. Therefore, the first two eigenvalues can be found as

$$\begin{aligned}\lambda_1 &= \frac{k}{m} \\ \lambda_2 &= \frac{k + 2k_3}{m}\end{aligned}\tag{2-4}$$

Using the numerical values of the physical parameters for the baseline sensor, the eigenvalues are

$$\lambda_1 = 2.00 \times 10^9 \quad \lambda_2 = 3.79 \times 10^{10}\tag{2-5}$$

The matrix of eigenvectors  $P$  is obtained for  $\lambda$  as

$$P = [v_1 \quad v_2] = \begin{bmatrix} -0.707 & 0.707 \\ 0.707 & 0.707 \end{bmatrix}\tag{2-6}$$

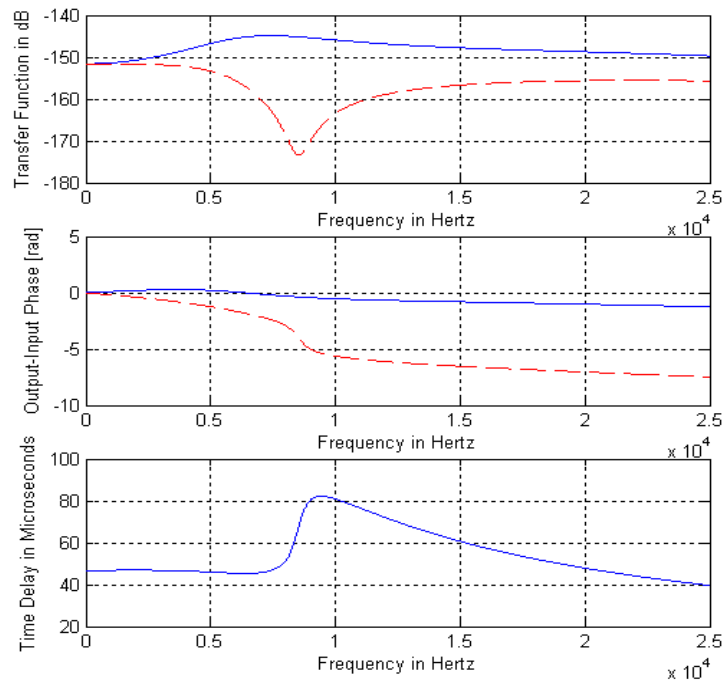


Figure 2.3: Mechanical responses obtained from the transfer functions in amplitude, phase, and time delay: Blue solid line and red dotted line represent responses of the transfer function 1 and 2

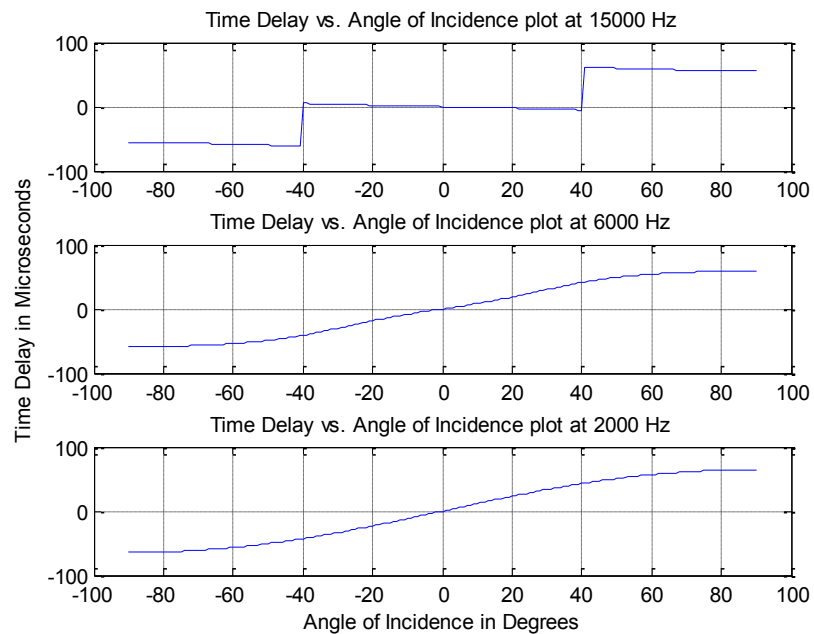


Figure 2.4: The predicted time delays between the mechanical response of  $x_1$  and  $x_2$  depending on the angle of incidence at various frequencies (2000, 6000, 15000 Hz).

Using the relationship between the eigenvalues and the natural frequencies  $\lambda_i = \omega_i^2$ , the normal mode angular frequencies are obtained. This is shown in Table 2-2.

Table 2-2: Natural frequencies of the baseline mechanically coupled sensor

		[Hz]
Natural Frequencies	Mode 1	7,118
	Mode 2	31,014

The eigenvector defines the relative displacement of each sensor plate,  $x_1$  and  $x_2$ . Hence, there exist two modes as calculated from Eq. 2.6, rocking (out of phase) mode and bending (in phase) mode with two corresponding natural frequencies,  $\omega_r$  and  $\omega_t$ , tabulated in Table 2-2. The subscript  $r$  and  $t$  represent rocking and translational bending mode. This is shown in Figure 2.5.

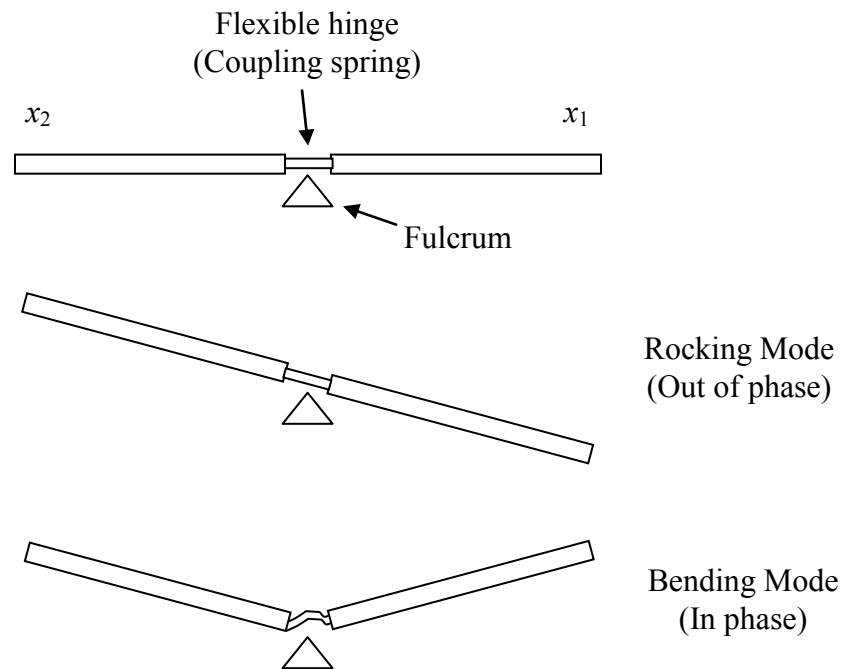


Figure 2.5: The simple model of the sensor and two vibrational modes.

## 2.3 Idealization of the Sensor

In order for the sensor system to be studied further, we need a more detailed model that contains material properties as well as geometry information so we can use it for design. Previously, the sensor inspired by the parasitoid fly, *Ormia Ochracea*, has been idealized by the second order ordinary differential equations as Eq. 2.1 based on lumped parameter approach. It shows the characteristics of the effect of the sensor's mechanical coupling well, however, it lacks the detailed geometrical and material information of the sensor to design, build, or optimize. For instance, the coupling spring  $k_3$  in Figure 2.1 is not practically idealized since  $k_3$  represents just the spring constant. Even though there are many design types available in this work, only three different types of idealization of the sensor are presented as an example. These three types are shown in Figure 2.1, Figure 2.6, and Figure 2.8.

### 2.3.1 Mode-Summation Model of the Sensor

If the sensor is considered to have continuously distributed mass and elasticity, it leads to an equation of motion that is a partial differential equation. For simple geometry it is convenient to choose a mode summation method to obtain an approximate solution to this equation.

Among many mode-summation procedures, component mode synthesis is chosen for the sensor modeling of which the deflection of each structural subcomponent is represented by the sum of polynomials instead of normal modes. The first step in the analysis is to select mode functions for each member and superpose these functions to define longitudinal, transverse and torsional vibrations throughout the system. We represent any one of these modes of vibration in terms of the selected functions and a set of coordinates as follows:

$$u, w, \theta = \sum_{j=1}^n \phi_j(x) p_j \quad (2-7)$$

in which  $u$  is the longitudinal displacement,  $w$  refers to transverse displacement,  $\theta$  denotes torsional displacement,  $\phi_j(x)$  is the  $j^{\text{th}}$  mode function,  $x$  indicates the independent variable measured along length of member, and  $p_j$  is the  $j^{\text{th}}$  coordinate. Although not explicitly noted,  $u$ ,  $w$ ,  $\theta$  are functions of time as well as of  $x$  and the  $p$ 's are functions of time. As indicated  $n$  functions and coordinates are chosen for the structure. In general, a wide choice exists in the selection of

functions with the boundary conditions on the structure as a whole. Boundary conditions imposed on the idealization shown in Figure 2.6 are such that for element (1) the bottom node is fixed in all degrees of freedom (DOF) and the top node is free to move. In this example, integral powers of  $(x/l)$  are used. Thus, displacements are represented by the series

$$u, w = 1(x)p_0 + \left(\frac{x}{l}\right)p_1 + \left(\frac{x}{l}\right)^2 p_2 + \dots + \left(\frac{x}{l}\right)^n p_n \quad (2-8)$$

W. Hurty [14] considered a simple beam with a  $90^\circ$  bend and compared the result with Bishop's [15] experimental result. The W. Hurty's result of first two natural frequencies shows a good agreement compared to Bishop's within 0.5 ~ 1.0 % error.

We first separate the sensor into three sections, (1), (2), and (3), whose coordinates are shown as  $w_1, x$ ;  $w_2, x$ ;  $u_2, x$ ;  $w_3, x$ ; and  $u_3, x$  where  $w$  and  $u$  represent vertical and axial displacements respectively. For element (1) from Figure 2.6, we assume the deflection to be

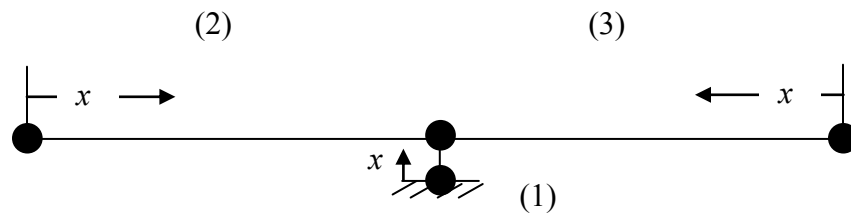


Figure 2.6: Representation of the sensor as beam sections 1, 2, and 3 with their coordinates.

$$\begin{aligned} w_1(x, t) &= \phi_1(x)p_1(t) + \phi_2(x)p_2(t) \\ &= \left(\frac{x}{l_c}\right)^2 p_1 + \left(\frac{x}{l_c}\right)^3 p_2 \end{aligned} \quad (2-9)$$

where  $l$  is the length of the element, subscript  $c$  is the center beam and  $p$ 's are generalized coordinates. The two mode functions satisfy the geometric and natural boundary condition of element (1) as follows:

$$\begin{aligned}
w_1(0) &= 0 & w_1(l) &= p_1 + p_2 \\
w_1'(0) &= 0 & w_1'(l) &= \frac{2}{l_c} p_1 + \frac{3}{l_c} p_2 \\
w_1''(0) &= \frac{M(0)}{EI_c} = \frac{2}{l_c^2} p_1 & w_1''(l) &= \frac{M(l_c)}{EI_c} = \frac{2}{l_c^2} p_1 + \frac{6}{l_c^2} p_2 \\
w_1'''(0) &= \frac{V(0)}{EI_c} = \frac{6}{l_c^3} p_2 & w_1'''(l) &= \frac{V(l_c)}{EI_c} = \frac{6}{l_c^3} p_2
\end{aligned} \tag{2-10}$$

Considering element (2) with the origin of the coordinates  $w_2$  and  $x$  at the free end, the following functions satisfy the boundary conditions of beam element (2):

$$\begin{aligned}
w_2(x, t) &= \phi_3(x)p_3(t) + \phi_4(x)p_4(t) + \phi_5(x)p_5(t) \\
&= 1 \cdot p_3 + \left(\frac{x}{l}\right) \cdot p_4 + \left(\frac{x}{l}\right)^4 \cdot p_5
\end{aligned} \tag{2-11}$$

$$\begin{aligned}
u_2(x, t) &= \phi_6(x)p_6(t) \\
&= 1 \cdot p_6
\end{aligned} \tag{2-12}$$

In the same manner considering element (3) with the origin of the coordinates  $w_3$  and  $x$  at the free end, the following functions can be achieved.

$$\begin{aligned}
w_3(x, t) &= \phi_7(x)p_7(t) + \phi_8(x)p_8(t) + \phi_9(x)p_9(t) \\
&= 1 \cdot p_7 + \left(\frac{x}{l}\right) \cdot p_8 + \left(\frac{x}{l}\right)^4 \cdot p_9
\end{aligned} \tag{2-13}$$

$$\begin{aligned}
u_3(x, t) &= \phi_{10}(x)p_{10}(t) \\
&= 1 \cdot p_{10}
\end{aligned} \tag{2-14}$$

The next step is to calculate the generalized mass from the equation

$$m_{ij} = \int_0^l m(x)\phi_i(x)\phi_j(x)dx \tag{2-15}$$

For element (1), we have

$$m_{11} = \int_0^l m_c(x) \phi_1(x) \phi_1(x) dx = \int_0^l m_c \left( \frac{x}{l_c} \right)^4 dx = 0.20 m_c l_c$$

$$m_{12} = m_{21} = \int_0^l m_c(x) \phi_1(x) \phi_2(x) dx = \int_0^l m_c \left( \frac{x}{l_c} \right)^5 dx = 0.166 m_c l_c$$

$$m_{22} = \int_0^l m_c(x) \phi_2(x) \phi_2(x) dx = \int_0^l m_c \left( \frac{x}{l_c} \right)^6 dx = 0.1428 m_c l_c$$

The generalized mass for element (2) and (3) is computed in a similar manner using  $\phi_3$  to  $\phi_6$  and  $\phi_7$  to  $\phi_{10}$  respectively:

$$m_{33} = \int_0^l m(x) \phi_3(x) \phi_3(x) dx = \int_0^l m \cdot 1 \cdot 1 dx = 1.0 ml = m_{77}$$

$$m_{34} = m_{43} = \int_0^l m(x) \phi_3(x) \phi_4(x) dx = \int_0^l m \cdot 1 \cdot \left( \frac{x}{l} \right) dx = 0.50 ml = m_{78} = m_{87}$$

$$m_{35} = m_{53} = \int_0^l m(x) \phi_3(x) \phi_5(x) dx = \int_0^l m \cdot 1 \cdot \left( \frac{x}{l} \right)^4 dx = 0.20 ml = m_{79} = m_{97}$$

$$m_{44} = \int_0^l m(x) \phi_4(x) \phi_4(x) dx = \int_0^l m \cdot \left( \frac{x}{l} \right) \cdot \left( \frac{x}{l} \right) dx = 0.333 ml = m_{88}$$

$$m_{45} = m_{54} = \int_0^l m(x) \phi_4(x) \phi_5(x) dx = \int_0^l m \cdot \left( \frac{x}{l} \right) \cdot \left( \frac{x}{l} \right)^4 dx = 0.166 ml = m_{89} = m_{98}$$

$$m_{55} = \int_0^l m(x) \phi_5(x) \phi_5(x) dx = \int_0^l m \cdot \left( \frac{x}{l} \right)^4 \cdot \left( \frac{x}{l} \right)^4 dx = 0.111 ml = m_{99}$$

$$m_{66} = \int_0^l m(x) \phi_6(x) \phi_6(x) dx = \int_0^l m \cdot 1 \cdot 1 dx = 1.0 ml = m_{1010}$$

Since there is no coupling between the longitudinal displacements  $u_2$  and  $u_3$  and the lateral displacements  $w_2$  and  $w_3$ ,  $m_{63} = m_{64} = m_{65} = 0$  and  $m_{107} = m_{108} = m_{109} = 0$ .

The generalized stiffness is found from the equation

$$k_{ij} = \int_0^l EI \phi_i''(x) \phi_j''(x) dx \quad (2-16)$$

Thus for element (1)

$$k_{11} = EI_c \int_0^l \phi_1''(x) \phi_1''(x) dx = EI_c \int_0^l \left( \frac{2}{l_c} \right)^2 dx = 4 \frac{EI_c}{l_c^3}$$

$$k_{12} = k_{21} = EI_c \int_0^l \left( \frac{2}{l_c} \right) \left( \frac{6x}{l_c^3} \right) dx = EI_c \int_0^l \left( \frac{2}{l_c} \right)^2 dx = 4 \frac{EI_c}{l_c^3}$$

$$k_{22} = EI_c \int_0^l \left( \frac{6x}{l_c^3} \right)^2 dx = 12 \frac{EI_c}{l_c^3}$$

For element (2) and (3)

$$k_{33} = EI \int_0^l \phi_3''(x) \phi_3''(x) dx = 0 = k_{77}$$

$$k_{34} = k_{43} = 0 = k_{78} = k_{87}$$

$$k_{35} = k_{53} = 0 = k_{79} = k_{97}$$

$$k_{44} = 0 = k_{88}$$

$$k_{45} = k_{54} = 0 = k_{89} = k_{98}$$

$$k_{55} = EI \int_0^l \phi_5''(x) \phi_5''(x) dx = EI \int_0^l \left( \frac{12x^2}{l^4} \right)^2 dx = 28.8 \frac{EI}{l^3} = k_{99}$$

The results computed for inertia and stiffness matrices are obtained as follows.

$$[m] = \begin{bmatrix} 0.2 m_c l_c & 0.166 m_c l_c & 0 & 0 & 0 & 0 & 0 & 0 & 0 & 0 \\ 0.166 m_c l_c & 0.1428 m_c l_c & 0 & 0 & 0 & 0 & 0 & 0 & 0 & 0 \\ 0 & 0 & ml & 0.5ml & 0.2ml & 0 & 0 & 0 & 0 & 0 \\ 0 & 0 & 0.5ml & 0.333 ml & 0.166 ml & 0 & 0 & 0 & 0 & 0 \\ 0 & 0 & 0.2ml & 0.166 ml & 0.111 ml & 0 & 0 & 0 & 0 & 0 \\ 0 & 0 & 0 & 0 & 0 & ml & 0 & 0 & 0 & 0 \\ 0 & 0 & 0 & 0 & 0 & 0 & ml & 0.5ml & 0.2ml & 0 \\ 0 & 0 & 0 & 0 & 0 & 0 & 0.5ml & 0.333 ml & 0.166 ml & 0 \\ 0 & 0 & 0 & 0 & 0 & 0 & 0.2ml & 0.166 ml & 0.111 ml & 0 \\ 0 & 0 & 0 & 0 & 0 & 0 & 0 & 0 & 0 & ml \end{bmatrix} \quad (2-17)$$

$$[k] = \begin{bmatrix} \frac{4E_c I_c}{l_c^3} & \frac{6E_c I_c}{l_c^3} & 0 & 0 & 0 & 0 & 0 & 0 & 0 & 0 \\ \frac{6E_c I_c}{l_c^3} & \frac{12E_c I_c}{l_c^3} & 0 & 0 & 0 & 0 & 0 & 0 & 0 & 0 \\ 0 & 0 & 0 & 0 & 0 & 0 & 0 & 0 & 0 & 0 \\ 0 & 0 & 0 & 0 & 0 & 0 & 0 & 0 & 0 & 0 \\ 0 & 0 & 0 & 0 & \frac{28.8EI}{l^3} & 0 & 0 & 0 & 0 & 0 \\ 0 & 0 & 0 & 0 & 0 & 0 & 0 & 0 & 0 & 0 \\ 0 & 0 & 0 & 0 & 0 & 0 & 0 & 0 & 0 & 0 \\ 0 & 0 & 0 & 0 & 0 & 0 & 0 & 0 & 0 & 0 \\ 0 & 0 & 0 & 0 & 0 & 0 & 0 & \frac{28.8EI}{l^3} & 0 & 0 \\ 0 & 0 & 0 & 0 & 0 & 0 & 0 & 0 & 0 & ml \end{bmatrix} \quad (2-18)$$

The synthesis is accomplished by using equations of constraint that follow from conditions of force equilibrium and deflection compatibility at the junctions. We have the following constraint equations at the junction between elements (1), (2), and (3).

$$\begin{aligned} w_1(l_c) + u_2(l) &= 0 & p_1 + p_2 + p_6 &= 0 \\ w_1(l_c) + u_3(l) &= 0 & p_1 + p_2 + p_9 &= 0 \\ w_2(l) &= 0 & p_3 + p_4 + p_5 &= 0 \\ u_2(l) &= 0 \\ w_3(l) &= 0 & p_7 + p_8 + p_9 &= 0 \end{aligned}$$

$$\begin{aligned}
& u_3(l) = 0 \\
& w_1'(l_c) - w_2'(l) = 0 \qquad \frac{2}{l_c} p_1 + \frac{3}{l_c} p_2 - \frac{1}{l} p_4 - \frac{4}{l} p_5 = 0 \\
& w_1'(l_c) + w_3'(l) = 0 \qquad \frac{2}{l_c} p_1 + \frac{3}{l_c} p_2 + \frac{1}{l} p_8 + \frac{4}{l} p_9 = 0 \qquad (2-19) \\
& EI [w_1''(l_c) + w_2''(l)] = 0 \qquad \frac{2}{l^2} p_1 + \frac{6}{l^2} p_2 + \frac{12}{l^2} p_5 = 0 \\
& EI [w_1''(l_c) + w_3''(l)] = 0 \qquad \frac{2}{l^2} p_1 + \frac{6}{l^2} p_2 + \frac{12}{l^2} p_9 = 0
\end{aligned}$$

Arranged in matrix form, the eight equations of constraint are

$$\begin{bmatrix}
1 & 1 & 0 & 0 & 0 & 1 & 0 & 0 & 0 & 0 \\
1 & 1 & 0 & 0 & 0 & 0 & 0 & 0 & 0 & 1 \\
0 & 0 & 1 & 1 & 1 & 0 & 0 & 0 & 0 & 0 \\
0 & 0 & 0 & 0 & 0 & 0 & 1 & 1 & 1 & 0 \\
\frac{2}{l_c} & \frac{3}{l_c} & 0 & -\frac{1}{l} & -\frac{4}{l} & 0 & 0 & 0 & 0 & 0 \\
\frac{2}{l_c} & \frac{3}{l_c} & 0 & 0 & 0 & 0 & 0 & \frac{1}{l} & \frac{4}{l} & 0 \\
\frac{2}{l_c^2} & \frac{6}{l_c^2} & 0 & 0 & \frac{12}{l^2} & 0 & 0 & 0 & 0 & 0 \\
\frac{2}{l_c^2} & \frac{6}{l_c^2} & 0 & 0 & 0 & 0 & 0 & 0 & \frac{12}{l^2} & 0
\end{bmatrix}
\begin{Bmatrix}
p_1 \\
p_2 \\
p_3 \\
p_4 \\
p_5 \\
p_6 \\
p_7 \\
p_8 \\
p_9 \\
p_{10}
\end{Bmatrix}
= 0 \qquad (2-20)$$

Since the total number of coordinates used is ten and there are eight constraint equations, the number of generalized coordinates for the system is two. We now can choose any two of the coordinates to be the generalized coordinates  $q$ 's. Let  $p_1 = q_1$  and  $p_6 = q_6$  be the generalized coordinates and express  $p_1, \dots, p_6$  in terms of  $q_1$  and  $q_6$ . This is accomplished in the following steps.

Rearrange Eq. 2.20 by shifting columns 1 and 6 to the right side

$$\begin{bmatrix} 1 & 0 & 0 & 0 & 0 & 0 & 0 & 0 \\ 1 & 0 & 0 & 0 & 0 & 0 & 0 & 1 \\ 0 & 1 & 1 & 1 & 0 & 0 & 0 & 0 \\ 0 & 0 & 0 & 0 & 1 & 1 & 1 & 0 \\ \frac{3}{l_c} & 0 & -\frac{1}{l} & -\frac{4}{l} & 0 & 0 & 0 & 0 \\ \frac{3}{l_c} & 0 & 0 & 0 & 0 & \frac{1}{l} & \frac{4}{l} & 0 \\ \frac{6}{l_c^2} & 0 & 0 & \frac{12}{l^2} & 0 & 0 & 0 & 0 \\ \frac{6}{l_c^2} & 0 & 0 & 0 & 0 & 0 & \frac{12}{l^2} & 0 \end{bmatrix} \begin{Bmatrix} p_2 \\ p_3 \\ p_4 \\ p_5 \\ p_7 \\ p_8 \\ p_9 \\ p_{10} \end{Bmatrix} = \begin{bmatrix} -1 & -1 \\ -1 & 0 \\ 0 & 0 \\ 0 & 0 \\ -\frac{2}{l_c} & 0 \\ -\frac{2}{l_c} & 0 \\ -\frac{2}{l_c^2} & 0 \\ -\frac{2}{l_c^2} & 0 \end{bmatrix} \begin{Bmatrix} p_1 \\ p_6 \end{Bmatrix} \quad (2-21)$$

Premultiply by the inverse of the 8 by 8 left hand side matrix on both sides and supplying the identity  $p_1 = q_1$  and  $p_6 = q_6$  to obtain the Eq. 2.21 in terms of the generalized coordinates.

$$\begin{Bmatrix} p_1 \\ p_2 \\ p_3 \\ p_4 \\ p_5 \\ p_6 \\ p_7 \\ p_8 \\ p_9 \\ p_{10} \end{Bmatrix} = \begin{bmatrix} 1 & 0 \\ -1 & -1 \\ -\frac{2l}{l_c} - \frac{l^2}{2l_c^2} + \frac{l^6}{144} \left( \frac{432}{l_c l^5} + \frac{216}{l_c^2 l^4} \right) & \frac{l^6}{144} \left( \frac{432}{l_c l^5} + \frac{216}{l_c^2 l^4} \right) \\ \frac{2l}{l_c} + \frac{2l^2}{3l_c^2} + \frac{l^6}{144} \left( -\frac{432}{l_c l^5} - \frac{288}{l_c^2 l^4} \right) & \frac{l^6}{144} \left( -\frac{432}{l_c l^5} - \frac{288}{l_c^2 l^4} \right) \\ \frac{l^2}{3l_c^2} & \frac{l^2}{2l_c^2} \\ 0 & 1 \\ \frac{2l}{l_c} - \frac{l^2}{2l_c^2} + \frac{l^6}{144} \left( -\frac{432}{l_c l^5} + \frac{216}{l_c^2 l^4} \right) & \frac{l^6}{144} \left( -\frac{432}{l_c l^5} + \frac{216}{l_c^2 l^4} \right) \\ -\frac{2l}{l_c} + \frac{2l^2}{3l_c^2} + \frac{l^6}{144} \left( \frac{432}{l_c l^5} - \frac{288}{l_c^2 l^4} \right) & \frac{l^6}{144} \left( \frac{432}{l_c l^5} - \frac{288}{l_c^2 l^4} \right) \\ \frac{l^2}{3l_c^2} & \frac{l^2}{2l_c^2} \\ 0 & -1 \end{bmatrix} \begin{Bmatrix} q_1 \\ q_6 \end{Bmatrix} = [C] \begin{Bmatrix} q_1 \\ q_6 \end{Bmatrix} \quad (2-22)$$

Application of the Lagrange equation/Hamilton's principle to the sensor system leads to the Eq. 2.23.

$$[m] \begin{Bmatrix} \ddot{p} \\ p \end{Bmatrix} + [k] \{p\} = 0 \quad (2-23)$$

Substituting Eq. 2.22 into Eq. 2.23, we get

$$[m][C] \begin{Bmatrix} \ddot{q} \\ q \end{Bmatrix} + [k][C] \{q\} = 0 \quad (2-24)$$

Premultiply by the transpose  $[C]^T$

$$[C]^T [m][C] \begin{Bmatrix} \ddot{q} \\ q \end{Bmatrix} + [C]^T [k][C] \{q\} = 0 \quad (2-25)$$

Thus, we have reduced the size of the sensor system from 10 by 10 to a 2 by 2 problem. Letting  $\begin{Bmatrix} \ddot{q} \\ q \end{Bmatrix} = -\omega^2 \{q\}$  from Eq. 2.25, we can obtain the characteristic equation of the eigenvalue problem for the sensor system. By using MATLAB, we find the two natural frequencies of the system from Eq. 2.25. For the base model, the result of the modal analysis *in vacuo* has been compared to that of the FEA and it is tabulated in Table 2-3.

Table 2-3: Comparison for natural frequencies of the mechanically coupled sensor

	Mode-Summation Model	FEA	% difference
1 <sup>st</sup> natural frequency	848 Hz	995 Hz	14.7
2 <sup>nd</sup> natural frequency	1351 Hz	1341 Hz	0.8

Figure 2.7 shows the mode shapes corresponding to the natural frequencies. Since the characteristic equation enables the solution of the eigenvectors only in terms of an arbitrary reference,  $q_6$  can be solved with  $q_1 = 1.0$ . The coordinates  $p$ 's are then found from Eq. 2.22, and the mode shapes are obtained from Eqs. 2.9, 2.11, 2.12, 2.13, and 2.14.

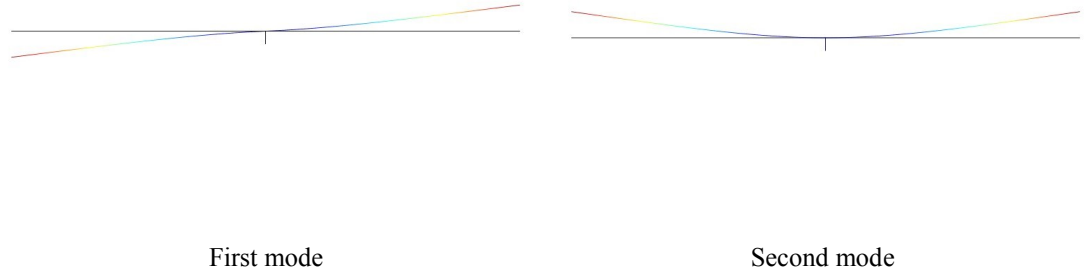


Figure 2.7: First and second mode shapes of Mode-Summation Sensor model.

### 2.3.2 Lumped Parameter Five DOF Discrete Model

The modeling method based on Mode-Summation works relatively well when compared to FEA results for the sensor, but with this method sometimes there exists difficulty in choosing the trial function. In addition to that, the discrepancy of the first natural frequency compared to FEA is not small enough to be overlooked. Although the finite element method considers continuous individual elements, it is in essence a discretization procedure, as it expresses the displacement at any point (node) of the continuous element in terms of a finite number of displacements at the nodal points multiplied by given interpolation functions. Sometimes the finite element method can be regarded as a special case of the Rayleigh-Ritz method and is used well beyond the original structural applications [16].

Idealization of the ear system of the *Ormia ochracea* shown in Figure 2.1 can be interpreted into various ways as a way of designing a sensor. In this section, another interpretation of the Figure 2.1 is made and represented as Figure 2.8. This modeling takes into consideration of the micro-fabrication process to make the sensor using currently available techniques.

The sensor system composed of Euler-Bernoulli Beams is shown in Figure 2.8 and it consists of 4 beams and 5 nodes where at node 1 there is one degree of freedom ( $\theta_1$ ), at nodes 2 and 3 there are 2 degrees of freedom ( $u_{y_2}, \theta_2$ ) and ( $u_{y_3}, \theta_3$ ). Constraining the node 1 this way wouldn't be easy using current micro-fabrication techniques. Additional beam at the node 1 as for the Mode-Summation based model or torsional spring can be added to satisfy the boundary condition while

seeking for a new fabrication method. At node 1, there is a common node between elements (1), and (2) which is  $\hat{\theta}_1$  of element (1), and  $\hat{\theta}_1$  of element (2). At each end of the beam, there is a spring support which is modeled as a PDMS beam attached in axial direction. Hence the total degrees of freedom of the system are 10 DOF (6 DOF from the poly-silicon beams, 8 DOF from the PDMS beams, and node 1, 2, and 3 are common nodes).

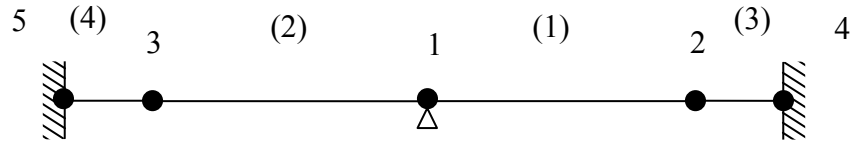


Figure 2.8: Representation of the sensor system composed of 4 beam elements.

The methods of weighted residuals are useful for deriving the system of equations. One of the popular methods is Galerkin's method. The system of equation for the mechanically coupled sensor can be represented as two second order ordinary differential equations without considering the damping term as shown in Eq. 2.26. Detailed derivation is omitted here since it is readily available from any FEM textbook.

$$M \cdot \ddot{u} + K \cdot u = f \quad (2-26)$$

If we were only taking 2 degrees of freedom (vertical and rotational) at all the nodes into consideration, the stiffness matrix of 1-D beam element is used for Eq. 2.26. Hence 4 by 4 stiffness matrix is represented in Eq. 2.27.

$$k = \frac{EI}{L^3} \begin{bmatrix} 12 & 6L & -12 & 6L \\ 6L & 4L^2 & -6L & 2L^2 \\ -12 & -6L & 12 & -6L \\ 6L & 2L^2 & -6L & 4L \end{bmatrix} \quad (2-27)$$

where  $E_{1,2} = 160e9$  [Pa],  $A_{1,2} = 1e-9$  [m<sup>2</sup>],  $L_{1,2} = 1e-3$  [m],  $b_{1,2}$  (width) =  $1e-3$  [m],  $h_{1,2}$  (thickness) =  $1e-6$  [m], and  $I_{1,2} = \frac{bh^3}{12} = \frac{(1e-3)(1e-6)^3}{12} = 8.3e-23$ . The subscript represents the element number. Elements 1 and 2 are made out of poly-silicon whereas elements 3 and 4 are made from PDMS and their material properties and geometry information are  $E_{3,4} = 8.7e6$  [Pa],  $A_{3,4} = 1e-9$  [m<sup>2</sup>],  $L_{3,4} = 5.03e-5$  [m],  $b_{3,4}$  (width) =  $1e-3$  [m],  $h_{3,4}$  (thickness) =  $1e-6$  [m], and  $I_{3,4} = \frac{bh^3}{12} = 1.04e-23$ .

For a 1-D beam element which only takes into account of transverse displacement and rotation at each node, the degrees of freedom at each node are  $u_{1,2} = [u_{1,y} \quad \phi_1 \quad u_{2,y} \quad \phi_2]^T$ . We can relate local nodal degrees of freedom to global degrees of freedom by the transformation matrix.

$$\begin{Bmatrix} \hat{u}_{1,y} \\ \hat{\phi}_1 \\ \hat{u}_{2,y} \\ \hat{\phi}_2 \end{Bmatrix} = \begin{bmatrix} -\sin \theta & \cos \theta & 0 & 0 & 0 & 0 \\ 0 & 0 & 1 & 0 & 0 & 0 \\ 0 & 0 & 0 & -\sin \theta & \cos \theta & 0 \\ 0 & 0 & 0 & 0 & 0 & 1 \end{bmatrix} \begin{Bmatrix} u_{1,x} \\ u_{1,y} \\ \phi_1 \\ u_{2,x} \\ u_{2,y} \\ \phi_2 \end{Bmatrix} \quad (2-28)$$

The axial effects are not yet included. The transformation matrix  $T$  shows that rotation is invariant with respect to either coordinate system. Therefore, the moment is unaffected as the element changes orientation in the  $x$ - $y$  plane. Substituting the above relationship for  $T$  into  $K = T^T \hat{K} T$  where  $\hat{K}$  represents the local stiffness matrix, we obtain the global element stiffness matrix as

$$K = \frac{EI}{L^3} \begin{bmatrix} 12 S^2 & -12 SC & -6LS & -12 S^2 & 12 SC & -6LS \\ -12 SC & 12 C^2 & 6LC & 12 SC & -12 C^2 & 6LC \\ -6LS & 6LC & 4L^2 & 6LS & -6LC & 2L^2 \\ -12 S^2 & 12 SC & 6LS & 12 S^2 & -12 SC & 6LS \\ 12 SC & -12 C^2 & -6LC & -12 SC & 12 C^2 & -6LC \\ -6LS & 6LC & 2L^2 & 6LS & -6LC & 4L^2 \end{bmatrix} \quad (2-29)$$

where  $C = \cos\theta$  and  $S = \sin\theta$ .

$$K = \frac{E}{L} \begin{bmatrix} AC^2 + \frac{12I}{L^2}S^2 & \left(A - \frac{12I}{L^2}\right)CS & -\frac{6I}{L}S & -\left(AC^2 + \frac{12I}{L^2}S^2\right) & -\left(A - \frac{12I}{L^2}\right)CS & -\frac{6I}{L}S \\ \left(A - \frac{12I}{L^2}\right)CS & AS^2 + \frac{12I}{L^2}C^2 & \frac{6I}{L}C & -\left(A - \frac{12I}{L^2}\right)CS & -\left(AS^2 + \frac{12I}{L^2}C^2\right) & \frac{6I}{L}C \\ -\frac{6I}{L}S & \frac{6I}{L}C & 4I & \frac{6I}{L}S & -\frac{6I}{L}C & 2I \\ -\left(AC^2 + \frac{12I}{L^2}S^2\right) & -\left(A - \frac{12I}{L^2}\right)CS & \frac{6I}{L}S & AC^2 + \frac{12I}{L^2}S^2 & \left(A - \frac{12I}{L^2}\right)CS & \frac{6I}{L}S \\ -\left(A - \frac{12I}{L^2}\right)CS & -\left(AS^2 + \frac{12I}{L^2}C^2\right) & -\frac{6I}{L}C & \left(A - \frac{12I}{L^2}\right)CS & AS^2 + \frac{12I}{L^2}C^2 & -\frac{6I}{L}C \\ -\frac{6I}{L}S & \frac{6I}{L}C & 2I & \frac{6I}{L}S & -\frac{6I}{L}C & 4I \end{bmatrix} \quad (2-30)$$

If we include the axial effects in the element, the element has three degrees of freedom per node. We can obtain the general transformation global stiffness matrix for a beam element that includes axial force, shear force, and bending moment effects as shown in Eq. 2.30.

For element 1, the angle between the global  $x$  and local  $\hat{x}$  axis is  $0^\circ$  because  $\hat{x}$  is directed from node 1 to node 2 meaning that global coordinate system coincides with that of local.

$$C = \cos 0^\circ = 1, S = \sin 0^\circ = 0$$

$$\frac{12I}{L^2} = \frac{12(8.3e-23)}{(1e-3)^2} = 1.0e-15 \text{ m}^2$$

$$\frac{6I}{L} = \frac{6(8.3e-23)}{(1e-3)} = 5.0e-19 \text{ m}^3$$

$$\frac{E}{L} = \frac{160 \text{ e}9}{(1e-3)} = 1.6e14 \text{ Pa/m}$$

We obtain the stiffness matrix for element 1 in terms of global coordinate system as

$$K^{(1)} = 1e5 \times \begin{bmatrix} u_{x1} & u_{y1} & \theta_1 & u_{x2} & u_{y2} & \theta_2 \\ 1.6 & 0 & 0 & -1.6 & 0 & 0 \\ 0 & 1.6e-6 & 8e-10 & 0 & -1.6e-6 & 8e-10 \\ 0 & 8e-10 & 5.3e-13 & 0 & -8e-10 & 2.7e-13 \\ -1.6 & 0 & 0 & 1.6 & 0 & 0 \\ 0 & -1.6e-6 & -8e-10 & 0 & 1.6e-6 & -8e-10 \\ 0 & 8e-10 & 2.7e-13 & 0 & -8e-10 & 5.3e-13 \end{bmatrix} \text{N/m}$$

where all diagonal terms are positive.

For element 2, the angle between the global  $x$  and local  $\hat{x}$  axis is  $180^\circ$  (counterclockwise) because  $\hat{x}$  is assumed to be directed from node 1 to node3. Therefore,

$$C = \cos 180^\circ = -1, S = \sin 180^\circ = 0$$

$$\frac{12 I}{L^2} = \frac{12 (8.3e-23)}{(1e-3)^2} = 1.0e-15 \text{ m}^2$$

$$\frac{6 I}{L} = \frac{6(8.3e-23)}{(1e-3)} = 5.0e-19 \text{ m}^3$$

$$\frac{E}{L} = \frac{160 e9}{(1e-3)} = 1.6e14 \text{ Pa/m}$$

We obtain the stiffness matrix for element 1 in terms of global coordinate system as

$$K^{(2)} = 1e5 \times \begin{bmatrix} u_{x1} & u_{y1} & \theta_1 & u_{x3} & u_{y3} & \theta_3 \\ 1.6 & 0 & 0 & -1.6 & 0 & 0 \\ 0 & 1.6e-6 & -8e-10 & 0 & -1.6e-6 & -8e-10 \\ 0 & -8e-10 & 5.3e-13 & 0 & 8e-10 & 2.7e-13 \\ -1.6 & 0 & 0 & 1.6 & 0 & 0 \\ 0 & -1.6e-6 & 8e-10 & 0 & 1.6e-6 & 8e-10 \\ 0 & -8e-10 & 2.7e-13 & 0 & 8e-10 & 5.3e-13 \end{bmatrix} \text{N/m}$$

In the same manner, stiffness matrices  $K^{(3)}$  and  $K^{(4)}$  can be attained. Principle of superposition and application of the boundary conditions  $u_{x1} = u_{y1} = 0$  at node 1 which represents the pinned coupling point and  $u_{x2} = u_{x3} = u_{x4} = u_{x5} = 0$  at nodes 2, 3, 4, and 5 yield the reduced set of equations for a longhand solution as

$$K_{reduced} = \begin{bmatrix} 1.06e-7 & -8e-5 & 2.66e-8 & 8e-5 & 2.66e-8 & 0 & 0 \\ -8e-5 & 1.77e-1 & -8e-5 & 0 & 0 & -1.74e-2 & 0 \\ 2.66e-8 & -8e-5 & 5.33e-8 & 0 & 0 & 0 & 0 \\ 8e-5 & 0 & 0 & 1.6e-1 & 8e-5 & 0 & 0 \\ 2.66e-8 & 0 & 0 & 8e-5 & 5.33e-8 & 0 & -1.74e-2 \\ \hline 0 & -1.74e-2 & 0 & 0 & 0 & 1.74e-2 & 0 \\ \hline 0 & 0 & 0 & -1.74e-2 & 0 & 0 & 1.74e-2 \end{bmatrix} \begin{Bmatrix} \theta_1 \\ u_{y2} \\ \theta_2 \\ u_{y3} \\ \theta_3 \\ u_{y4} \\ u_{y5} \end{Bmatrix} \quad (2-31)$$

This reduced stiffness matrix can be further reduced by applying a boundary condition at node 4 and 5 from Figure 2.8. Hence we are left with 5 by 5 stiffness matrix as shown in Eq. 2.31.

Now we find the first term of the Eq. 2.26 which is the inertia term for the sensor system. Eq. 2.32, Eq. 2.3, and Eq. 2-34 represent the mass matrix for a 1-D beam, a bar, and 2-D beam element, respectively.

$$M_{beam} = \frac{\rho AL}{420} \begin{bmatrix} 156 & 22L & 54 & -13L \\ 22L & 4L^2 & 13L & -3L^2 \\ 54 & 13L & 156 & -22L \\ -13L & -3L^2 & -22L & 4L^2 \end{bmatrix}, \quad (2-32)$$

$$M_{bar} = \frac{\rho AL}{6} \begin{bmatrix} 2 & 1 \\ 1 & 2 \end{bmatrix}, \quad (2-33)$$

$$M = \frac{\rho AL}{6} \begin{bmatrix} 2 & 0 & 0 & 1 & 0 & 0 \\ 0 & \frac{156}{70} & \frac{22L}{70} & 0 & \frac{54}{70} & \frac{-13L}{70} \\ 0 & \frac{22L}{70} & \frac{4L^2}{70} & 0 & \frac{13L}{70} & \frac{-3L^2}{70} \\ 1 & 0 & 0 & 2 & 0 & 0 \\ 0 & \frac{54}{70} & \frac{13L}{70} & 0 & \frac{156}{70} & \frac{-22L}{70} \\ 0 & \frac{-13L}{70} & \frac{-3L^2}{70} & 0 & \frac{-22L}{70} & \frac{4L^2}{70} \end{bmatrix} \quad (2-34)$$

where  $\rho = 2320 \text{ kg/m}^3$ ,  $A_{1,2} = 1e-9 \text{ m}^2$ ,  $L = 1e-3 \text{ m}$ .

Substituting for  $M = T^T \hat{M} T$ , we obtain the global element mass matrix for element 1 as

$$M_1 = 1e-9 \times \begin{bmatrix} u_{x1} & u_{y1} & \theta_1 & u_{x2} & u_{y2} & \theta_2 \\ 0.773 & 0 & 0 & 0.386 & 0 & 0 \\ 0 & 0.861 & 1.21e-4 & 0 & 0.298 & -7.18e-5 \\ 0 & 1.21e-4 & 2.2e-8 & 0 & 7.18e-5 & -1.65e-8 \\ 0.386 & 0 & 0 & 0.773 & 0 & 0 \\ 0 & 0.298 & 7.18e-5 & 0 & 0.861 & -1.21e-4 \\ 0 & -7.18e-5 & -1.65e-8 & 0 & -1.21e-4 & 2.2e-8 \end{bmatrix} \text{ kg}$$

In the same manner, mass matrices  $M_2$ ,  $M_3$  and  $M_4$  can be obtained. Principle of superposition and application of the boundary conditions  $u_{x1} = u_{y1} = 0$  at node 1 which represents the pinned coupling point and  $u_{x2} = u_{x3} = u_{x4} = u_{x5} = 0$  at nodes 2, 3, 4, and 5 yield the reduced set of equations as Eq. 2.35.

$$M_{reduced} = 1e-8 \times \begin{bmatrix} 4.4e-9 & 7.18e-6 & -1.65e-9 & -7.18e-6 & -1.65e-9 \\ 7.18e-6 & 0.0861 & -1.21e-5 & 0 & 0 \\ -1.65e-9 & -1.21e-5 & 2.2e-9 & 0 & 0 \\ -7.18e-6 & 0 & 0 & 0.0861 & 1.21e-5 \\ -1.65e-9 & 0 & 0 & 1.21e-5 & 2.2e-9 \end{bmatrix} \begin{Bmatrix} \ddot{\theta}_1 \\ \ddot{u}_{y2} \\ \ddot{\theta}_2 \\ \ddot{u}_{y3} \\ \ddot{\theta}_3 \end{Bmatrix} \text{ kg} \quad (2-35)$$

The comparison is made between the simulation results of the 5 DOF lumped parameter sensor model against the FEA result which is shown in Table 2-4. The corresponding mode shapes are shown in Figure 2.9.

Table 2-4: Comparison for natural frequencies of between 5 DOF and FEA model

	5 DOF model	FEA	% difference
1 <sup>st</sup> natural frequency	3054 Hz	3085 Hz	1
2 <sup>nd</sup> natural frequency	4466 Hz	4430 Hz	-0.8

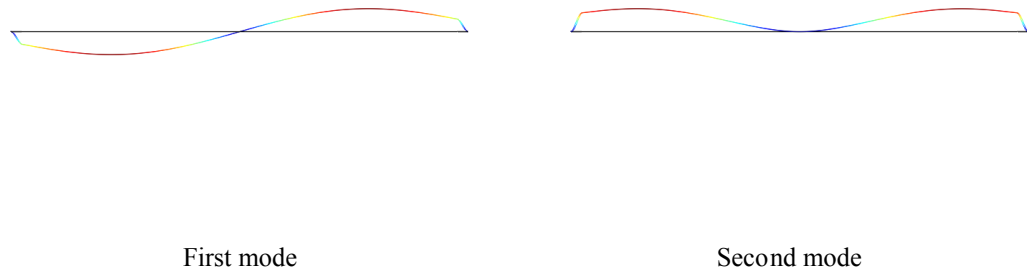


Figure 2.9: First and second mode shapes of the 5 DOF lumped parameter sensor model.

Eq. 2.26 is used to determine the transfer function between each response coordinate,  $x_1(t)$  and  $x_2(t)$ , and the incident pressure where  $x_1(t)$  is  $u_{y2}$  and  $x_2(t)$  is  $u_{y3}$ . As shown in Eq. 2.31 and Eq.

2.35, we are left with the reduced order of 5 by 5 system of equation for the sensor. Symbolically this gives us four simultaneous equations as in Eq. 2.36.

$$\begin{aligned}
& \left( m_{11} \ddot{x}_1 + m_{12} \ddot{x}_2 + m_{13} \ddot{x}_3 + m_{14} \ddot{x}_4 + m_{15} \ddot{x}_5 \right) + (k_{11} x_1 + k_{12} x_2 + k_{13} x_3 + k_{14} x_4 + k_{15} x_5) = 0 \\
& \left( m_{21} \ddot{x}_1 + m_{22} \ddot{x}_2 + m_{23} \ddot{x}_3 + m_{24} \ddot{x}_4 + m_{25} \ddot{x}_5 \right) + (k_{21} x_1 + k_{22} x_2 + k_{23} x_3 + k_{24} x_4 + k_{25} x_5) = f_1 \\
& \left( m_{31} \ddot{x}_1 + m_{32} \ddot{x}_2 + m_{33} \ddot{x}_3 + m_{34} \ddot{x}_4 + m_{35} \ddot{x}_5 \right) + (k_{31} x_1 + k_{32} x_2 + k_{33} x_3 + k_{34} x_4 + k_{35} x_5) = 0 \quad (2-36) \\
& \left( m_{41} \ddot{x}_1 + m_{42} \ddot{x}_2 + m_{43} \ddot{x}_3 + m_{44} \ddot{x}_4 + m_{45} \ddot{x}_5 \right) + (k_{41} x_1 + k_{42} x_2 + k_{43} x_3 + k_{44} x_4 + k_{45} x_5) = f_2 \\
& \left( m_{51} \ddot{x}_1 + m_{52} \ddot{x}_2 + m_{53} \ddot{x}_3 + m_{54} \ddot{x}_4 + m_{55} \ddot{x}_5 \right) + (k_{51} x_1 + k_{52} x_2 + k_{53} x_3 + k_{54} x_4 + k_{55} x_5) = 0
\end{aligned}$$

where  $x_1 = \theta_1$ ,  $x_2 = u_{y2}$ ,  $x_3 = \theta_2$ ,  $x_4 = u_{y3}$ , and  $x_5 = \theta_3$ . Eq. 2.36 can quickly be put into the form as preparation for applying determinants.

$$\begin{aligned}
& (m_{11} D^2 + k_{11})x_1 + (m_{12} D^2 + k_{12})x_2 + (m_{13} D^2 + k_{13})x_3 + (m_{14} D^2 + k_{14})x_4 + (m_{15} D^2 + k_{15})x_5 = 0 \\
& (m_{21} D^2 + k_{21})x_1 + (m_{22} D^2 + k_{22})x_2 + (m_{23} D^2 + k_{23})x_3 + (m_{24} D^2 + k_{24})x_4 + (m_{25} D^2 + k_{25})x_5 = f_1 \\
& (m_{31} D^2 + k_{31})x_1 + (m_{32} D^2 + k_{32})x_2 + (m_{33} D^2 + k_{33})x_3 + (m_{34} D^2 + k_{34})x_4 + (m_{35} D^2 + k_{35})x_5 = 0 \\
& (m_{41} D^2 + k_{41})x_1 + (m_{42} D^2 + k_{42})x_2 + (m_{43} D^2 + k_{43})x_3 + (m_{44} D^2 + k_{44})x_4 + (m_{45} D^2 + k_{45})x_5 = f_2 \\
& (m_{51} D^2 + k_{51})x_1 + (m_{52} D^2 + k_{52})x_2 + (m_{53} D^2 + k_{53})x_3 + (m_{54} D^2 + k_{54})x_4 + (m_{55} D^2 + k_{55})x_5 = 0
\end{aligned} \quad (2-37)$$

Our general definition of transfer function uses the operator notation of  $D^2 x = \frac{d^2 x}{dt^2}$ . The external driving forces are sound wave pressure impinging on the surface area of the sensor.

We can now have five single equations in a single unknown for each of the unknown displacements  $x_2$  and  $x_4$  by working out the appropriate determinants. The equations have two of the driving forces as inputs on the right hand side. That is, the motion of any one mass is caused by a superposition of the effects of each of the two inputs. We can define and use two transfer functions from each of the five single equations. Transfer function 1 and 2 are shown in Eq. 2.38

and Eq. 2.39, respectively. Expanding the determinants using Mathematica®, we obtain two transfer functions by setting  $D = j\omega$ . Details of this derivation can be found in Appendix A.

$$tf_1 = \frac{x_2}{f_1} = \frac{\begin{vmatrix} m_{11}D^2 + k_{11} & 0 & m_{13}D^2 + k_{13} & m_{14}D^2 + k_{14} & m_{15}D^2 + k_{15} \\ m_{21}D^2 + k_{21} & f_1 & m_{23}D^2 + k_{23} & m_{24}D^2 + k_{24} & m_{25}D^2 + k_{25} \\ m_{31}D^2 + k_{31} & 0 & m_{33}D^2 + k_{33} & m_{34}D^2 + k_{34} & m_{35}D^2 + k_{35} \\ m_{41}D^2 + k_{41} & f_2 & m_{43}D^2 + k_{43} & m_{44}D^2 + k_{44} & m_{45}D^2 + k_{45} \\ m_{51}D^2 + k_{51} & 0 & m_{53}D^2 + k_{53} & m_{54}D^2 + k_{54} & m_{55}D^2 + k_{55} \end{vmatrix}}{\begin{vmatrix} m_{11}D^2 + k_{11} & m_{12}D^2 + k_{12} & m_{13}D^2 + k_{13} & m_{14}D^2 + k_{14} & m_{15}D^2 + k_{15} \\ m_{21}D^2 + k_{21} & m_{22}D^2 + k_{22} & m_{23}D^2 + k_{23} & m_{24}D^2 + k_{24} & m_{25}D^2 + k_{25} \\ m_{31}D^2 + k_{31} & m_{32}D^2 + k_{32} & m_{33}D^2 + k_{33} & m_{34}D^2 + k_{34} & m_{35}D^2 + k_{35} \\ m_{41}D^2 + k_{41} & m_{42}D^2 + k_{42} & m_{43}D^2 + k_{43} & m_{44}D^2 + k_{44} & m_{45}D^2 + k_{45} \\ m_{51}D^2 + k_{51} & m_{52}D^2 + k_{52} & m_{53}D^2 + k_{53} & m_{54}D^2 + k_{54} & m_{55}D^2 + k_{55} \end{vmatrix}} \quad (2-38)$$

$$tf_2 = \frac{x_4}{f_2} = \frac{\begin{vmatrix} m_{11}D^2 + k_{11} & m_{12}D^2 + k_{12} & m_{13}D^2 + k_{13} & 0 & m_{15}D^2 + k_{15} \\ m_{21}D^2 + k_{21} & m_{22}D^2 + k_{22} & m_{23}D^2 + k_{23} & f_1 & m_{25}D^2 + k_{25} \\ m_{31}D^2 + k_{31} & m_{32}D^2 + k_{32} & m_{33}D^2 + k_{33} & 0 & m_{35}D^2 + k_{35} \\ m_{41}D^2 + k_{41} & m_{42}D^2 + k_{42} & m_{43}D^2 + k_{43} & f_2 & m_{45}D^2 + k_{45} \\ m_{51}D^2 + k_{51} & m_{52}D^2 + k_{52} & m_{53}D^2 + k_{53} & 0 & m_{55}D^2 + k_{55} \end{vmatrix}}{\begin{vmatrix} m_{11}D^2 + k_{11} & m_{12}D^2 + k_{12} & m_{13}D^2 + k_{13} & m_{14}D^2 + k_{14} & m_{15}D^2 + k_{15} \\ m_{21}D^2 + k_{21} & m_{22}D^2 + k_{22} & m_{23}D^2 + k_{23} & m_{24}D^2 + k_{24} & m_{25}D^2 + k_{25} \\ m_{31}D^2 + k_{31} & m_{32}D^2 + k_{32} & m_{33}D^2 + k_{33} & m_{34}D^2 + k_{34} & m_{35}D^2 + k_{35} \\ m_{41}D^2 + k_{41} & m_{42}D^2 + k_{42} & m_{43}D^2 + k_{43} & m_{44}D^2 + k_{44} & m_{45}D^2 + k_{45} \\ m_{51}D^2 + k_{51} & m_{52}D^2 + k_{52} & m_{53}D^2 + k_{53} & m_{54}D^2 + k_{54} & m_{55}D^2 + k_{55} \end{vmatrix}} \quad (2-39)$$

In dynamic system damping plays an important role. Despite the limitation in our knowledge about damping, Rayleigh damping can be incorporated with the 5 DOF lumped parameter sensor model (Eq. 2.26) to study the damping effect in form of

$$M \cdot \ddot{u} + C \cdot \dot{u} + K \cdot u = f \quad (2-40)$$

where  $C = \alpha \cdot M + \beta \cdot K$

The damping matrix  $C$  can be obtained by setting  $\alpha = 0$  and solving for  $\beta$  from FEA using the half power bandwidth method. With  $\alpha = 0$ , the higher modes will be heavily damped. The damping matrix  $C$  becomes

$$C = \beta \frac{E}{L} \begin{bmatrix} AC^2 + \frac{12I}{L^2}S^2 & \left(A - \frac{12I}{L^2}\right)CS & -\frac{6I}{L}S & -\left(AC^2 + \frac{12I}{L^2}S^2\right) & -\left(A - \frac{12I}{L^2}\right)CS & -\frac{6I}{L}S \\ \left(A - \frac{12I}{L^2}\right)CS & AS^2 + \frac{12I}{L^2}C^2 & \frac{6I}{L}C & -\left(A - \frac{12I}{L^2}\right)CS & -\left(AS^2 + \frac{12I}{L^2}C^2\right) & \frac{6I}{L}C \\ -\frac{6I}{L}S & \frac{6I}{L}C & 4I & \frac{6I}{L}S & -\frac{6I}{L}C & 2I \\ -\left(AC^2 + \frac{12I}{L^2}S^2\right) & -\left(A - \frac{12I}{L^2}\right)CS & \frac{6I}{L}S & AC^2 + \frac{12I}{L^2}S^2 & \left(A - \frac{12I}{L^2}\right)CS & \frac{6I}{L}S \\ -\left(A - \frac{12I}{L^2}\right)CS & -\left(AS^2 + \frac{12I}{L^2}C^2\right) & -\frac{6I}{L}C & \left(A - \frac{12I}{L^2}\right)CS & AS^2 + \frac{12I}{L^2}C^2 & -\frac{6I}{L}C \\ -\frac{6I}{L}S & \frac{6I}{L}C & 2I & \frac{6I}{L}S & -\frac{6I}{L}C & 4I \end{bmatrix}$$

There are three different models for the sensor so far. They all work the same way such that they take advantage of first two eigenmodes in order to enhance the phase difference.

In a later chapter, these transfer functions with respect to outputs,  $u_{y2}(x_2)$  and  $u_{y3}(x_4)$ , and input which is plane sound wave are analyzed in terms of frequency domain by taking into consideration of fluid loaded mass to complete the sensor model in water.

All three sensor models, 2 DOF lumped-parameter model, Mode-Summation model, and 5 DOF lumped-parameter model, are the idealization of the Figure 2.1 which has two important modes.

## 2.4 Capacitive Sensing

In order to transduce the response of each sensor's diaphragm into an electrical signal, it is proposed to incorporate a capacitive sensing scheme since capacitive sensing techniques are generally accepted as the ultimate standard in terms of size and detection capability. Besides, capacitive sensing technique provides the cost effective method of the sensor development. The movement of each sensor's end relative to the fixed one varies the capacitance, thereby allowing creation of an electrical signal responsive to varying sound pressure at the diaphragm. The value of capacitance  $C$  between the two plates is defined as Eq. 2.41 where  $Q$  is the amount of stored charge and  $V$  is the electrostatic potential.

$$C = Q/V \quad (2-41)$$

The capacitance is directly proportional to the surface area of the objects and the dielectric constant of the material between them, and inversely proportional to the distance between them. The two parallel capacitive plates are given by Eq. 2.42.

$$C = \frac{\epsilon A}{d + x} \quad (2-42)$$

where  $\epsilon$  = permittivity of water (80) in [farads/meter]. The magnitude of the force is given by Eq. 2.43.

$$f = \frac{-V_b^2 \cdot \epsilon \cdot A}{2(d + x)^2} \quad (2-43)$$

which has nonlinear dependence of  $x$  as shown.

The parallel-plate capacitor considered for our sensor which is shown in Figure 2.10 is a versatile platform for physical, chemical, and biological sensors.

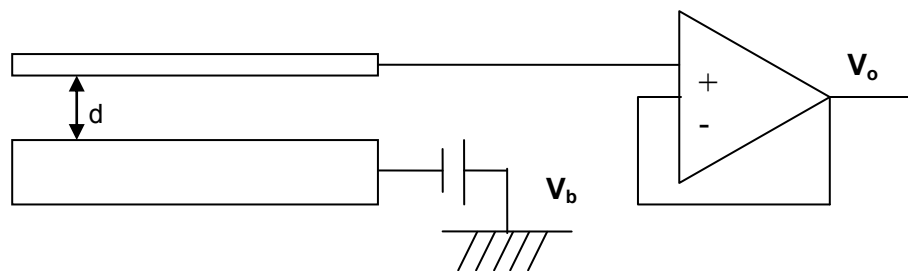


Figure 2.10: A parallel-plate capacitance with an overlapping area  $A$  and a spacing  $d$ .

In order to increase the sensitivity, the bias voltage  $V_b$  can be increased. However, if the bias voltage becomes too big, collapsing occurs. To get around this tradeoff between the sensitivity and collapsing, the multiple fingers (digitated) techniques can be chosen which allow the high voltage

relative to conventional one. In constant voltage biasing scheme, the formula to calculate the collapse voltage is presented in Eq. 2.44 [17].

$$V_{collapse} = \sqrt{\frac{8}{27} \frac{K \cdot h^3}{\epsilon \cdot A}} \quad (2-44)$$

where  $K$  = low equivalent mechanical stiffness (diaphragm stiffness) and  $h$  = gap between the diaphragm and the back-plate shown in Figure 2.10. To avoid collapse, one must have

$$V_b \ll V_{collapse} \quad (2-45)$$

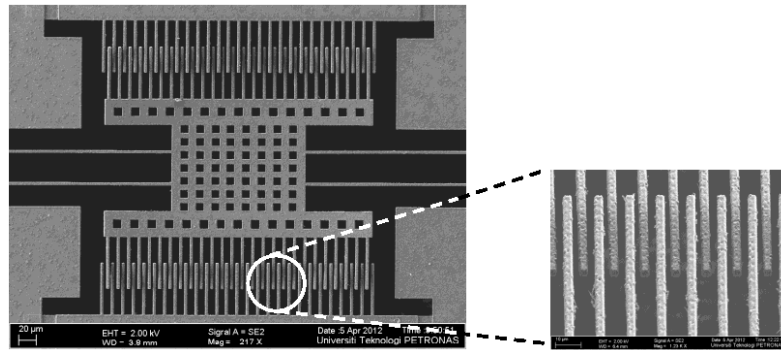


Figure 2.11: Image of typical comb fingers [18]

The total capacitance  $C$  of the capacitive sensor using the interdigitation technique may be roughly estimated by Eq. 2.46.

$$C = \frac{\epsilon(h-x)}{d} l \cdot 2 \cdot N \quad (2-46)$$

Bias voltage  $V_b$  has only minimal effect on the dynamic response of the interdigitated diaphragm and does not affect the stability of the diaphragm's motion due to the advantage of the its configuration shown in Figure 2.11. There are many methods to convert this variation in capacitance to an electrical signal.

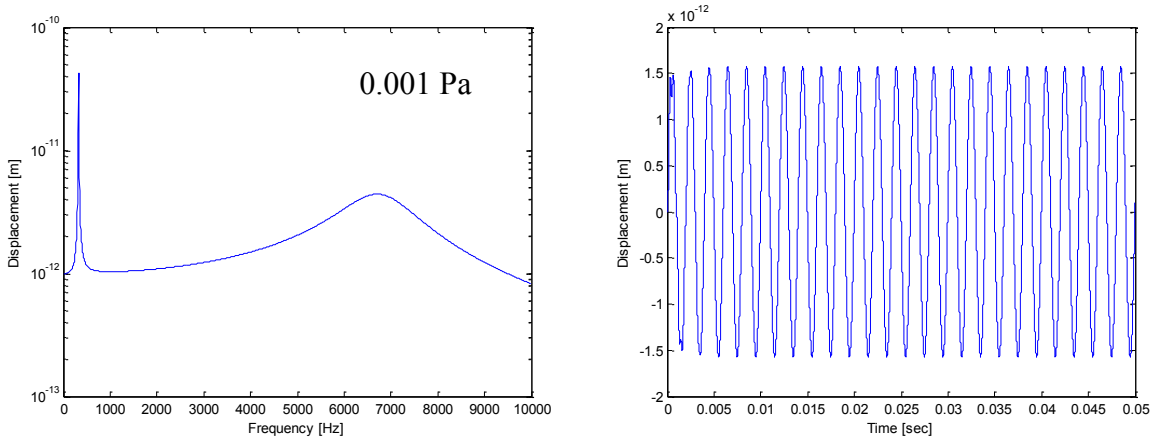


Figure 2.12: Left: Harmonic response of the sensor for ambient noise of 0.001 Pa. Right: Displacement of the sensor.

It is important for the sensor to be able to detect the small sound pressure and convert it into an electrical signal. Ensuring this, a finite element model of the sensor was used to investigate its behavior for ambient noise level pressure (0.001 Pa), sea state 0 (flat calm) in water [39]. Figure 2.12 shows the harmonic response of the sensor and the displacement of the sensor when impinged by 0.001 Pa sound wave. Figure 2.13 shows the capacitance plot based on Figure 2.12 using Eq. 2.41. In practice, typical devices have capacitances ranging from microfarads ( $1 \mu\text{F} = 10^{-6} \text{ F}$ ) to picofarads ( $1 \text{ pF} = 10^{-12} \text{ F}$ ) and this corresponds with Figure 2.13. This shows that the capacitance sensing can be used to detect the ambient noise sound via the displacement of the sensor. Figure 2.13 also shows the good linearity between the capacitance  $C$  calculated for the sensor and the displacement  $x_1$ . For the better performance, Eq. 2.46 of the interdigitated sensor can be used.

Our sensor has rotating motion which composes of rocking and bending modes with respect to the coupling point. The capacitor is formed by two nonparallel plates, each of area  $A$  and its view of the arrangement is shown in Figure 2.14 where only the right side of the sensor is shown. Note that the top plate is tilted relative to the bottom plate so that on one edge the plate separation is  $d + x$ , while on the other edge is  $d - x$ . Assuming that  $x \ll d$  and that  $d$  is small compared with the length of the plate. The capacitance can be calculated using Eq. 2.47.

$$C = \frac{\varepsilon \cdot A}{d} \left[ 1 + x + \frac{1}{2} \left( \frac{x}{d} \right)^2 \right] \quad (2-47)$$

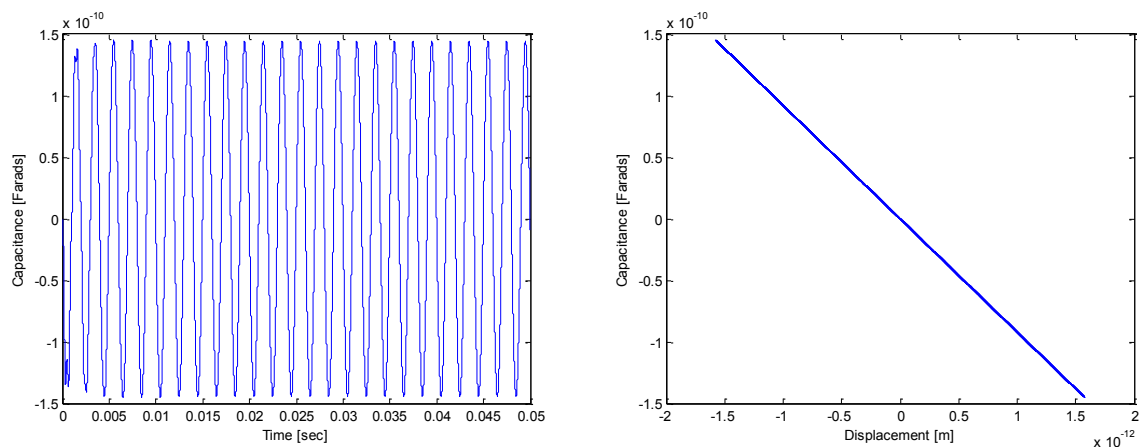


Figure 2.13: Left: Capacitance vs. time plot based on Figure 2.12. Right: Capacitance and Displacement show a linear relationship.

Motion detectors using capacitive sensing technique can detect  $10^{-14}$  m displacements with good stability, high speed, and wide extremes of environment. Besides capacitive technology is displacing piezo-resistance in silicon implementations of accelerometers and pressure sensors, and innovative applications like fingerprint detectors and infrared detectors are appearing on silicon with sensor dimensions in the micron range [19].

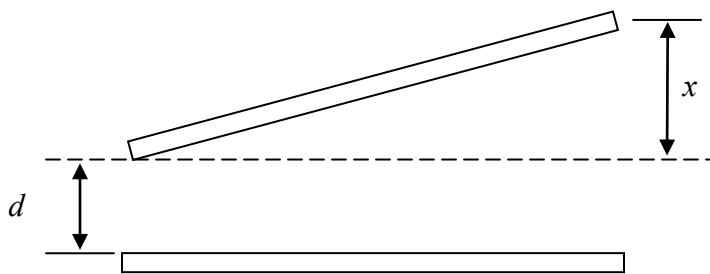


Figure 2.14: Capacitor formed by two nonparallel plates.

Capacitive sensing, either through the use of a charged electrets or a biased back-plate, is employed in the vast majority of miniature microphones that have sufficiently low noise and high sensitivity to be candidates for use in our sensor.

In addition to Miles model, two different types of the sensor model have been developed with different idealization as a way to designing a sensor. While many researches have been conducted

in the sensor application based on the parasitoid fly *Ormia Ochracea*, they all routinely use Miles' mathematical model. This idealization methods hope to fill that void somewhat by introducing mathematical models that contains sensor's geometry and material properties. Our sensor model will be incorporated with the frequency variable fluid loading mass in Chapter 4. The effect of the natural frequencies on the sensor performance will be studied in Chapters 4 and 6. Our sensor has two natural frequencies and the corresponding modes. These natural frequencies and mode shapes play an important role in characterizing the sensor as well as amplifying the time delay for better sensor performance.

## Chapter 3. Detection of Direction of the Sound Source

### 3.1 Introduction

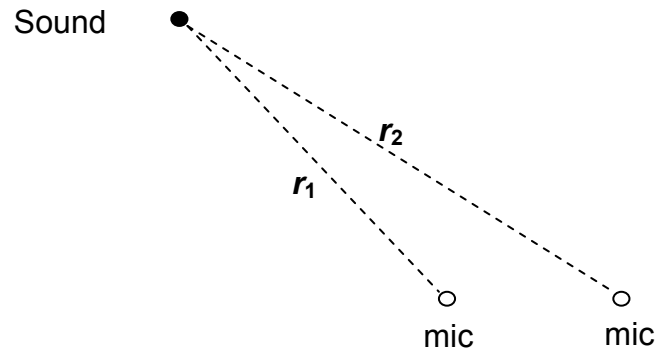


Figure 3.1: Sound field description.

Consider a sound field consisting of a source and two receivers with propagation distances  $r_1$  and  $r_2$ , such as depicted in Figure 3.1. It is often useful to express the path difference in terms of the phase difference  $\Delta\phi$  between the two waves considering the sound field depicted in Figure 3.1. Since a path difference of one wavelength corresponds to a phase difference of  $2\pi$  radians, it is obtained as

$$\delta = r_2 - r_1 = \Delta r = \frac{\lambda}{2\pi} \Delta\phi \quad (3-1)$$

where  $\delta$  is path difference and  $\lambda$  is wave length. It is known from the interference of waves that the path difference  $\delta$  is

$$\delta = r_2 - r_1 = \Delta r = d \cdot \sin \theta \quad (3-2)$$

where  $d$  is the distance difference between two microphone and  $\theta$  is the angle relative to the longitudinal axis.

From Eq. 3.1 with a fact that

$$\lambda = \frac{v}{f} = \frac{c}{f} \quad (3-3)$$

where  $\lambda$  is wavelength,  $v$  is the propagation speed  $c$  is the speed of sound, and  $f$  is its frequency, it becomes

$$\delta = \frac{\lambda}{2\pi} \Delta\phi = \frac{c/f}{2\pi} \Delta\phi = c \frac{\Delta\phi}{2\pi f} = c \frac{\Delta\phi}{\omega} = c\tau \quad (3-4)$$

where  $\tau$  is time delay. Equating Eq. 3.2 and Eq. 3.4, we obtain

$$\tau = d \cdot \sin \theta / c \quad (3-5)$$

Eq. 3.5 has been used to measure directivity of the sound source using arrays of microphones, however with a distance  $d$  being too small there is a great deal of ambiguity in determining its directivity. The physical action of the mechanical coupling sensor structure is to convert small acoustic interaural time differences (ITD) into larger time and amplitude differences at the mechanical level. This process of mechanical coupling between tympanal membranes, and its amplification effect on interaural auditory cues, is unique to flies.

Animals generally have a plane of symmetry, and therefore two ears. Human hearing range goes between 15 ~ 20,000 Hz, and SONAR (Sound Navigation And Ranging) usually operates at frequencies in the 10,000 ~ 50,000 Hz range whereas there are low and high frequency SONAR available [20]. For SONAR, though higher frequencies provide more accurate location data, propagation losses also increase with frequency. Lower frequencies are therefore used for longer range detection (up to 10 mile [17,600 yd]) at the cost of location accuracy. For sound of frequencies sufficiently low that the distance between the ears is much less than the sound wavelength, the sound pressure is essentially the same at the two ears, but there is a slight difference in phase that depends upon the separation of the ears, the frequency, and the direction from which the sound is coming. It would be useful if we could obtain the accurate directivity

from the low frequency signals. In this dissertation, we will show that our sensor can be used to detect of low frequency (less than 2000 Hz) signals.

Using our sensor model, the whole process will be simulated from data collection of the sensor when impinged by various sound signals, DSP, and calculating the output time delay.

### **3.2 Digital Signal Analysis for Directivity**

The basic principles of sound detection are that sound moves at a steady rate through a given medium, such as air or water, and that objects produce certain types of sounds with certain frequency. With this knowledge, calculations can determine the directivity to an object and identify it with reasonable certainty.

In order to find the direction of the sound source, it is necessary to collect the displacement data  $x_1$  and  $x_2$  from the sensor system. The method of operation is simple once data has been collected. Considering a single sinusoidal wave, first step is to find the frequency of the incoming sound signal using Fast Fourier Transform (FFT). Finding the frequency of the signal from  $x_1$  and  $x_2$ , it is possible to find a phase of each signal, hence the difference of its phase. Then, the output time delay  $\tau_o$  can be found by solving  $\tau_o = \Delta\phi/\omega$  where subscript “o” represent output,  $\Delta\phi$  is phase difference between  $x_1$  and  $x_2$  in radian, and  $\omega$  is frequency of the signal in radian per second. This data is now compared to the mapping plots of the output time delays vs. frequency and angle of incidence calculated from frequency domain through transfer function prior to the simulation.

The response of the system to a periodic input is simulated by our model and is fed to the signal analysis program to find the time delay. Three different cases are considered.

- 1) Single source with one frequency
- 2) Multiple sources with multiple frequencies
- 3) Single source with band-limited noise

#### **3.2.1 Single Source with One Frequency**

A sinusoidal input of frequency of 2000 Hz is fed into the sensor model, which is chosen as one of many choices among the low frequencies below the first natural frequency of the sensor to evaluate the performance. Another reason for the use of that frequency is that the experimental data in air are readily available at frequencies of 2000, 6000, and 15,000 Hz from the work of

Miles, Robert and Hoy (1995) so that our analysis can be validated against. The responses of the system  $x_1$  and  $x_2$  are obtained where the response of  $x_2$  is the same with  $x_1$ 's with different phase. Simulation time has been chosen to ensure for the responses of the system to reach the steady state, hence it can be different depending on the input frequency. Among the fixed step continuous solver, *ode5* the Dormand-Prince formula, which is the fixed-step version of *ode45*, is chosen to increase the order of accuracy. The choice between the fixed-step and variable-step solver types depends on the model and its dynamics. To simulate the real-time clock, fixed-step solver is chosen over variable one despite it requires more time. Based on the Nyquist Shannon sampling theorem, sampling frequency  $f_s$  must be greater than twice of the maximum frequency. This means that sampling frequency should be greater than 30000 Hz since the maximum frequency is 15000 Hz for analysis, however, sampling at exactly 2 times the highest frequency is often unacceptable, especially in applications where the shape (time-domain representation) of the signal is important. When sampling a pure sine wave, it is safe to sample at least 10 times the frequency of that sine wave to properly capture the shape of the signal. There are other factors that will affect the sample rate: the bandwidth and on-board memory. Since the simulation time is short, finite acquisitions, the fixed step size of  $4.5 \times 10^{-7}$  is chosen to cover input frequency ranges of 2000 ~ 15000 Hz where the highest frequency is 15000 Hz. This frequency is chosen as one of many choices among high frequencies below the second natural frequency of the sensor.

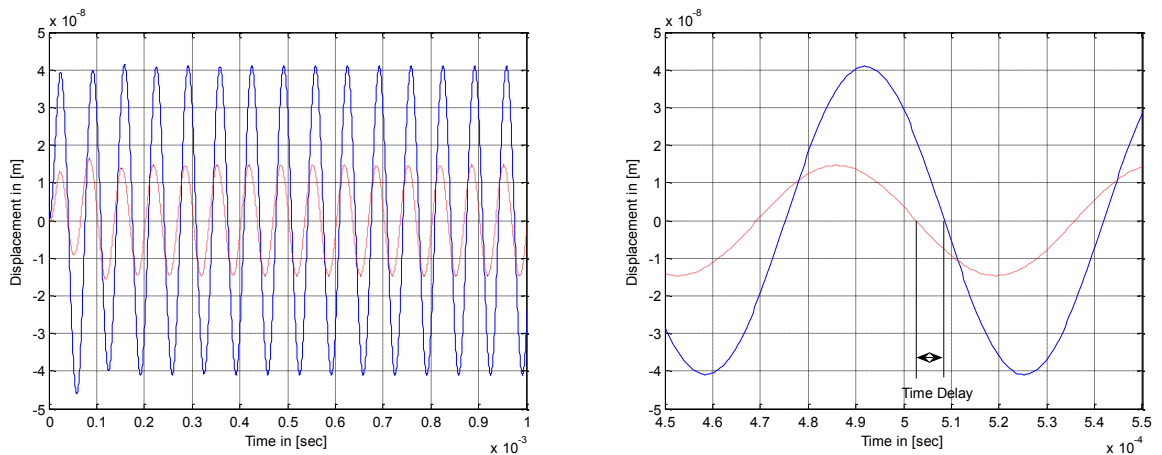


Figure 3.2: Left: Time response at 15000 Hz with  $45^\circ$  incidence angle. Right: Zoom-in plot in which the time-delay is measured.

Time delay is defined as “the amount of time by which an event is retarded or the time between the instant at which a given event occurs and the instant at which a related aspect of that event occurs.” For the reason, it is easily measured or calculated in time domain. This is shown in Figure 3.2 at the frequency of 15000 Hz. Using our model, time delay has been calculated and tabulated vs. angle of incidence at different input frequencies to be compared with frequency domain analysis data. Mapping the time delay  $\tau$  vs. incident angle  $\theta$  from the time domain simulation, the angles of incidence of  $-90^\circ$ ,  $-65^\circ$ ,  $-45^\circ$ ,  $-20^\circ$ ,  $0^\circ$ ,  $20^\circ$ ,  $45^\circ$ ,  $65^\circ$ , and  $90^\circ$  are used to calculate time delays whereas from frequency domain simulation all the angles between  $-90^\circ$  through  $90^\circ$  are used with an increment of  $1^\circ$ . The rest of the angles are covered via performing a linear interpolation. For the reason mapping data from frequency domain analysis is more accurate and it is used as a baseline data which can be compared with that of time domain analysis to find the direction of the sound source. The comparison plot of this is shown in Figure 3.3 where time delays measured from frequency and time domains show strong agreement to each other. This can be seen from the left plot of Figure 3.3. There can also be little discrepancy between two different domain plots from the right plot of Figure 3.3. However, this can be improved significantly by taking more data points for interpolation.

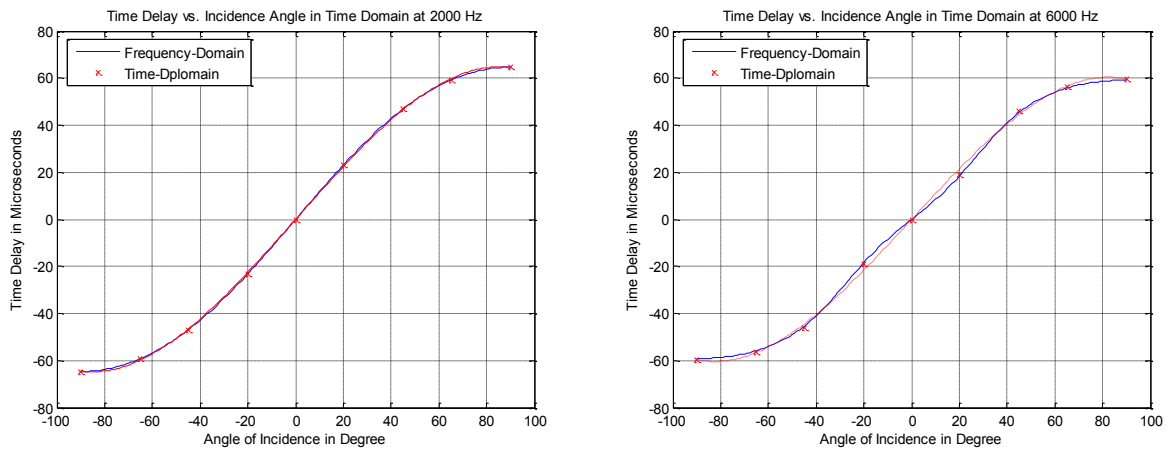


Figure 3.3: Left: Comparison plot of  $\tau$  vs.  $\theta$  at 2000 Hz. Right: at 6000 Hz.

### 3.2.2 Multiple Sources with Multiple Frequencies

For the multi-harmonic sinusoidal input case, the output of  $x_1$  is shown in Figure 3.4 as a combination of three sinusoidal signals with different frequencies as well as different angles of

incidence. The Fast Fourier Transformation (FFT) result shows the three separate frequency components of the modulation signal. The directivity for each sound source can be found by the information taken from each input frequency along with output time delay of the phase difference between  $x_1$  and  $x_2$ , which is based on the operation method described previously due to the direct relationship between the phase difference and the output time delay as shown in Eq. 3.4.

For a single sinusoidal input case, time delay can be measured directly from the data obtained from the simulation in time domain. However, for the case of multiple harmonic sinusoidal inputs, it is necessary to separate signals with different frequencies using filters so that each can be treated as a single sinusoidal signal. Digital filters have been added to our model, which of them are low pass, band pass, and high pass filters. They are all based on Butterworth filter design which is a type of signal processing filter designed to have as flat a frequency response as possible in the pass band. Time delay has been calculated based on the same method as for a single input case. Time delays calculated from the filtered data from multi-tone and the one from single frequency signal without filter show the identical correlation. Hence with the calculated output time delay of the input signal to the system, it can be found which angle of incidence the input signal is coming from at the specific frequency from the plot.

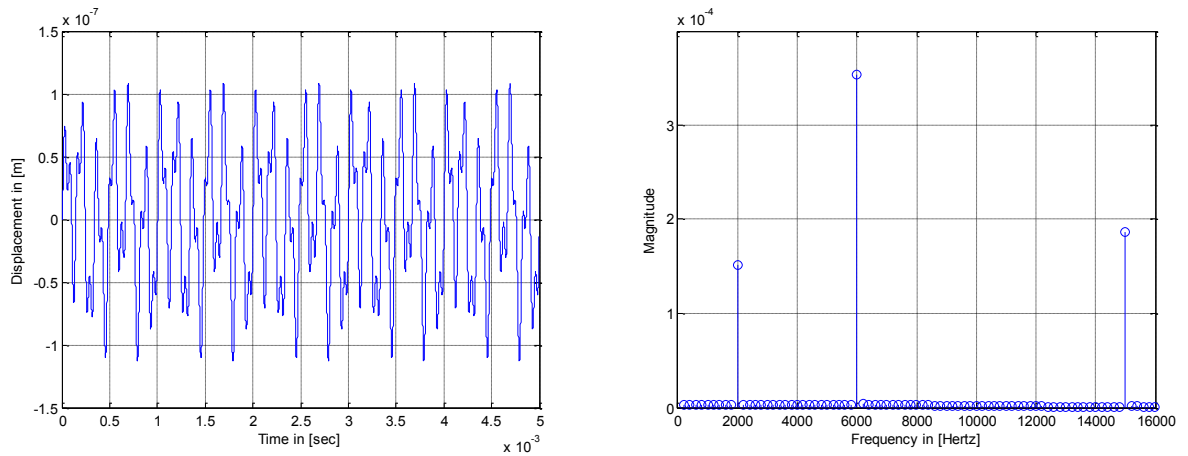


Figure 3.4: Left: Time domain representation of  $x_1$  with a modulation signal composed of three sinusoids. Right: Frequency domain representation of  $x_1$  signal composed of three sinusoids.

### 3.2.3 Single Band-Limited White Noise Source

In the case of real applications such as a submarine detection, acoustic sensors are the primary sensor of choice to detect threat from the submarines operating below periscope depth. Unlike the single sinusoidal signal case discussed previously, this could be band-limited white noise like signal which is a random signal with a flat power spectral density within the bandwidth, i.e., the signal contains equal power within a fixed bandwidth at any center frequency. The key in long distance detection so far lies in finding the frequency of sounds using Fast Fourier Transform (FFT). However for the band-limited white noise signal, as a better method among many DSP techniques, Cross Correlation have been considered and used for time delay calculation to detect time delays between two signals with a different phase.

Both in signal and system analyses, the concept of Auto Correlation and Cross Correlation play an important role, especially in signal detection and time-delay estimations, respectively. The Auto Correlation function of a random signal describes the general dependence of the values of the samples at one time on the values of the samples at another time. The Cross Correlation function, however, measures the dependence of the values of one signal on another. For two sound source signals  $x(t)$  and  $y(t)$  it is describe by

$$R_{xy}(\tau) = \lim_{T \rightarrow \infty} \frac{1}{T} \int_{-T}^T x(t)y(t + \tau)dt \quad (3-6)$$

where  $T$  is the period of observation. This method to estimate the time delay is simply to locate the maximum value in the cross correlation coefficient function. The time at which this peak value occurs is then taken as an estimate of the output time delay  $\tau_0$ . Notice that when Matlab function *xcorr* is implemented to estimate the Cross Correlation sequence, it has its origin in the middle of the figure (here it is at lag =  $6.2 \times 10^{-5}$  seconds) which is shown in the Figure 3.5.

Once the output delay  $\tau_0$  is found, we can find its dependency against the angle of incidence based on the technique used for a single periodic signal case. This can be done by using band-pass filter to narrow the limited band noise so that the signal can be identified because certain types of engines for submarines vibrate at certain frequencies. In order to guarantee the performance, it is suggested to use of state observer to estimate the input signals and calculate the input time delay  $\tau_i$

to calculate the incidence angle of the sound using the Eq. 3.7 and compare the results with that of output case.

$$\theta = \sin^{-1}\left(\frac{\tau \cdot c}{d}\right) \quad (3-7)$$

where  $\theta$ ,  $d$  represent the angle of incidence and the distance between two microphone, respectively. Two simulation results between frequency analysis of a single periodic case and wide-band noise are shown in Figure 3.6. They show a good agreement.

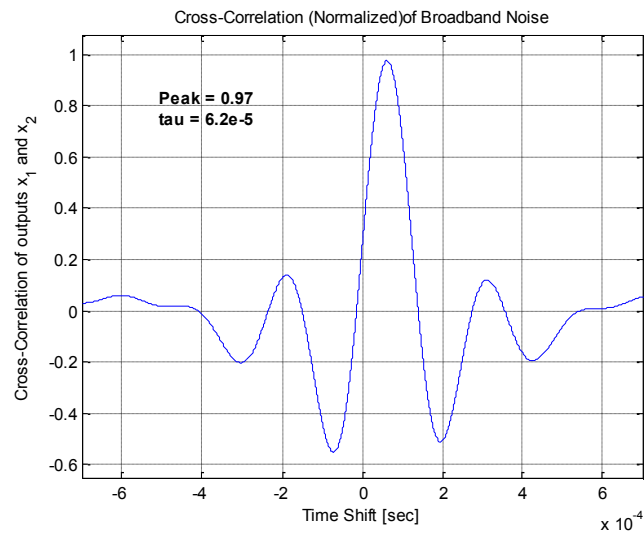


Figure 3.5: Time delay by *xcross* on broadband noise of 1000 ~ 5000 Hz.

The method described based on Cross-Correlation function analysis appear to be the most useful in the application of predicting time delays for noise like signals whereas Fast Fourier Transform method works well for single and multiple harmonic signals. This is because white noise like signal contains many different frequencies embedded in it to be treated like a single frequency signal. However since the wide-band noise like signal carries many different frequencies, it is important to narrow the frequency of our interest to find the directivity of the sound source with the help of band-pass filter.

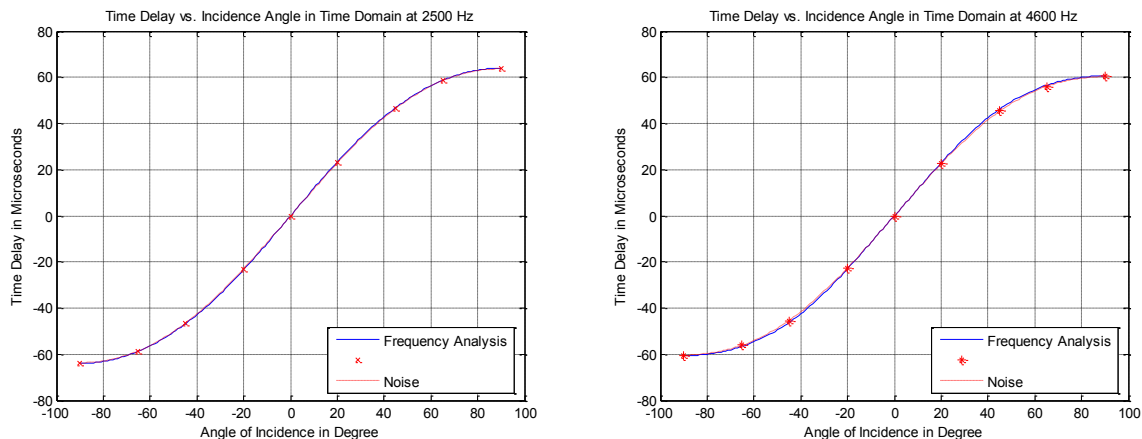


Figure 3.6: Comparison plot of  $\tau$  vs.  $\theta$  between frequency analysis and wide-band noise Left: at 2500 Hz. Right: at 4600 Hz.

As outlined in the previous section, the method for finding the directivity of the sound source should have ability to find a phase difference from the displacements ( $x_1$  and  $x_2$ ) and this leads to be able to find the direction of the source. It has been shown that our sensor can be used to find the directivity of the various types of sound sources with a help of DSP analyses.

## Chapter 4. Parametric Study of Underwater Sensor for Directivity

So far the use of our sensor inspired by the parasitoid fly, *Ormea Ochracea*, in air has been discussed. However, in order to use the sensor in water, there are many factors to take into consideration such as density changes (thus speed of sound), fluid mass loading effects, and other intrinsic underwater effects. Since our objective is the study of feasibility/design with the hydro-acoustic sensor for directivity, the simplest way to implement the underwater characteristic analysis of the sensor is to change the density of the medium from air to water and include the effect of fluid loading.

In a fluid-structure interaction system, the motion of the fluid and that of the solid are not independent from each other but constrained by a few kinematical and dynamical conditions. This means that the fluid and the structure behave as a dynamically coupled system. In turn, the characteristics of the system changes by submerging the sensor in the water. Hence, parametric analyses are needed to study the feasibility/design of the sensor submerged in water.

### 4.1 Added Mass due to Fluid Loading

Added mass is an inertia term added to a lumped parameter system because of the forced movement of the surrounding fluid. Archimedes' principle states that "Any object, wholly or partially immersed in a fluid, is buoyed up by a force equal to the weight of the fluid displaced by the object". Hence, any object that sinks will displace an amount of water equal to its own volume because the object and fluid cannot occupy the same space simultaneously. In fluid mechanics, this is modeled as control volume of fluid moving with the object. In reality, all the fluid will be accelerated, to various degrees. However, one cannot point at a specific volume of fluid that is dragged along with an accelerating object. Nevertheless, the overall pattern of flow around an accelerating object can be conveniently described as if there were a defined added mass of fluid. Generally, the added mass defined is varied based on the geometry, boundary condition, and frequency. Simple one dimensional to the two dimensional potential flow approach added mass models will be addressed. Various added mass terms from the literature will be studied to find the added mass calculation method that can be used for our sensor model and compared to each other and to FEA (Finite Element Analysis).

### ***Junger and Feit***

Junger and Feit (1972, 1986) reported a formula for the fluid loaded mass of a vibrating rigid piston based on the previous work by Kinsler *et al.* (1982), Reynolds (1981), and Ford (1970). The effects of the mass loading for a vibrating circular piston, which is mounted on an infinite rigid baffle, can be estimated to be:

$$M_r = \frac{8\rho_o z^3}{3} \quad (2kz \ll 1) \quad (4-1)$$

$$M_r = \frac{2\rho_o z}{k^2} \quad (2kz \gg 1) \quad (4-2)$$

where  $z$  is the equivalent radius of the circular piston

$$k \text{ (wavenumber)} = \frac{\omega}{c}$$

$\rho_o = 995.6 \text{ [kg/m}^3\text{]}$ : density of water at 27 °C

$c = 1483 \text{ [m/s]}$ ; speed of sound for fresh water at 20 °C

Equating the area of the sensor to that of a circular piston, the equivalent radius of the 0.02 m by 0.02 m plate,  $z$ , is 0.0113 m which is small but not small enough to be categorized as  $2kz \ll 1$ , which is for lower frequencies. In order to define a transition point between the two regions ( $kz \ll 1$ , and  $kz \gg 1$ ), the added mass for low and high frequencies is plotted as a function of  $kz$  and frequency in Figure 4.1.

In Figure 4.1, red solid-dotted line and blue solid line represent Eq. 4.1 and Eq. 4.2 respectively. It is important to note that this transition point is not a constant but is a function of radius – i.e. the transition frequency increases inversely with increasing piston radius is.

### ***Fahy***

Fahy (1985) presents an approximation of the effective mass per unit area of a fluid loaded flexible plate as,

$$m_e \cong \rho_0 / (m \pi / l) = \rho_0 / k_m \quad (4-3)$$

where  $\rho_0$  = density of water at 20°C

$m$  = wavenumber spectrum of the spectrum of the fundamental mode

$l$  = length of the diaphragm

$k_m$  = the primary modal wavenumber component

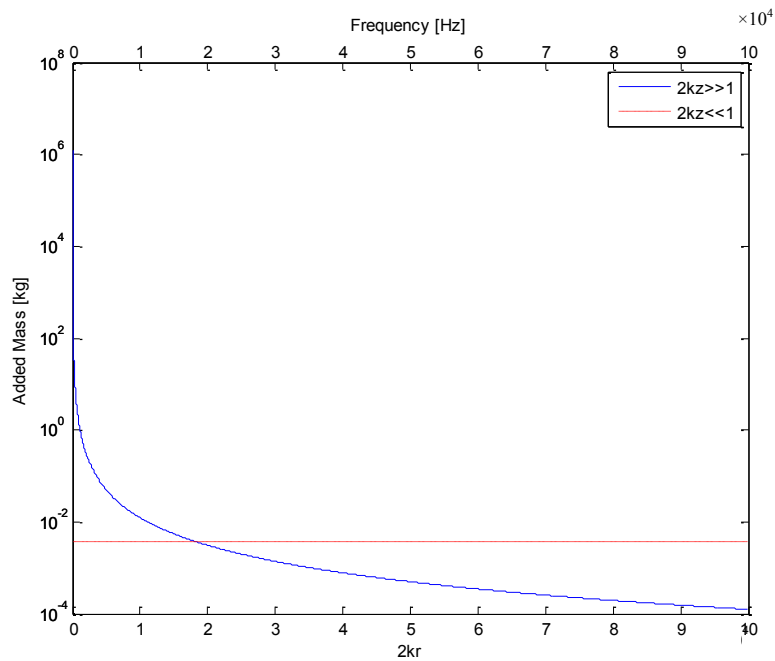


Figure 4.1: Added mass of 20 by 20 mm plate vs.  $2kr$  and frequency

For modes that have natural frequencies just below the critical frequency, the inertial component of fluid loading of a one-dimensional plate will be somewhat larger than that given by Eq. 4.3 and smaller if the natural frequencies are above the critical frequency. The inertial loading of a two-dimensional plate with a mode of order  $(p, q)$  at frequencies well below the critical frequency is also given by Eq. 4.3, with  $k_m$  equal to  $[(p\pi/a)^2 + (q\pi/b)^2]^{1/2}$  where  $a$  and  $b$  are widths of the plate. Eq. 4.3 can then be written as,

$$m_e \cong \rho_0 / k_m = \rho_0 / \left[ (p\pi/a)^2 + (q\pi/b)^2 \right]^{1/2} \quad (4-4)$$

For the size of a 0.02 m by 0.02 m plate with  $1.2 \times 10^{-3}$  m thickness, Eq. 4.3 and Eq. 4.4 result in the same added mass.

According to Fahy, the natural frequencies of a fluid loaded plate can be approximated by Eq. 4.5 below the critical frequency. The reason why it is below the critical frequency is that as the wave number increases, the fluid loading has a smaller effect on the natural frequencies [21]. This can be seen by Figure 4.1. The critical frequency can be obtained by equating the bending wave velocity to the speed of sound in the fluid.

$$\omega'_m \cong \omega_m \left( 1 + \rho_0 / m_{avg} k_m \right)^{-1/2} \quad (4-5)$$

where  $\omega_m = in\ vacuo$  natural frequency

$k_m =$  the primary modal wavenumber component which is  $m\pi/l$  for 1-D or  $[(p\pi/a)^2 + (q\pi/b)^2]^{1/2}$  for 2-D

$m_{avg} =$  the average structural mass per unit area

### ***Techet***

A. Techet (2005) reported that there is an additional effect (force) acting on a structure for the case of unsteady motion of bodies under water or unsteady flow around objects. Theoretically he represents the formula for the added mass of simple geometric shapes such as a cylinder and a sphere [22]. However, he only provides the section of the body which has a square shape. For a thin plate, it is approximated based on the square shape as Eq. 4.6.

$$m_a = \rho \cdot \forall = \rho \cdot A \cdot t = \rho \cdot (l \times l) \cdot t \approx 4.754 \cdot \rho \cdot (l/2)^2 \cdot t \quad (4-6)$$

where  $l$  is the length of the sensor and  $t$  is its thickness.

Techet suggests that his approximation is acceptable for small amplitude oscillations in low natural frequency. The natural frequency can be obtained by Eq. 4.7 for a simple one degree-of-freedom spring mass system with a new mass  $m' = m + m_{added}$ .

$$\omega' = \sqrt{\frac{k}{m'}} = \sqrt{\frac{k}{m + m_{added}}} \quad (4-7)$$

### ***Brennen***

Brennen (1982) did extensive work on the added mass for several different shaped objects based on two-dimensional potential flows. He regarded the added mass as an additional fluid force which acts on the surfaces in contact with the fluid. He determines the added mass by finding the necessary work done to change the kinetic energy associated with the motion of the fluid. Any motion of fluid such as that which occurs when an object moves through it implies a certain positive, non-zero amount of kinetic energy associated with the fluid motions. Examining the idealized potential flows past objects such as a sphere and a cylinder and by the use of solutions of Laplace equation  $\nabla^2 \phi = 0$  where the left hand side term represents the velocity potential for irrotational incompressible flow and the right hand side represents the Stokes flow due to the effect of the boundaries, the added mass formula has been evaluated [23, 36].

For the case of cylinder, the added mass is equal to the mass of the fluid displaced by the body, whereas the added mass of the sphere is one half of the displaced mass. These are algebraically the simplest potential flows for which the added mass can be evaluated. However there is no general correlation between added mass and displaced fluid mass as was developed for an added mass of the sphere that was defined as one half of the displaced fluid mass. Thus the displacement fluid mass may not even be a good first approximation to the added mass except for the case of the cylinder. Furthermore the value of the added mass depends on the direction of acceleration in general. For instance, the idealized potential flow solution for the thin flat plate accelerated in a tangential rather than a normal direction yields zero added mass.

Brennen observed that for simple geometry object such as a circular cylinder, in the ideal case of potential flow around it in rectilinear motion the added mass is equal to the mass of fluid displaced by the cylinder. He regarded this as coincidental and finds no general correlation between added mass and displaced fluid mass. Furthermore the idealized potential flow past an thin flat plate accelerated normal to itself has an added mass equal to the mass of a circular cylinder of fluid with a diameter equal to the width of the plate [23, 36]. This is represented in Eq. 4.8.

$$M = \pi \cdot \left( \frac{\text{width}}{2} \right)^2 \cdot \rho \text{ per unit thickness} \quad (4-8)$$

For the added mass of the section through body based on two dimensional potential flows, Brennen provides the Eq. 4.8 by assuming that the ratio of the width and the height is infinity for any of such ratio is greater than 10. The ratio between the width and the height of the body section we are analyzing for our sensor is about 17.

#### 4.1.1 Added Mass for a Translating Rigid Plate

Fluid loading added mass calculated with the discussed methods is compared in Table 4-1. In order to study the sensitivity of added mass to the size of the rigid plate, two different plate sizes are considered for the analysis: 1 mm by 1 mm with  $1 \times 10^{-6}$  m thickness and 20 mm by 20 mm with  $1.2 \times 10^{-3}$  m thickness.

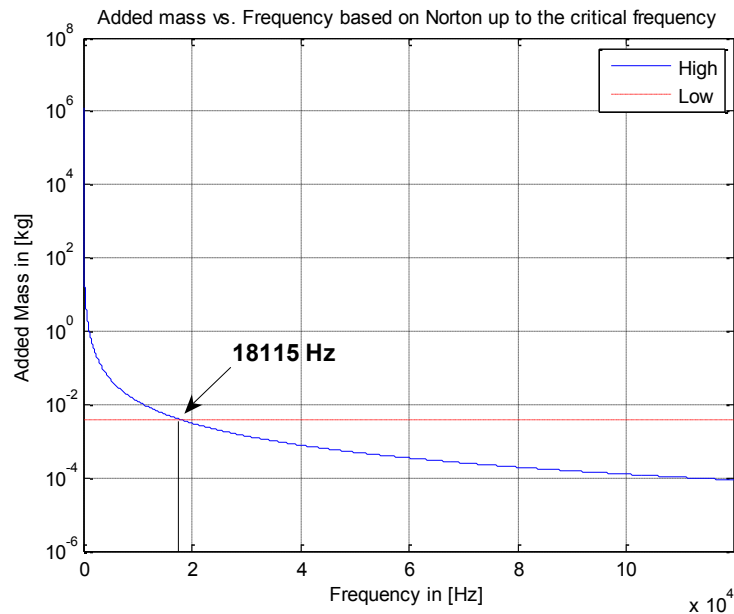


Figure 4.2: Plot of added mass vs. frequency up to critical frequency.

While Junger and Feit's method requires one to choose expression depending on frequency, the other methods do not require any frequency related information. However, Fahy suggests that the

formula is only good for frequencies well below the critical frequency. We have therefore chosen frequency 18,115 Hz for our added mass comparison in Table 4-1. This is the frequency for which the two expressions in Junger and Feit's method yield identical added masses for the 20 mm by 20 mm case. It is also well below the critical frequency. Figure 4.2 shows the added mass versus frequency up to critical frequency based on Junger and Feit. As seen in Table 4-1, the added masses found by the different methods vary significantly. To determine which methods would produce the most accurate result in our investigation we also performed a detailed FEA analysis of the system. The result of this analysis is shown in the last row of Table 4-1.

Table 4-2 shows the corresponding results for a smaller size plate of 1 mm by 1 mm of 1  $\mu$ m thickness. Since  $2kz \ll 1$  due to the smaller value of  $z$ , we chose the Eq. 4-1 when calculating the added mass using Junger and Feit's.

The added masses obtained by Junger and Fahy's expressions are greater than others and at the same time closer to that of FEA. This is shown in Table 4-1 as well as Table 4-2. The large discrepancies between the added mass obtained by FEA and that by the other methods indicate that the assumptions made for each method cannot be considered to be complete and/or accurate. In addition to the shown discrepancies, it is important to note that added mass is not constant but rather varies as frequency changes. In section 4.1.3, not only the first natural frequency but also the second natural frequency will be simulated using FEA to demonstrate the relationship between the added mass and frequency.

Comparing of geometry between two different size of the same shape, 20 mm by 20 mm and 1 mm by 1 mm, it is observed that the percent increase of added mass is different. According to Junger's method and the result of FEA, the percentage increase of added mass is increased as the size of the plate gets larger, which makes more sense. In order to see the relationship between the size of the given shape and the percentage increase of the added mass, different sizes of the shape are simulated and tabulated in Tables 4-1 through 4-6.

#### **4.1.2 Added Mass for a Rotating Rigid Plate**

In this section, added mass of a rotating plate due to fluid loading is compared to each other based on the previously discussed methods. Brennen estimates the added mass for a rotating plate based on 2-D potential flow. Eq. 4.8 above represents the added mass for two-dimensional potential flow

perpendicular to the face of the plate. Considering a rotating plane lamina with respect to one edge, the kinetic energy associated the motion due to flow can be represented as

$$T = \frac{9}{16} \rho \pi g^4 \omega^2 = \frac{1}{2} \left( \frac{9}{8} \rho \pi g^4 \left( \frac{v}{r} \right)^2 \right) = \frac{1}{2} \left( \frac{9}{8} \rho \pi g^2 \right) v^2 \quad (4-9)$$

where  $g$  = half of the length of the thin plate.

The formula inside the parenthesis in Eq. 4.9 represents the effective added mass per unit thickness due to fluid loading. Thus the effective added mass due to fluid loading for rotating thin plates becomes

$$M_{eff\_fluid} = \frac{9}{8} \cdot \rho \cdot \pi \cdot a^2 \cdot t = \frac{9}{8} \cdot \rho \cdot \pi \cdot \left( \frac{L}{2} \right)^2 \cdot t \quad (4-10)$$

Comparing Eq. 4.8 and 4.10, the difference is observed between the effective rotational added mass and the translational added mass due to fluid loading. The work of Brennen's provides the formula for the effective rotational added mass by the energy method. FEA results are calculated by comparing the results of the time harmonic analysis in water and *in vacuo*.

Table 4-1: Comparison of added mass at 18,115 Hz for 20 mm by 20 mm plate (Translational)

	$m_{added}$ in [kg]	$m_{total}$ in [kg]	Based shape	% increase of $m_{added}^{**}$
No fluid	N/A	0.0011*	N/A	N/A
Junger & Feit	0.0038	0.0049	Cylinder	241.0
Fahy	0.0076	0.0087	Plane lamina	579.5
Techet	$4.77 \times 10^{-4}$	0.0016	Cylinder/sphere	-57.3
Brennen	$3.75 \times 10^{-4}$	0.0015	Plane lamina	-66.4
FEA***	0.0027	0.0038	Thin square plate	145.4

\* represents  $m_0$ , sensor's translational effective mass. \*\* % difference =  $100 \times ((m_{added} - m_0)/m_0)$ .

\*\*\* represents FEA result for 20 mm by 20 mm plate with 1.2e-3 m thickness.

Table 4-2: Comparison of added mass for 1 mm by 1 mm plate (Translational)

	$m_{\text{added}}$ in [kg]	$m_{\text{total}}$ in [kg]	Based shape	% increase of $m_{\text{added}}$ **
No fluid	N/A	$2.33 \times 10^{-9}$ *	N/A	N/A
Junger & Feit	$4.76 \times 10^{-7}$	$4.79 \times 10^{-7}$	Cylinder	$2.0 \times 10^4$
Fahy	$3.16 \times 10^{-7}$	$3.17 \times 10^{-7}$	Plane lamina	$1.3 \times 10^4$
Techet	$9.95 \times 10^{-10}$	$1.77 \times 10^{-9}$	Cylinder/sphere	28.2
Brennen	$7.81 \times 10^{-10}$	$1.56 \times 10^{-9}$	Plane lamina	0.6
FEA***	$2.01 \times 10^{-7}$	$2.03 \times 10^{-7}$	Thin square plate	$0.8 \times 10^4$

\* represents  $m_0$ , sensor's translational effective mass. \*\* % difference =  $100 \times ((m_{\text{added}} - m_0)/m_0)$ .

\*\*\* represents FEA result for 1 mm by 1 mm plate.

Table 4-3: Comparison of added mass at 18,115 Hz for 20 mm by 20 mm (Rotational)

	$m_{\text{added}}$ in [kg]	$m_{\text{total}}$ in [kg]	Based shape	% increase of $m_{\text{added}}$ **
No fluid	N/A	$3.72 \times 10^{-4}$ *	N/A	N/A
Junger & Feit	0.0013	0.0016	Cylinder	249.4
Fahy	0.0025	0.0029	Plane lamina	572.0
Techet	$1.59 \times 10^{-4}$	$5.32 \times 10^{-4}$	Cylinder/sphere	-57.2
Brennen	$4.22 \times 10^{-4}$	$7.95 \times 10^{-4}$	Plane lamina	13.4
FEA***	0.0013	0.0017	Thin square plate	249.4

\* represents  $m_0$ , sensor's rotational effective mass. \*\* % difference =  $100 \times ((m_{\text{added}} - m_0)/m_0)$ .

\*\*\* represents FEA result for 20 mm by 20 mm cantilever beam with 1.2e-3 m thickness.

Table 4-4: Comparison of added mass for 1 mm by 1 mm (Rotational)

	$m_{\text{added}}$ in [kg]	$m_{\text{total}}$ in [kg]	Based shape	% increase of $m_{\text{added}}$ **
No fluid	N/A	$7.76 \times 10^{-10}$ *	N/A	N/A
Junger & Feit	$1.58 \times 10^{-7}$	$1.59 \times 10^{-7}$	Cylinder	$2.0 \times 10^4$
Fahy	$1.05 \times 10^{-7}$	$1.06 \times 10^{-7}$	Plane lamina	$1.3 \times 10^4$
Techet	$3.31 \times 10^{-10}$	$1.10 \times 10^{-9}$	Cylinder/sphere	-57.2
Brennen	$8.79 \times 10^{-10}$	$1.65 \times 10^{-9}$	Plane lamina	13.2
FEA***	$1.44 \times 10^{-7}$	$1.44 \times 10^{-7}$	Thin square plate	$1.8 \times 10^4$

\* represents  $m_0$ , sensor's effective mass. \*\* is percentage increase compared to \*.

\*\*\* represents FEA result for 1 mm by 1 mm sensor's plate.

Table 4-5: Comparison table of added mass for 10 mm by 10 mm (Rotational)

	$m_{\text{added}}$ in [kg]	$m_{\text{total}}$ in [kg]	% increase of $m_{\text{added}}$
No fluid	N/A	$9.32 \times 10^{-5*}$	N/A
Junger & Feit	$1.58 \times 10^{-4}$	$2.52 \times 10^{-4}$	70.5
Fahy	0.0013	0.0014	$1.2 \times 10^3$
Techet	$3.9 \times 10^{-5}$	$1.3 \times 10^{-4}$	-57.2
Brennen	$1.05 \times 10^{-4}$	$1.98 \times 10^{-4}$	13.2
FEA	$1.96 \times 10^{-4}$	$2.9 \times 10^{-4}$	111.1

Thickness =  $1.2 \times 10^{-3}$  [m]

Table 4-6: Comparison table of added mass for 25 mm by 25 mm (Rotational)

	$m_{\text{added}}$ in [kg]	$m_{\text{total}}$ in [kg]	% increase of $m_{\text{added}}$
No fluid	N/A	$5.82 \times 10^{-4*}$	N/A
Junger & Feit	0.0025	0.0031	326.3
Fahy	0.0032	0.0038	449.3
Techet	$2.48 \times 10^{-4}$	$8.31 \times 10^{-4}$	-57.2
Brennen	$6.59 \times 10^{-4}$	0.0012	13.2
FEA	0.0023	0.0029	295.1

Thickness =  $1.2 \times 10^{-3}$  [m]

Table 4-3 shows the added mass comparison at the frequency of 18,115 Hz for the rotating plate. Added mass varies significantly depending on the method. In order to demonstrate the fluid loading effect further, more different sizes of the plate are simulated and tabulated for comparison in Tables 4-4, 4-5, and 4-6. Discrepancy between each data and FEA result can be due to: (i) difference between rigid body and deformable FEA model, and (ii) boundary condition imposed on FEA. The FEA model used for rotating case is the cantilever plate.

For FEA data of the rotational case in Table 4.3, fluid loading added mass has been evaluated by comparing the natural frequencies of a 20 mm by 20 mm rotating plate (cantilever beam) with  $1.2 \times 10^{-3}$  m thickness in water from the time harmonic analysis and the natural frequency *in vacuo* from the modal analysis. This is shown in Eq. 4.11.

$$\sqrt{\frac{m_{\text{fluid}}}{m_{\text{vac}}}} = \frac{11,515 \text{ Hz}}{7,300 \text{ Hz}} \rightarrow \frac{m_{\text{fluid}}}{m_{\text{vac}}} = \left( \frac{11,515}{7,300} \right)^2 \approx 2.4 \quad (4-11)$$

It is noted that the method based on Junger and Feit gives rise to the same order of the added mass compared to that of FEA for the rotating plate and the added mass increases as the size of the sensor increases. All methods other than Junger's and Fahy's show the same percent of increase from the effective mass of the plate regardless of the size changes.

In the next section, the added mass effect will be investigated by increasing frequency and the relationship between the added mass and the frequency will be studied. Based on the further study, best suitable method of added mass will be chosen for our sensor.

#### 4.1.3 Added Mass Effect on Higher Frequency of a Vibrating Cantilever Beam/Sensor

Added mass effect due to fluid loading can be evaluated by comparing the natural frequencies of the cantilever beam vibrating in air (or *in vacuo*) and in water. Consequently, FEA simulation is carried out to determine the natural frequencies and mode shapes. Details about FEA simulation is discussed later in chapter 5. The comparison of the results, including the mode shapes, is shown in Figure 4.3. Due to the added mass effect, a significant decrease of the natural frequencies is observed in the water.

The fluid added mass effect is estimated by calculating the frequency reduction ratio,  $\delta$ , of each mode, defined as Eq. 4.12:

$$\delta = (f_a - f_w)/f_a \quad (4-12)$$

where  $f_w$  and  $f_a$  are the natural frequencies in water and in air respectively and given in Figure 4.3. It can be noticed that the natural frequencies are considerably reduced by the presence of fluid. The frequency reduction ratio does not remain constant for all modes, but varies in a range of 0.60 – 0.79 depending on the corresponding mode shape.

The reduction ratio of the added mass shown in Figure 4.4 demonstrates that the effect of the added mass become smaller as frequency increases. It is observed that the added mass due to fluid loading is not constant with respect to frequency. Hence, the method based on Junger and Feit is better suited for our analysis. Besides, Table 4.3 and 4.4 shows that the percentage increase of added mass based on Junger and Feit's method corresponds well with the FEA result.

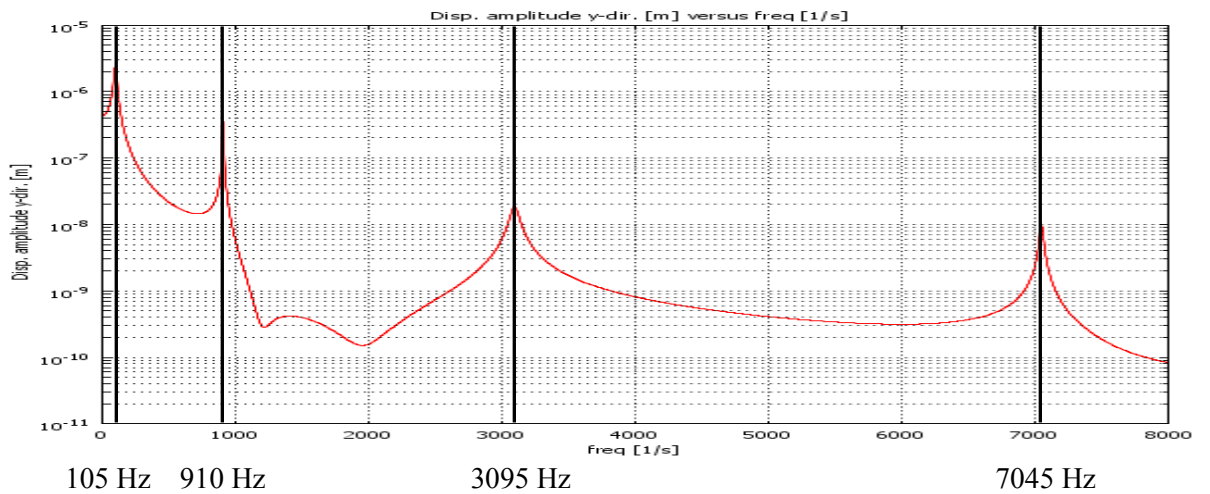
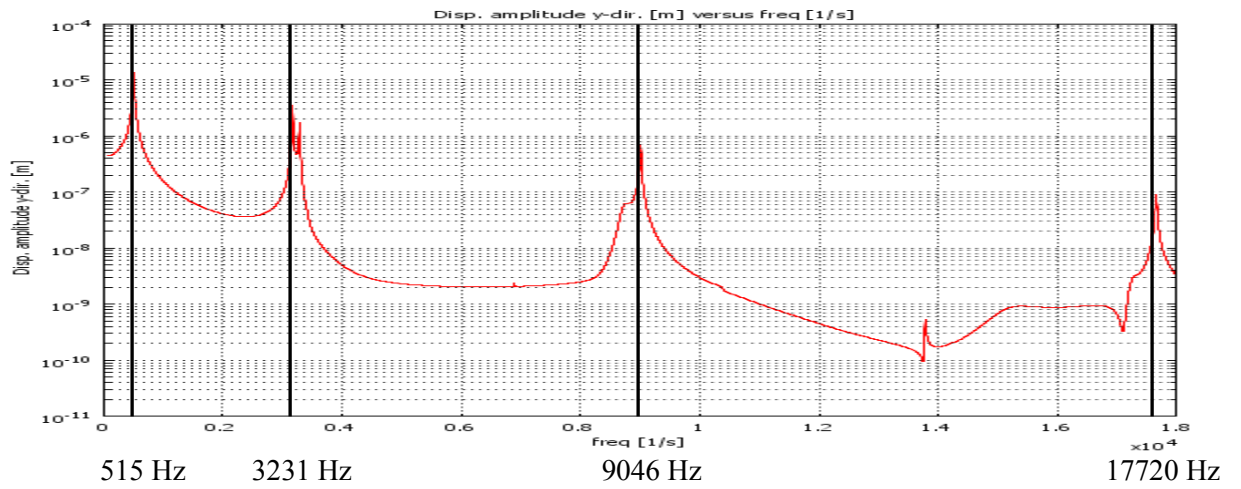


Figure 4.3: Comparison between FEA simulation of cantilever beam in air (upper row) and in water (lower row).

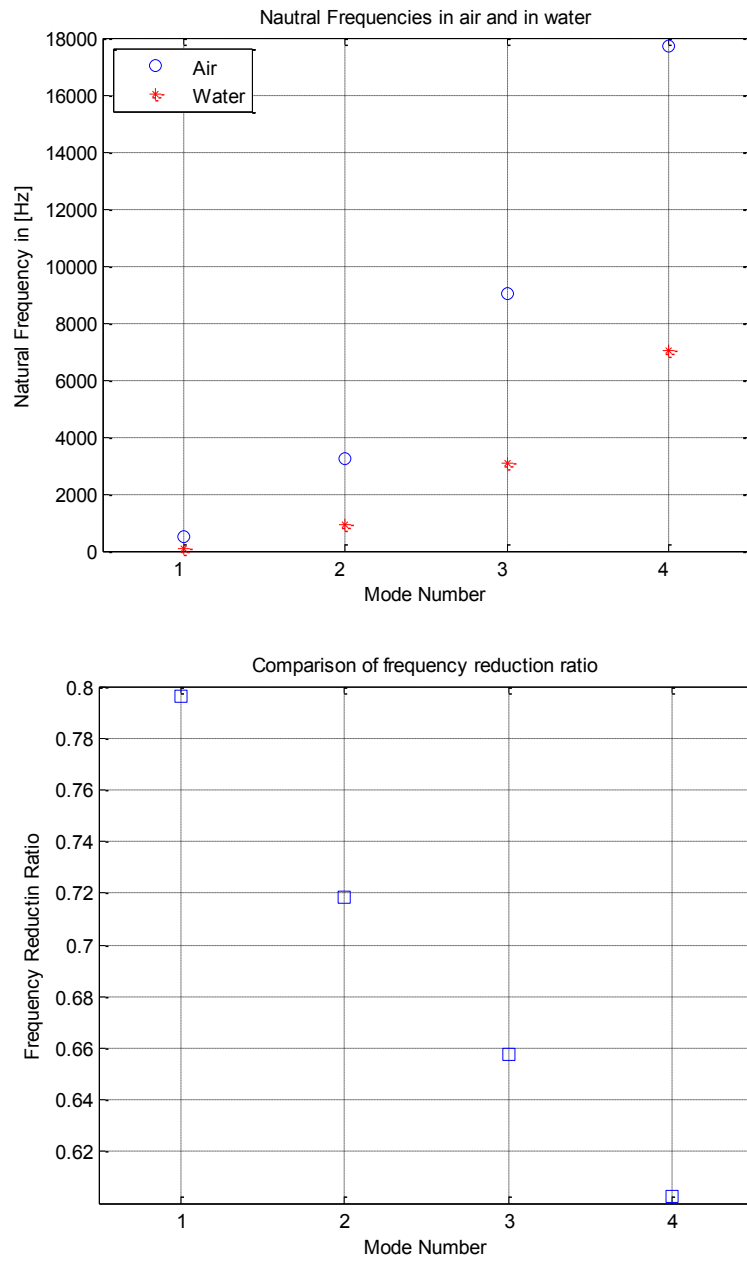


Figure 4.4: Top: Natural frequencies in air and in water based on FEA simulation, Bottom: Comparison of frequency reduction ratio by simulation.

Added mass effect of the sensor is investigated based on the same method for the cantilever plate; the modal characteristics of the free vibration in water are calculated. Table 4-7 shows the natural frequencies obtained from the FEA simulation in different medium. The comparison of the results, including the mode shapes of the sensor, is shown in Figure 4.5.

Table 4-7: Natural frequencies of the sensor in water (Hz): Simulation results

	$f_1$	$f_2$	$f_3$	$f_4$
Air	1955	4110	18870	25406
water	1020	1760	12350	13739

The added mass effect has been calculated by the Eq. 4.12 and the frequency reduction ratio of each mode has been plotted in Figure 4.5. It is observed that noticed that not only the natural frequencies are considerably reduced by the presence of water, but also the first and the second natural frequency reduction ratio work in tandem and so do the third and the fourth. The second and the fourth natural frequencies have bigger reduction ratio than the first and the third. This is different from the cantilever plate case, which is as the frequency increases the reduction ratio decreases. The frequency reduction ratio does not remain constant for all modes again, and varies in a range of 0.34 – 0.57 depending on the corresponding mode shape. Figure 4.6 shows that the reduction ratio for mode 3 is minimal and for mode 2 is maximal. From the each pair of the modes, the second mode has increasing reduction ratio. This observation will be used to choose the added mass model for our sensor.

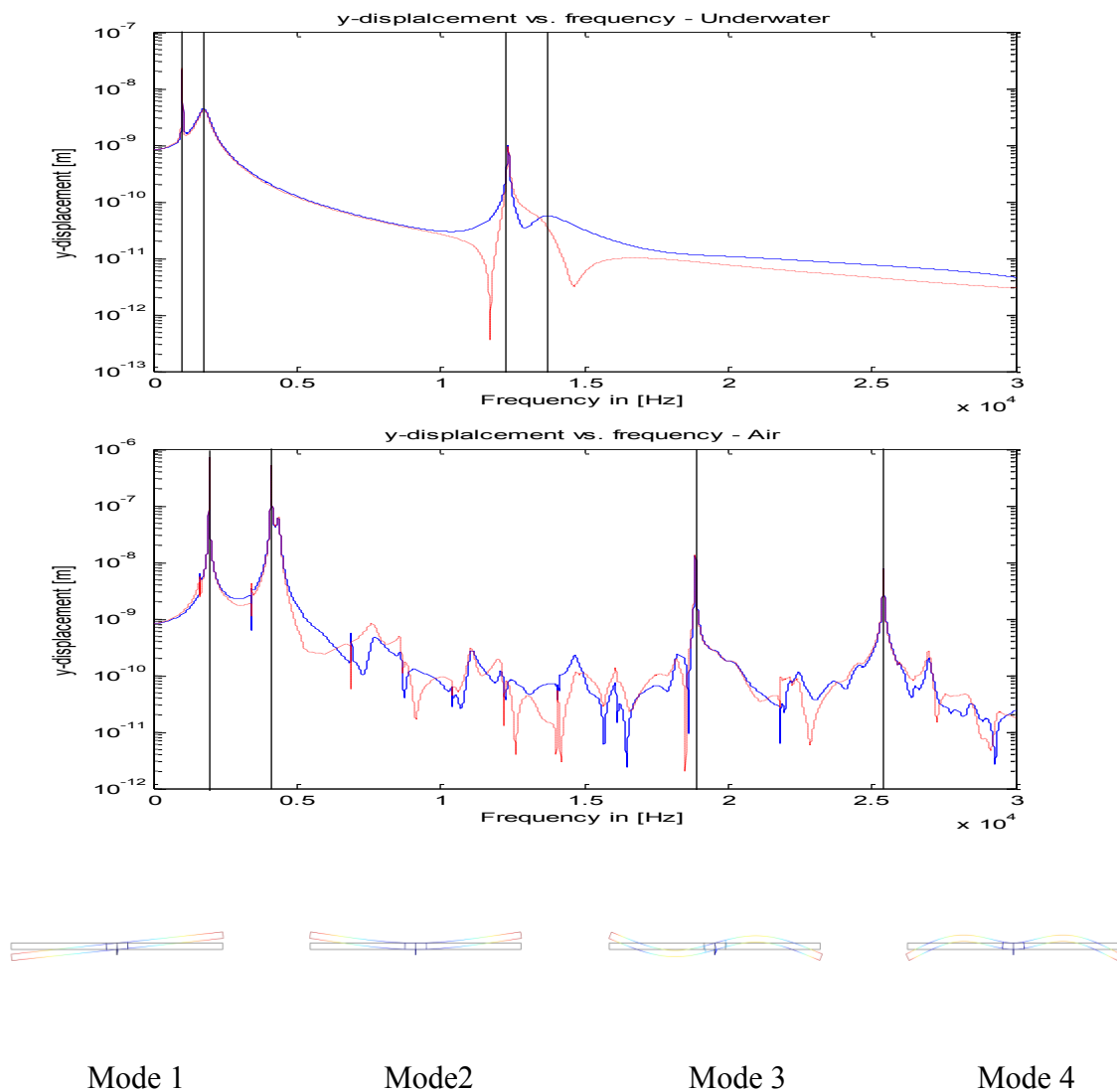


Figure 4.5: Comparison of simulation between in water, in air, and *in vacuo* mode (top to bottom order).

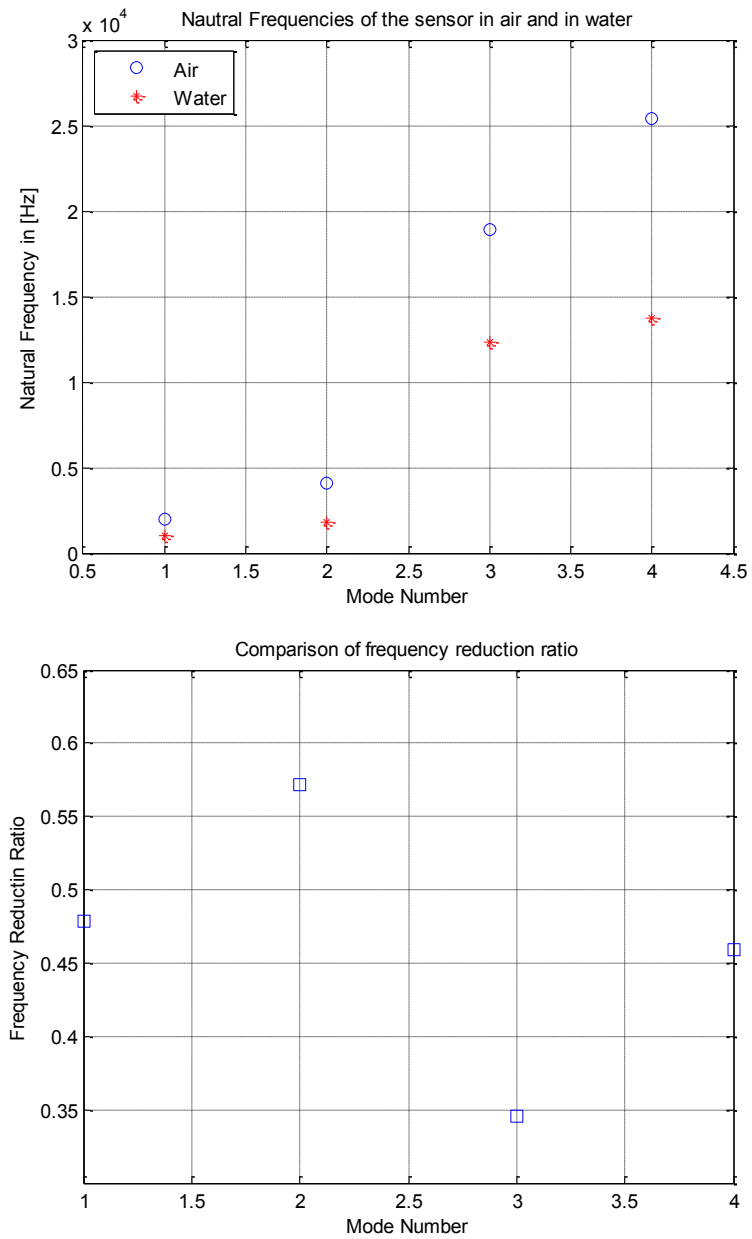


Figure 4.6: Top: Natural frequencies in air and in water based on FEA simulation, Bottom: Comparison of frequency reduction ratio by simulation of the sensor

## 4.2 Modeling of Variable Fluid Loaded Mass for the Hydro-Sensor

It is necessary for us to model the fluid loaded mass of the sensor for the first mode as well as the second. Our sensor shown in Figures 2.1 and 2.5 is modeled as square shaped plates coupled together that act like a teeter-totter at least for the first mode which can be calculated based on the effective mass of Eq. 4.1. Modeling the fluid loaded mass for the 5 DOF lumped parameter sensor model shown in Figure 2.8, there are two types of mass matrices which are the lumped and consistent-mass matrices involved in the analysis of the beam which are shown in Eq. 2.26. Eq. 2.34 represents the mass matrix of a beam element, which can be either lumped or consistent mass matrix. The lumped-mass matrix has only diagonal terms which facilitate the computational efficiency. However, solution accuracy is not as good as that of the consistent-mass matrix. What makes the consistent-mass matrix different from the lumped one is that instead of applying same amount of mass is being distributed at each node uneven amount of mass is being distributed at each node based on the shape function as shown in Figure 4.5. The consistent-mass matrix can be found using the principle of minimum potential energy as shown in Eq. 4.13.

$$m_{consistent} = \iiint_V \rho \cdot N^T \cdot N dV \quad (4-13)$$

where  $N$  is the shape function. Each element in this shape function is defined by

$$[N] = [N_1 \quad N_2 \quad N_3 \quad N_4 \quad N_5 \quad N_6] \quad (4-14)$$

$$\begin{aligned} \text{where } N_1 &= 1 - \frac{\hat{x}}{L} \\ N_2 &= \frac{1}{L^3} \left( 2\hat{x}^3 - 3\hat{x}^2 L + L^3 \right) \\ N_3 &= \frac{1}{L^3} \left( \hat{x}^3 - 3\hat{x}^2 L + 2\hat{x}L^2 - L^3 \right) \\ N_4 &= \frac{\hat{x}}{L} \end{aligned}$$

$$N_5 = \frac{1}{L^3} \left( -2 \hat{x}^3 + 3 \hat{x}^2 L \right)$$

$$N_6 = \frac{1}{L^3} \left( \hat{x}^3 L - \hat{x}^2 L^2 \right)$$

Even though Eq. 4.1 can approximate for the first natural frequency of the sensor in water, the way to estimate the second natural frequency has to be found since our sensor takes advantage of first two modes. This is because the added mass due to fluid loading is not constant but rather a function of frequency as Junger and Feit (1987) suggested. Figure 4.6 also shows that the added mass of the sensor is not a constant as frequency is varied. Hence, the formula used to calculate the added mass for our sensor is chosen as Eq. 4.1 for the first natural frequency and Eq. 4.2 for the second natural frequency. However, there exists the transitional region in Figure 4.1 where the Eq. 4.1 and Eq. 4.2 coexist based on the fluid loaded mass formula by Junger and Feit. In order to solve this coexistence problem in the transitional region, Eq. 4.1 and Eq. 4.2 are used to calculate the added mass for our sensor such that Eq. 4.1 is used to find the first natural frequency of the sensor in water and then Eq. 4.2 is used to estimate the second natural frequency by starting the parabolic added mass curve based on Eq. 4.2 from where the first natural frequency is calculated.

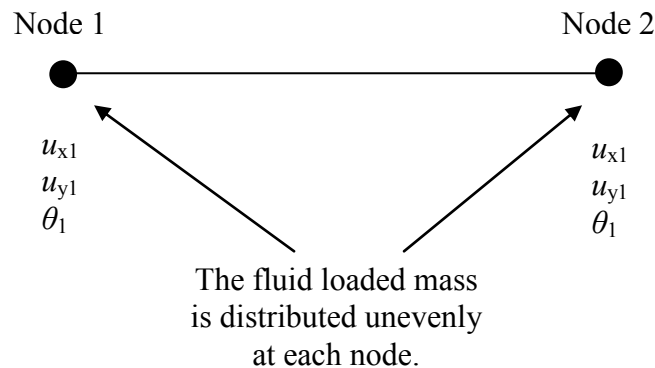


Figure 4.7: Beam element with nodal degrees of freedom.

Table 4-8: Comparison of first two natural frequencies for  $6e-6$  m thickness sensor.

	FEA	Eq. 4.1 & 4.2
1 <sup>st</sup> natural frequency [Hz]	143	148
% Difference	N/A	3
2 <sup>nd</sup> natural frequency [Hz]	1153	1131
% Difference	N/A	2

For 1 mm by 1 mm sensor with a thickness of  $6e-6$  m, the comparison of the first two natural frequencies between the FEA simulation result and our sensor model based on Eq. 2.38 and Eq. 2.39 of 5 DOF lumped parameter model with the added mass formula chosen are made and tabulated in Table 4-8. The comparison between two simulations shows the small percentage difference. Figure 4.8 shows the frequency response of the sensor in water based on the 5 DOF lumped parameter model with added mass on the left side and the plot of fluid loaded mass versus frequency.

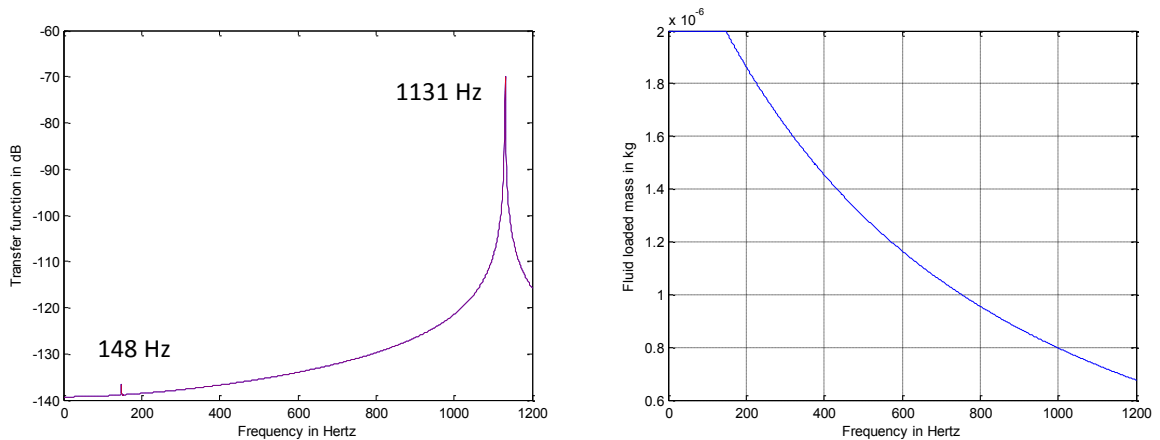


Figure 4.8 Left: Frequency response of 1mm by 1 mm sensor with  $6e-6$  m thickness in water, Right: Fluid loaded mass vs. frequency based on Eq. 4.1 and Eq. 4.2.

The amplitude of the frequency response at each natural frequency and the damping effect will be discussed in Chapter 6 by comparing against the FEA simulation result.

### 4.3 Parametric Study

For the simulation of the response of the submerged sensor in water instead of air, using a lumped parameter model based on Figure 2.1, we need to add the fluid loading and make the appropriate changes in the speed of sound and density of the surrounding medium. Viscous and radiation damping are also added to the analysis in order to incorporate the full effect of the fluid-structure interaction.

1. Speed of sound ( $c_{\text{water}} = 1482$  [m/s], compared to  $c_{\text{air}} = 344$  [m/s]),
2. Density change ( $\rho_{\text{water}} = 995.6$  [kg/m<sup>3</sup>], compared to  $\rho_{\text{air}} = 1.2$  [kg/m<sup>3</sup>]), and
3. Fluid-structure interaction (Added mass and damping).

The changes in these parameters make a tremendous difference in the characteristics of the acoustic sensor between in air and in water. Because the speed of sound in water is about 4.3 times greater than in air, the wavelength  $\lambda$  at any frequency is larger in water than in air by a factor of 4.3. Generally the sound wave detection for the directionality is best at high frequencies where the wavelength is smaller than the dimensions of the sensor. The goal of this research is to remove this limitation by designing a small sensor that can detect the direction of sound for low frequencies.

The feasibility and the performance of the sensor system is strongly dependent on the geometrical and mechanical properties of the sensor such as geometrical dimension and material density, and other design parameters such as the stiffness of the springs shown in Figure 2.1. It is therefore essential to study the design parameter space of the sensor carefully in order to understand how one can optimize the performance of the sensor.

In order to compare the performance in water to that of air a simulation was carried out using added mass method suggested by Junger and Feit. As can be seen in Figure 4.9, there is a substantial difference between the two different mediums. There is only small amplitude difference in water between displacement at each end of the sensor ( $x_1$  and  $x_2$ ) whereas there is a large difference in air; however, only the phase difference amplification is needed to find directivity. Comparing the time delay of air and water as shown in Figure 4.10, it is noted that the natural frequency has been significantly lowered due to the added mass. We can also see that in water the time delay crosses zero at approximately 2,500 Hz while there is no zero crossing in air for frequencies less than 25 kHz. It is the location of the natural frequency where the resonant peak

occurs. For instance, Figure 4.9 shows that the resonant peak is at 7,500 Hz in air and at 2,500 Hz in water.

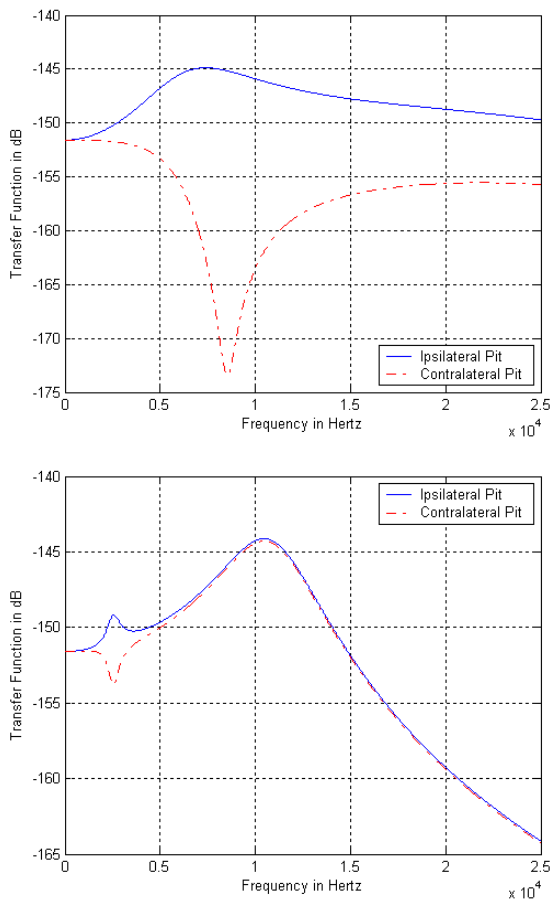


Figure 4.9: Comparison of frequency responses between in air (Top) and in water (Bottom).

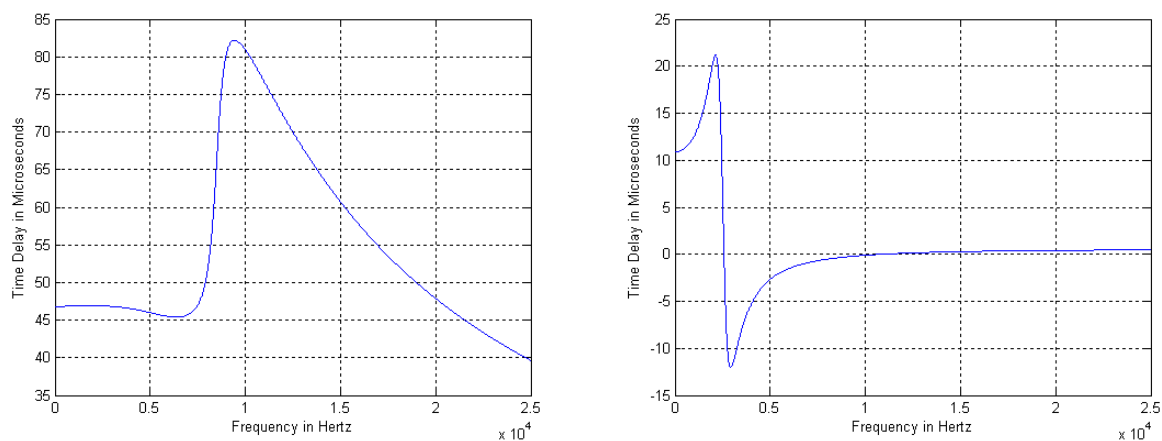


Figure 4.10: Comparison of time delay between in air (Left) and in water (Right)

Additional discussion of the zero crossing is presented separately in Chapter 6 since it greatly affects the performance and the characteristics of the sensor. Zero crossings can also be observed from time domain simulations. This is shown in Figure 4.11 for the frequencies of 2,400 Hz and 3,500 Hz. In the top plot, which corresponds to 2,400 Hz,  $x_1$  (blue solid line) can be seen to precede  $x_2$  (red dotted line). In contrast,  $x_2$  precede  $x_1$  for as the frequency has been increased to 3,500 Hz (the bottom plot).

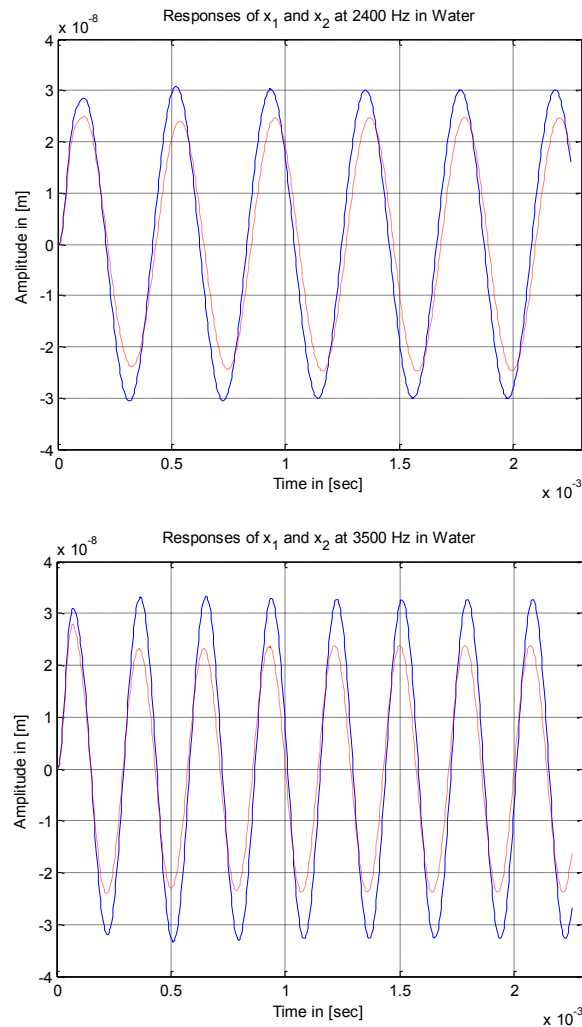


Figure 4.11: Response of the sensor in water of frequencies at 2400 Hz (Top), and 3500 Hz (Bottom)

### 4.3.1 Spring constants $k_1$ , $k_2$ , and $k_3$

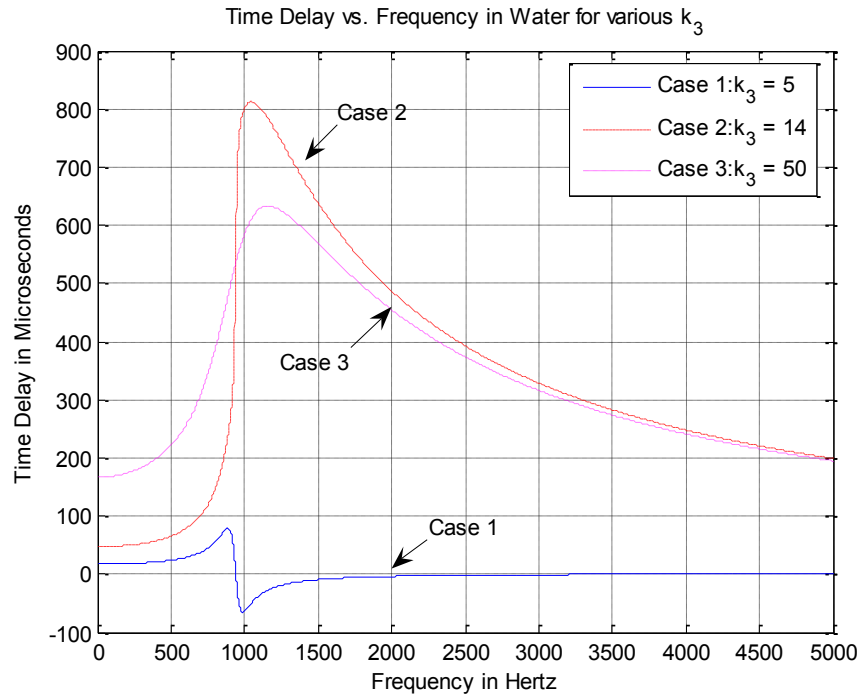


Figure 4.12: Time delay  $\tau$  vs. Frequency  $f$  with variable coupling spring constant  $k_3$  (5 ~ 50 N/m).

Keeping the linear springs  $k_1$ ,  $k_2$  as constant while increasing the coupling spring  $k_3$  in Figure 2.1, it makes zero crossing go away and increases the time delay amplification throughout the bandwidth frequency of the sensor. As the numerical value of  $k_3$  increases further, the bandwidth becomes smaller with more output time delay amplification. If the coupling spring  $k_3$  is increased even further, the bandwidth frequency of the sensor becomes bigger with the lesser time delay amplification within the bandwidth frequency. This is shown in Figure 4.12 with three different numerical values of  $k_3$ . Detailed analysis of this will be discussed with an example in Chapter 6 in terms of design point of view. However, at this stage we don't know if these coupling spring constants are possible to achieve physically for our small sensor. This will be investigated through the use of our 5 DOF lumped parameter model shown in Figure 2.8, which has material as well as geometry information of the sensor. On the contrary to the coupling spring  $k_3$ , increasing  $k$  gives rise to higher natural frequency for the first mode since  $\omega = \sqrt{(k/m)}$ . Detailed description of proper combination of  $k$  and  $k_3$  and their relationship with the first two natural frequencies will be discussed in the design section of Chapter 6.

### 4.3.2 Area

As the area of the plate of the sensor increases with the constant density, the natural frequency becomes smaller since  $\omega = \sqrt{k/m}$  and since the mass is increased as the area is increased. There also is a tradeoff between the amplitude of the output time delay and the bandwidth which is related with the first natural frequency. The first natural frequency is moved to the lower frequency as the mass of the sensor is increased and vice versa. This is shown in Figure 4.13.

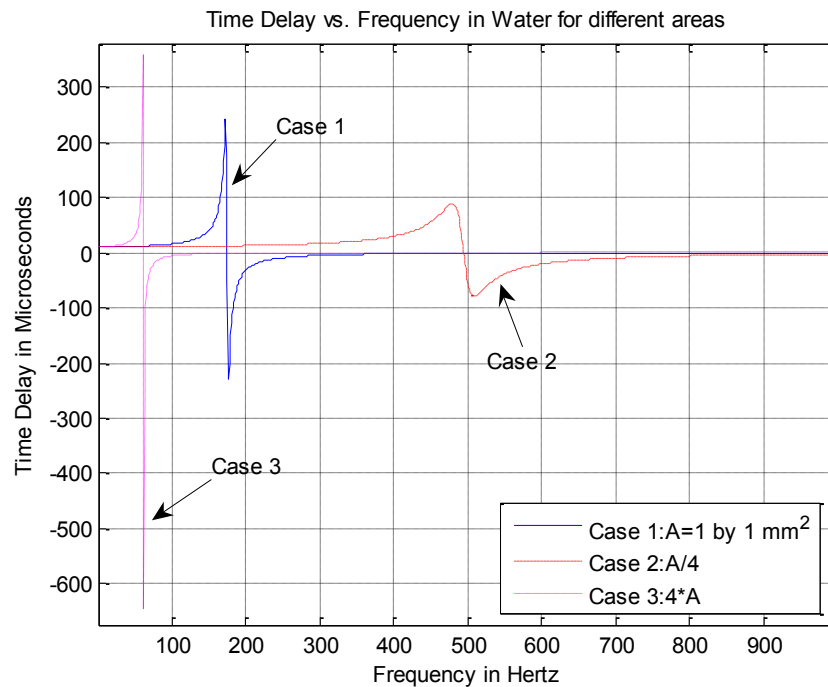


Figure 4.13: Time delay  $\tau$  vs. Frequency  $f$  with variable area.

### 4.3.3 Angle of Incidence $\theta$

Figure 4.14 shows the output time delay versus frequency for various incident angles. As shown in this figure, output time delay for each angle is different which enables us to detect the directivity of the sound. If there were no difference in time delay in terms of the angle of incidence, there would be no directional sensitivity, hence the sensor would become omni-directional. This angle of incidence dependency of the sensor will be used to optimize for designing a sensor in Chapter 6.

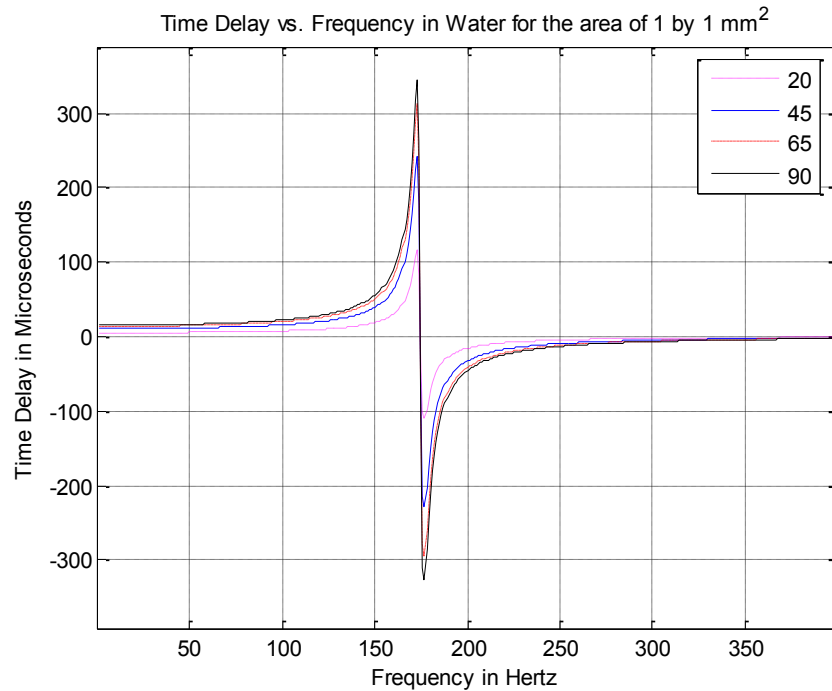


Figure 4.14: Time delay  $\tau$  vs. Frequency  $f$  in water for variable angle of incidence  $\theta$ .

#### 4.3.4 Thickness $t$

Varying thickness of the plate of the sensor has the same effect as varying the mass. As the thickness of the plate is increased the natural frequency is decreased and the time delay is increased. However there is a limitation in Miles' sensor model shown in Eq. 2-1. Other sensor models such as the one based on Mode-Summation method shown in Figure 2.6 and 5 DOF lumped parameter model shown in Figure 2.8 show that as you increase the thickness of the plate the stiffness is increased which prevent the natural frequency to go down. This corresponds well with FEA simulation result which is discussed in Chapter 5.

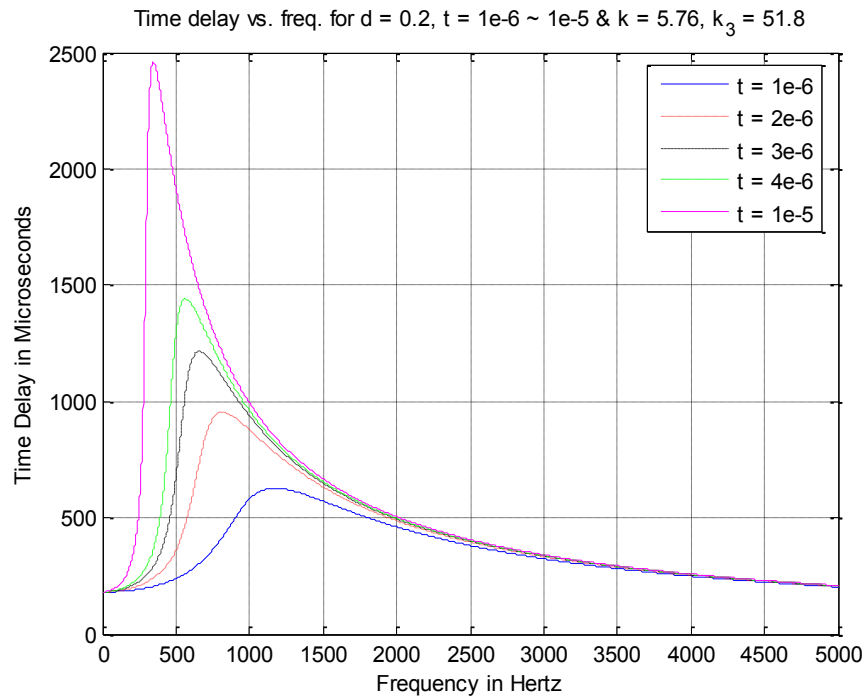


Figure 4.15: Time delay  $\tau$  vs. Frequency  $f$  in water for variable thickness,  $t$ .

### 4.3.5 Damping constants $d_1$ , $d_2$ , and $d_3$

In the fluid-structure interaction problem, there are three types of damping mechanisms present: viscous, acoustic radiation, and/or internal structural damping. In order to consider the damping effect due to fluid-structure interaction, FEA is performed. Harmonic response of the sensor is investigated under applying plane wave on the diaphragm for this. Figure 4.16 shows the simulation results of the harmonic analysis between two medium: air and water. Figure 4.16 shows that the damping effect on the second natural frequency is greater than the first.

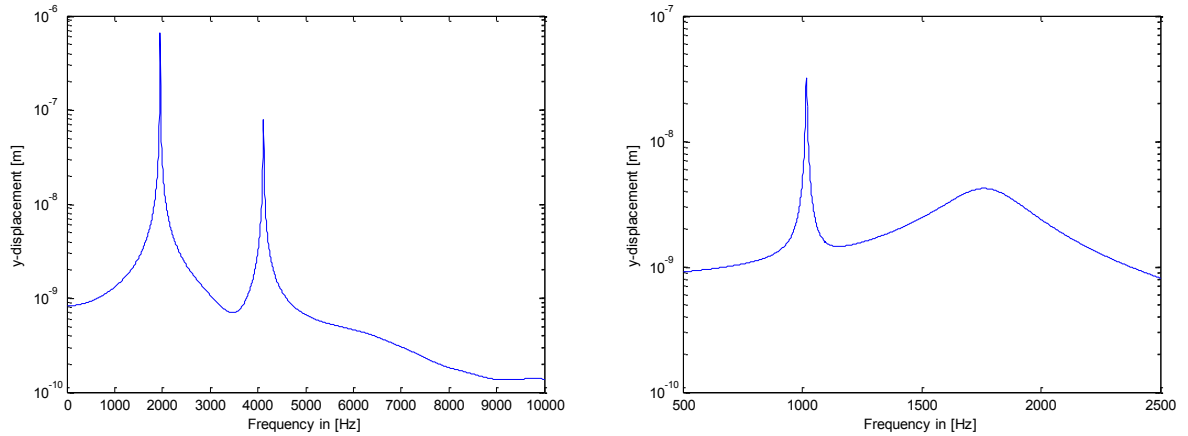


Figure 4.16: Damping effect between air and water based on FEA: Left: Air, Right: Water.

The value of the amplitude ratio at resonance is known as  $Q$  factor or quality factor. The half-power bandwidth method can be used to estimate the damping ratio based on the corresponding  $Q$  value from the frequency response function of a sensor which has been excited by far field sound wave impinged on the sensor. The harmonic responses of the sensor in air and water are shown in Figures 4.17 and 4.18. Table 4-9 shows that there is more damping effect in the second natural frequency than the first and there is prominent damping effect in water than in air.

Table 4-9: Comparison table of the damping effect based on FEA simulation

Water	Difference	Air
$\zeta_{\text{HPB}_1} = 0.0024$	$\Delta\zeta_{\text{HPB}_1} = \mathbf{0.0023}$	$\zeta_{\text{HPB}_1} = 0.00013$
$\zeta_{\text{HPB}_2} = 0.099$	$\Delta\zeta_{\text{HPB}_2} = \mathbf{0.098}$	$\zeta_{\text{HPB}_2} = 0.0011$

Based on the Miles sensor model shown in Eq. 2.1, the relationship between the damping ratio and each damping coefficient can be found via modal analysis. By uncoupling the equations of motion in Eq. 2.1, we obtain

$$\begin{aligned}
 2 \cdot \zeta_1 \cdot \omega_1 &= \frac{c}{m} \\
 2 \cdot \zeta_2 \cdot \omega_2 &= \frac{(c + 2 \cdot c_3)}{m}
 \end{aligned}
 \tag{4-15}$$

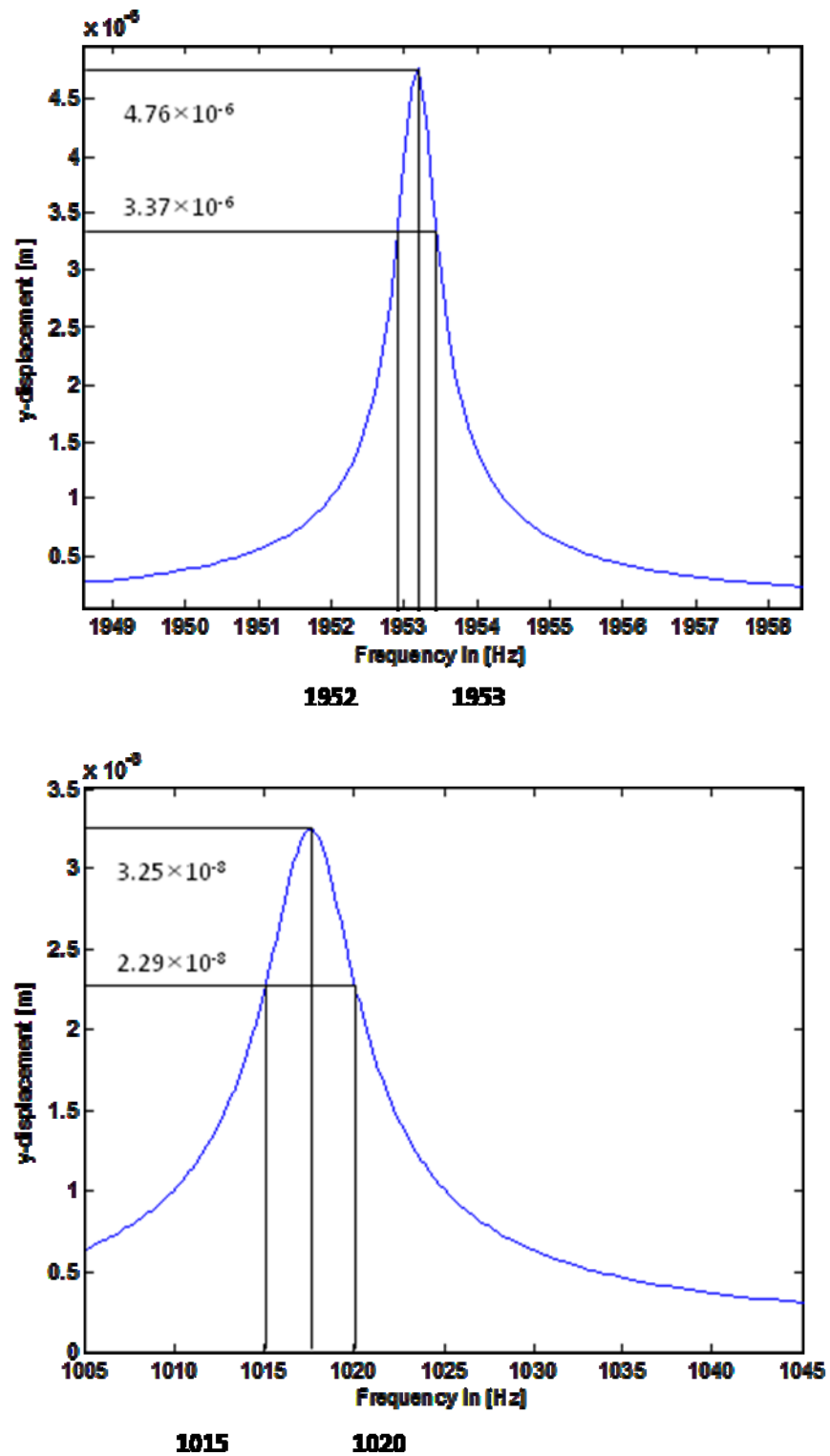


Figure 4.17: Harmonic responses showing half-power points and bandwidth for the first natural frequency of the sensor in air (Top) and in water (Bottom).

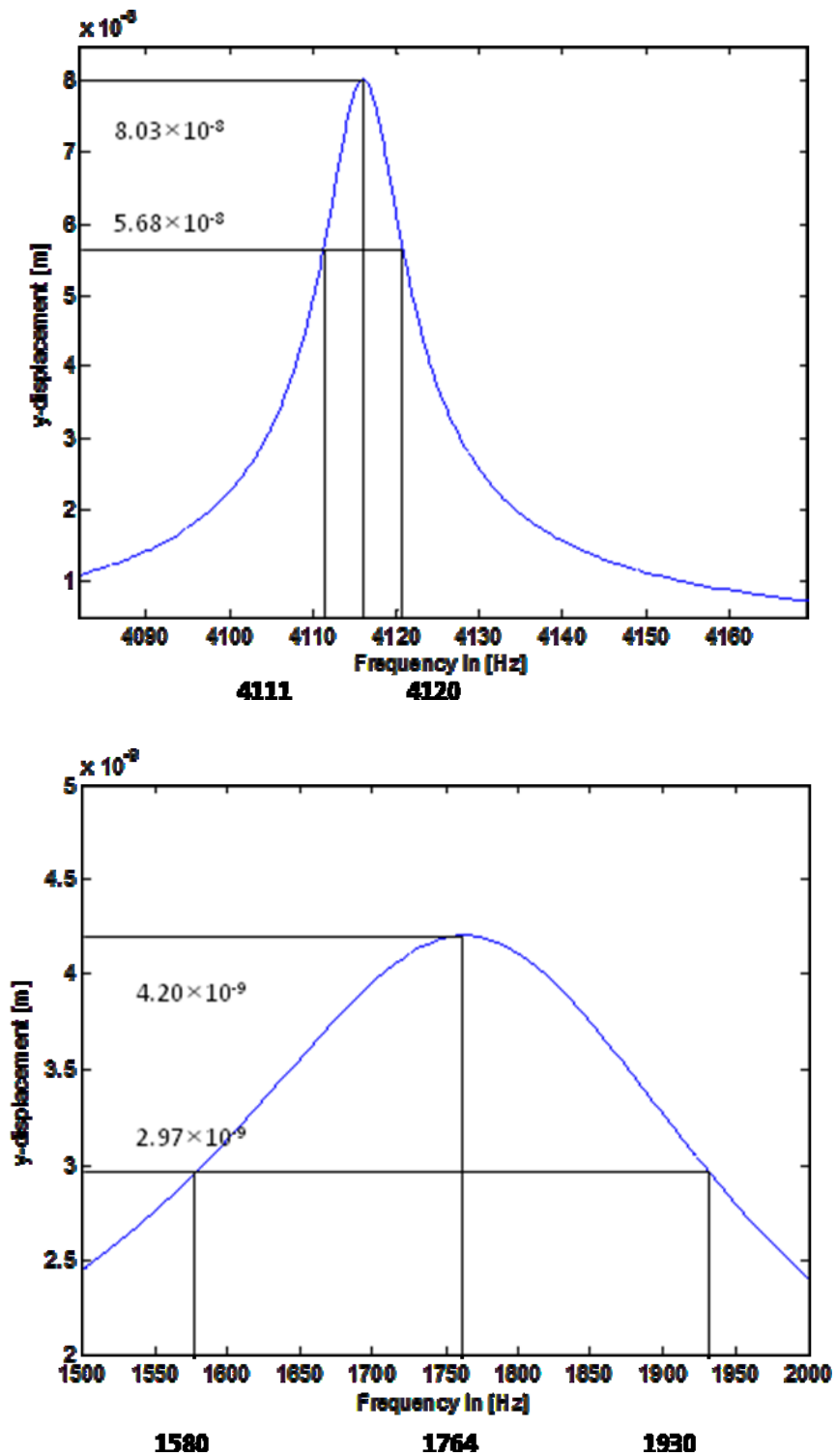


Figure 4.18: Harmonic responses showing half-power points and bandwidth for the second natural frequency of the sensor in air (Top) and in water (Bottom).

Zhang and Turner (2006) reported that the damping ratio in liquid tends to be in the range of 0.05 to 0.5 [25]. Our FEA simulation results show that the additional damping ratios for  $\zeta_1$  and  $\zeta_2$  due to viscosity and sound ration in water are 0.0023 and 0.0982, respectively. The fluid damping suggested by Zhang and Turner seems too large compared to our FEA result. However in order to take into consideration of the extreme damping case, the fluid damping suggested by Zhang and Turner is used to investigate the damping effect in water for parametric damping study.

The damping ratio to be used for the parametric damping study is calculated by adding internal damping constant and the damping ration in liquid suggest by Zhang and Turner. The internal damping ratios for the first and second resonant modes are assumed to be 0.44 and 0.62 [11]. Hence, the range of interest would be between combination values of  $0.49 \leq \zeta_1 \leq 0.94$  and  $0.67 \leq \zeta_2 \leq 1.12$ . The corresponding damping constants are  $1.27 \times 10^{-5} \leq c \leq 2.43 \times 10^{-5}$  and  $3.12 \times 10^{-5} \leq c_3 \leq 5.06 \times 10^{-5}$  by assuming  $c = c_1 = c_2$ . However, Figure 4.19 shows that the characteristic of the sensor is insensitive to the coupling damping constant  $c_3$ . It is not presented here for the parametric study.

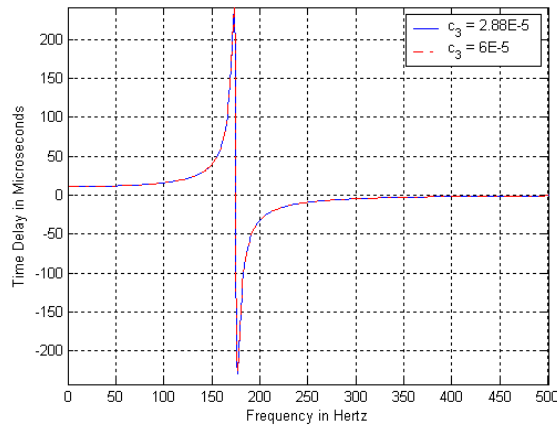


Figure 4.19: Time delay  $\tau$  vs. Frequency  $f$  in water for different damping constant,  $c_3$

Two different sizes of the sensor are investigated for the damping effect by increasing damping constants  $c_1$  and  $c_2$  in Figure 2.1; (i) the sensor size of 1 mm by 1 mm plate with  $10 \mu\text{m}$  thickness, (ii) 3.5 mm by 3.5 mm plate with  $3.5 \mu\text{m}$  thickness. Starting with the low damping constant ( $c = c_1 = c_2$ ), it is gradually increased to see the damping effect on the output time delay of the sensor. Damping constant cases 1 and 2 are the minimum ( $1.27 \times 10^{-5}$ ) and the maximum ( $2.43 \times 10^{-5}$ ) damping constants since  $1.27 \times 10^{-5} \leq c \leq 2.43 \times 10^{-5}$ . Figure 4.20 shows the comparison between

damping cases 1 and 2. The higher damping constant  $c$  gives rise to greater peak amplification of the time delay with less bandwidth. Damping constant  $c$  is increased further up to case 7 as seen in Figure 4.20. As the damping constant  $c$  is increased beyond the case 2, the same trend is observed until zero crossing occurs. The damping case 6 in Figure 4.20 is the one causes the zero crossing. Once the zero crossing occurs with case 6 damping constant  $c$ , the amplification is decreased as the damping constant  $c$  increases. Once the zero crossing occurs, increasing damping only reduces the amplitude of the time delay amplification.

As the plate size of the sensor is increased, the damping constant  $c$ , which causes the zero crossing, goes up. Figure 4.21 demonstrates for the bigger sensor (ii) of the plate size 3.5 mm by 3.5 mm with 3.5  $\mu\text{m}$  thickness for three different damping constant. Damping constant case 1 and 2 are the same damping constant used for investigating the smaller sensor (i) in Figure 4.20. Damping constant case 3 for the bigger sensor (ii) is the one that makes the zero crossing of the smaller sensor (i) shown in Figure 4.20. However, as shown in Figure 4.21, there is no zero crossing even with the case 3 for the bigger sensor in terms of the size. The damping constant effect on the bigger sensor (ii) follows the same trend as for the smaller sensor (i) which is not shown in Figure 4.21.

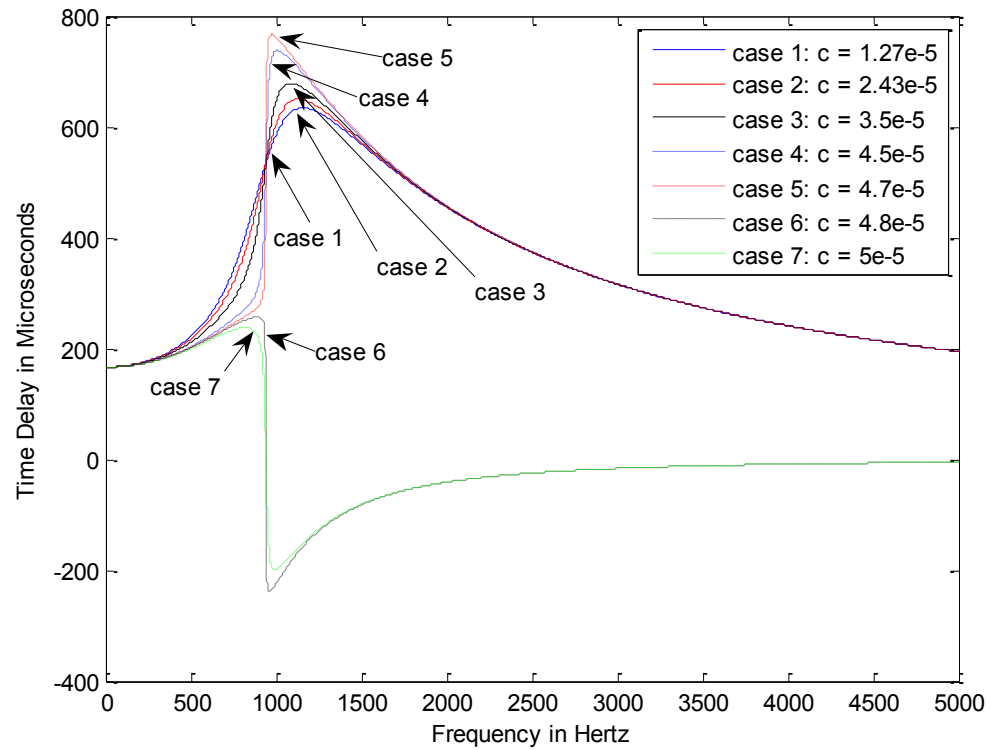


Figure 4.20: Time delay vs. frequency with varying damping constant  $d$  for smaller sensor (i).

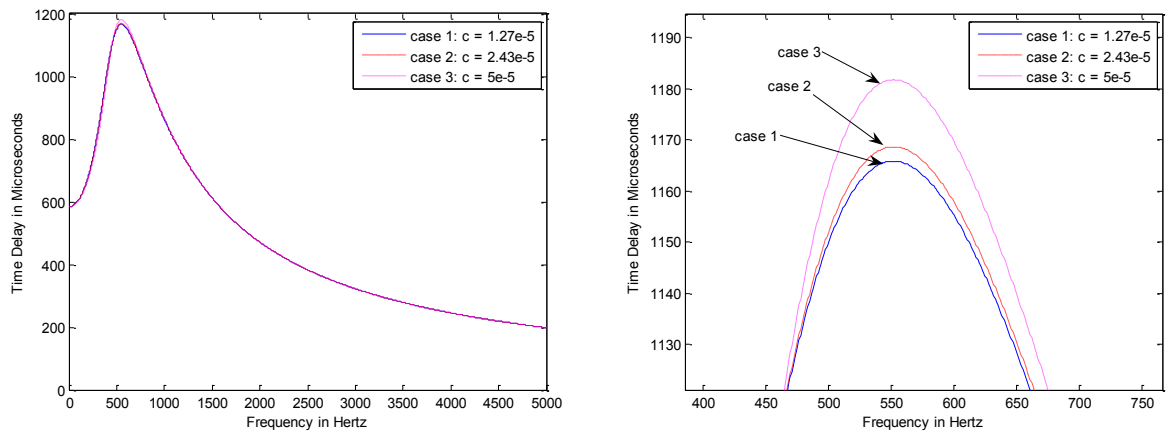


Figure 4.21: Time delay vs. frequency for varying damping constant  $d$  for bigger sensor (ii).

#### 4.4 Sensitivity Analysis

So far we have studied the effect of each design parameters on the sensor characteristics. It is also important to know overall sensitivity of the sensor in order to understand how to amplify the time delay.

A conventional array of uncoupled omni-directional sensors (microphones or hydrophones) has a delay in between sensors  $\tau = d \cdot \sin\theta / c$  that is almost four times in air compared to water (where  $d$  is the separation of the sensors and  $\theta$  is the angle of the incoming plane wave with the longitudinal axis of the array). This is of course due to the difference in the speed of sound which affects  $\tau = d \cdot \sin\theta / c$  where  $c_{\text{air}}$  is 344 [m/s] and  $c_{\text{water}}$  is 1483 [m/s].

The sensitivity of the sensor was investigated in order to determine how to increase the output time delay for the water submerged sensor. The sensitivity analysis of the sensor is carried out based on Eq. 2-2 of the lumped parameter model. Figures 4.22 and 4.23 show the frequency response of the sensor, which is subdivided by two red straight lines. The first red line from the left is located at  $\omega = \omega_r$  which corresponds to the rocking mode (out of phase mode) and the right line is at  $\omega = \omega_t$  which corresponds to the translational mode (in phase mode). Table 4-10 shows the dominant terms for each frequency range of interests. As shown in this table, the sensor's sensitivity is a function of many variables, especially in between the first natural frequency  $\omega_r$  and the second natural frequency  $\omega_t$ .

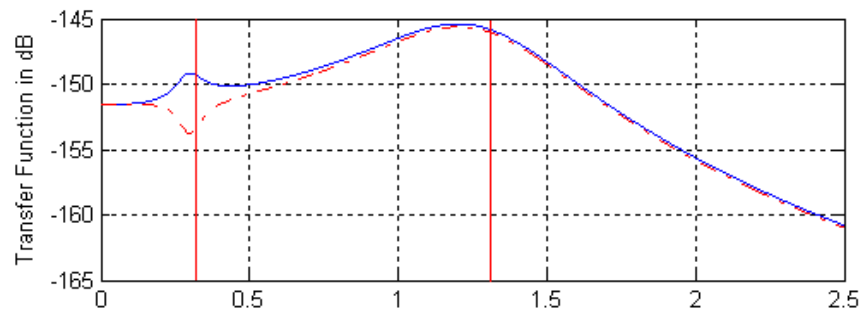
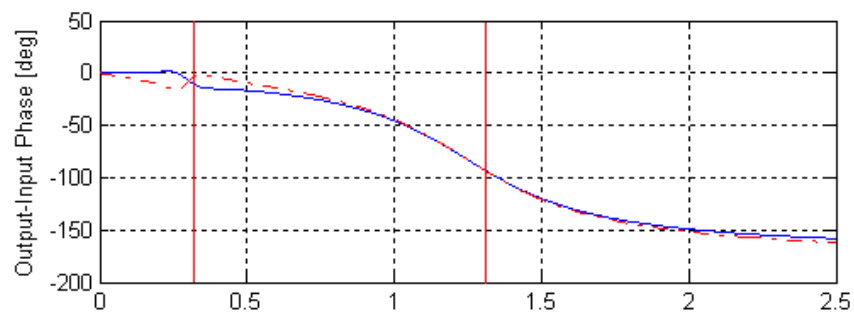
The overall sensitivity has been obtained from Eq. 2-1 by multiplying the mechanical sensitivity by  $V_b/h$  where  $V_b$  is the bias voltage and “ $h$ ” is the thickness of the gap between the diaphragm and the biased backplate [26].  $V_b/h$  is multiplied because the capacitance sensing technique is assumed to be incorporated with the sensor.

$$S = \frac{X_1 - X_2}{P} \cdot \frac{V_b}{h} = \frac{L \cdot \Theta}{P} \cdot \frac{V_b}{h} = \frac{V_b \cdot 2 \cdot s i \cdot \omega \cdot (L/2)^3 \cdot \cos(\phi) / (c \cdot I \cdot h)}{\omega_1^2 - \omega^2 + i \cdot \omega \cdot 2 \cdot \zeta_1 \cdot \omega_1} \quad (4-16)$$

To examine the sensitivity, the mass moment of inertia  $I = (1/3) \cdot m \cdot (L/2)^2$  is assumed as a thin plate. The total sensitivity is thus roughly proportional to the distance  $L$ , and the area  $s$ , and is inversely proportional to the total mass  $m$ . In short the overall sensitivity can be represented as Eq. 4.17. The detailed derivation, nomenclature, and the analysis can be found in Appendix B.

Table 4-10: Table of dominant terms for each frequency of interests

	Dominating term (Magnitude)	
	$H_{f_r}(\omega)$	$H_{f_t}(\omega)$
$\omega \approx 0$	$\frac{s/m}{\omega_t^2}$	
$\omega \approx \omega_r < \omega_t$	$\frac{s \hat{i} \sin(\omega\tau/2)/m}{2\omega_r \xi_r \hat{i} \omega}$	$-\left(\frac{s \hat{i} \sin(\omega\tau/2)/m}{2\omega_r \xi_r \hat{i} \omega}\right)$
$\omega_r < \omega < \omega_t$	$\frac{s \hat{i} \sin(\omega\tau/2)/m}{\omega_r^2 - \omega^2 + 2\omega_r \xi_r \hat{i} \omega} + \frac{s \cos(\omega\tau/2)/m}{\omega_t^2 - \omega^2 + 2\omega_t \xi_t \hat{i} \omega}$	$\frac{s \cos(\omega\tau/2)/m}{\omega_t^2 - \omega^2 + 2\omega_t \xi_t \hat{i} \omega} - \frac{s \hat{i} \sin(\omega\tau/2)/m}{\omega_r^2 - \omega^2 + 2\omega_r \xi_r \hat{i} \omega}$
$\omega \approx \omega_t > \omega_r$	$\frac{s \cos(\omega\tau/2)/m}{2\omega_t \xi_t \hat{i} \omega}$	

Figure 4.22: Magnitude vs. frequency in water with the spacing  $d = 1.2$  mm and 1mm by 1 mm diaphragm.Figure 4.23: Phases vs. frequency in water with the spacing  $d = 1.2$  mm and 1mm by 1 mm diaphragm.

$$S \approx \text{function} (V_b, L, s, \omega, \phi, c, m, h, \omega_1, \zeta) \quad (4-17)$$

However, some of the parameters in the parenthesis of Eq. 4.17 are not controllable, meaning that they are not design parameters and we do not have any control over them. For instance, we do not have control on these parameters,  $V_b$ ,  $\phi$ ,  $c$ , and  $\zeta$ . The overall sensitivity function can therefore be represented as

$$S \approx \text{function} (L, s, m, \omega_2) \quad (4-18)$$

In Eq. 4.18,  $L$ ,  $s$ ,  $m$ , and  $\omega_2$  are the length of the sensor, the effective area of the sensor plate, mass of the sensor plate, and the second natural frequency, respectively.

Figure 4.24 shows the sensitivity of 1 mm by 1mm size sensor of in water and in air in terms of frequency. The comparison made in Figure 4.24 is based on 1mm by 1mm size plate of the sensor since the smaller sensor size in micron range is the size of our interest in this research. Figure 4.24 shows that the maximum sensitivity of the sensor occurs near the first natural frequency  $\omega_r$ . Comparing from each sensitivity plot, it is observed that the sensor in water has higher sensitivity in the lower frequency region.

Considering the feasibility and the design of the acoustic sensor in water, the simulation has been performed by varying design parameters in this chapter. As a result we have obtained the relationship between the characteristics of the sensor and each parameters of the lumped parameter based model in Eq. 2.1. Based on the parametric analyses, the design methodology will be studied in Chapter 6. This includes the relationship between first two natural frequencies  $\omega_r$ ,  $\omega_t$  and peak frequency as well as the bandwidth frequency.

The important design parameters are spring constants  $k_1$ ,  $k_2$ ,  $k_3$ , the size, and the type of material of the sensor since they are directly related to the natural frequency of the sensor. Additional damping sometime gives rise to the amplification of the time delay or reduction depending on the size of the sensor. Figures 4.20 and 4.21 show the additional damping effect on the different size of the sensor.

Added mass due to fluid loading shown to be not constant but rather a function of frequency based on FEA analysis. This can be seen from Table 4.6. Based on the fact, the frequency variable

mass formula for our sensor is incorporated into the 5 DOF lumped parameter model in Eq. 2.38 and Eq. 2.39. The simulated results based on the discrete model and FEA model show small percentage difference as shown in Table 4.8.

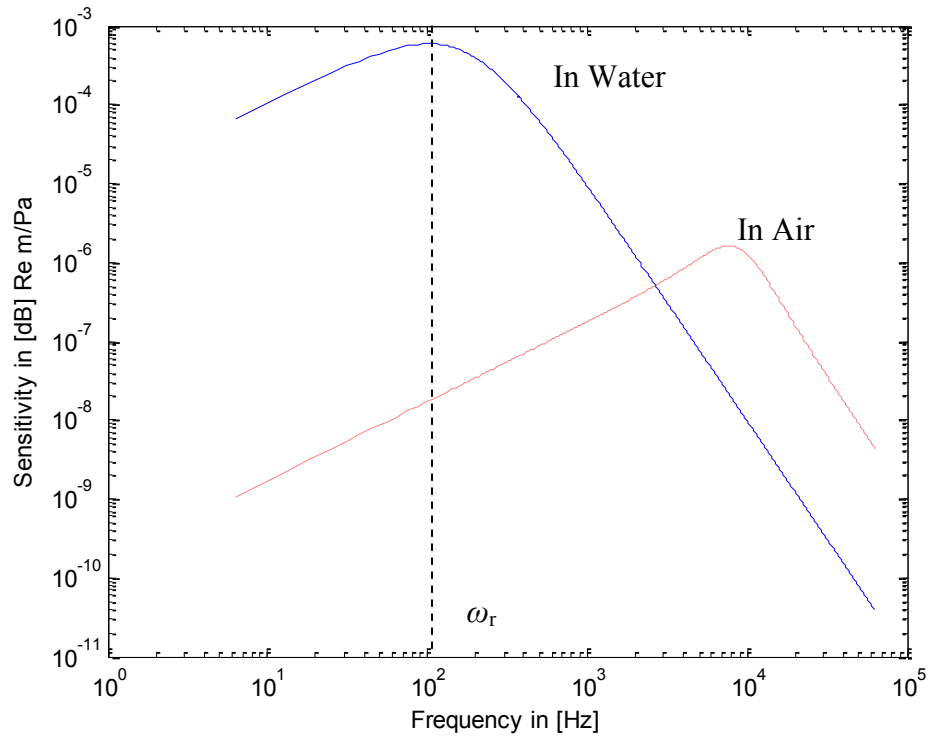


Figure 4.24: Predicted Sensitivity of 1 mm by 1mm Plate of the Sensor in Water and in Air.

## Chapter 5. Finite Element Analysis

### 5.1 Introduction

In the previous chapter, it has been shown that there are factors to be considered when analyzing the hydro-acoustic sensor submerged in water. In fluid-structure interaction system, added mass is shown to be sensitive to frequency. In addition, the sensor can become dynamically coupled with the fluid when it is placed in water.

Further investigation of the effect of the fluid loading and sound radiation due to fluid-structure interaction was performed using finite element analysis (FEA). FEA analysis was also used to determine the appropriate stiffness of the springs in the model presented in Chapter 2. Tables 2-3 and 2-4 show the simulated FEA results and the comparison with the discrete models.

### 5.2 Modal Analysis

Using FEA analysis, it is possible to perform accurate modal analysis of the sensor as distributed system. This will allow to relate the first two modes of the sensor to the two modes of our lumped parameter model and to obtain accurate estimates of the lumped parameters.

Thus it can be used to help determine the design parameters that will optimize the device performance.

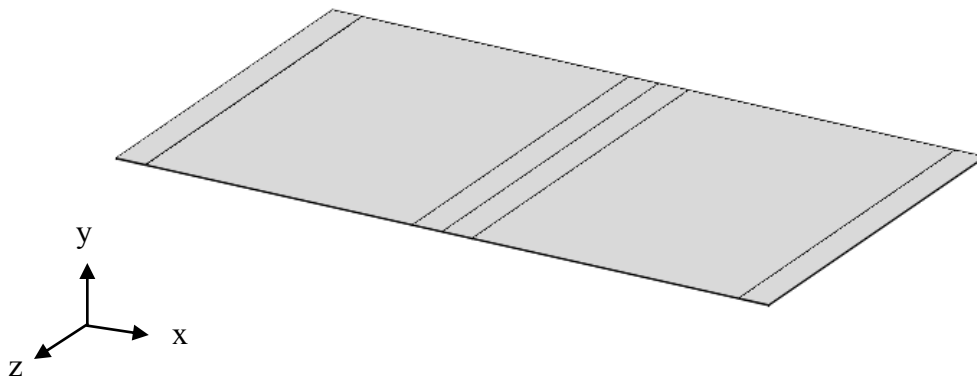


Figure 5.1: Three dimensional FE model with axes.

A 2-D FE sensor model is built assuming plane strain. The assumption of plane strain is made since the cross-sectional geometry of the sensor and the loading do not vary in the z-direction in Figure 5.1.

As shown in Figure 2.6, the geometry consists of two plates with one vertical member which supports at the coupling point. FEA Simulation result is tabulated and compared with the Mode-Summation based model in Table 2-3 and first two modes are shown in Figure 5.2.

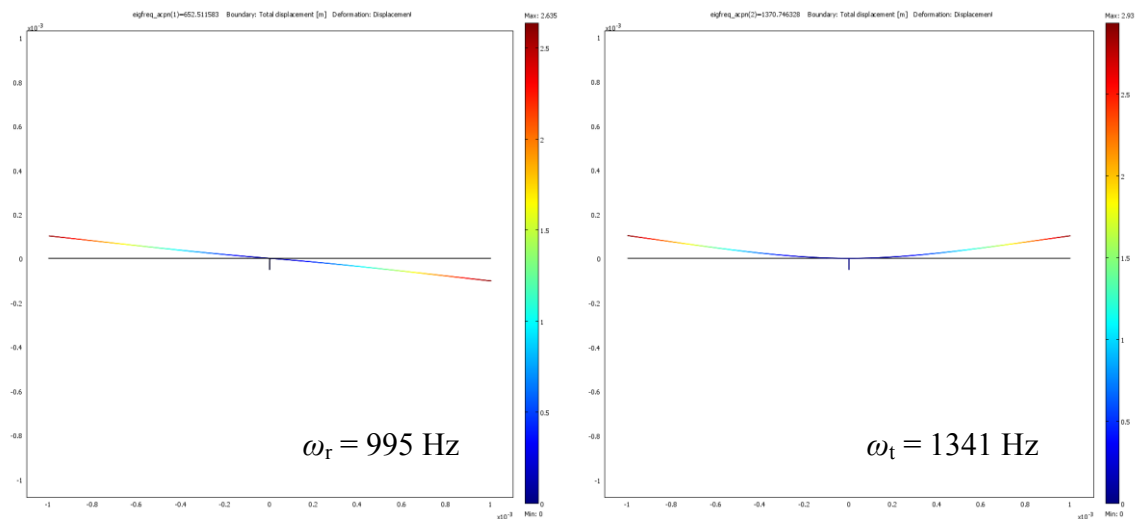


Figure 5.2: Left: Rocking, out-of-phase mode. Right: Bending (translational), in-phase mode.

The cross section of both members has an area,  $A = 0.001$  by  $0.001$  m<sup>2</sup> with the thickness of  $1$   $\mu$ m. The material properties used in all analyses and calculations are of modulus of elasticity,  $160 \times 10^9$  Pa, density equal to  $2320$  kg/m<sup>3</sup>, and Poisson's ratios equal to  $0.22$ . In Figure 2.6, the sensor is fixed at the bottom of the vertical member at  $x = 0$ ,  $y = 0$ , meaning that the displacements are constrained whereas the rotational degrees of freedom are free. The two resonant mode shapes are shown in Figure 5.2 with the corresponding eigen frequencies. It can be seen that the first two modes are a rocking mode and a bending (translational) mode. These are the same modes we obtained via lumped parameter analysis.

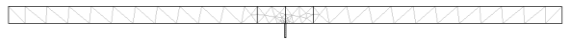
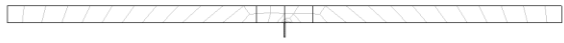
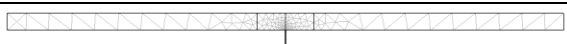

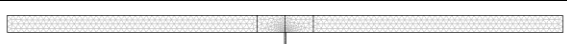
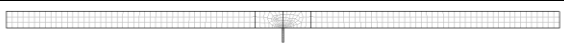
### 5.2.1 FEA model and mesh sensitivity analysis

The FEA sensor model is constructed with the dimensions shown in Figure 5.3. The material used is a poly-silicon whose properties are the same as above. The small thickness-width ratio is

challenging in FEA modeling. It is not uncommon that a large number of elements is required when analyzing slender structures.

Therefore, prior to defining the final mesh configuration, it was necessary to investigate the influence of the element shape and of the mesh density. Two types of elements, triangular and quadrilateral, were considered. For each element type, three different numbers of meshes were built and shown in Table 5-1.

Table 5-1: Number of elements and nodes for three meshes of each element type

Mesh ( <i>Triangular</i> Element)	Mesh ( <i>Quadrilateral</i> Element)
 Mesh: <i>Coarse</i> Element number: 152 Node number : 118	 Mesh: <i>Coarse</i> Element number: 66 Node number : 107
 Mesh: <i>Normal</i> Element number: 265 Node number : 182	 Mesh: <i>Normal</i> Element number: 96 Node number : 145
 Mesh: <i>Fine</i> Element number: 1029 Node number : 636	 Mesh: <i>Fine</i> Element number: 410 Node number : 540

It is shown in Figure 5.3 that the lowest natural frequencies obtained by 2D finite element analysis are not sensitive to mesh density and element type. This allows us to use a rather coarse mesh without sacrificing modeling accuracy.

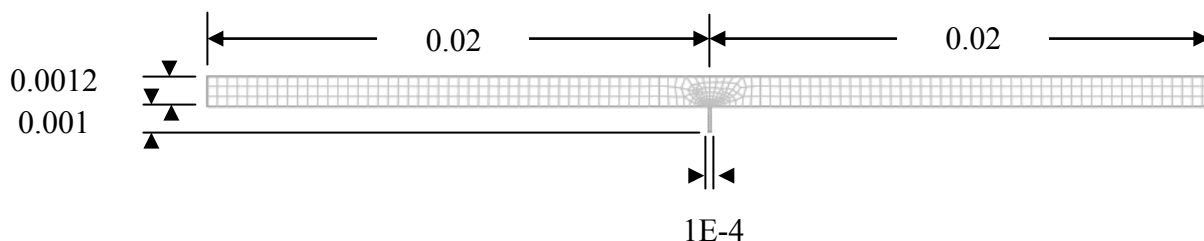


Figure 5.3: Geometry of the 2-D sensor model in discretized finite element mesh with quadrilateral element (all dimensions are in meters)

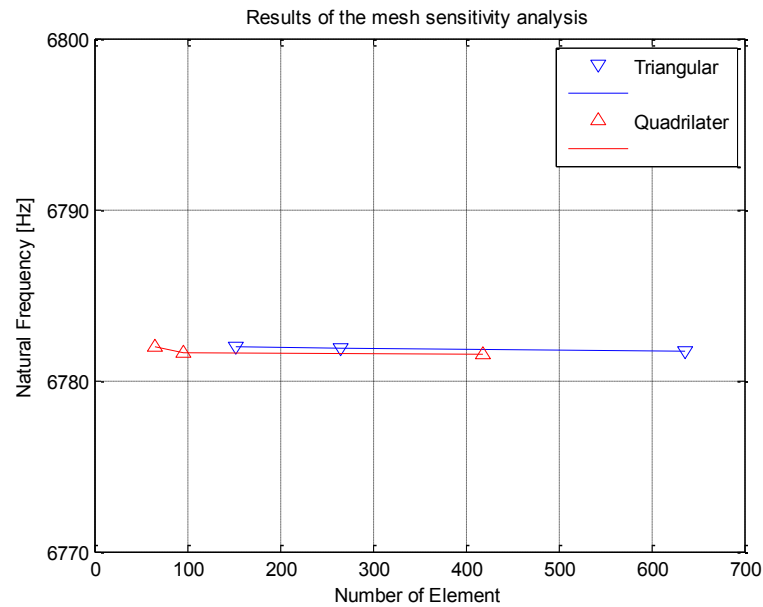


Figure 5.4: Results of the mesh sensitivity analysis.

### 5.3 2-D Parametric Analysis of the Sensor with Fluid-Structure Interaction

In COMSOL multiphysics coupling of the acoustics medium with the structure takes place via a structural load through sound pressure and an acceleration of the fluid particles through the motion of the structure. This is accomplished by the use of two subdomains, one corresponding to the structure and on to the fluid. The acoustic (fluid) subdomain here is modeled as a square area, and is used to surround the sensor. The area is in turn enclosed by another square area that acts as a perfectly matched layer (PML). The PML is used to absorb acoustic energy, to simulate a free field effect, thereby eliminating acoustic energy being reflected back into the square area from the square's outer shell. Since it is assumed that the fluid area is unbounded (e.g. a sensor submerged in an infinite area of fluid) to avoid standing waves and hence not to sustain natural frequencies, the PML is chosen for the simulation. The acoustic subdomain is modeled as water with a density of  $995.6 \text{ kg/m}^3$ , a speed of sound of  $1482 \text{ m/s}$ , and a bulk viscosity of  $3.38 \times 10^{-3} \text{ Pa}\cdot\text{s}$ . The solid subdomain is modeled as poly-silicon with the properties given above. The structure of the sensor model is shown in Figure 5.3. The sensor within the square domain of the fluid and the PML is shown in mesh mode at Figure 5.5.

Boundary conditions for our model are fixed lower end of the supporting beam and fluid load on the upper area of the sensor. The key point is the interface between the sensor and water. To couple the acoustic pressure wave to the sensor, the boundary load on the sensor is set to  $F = -n_s \cdot p$

where  $n_s$  is the outward pointing unit normal vector seen from inside the sensor domain and the subscript  $s$  represent surface. To couple the frequency response of the sensor back to the acoustics problem, the normal acceleration  $a_n$  has to be equal to that of the acceleration of the boundary of the sensor. This can be represented as:

$$a_n = -n_a \cdot \left( -\frac{1}{\rho_0} (\nabla p - q) \right) \quad (5-1)$$

where  $n_a$  is the outward pointing unit normal vector seen from inside the acoustic domain,  $p$  is the acoustic pressure,  $\rho_0$  is the density of the medium, and  $q$  is an optional dipole source. In our model, no dipole source is included.

The equation for the interaction between the fluid and the structure is derived from the continuity requirement at the interface boundary. The normal displacement of the structure must be identical to that of the fluid. Therefore, the fluid momentum equation yields the following relationships between the normal pressure gradient of the fluid and the normal acceleration of the structure at the fluid-structure interface.

$$\{n\} \cdot \{\nabla P\} = -\rho_0 \cdot \{n\} \cdot \frac{\partial^2 U}{\partial t^2} \quad (5-2)$$

where  $U$  is the displacement vector of the structure at the interface.

Boundary conditions used in the simulation are described and specified on the boundaries of the FEA model accordingly as follows:

- *Fluid-structure interaction (FSI) boundary:*

On the fluid structure interface, the displacement of the structure must be identical to that of the fluid in the normal direction of the structure (sensor). Therefore, the equation of motion for fluid particles must be applied at the interface boundary by normal displacements of the structure as described by Eq. 5.2. This boundary condition is applied at the interaction boundaries between the sensor and the fluid domain shown in Figure 5.5.

- *Infinite boundary (absorbing boundary):*

If the dimensions of the fluid domain are large or infinite, the numerical model has to be truncated at some reasonable distance from the structure. The reflection of pressure wave has to be prevented at these artificial boundaries since they do not exist in the non-truncated domain. PML is the method of choice to accomplish the absorption of the outward propagating waves hit the truncated fluid domain boundary. PML is applied box areas outside the fluid domain in Figure 5.5.

- *Rigid wall boundary (reflect boundary):*

On the rigid wall, the nodal displacement equals zero. Moreover, the absorption coefficient also equals zero to indicate that there is no energy loss at the boundary. Therefore Eq. 5-6 can be simplified to the following form to describe this condition. This boundary condition will be used in the next section.

$$\{n\} \cdot \{\nabla P\} = 0 \quad (5-3)$$

- *Free surface boundary (open boundary) on the top surface:*

The free surface contacts the air where the reference pressure is specified to zero. This boundary condition will be used in the next section.

- *Neutral boundary (open cavity) on the top surface:*

The neutral boundary condition states that transport by shear stresses is zero across a boundary. It does not put any constraints on the velocity and states that there are no interactions across the modeled boundary. The neutral boundary condition means that no forces act on the fluid

$$\eta (\nabla u + (\nabla u)^T)_n = 0 \quad (5-4)$$

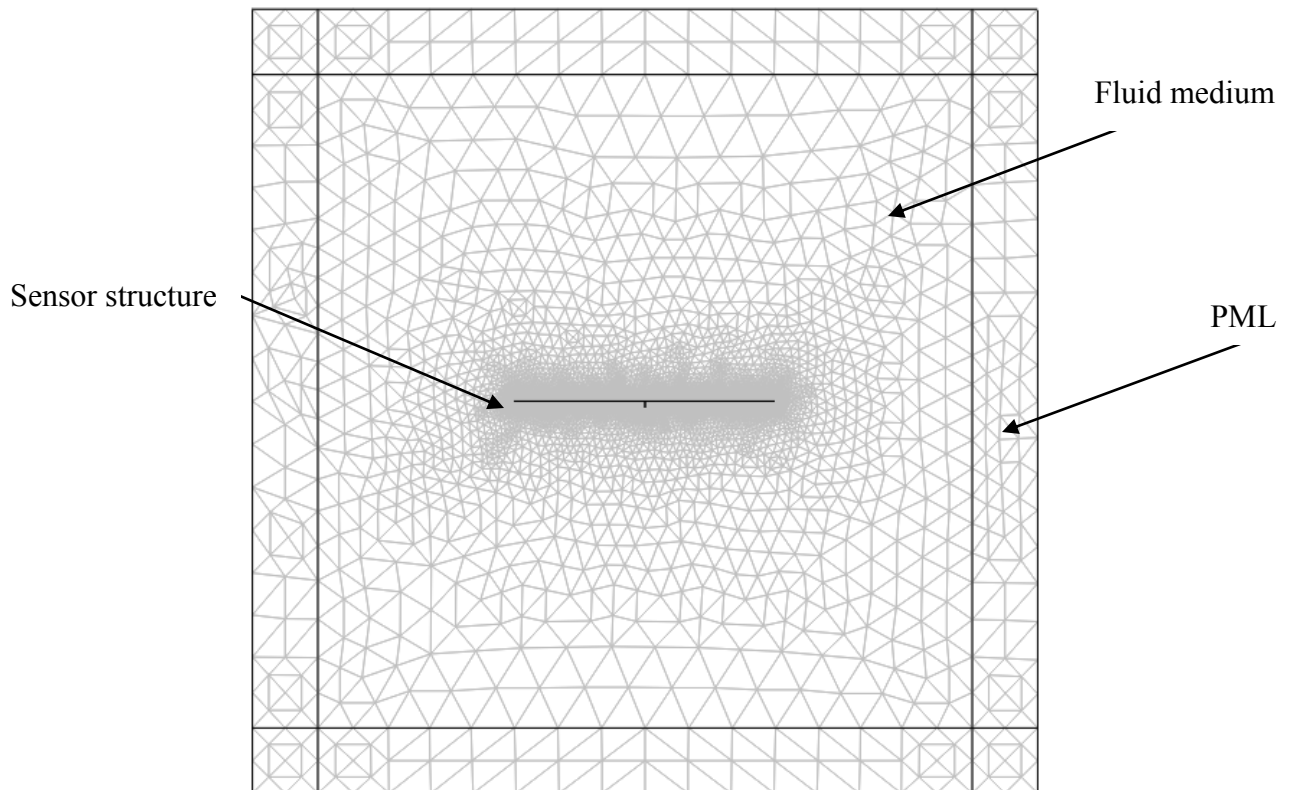


Figure 5.5: Mesh Mode in FEA

The most vital section to be meshed for this model is the sensor itself since it is modeled as relatively small size (0.02 m by 0.02 m with 1.2e-3 m thickness). The maximum element size is set to 0.025. This is because it is important to make meshes sufficiently resolved in the acoustic domain. The rule of thumb is that the minimum of ten to twelve degrees of freedom per wavelength are need for the solution to be reliable with the (default) second-order elements [27].

In the case of the acoustic domain, at least five mesh elements per wavelength must be used [27]. Thus, the mesh size depends on the frequencies involved. The numerical value of 0.06 is used as Maximum element size  $h_{\max}$  which corresponds to  $0.2\lambda$ , where  $\lambda$  is the wavelength of the sound waves in the acoustic domain. This is because the solutions to acoustic problems are wave like and the waves are characterized by a wavelength  $\lambda$  which is defined as  $\lambda = c/f$  where  $c$  is the speed of sound in water and  $f$  is frequency. Hence, the wavelength  $\lambda$  has to be resolved by the mesh [27]. Figure 5.5 shows that the fluid mesh is extended from the structure (sensor) mesh so that the same

set of nodes is shared between both domains on the interface and surrounded by PML. The same type of triangular element was used to build up the fluid mesh.

The source of the plane wave is

$$\text{Incident Acoustic Pressure} = e^{[-i*(kx*x+ky*y)]} \quad (5-5)$$

where  $kx = k\cos\theta$ ,  $ky = k\sin\theta$ , and  $x$  and  $y$  are the Cartesian coordinates. Eq. 5.2 represents a plane wave in 2-D. Introducing the sound wave as a plane wave assumes the sensor is at the far-field from the source of sound.

In Chapter 4, the effect of the added mass due to the fluid has been evaluated using FEA by comparing the natural frequencies of the sensor model vibrating in air and in water. Since the air effect on the structure is negligibly small, the corresponding simulation is carried out in air instead of *in vacuo*.

The displacement shape of the plate modes is studied by Hull (2002) with respect to fluid loading on one or both sides of the plate. It was found to be that the mode shapes of the plate are identical for a plate with no fluid loading and that for a plate with fluid loading on a single side. However, it was found that fluid loading on both sides produced a different displacement shape [28]. The underwater harmonic analysis is simulated assuming the unbounded boundary using PML in order to purely capture the fluid loading effect of the sensor in water without standing waves. Fluid-structure interaction is applied on a single side and the mode shapes are expected to remain unchanged in water from ones attained from *in vacuo* or in air [28].

## 5.4 Validation of FEA Simulation

There are numerous factors which affect the motions of the underwater structures. In order to capture the simulated FEA result of the mechanically coupled underwater sensor without loss of generality, boundary conditions that can simulate the underwater motion of the sensor have been chosen as above. FEA was used to validate the sensor model in Chapter 2, added mass in Chapter 4, and will be used to show that the sensor is capable of detecting directivity of sound and amplifying time delay under water within the sensor's frequency bandwidth in Chapter 6.

To investigate the accuracy of our finite element approach we compare it with previously published acoustic/structure interaction findings. The validation data have been extracted from the

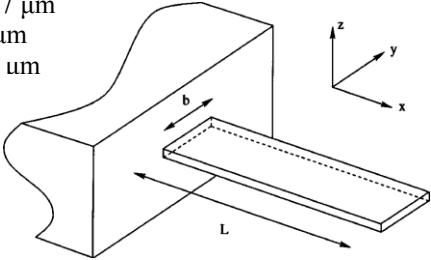
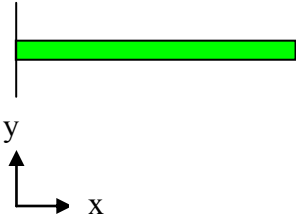
work by Sader *et al.* (2000) [29] on cantilever beams. The geometry data used in Sader's work is shown in Table 5-3.

First natural frequency of the cantilever beam has been calculated as

$$\omega_n = \left( \frac{1.875^2}{L^2} \right) \sqrt{\frac{EI}{\rho_b A_b}} = 1.069e5 \text{ rad/s} = 1.702e4 \text{ Hz} \quad (5-6)$$

where  $L = 397 \mu\text{m}$ ,  $E = 160e9$ ,  $I = \frac{bh^3}{12} = \frac{(29 \mu\text{m})(2 \mu\text{m})^3}{12} = 1.933e-23$ ,  $\rho_b = 2320 \text{ kg/m}^3$ , and  $A_b = bh = 5.8e-11 \text{ m}^2$ . This analytical value comes close to that obtained by modal analysis done by 2-D FE simulation, 17,452 Hz.

Table 5-2: Natural frequencies of the cantilever beam in various medium (kHz): Experimental and Simulation results

	$\omega_{\text{vacuo}}$ [kHz]	$\omega_{\text{air}}$ [kHz]	$\omega_{\text{water}}$ [kHz]		Description of Cantilever Beam
From the paper [29] (Experiment)	17.52	17.36	5.04		$L = 397 \mu\text{m}$ $h = 2 \mu\text{m}$ $b = 29 \mu\text{m}$ 
Our analysis (FEA)	17.45	17.07	2.45*	5.42**	
% Difference	0.3	1.6	51	7.5	N/A

\*, \*\* represent boundary conditions of PML (Perfectly Matched Layer) and control area with neutral and sound hard boundaries, respectively.

For the second natural frequency of the cantilever beam which is for  $n = 2$ ,

$$\omega_n = \beta_n^2 \sqrt{\frac{EI}{\rho_b A_b}} = 6.703e5 \text{ rad/s} = 1.066e5 \text{ Hz} \quad (5-7)$$

where  $\beta_n \cdot \ell = 4.694 \rightarrow \beta_n = \frac{4.694}{397 e - 6} = 1.182e4 \rightarrow \beta_n^2 = 1.398e8$ . This analytical value comes close to that of 2-D FE modal analysis which gives us 1.093e5 Hz (whereas FEA beam element model gives us 1.066e5 Hz).

Simulating with rigid wall boundary condition with neutral boundary (water on the top surface instead of using PML) can simulate the actual experimental condition using COMSOL. This gives non anechoic conditions to our water subdomains, meaning that, there are standing waves or theoretically reflected energy from the boundaries. This explains the discrepancy of  $\omega_{\text{water}}$  between the experimental data and that of FEA using PML in Table 5-2. The experimental data for Sader's paper must have been collected from the small container with the opening on top which interfaces with air. Considering this hypothesis regarding the boundary condition, FEA is simulated and compared with the experimental data again. This shows a better agreement with about seven percentage difference.

Table 5-3: Fundamental resonant frequencies *in vacuo* and air: FEM and Sader [29]

Cantilever	Experiments [30]		FEM			
	$f_{\text{air}}$ (kHz)	$f_{\text{vac}}$ (kHz)	$f_{\text{air}}$ in 3-D (kHz)	$f_{\text{air}}$ in 2-D (kHz)	$f_{\text{vac}}$ in 2-D (kHz)	$f_{\text{vac}}$ w/ beam element (kHz)
1 <sup>st</sup> natural frequency	17.36	17.52	17.07	17.07	17.45	17.02
% difference	N/A	N/A	1.6	1.6	0.4	2.8

The theoretical value of the cantilever beam *in vacuo* from Eq. 5.6 shows a good agreement with the experimental [30] and FEA data in Table 5-2. Table 5-3 also shows the simulation results of cantilever beam using FEA in air that show the small percentage difference with theoretical value as well as experimental one from Sader *et al.* (2000). However, in water, due to the heavy

mass loading and its dependency of boundary conditions (reflections and standing waves), it is important to use the proper boundary condition when conducting FEA simulation of the underwater sensor.

## Chapter 6. Design Optimization of the Sensor

### 6.1 Design Consideration of Acoustic Sensor

In the design of an acoustic sensor, it is useful to study zero crossing phenomenon discussed in Chapter 4. In this chapter, we will demonstrate zero crossing phenomenon is closely related with the performance of the sensor, the natural frequencies, and the angle of incidence. There is a drawback to zero crossing in terms of output time delay. As the first two natural frequencies  $\omega_r$  and  $\omega_t$  move towards each other, the displacement of each diaphragm  $x_1, x_2$  start moving in phase as one rigid bar. This can make the zero crossing go away for the price of no amplification in  $\tau_o$ . This is because the sensor becomes a rigid bar without any coupling mechanism by moving the first natural frequencies  $\omega_r$  and  $\omega_t$  close such that  $\omega_r \approx \omega_t$ .

Figure 6.1 (a) shows the effect of zero crossing by comparing bottom plot of Figure 6.1 (a) with bottom plots of Figure 6.1 (b), (c), and (d). As shown in the bottom plot of Figure 6.1 (a), when there is a zero crossing, the positive output time delay crosses zero and then it becomes the negative time delay once the time delay reaches the peak. Figure 6.1 shows that the sensor's amplification performance is lowered at the incidence angle of  $20^\circ$  due to a zero crossing at around 500 Hz. This shows the angle of incidence dependency to the zero crossing. There is no occurrence of zero crossing of the output time delay for all angles ( $45, 65, 90^\circ$ ) except at  $20$ . This was found by decreasing the angle of incidence by  $1^\circ$  from  $90^\circ$ . This will be corrected through the design process via trial and error. The relationship between design parameters and factors that change the output time delay amplification and zero crossing will be investigated base on the design effort in this chapter.

This geometry of the sensor in Figure 6.1 is chosen by trial and error to have a first natural frequency  $\omega_r$  at 500 Hz with the most amplification. Detailed data for the selection of the sensor size can be found in Appendix C.

Based on the parametric study regarding the coupling spring  $k_3$  from Chapter 4, zero crossing at  $20$  incident angle is prevented and the output time delay is amplified at the frequency of 500 Hz by increasing the coupling spring constant  $k_3$ . Figures 6.1, 6.2, and 6.3 demonstrate this. From this, it is noted that we need to consider the sensor performance in terms of frequency as well as angle of incidence due to the zero crossing's dependency of the incident angle. Figure 6.3 shows the time

delay versus frequency at the incidence angle of  $20^\circ$  after design modification to remove zero crossing, which can be compared with Figure 6.1 (a).

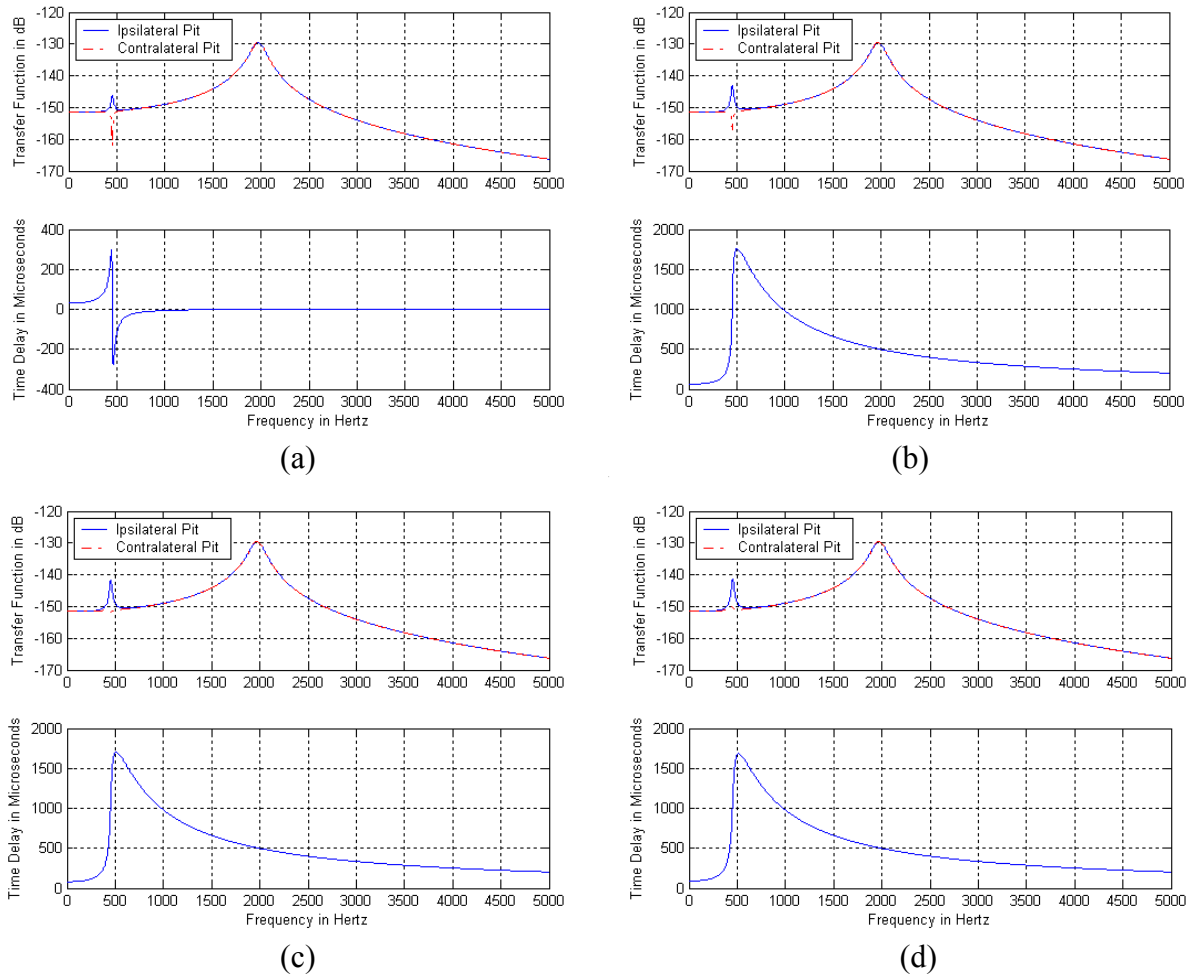


Figure 6.1: Time delay vs. frequency at various angles with 3.5 mm by 3.5 mm diaphragm for frequencies 500 Hz and up with an amplification at 500 Hz ( $\omega_r = 453$  [Hz],  $\omega_t = 1975$  [Hz],  $k = 0.576$  N/m,  $k_3 = 5.18$  N/m): (a)  $20^\circ$ , (b)  $45^\circ$ , (c)  $65^\circ$ , and (d)  $90^\circ$ .

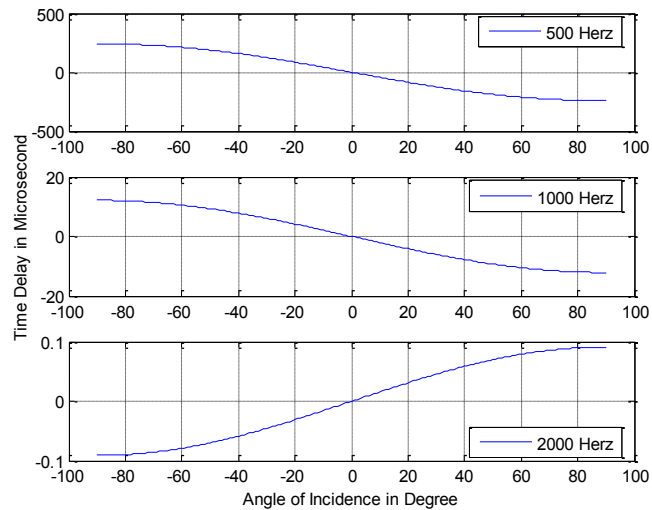


Figure 6.2: Time delay amplification vs. angle of incidence in water at various frequencies.

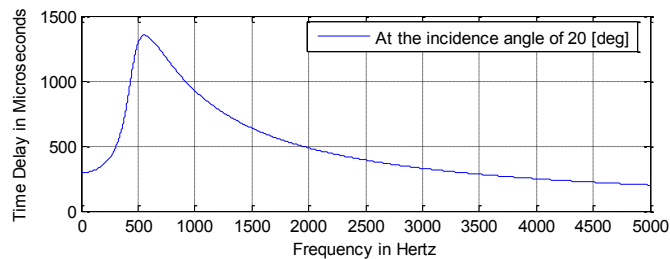


Figure 6.3: Time delay vs. angle of incidence in water at 20° incidence angle ( $k_3$ : 5 → 50 N/m).

### 6.1.1 Design Consideration with Spring Constants and Natural Frequencies

In this section, the relationship between the spring constants  $k_1$ ,  $k_2$ ,  $k_3$  and the first two natural frequencies  $\omega_r$ ,  $\omega_t$  will be investigated in terms of designing a sensor. Prior to that, parametric analyses of the spring constants  $k_1$ ,  $k_2$ ,  $k_3$  based on Chapter 4 can be summarized as below. The coupling spring constant  $k_3$  plays an important role regardless of the size of the sensor. Unlike the linear spring constants  $k_1$  and  $k_2$ , which move the first natural frequency into higher frequency ranges as their stiffness is increased ( $k_1$  and  $k_2$  are increased equally), the coupling spring  $k_3$  can prevent the zero crossing from occurring and increase the output time delay by moving the second natural frequency to higher frequency ranges. This was shown in Figure 4.12. Hence, the coupling spring constant  $k_3$  is related to the overall output time delay amplification. However, if you increase the coupling spring constant  $k_3$  too much, the amplification of the time delay moves in the

lower frequency ranges instead of around the first natural frequency. Figure 6.4 shows the progressing trend of the time delay as the coupling spring constant  $k_3$  is varied.

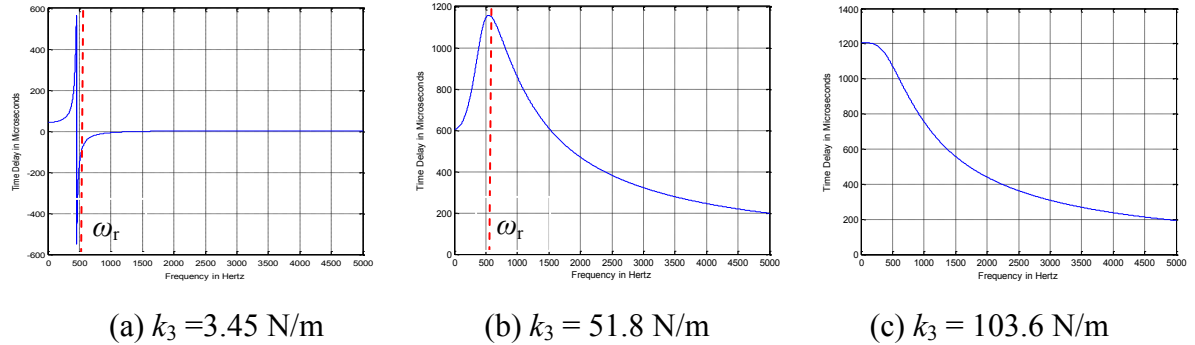


Figure 6.4: Time delay vs. Frequency progression as the coupling spring constant  $k_3$  varies.

Figure 6.4 (a) shows that zero crossing is occurred at the first natural frequency which is normally located at the peak amplitude when zero crossing is prevented as shown in Figure 6.4 (b). The red dotted line shows the location of the first natural frequency  $\omega_r$ . Hence, it is shown that the first natural frequency is related to the location of occurrence of zero crossing and peak amplitude in time delay plot. Next the relationship between the second natural frequency and the time delay response will be investigated. The cutoff frequency is located at around where the time delay crosses the zero in frequency domain upon the occurrence of zero crossing. In this case, the cutoff frequency is located at where the first natural frequency  $\omega_r$  is.

Figures 2.3 and 2.4 are shown in Figure 6.5 as an example to investigate the relationship between the second natural frequency and the cutoff frequency where there is no zero crossing. Figure 6.5 shows that even if there is no occurrence of zero crossing in time delay versus frequency plot, there is a noticeable jump in time delay versus the angle of incidence plot at 15,000 Hz. This causes the incoherent detection of the direction of the sound wave. Hence, when there is no zero crossing, it is necessary to investigate the time delay versus the angle of incidence plot. This leads to investigate the directional sensitivity of the sensor and the second natural frequency  $\omega_t$ . In the next sections, this will be studied.

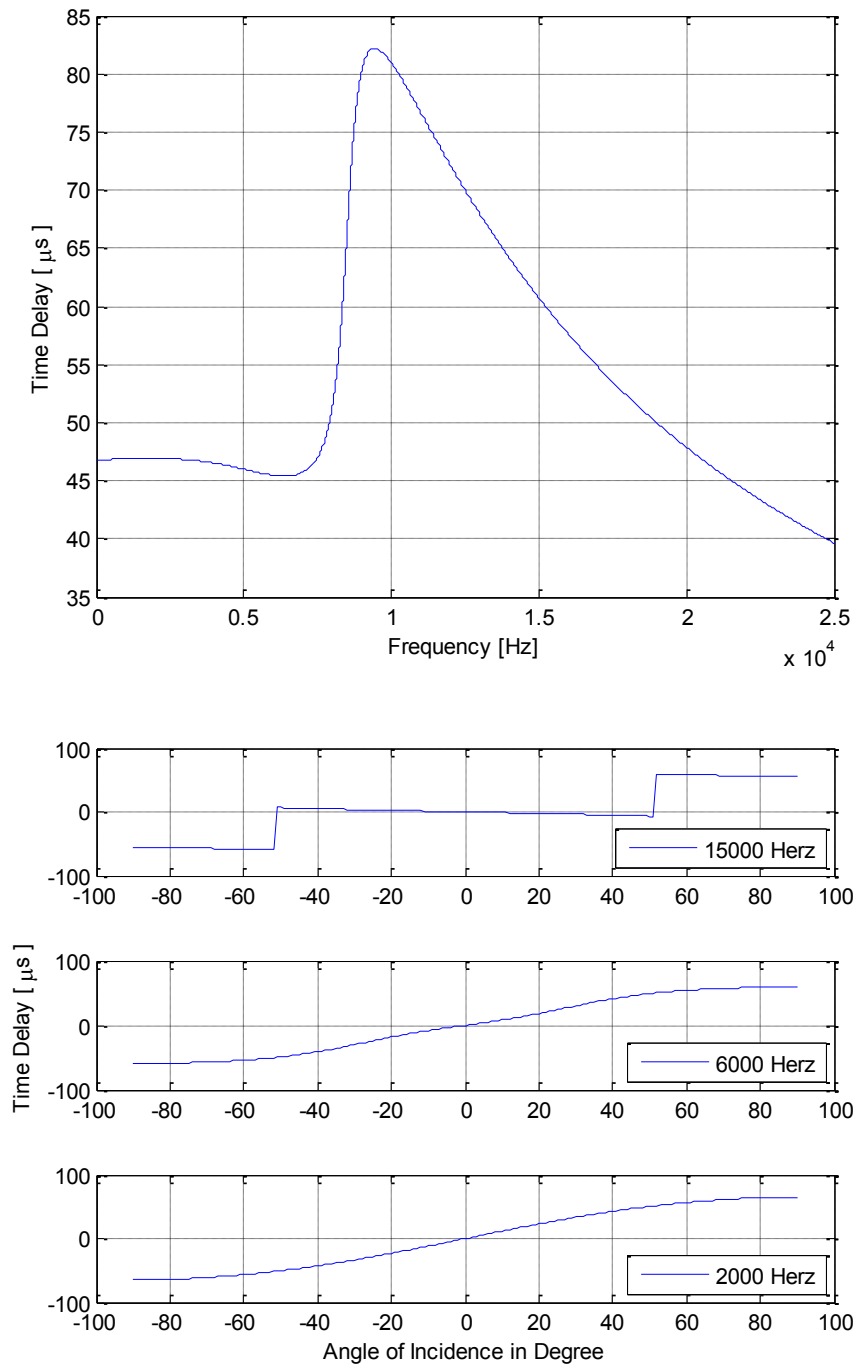


Figure 6.5: Top: Time delay vs. Frequency plot, Bottom: Time delay vs. Angle of Incidence plot.

## 6.2 Directional Sensitivity and the Location of Natural Frequencies

Our sensor's performance is a function of the first two natural frequencies  $\omega_r$ ,  $\omega_t$  and their corresponding mode shapes. Designing a sensor requires specific objectives such as sensitivity and bandwidth. Depending on design objectives, the first two natural frequencies  $\omega_r$ ,  $\omega_t$  of the sensor must be determined.

The intent of the hydro acoustic sensor is to provide greater amplification of the phase difference for underwater sounds arriving from 0 to 180 degrees. In order to show the directional response of our sensor better, polar plots are useful. The graphical display of the output from different directions is referred to as a polar plot. Polar plots will vary by both sensor design and by frequency. The response at each angular increment is normalized by the on-axis response to create a curve. This removes the influence of the sensor frequency response and sensitivity, such that the polar plot only shows the directional sensitivity in terms of output time.

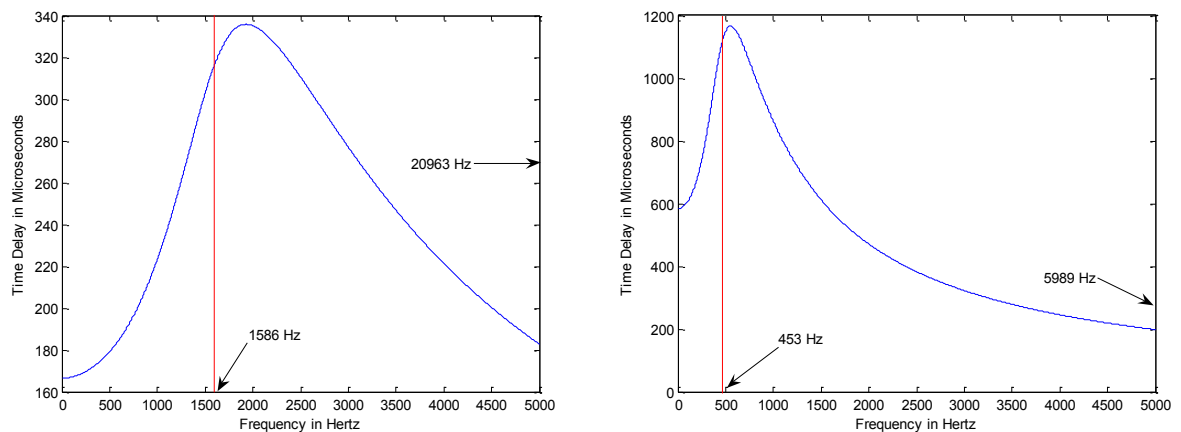


Figure 6.6: Time delay vs. frequency: Left: 1 mm by 1 mm, Right: 3.5 mm by 3.5 mm sensor.

The design goal is to get a time delay difference as a sensitive function of angle of incidence with a large amplification of the time delay. Ideally the time delay should vary smoothly from zero to a maximum value (which should be significantly larger than the arrival time difference of the plane wave) as the incident angle goes by zero to 90 degrees. The polar plot would then have the same shape as in Figure 6.11a. The relationship can be found between the time delay versus the angle of incidence plot shown in Figures 6.9 and 6.10 and the polar plot shown in Figure 6.11. It can be observed that the directional sensitivity becomes incoherent if there is a sudden step-like

jump in the time delay versus the angle of incidence plot. However, as long as the time delay varies smoothly with respect to the angle of incidence and is amplified significantly compared to the input time delay, the sensor becomes directionally sensitive. For the example of a directionally sensitive response of the sensor, Figures 6.11a and 6.11b are the polar representation of Figure 6.9 at the frequencies of 500 Hz and 1,000 Hz. The polar plot shapes are circular and the time delay varies smoothly as the angle of incidence varies. For the example of a directionally insensitive response of the sensor, Figures 6.11e and 6.11f show the polar plot of Figure 6.10 at the frequencies of 1,000 Hz and 2,000 Hz. The shape of the polar plot becomes omni-directional.

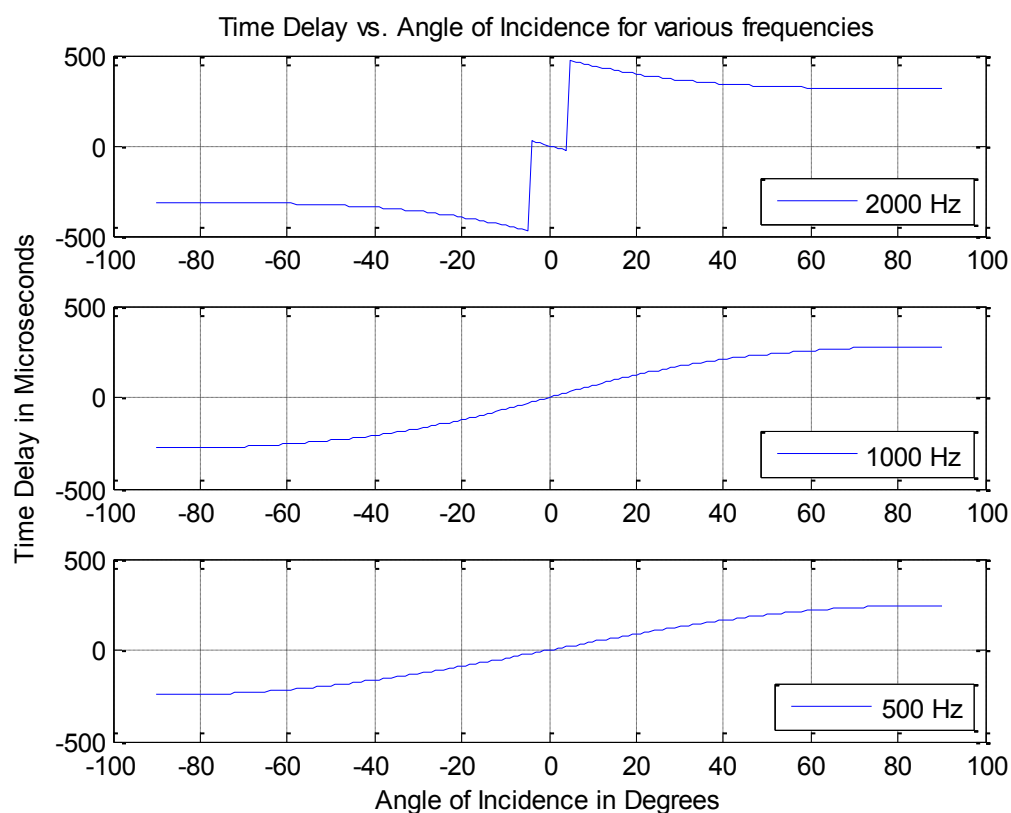


Figure 6.7: Time delay vs. angle of incidence for 1 mm by 1 mm sensor.

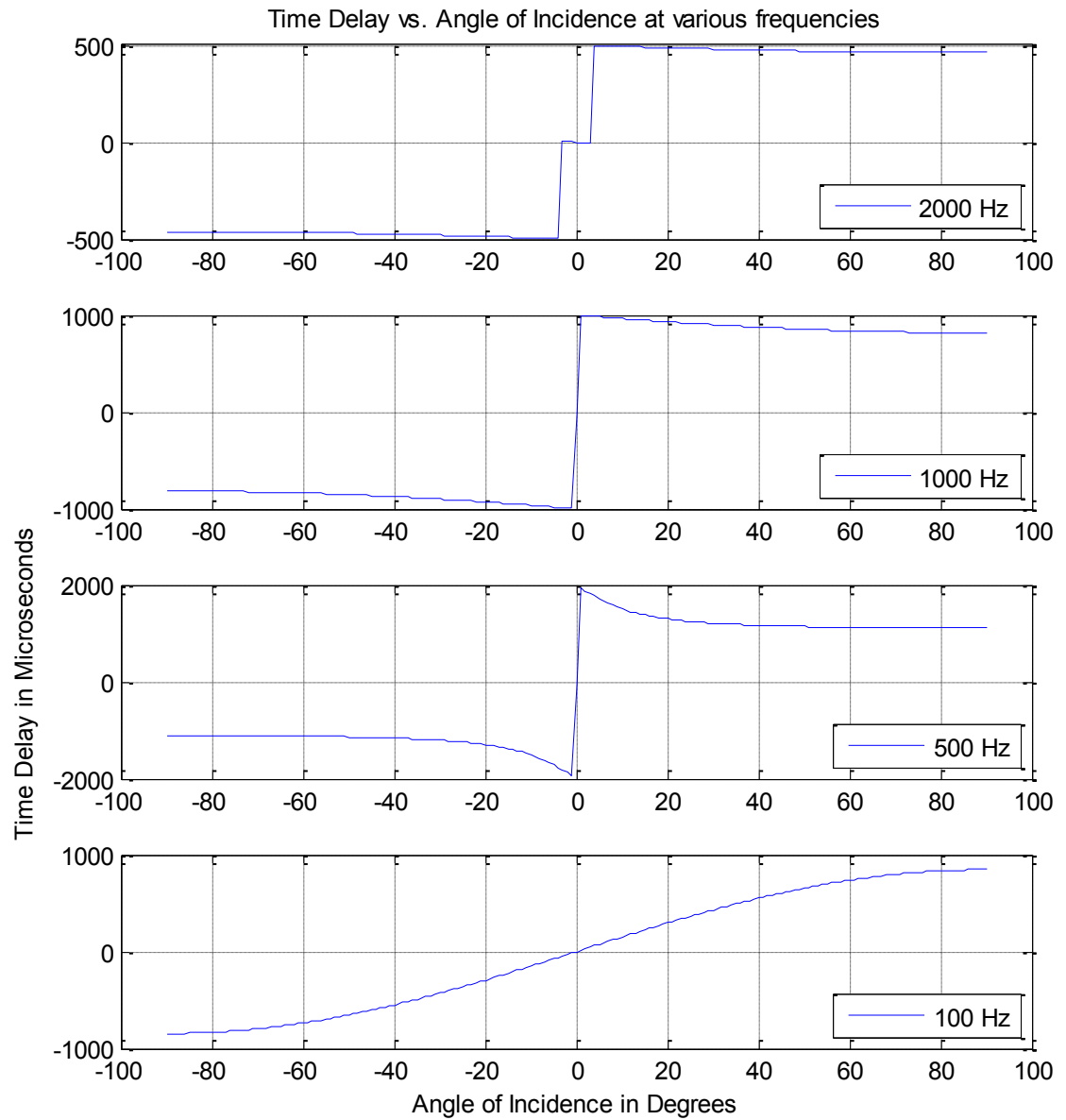


Figure 6.8: Time delay vs. angle of incidence for 3.5 mm by 3.5 mm sensor.

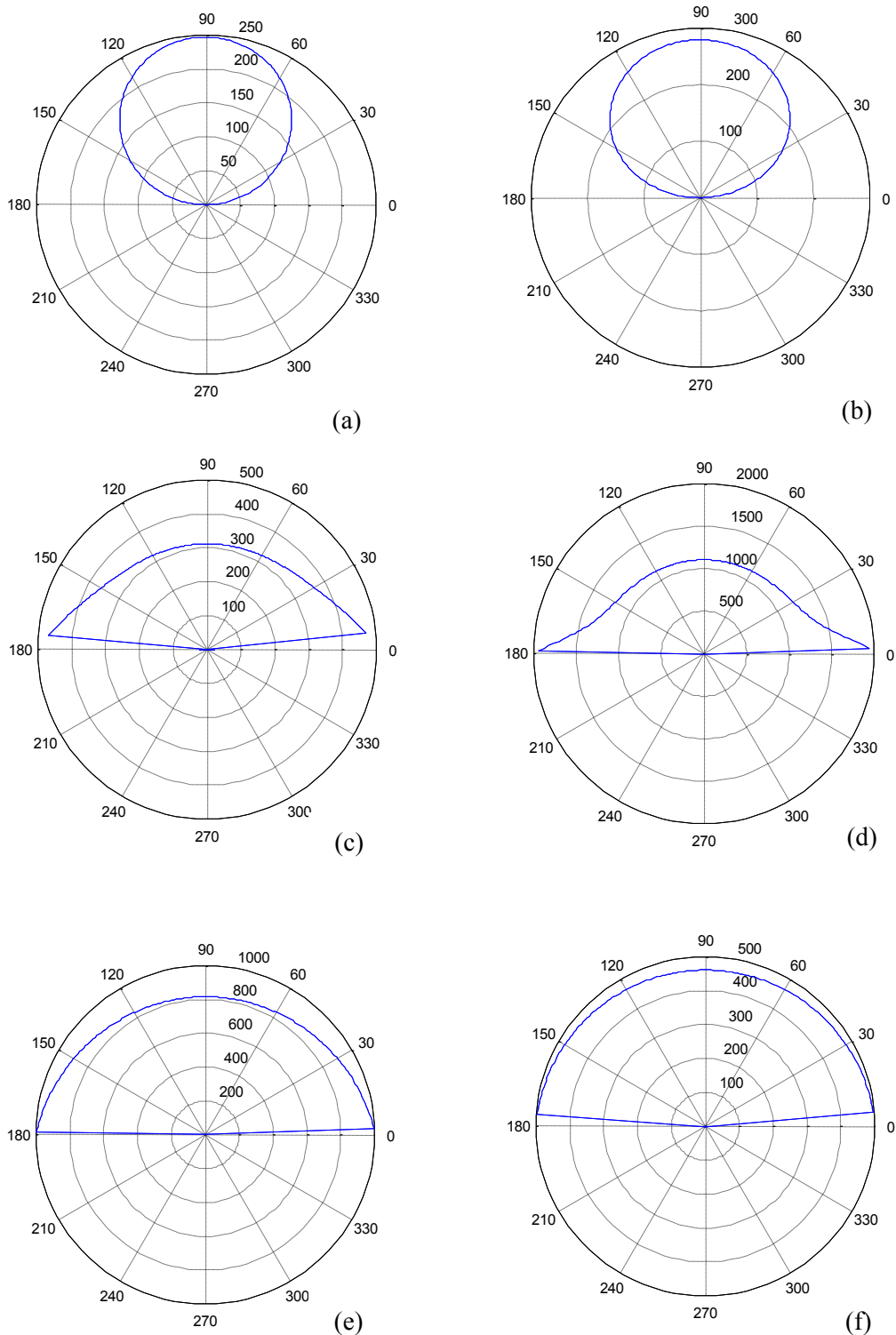


Figure 6.9: Directional sensitivity polar plot for 1 mm by 1 mm: (a) 500 Hz (b) 1000 Hz (c) 2000 Hz, and for 3.5 mm by 3.5 mm: (d) 500 Hz (e) 1000 Hz (f) 2000 Hz.

### 6.3 Location of the Second Natural Frequency and the Need for Design Optimization

It has been shown that the mechanically coupled hydro acoustic sensor can be designed to amplify the output time delay  $\tau_0$  over a specific frequency range (bandwidth). It was shown in the previous section that the first natural frequency  $\omega_r$  is where the time delay takes on a maximum and determines the bandwidth of the sensor when zero crossing occurs. The second natural frequency  $\omega_t$  dictates the amplification of the time delay as well as the size of the bandwidth of the sensor. The relationship between the first and second natural frequency is that the second natural frequency  $\omega_t$  needs to be placed not too close to the first natural frequency  $\omega_r$ , otherwise the sensor loses its mechanically coupling advantage since the sensor behaves as a rigid bar when  $\omega_r$  and  $\omega_t$  are located close each other. However, as shown in Figure 6.4c when the second natural frequency  $\omega_t$  is located too far away from the first natural frequency  $\omega_r$ , the amplification of the time delay moves to the low frequency ranges. This trend of the time delay by varying the coupling spring constants  $\omega_t$  is shown in Figure 6.10. Starting with the coupling spring constant  $k_3$  as 1, it is gradually increased up to 110. The units for the coupling spring constant  $k_3$  are all in N/m. With the smaller  $k_3$  for the 3.5 mm by 3.5 mm size sensor with 3.5  $\mu\text{m}$  thickness, there is zero crossing. As  $k_3$  is increased gradually, the time delay amplification increases. (1), (2), (3) in Figure 6.10 show this trend when there is zero crossing. If  $k_3$  is increased further, higher coupling spring constant  $k_3$  prevent zero crossing from occurring which increases the overall time delay amplification. (4) in Figure 6.10 shows this. From the coupling spring constant for (4) in Figure 6.10, increasing  $k_3$  moves the time delay amplification to the low frequency ranges. (5), (6), and (7) in Figure 6.10 show this trend.

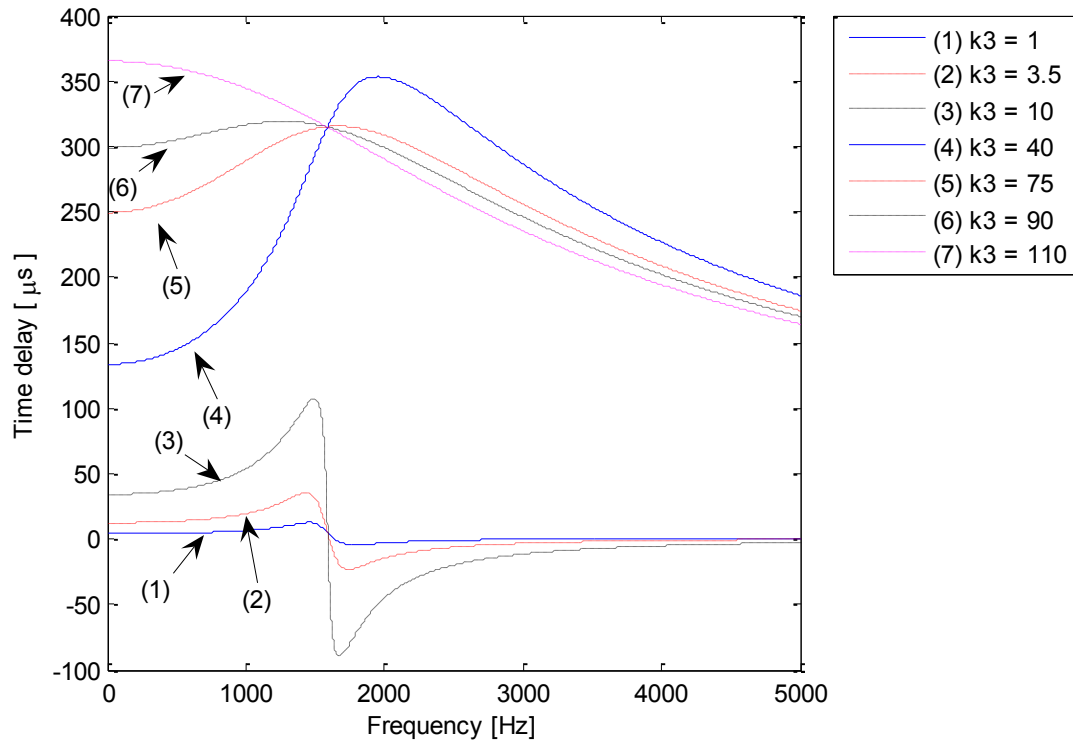


Figure 6.10: Time delay vs. Frequency plot: varying coupling spring constant  $k_3$

The location of the second natural frequency  $\omega_t$  in terms of sensor design is studied through four different examples. Four different sizes are chosen via sensor size selection matrix similar to Appendix C.

Table 6-1: Sensor sizes for the second natural frequency study.

	Length, $L$	Thickness, $t$	Spring constant, $k$
Case 1	$7e-3$ m	$3.5e-6$ m	0.576 N/m
Case 2	$5e-3$ m	$3.5e-6$ m	0.576 N/m
Case 3	$4e-3$ m	$3.5e-6$ m	0.576 N/m
Case 4	$2e-3$ m	$3.5e-6$ m	0.576 N/m

### 6.3.1 Case 1.

Figure 6.11a shows the output time delay  $\tau_o$  plot for the coupling spring constant  $k_3$  of 51.8 N/m. First two natural frequencies  $\omega_r$ ,  $\omega_t$  of the sensor are located at 453 and 6095 Hz. In order to

determine the sensor's ability to detect the directivity of the sound and the bandwidth, the output time delay  $\tau_o$  has been plotted against the incidence of angle at various frequencies shown in Figure 6.11.

The useful frequency ranges are up to 400 Hz and the gradual step-like jump appears in the time delay versus the angle of incidence plot in Figures 6.11c and 6.11d. As discussed with the polar plot, the shape of the polar plot becomes no longer circular shape. This can only be seen from the time delay plot against the angle of incidence in Figure 6.11 (b), (c), and (d) not (a).

It is shown in Figure 6.11 that the frequency region in which amplification of the time delay takes place is moved to lower frequencies as the coupling spring constant  $k_3$  is doubled to 103.6 N/m from 51.8 N/m. This is rather expected result since the relationship between the coupling constant  $k_3$  and the amplification of the time delay has been studied in the previous section as in Figure 6.10.

For the this specific size sensor of case 1, decreasing the coupling spring constant  $k_3$  to 3.45 N/m or lower produces the zero crossing as shown in Figure 6.13. In order to find the zero crossing triggering condition of the coupling spring constant  $k_3$ ,  $k_3$  was gradually decreased and the ratio of the second natural frequency  $\omega_t$  to the first natural frequency  $\omega_r$  is calculated since  $\omega_r$  and  $\omega_t$  are related to the spring constants  $k_1$ ,  $k_2$ , and  $k_3$  according to Eq. 6.1 where  $k = k_1 = k_2$ . The condition for the zero crossing to occur for the case 1 is that the second natural frequency  $\omega_t$  is found to be 3.6 times greater or less than the first natural frequency  $\omega_r$  since the ratio of two natural frequencies  $\omega_t/\omega_r = 1633/456 = 3.6$ .

$$\begin{aligned}\omega_r &= 2\pi\sqrt{\frac{k}{m}} \\ \omega_t &= 2\pi\sqrt{\frac{k+2k_3}{m}}\end{aligned}\tag{6-1}$$

The useful frequency range, i.e. bandwidth, of the sensor can be found from Figure 6.11a, b, c, d. In order for the sensor to be directivity sensitive, the polar plot should look like circular shape. In terms of time delay versus the angle of incidence plot, the smooth and gradually increasing time delay versus the angle of incidence is sensitive to directivity. In the same manner, the bandwidth

frequency of the sensor is found. It turns out to be the same regardless of the coupling spring  $k_3$ , however, the amplification of the time delay changes.

One advantage of zero crossing is that there is frequency range that is directivity sensitive after the time delay crosses with zero in terms of frequency until it decays to zero. Figure 6.13d show the time delay versus the angle of incidence for the frequency range after the time delay crosses zero.

### 6.3.2 Case 2.

Figures 6.14, 6.15, and 6.16 show the time delay plots of case 2 against the frequency and angle of incidence at various frequencies. Similar phenomena as case 1 have been observed except that the first two natural frequencies  $\omega_r$ ,  $\omega_t$  are 634 and 2667 Hz and the zero crossing triggering frequency ratio between first and second natural frequencies,  $\omega_t/\omega_r$ , is equal or less than 4.2 (2667 Hz/634 Hz) which is different from the case 1.

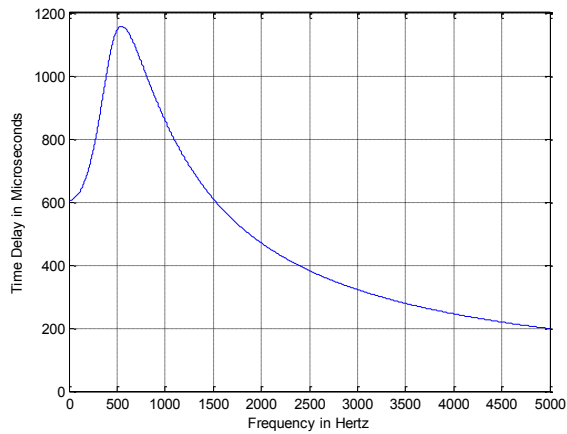
### 6.3.3 Case 3.

Figures 6.17 and 6.18 show the time delay plots of case 3 against the frequency and angle of incidence at various frequencies. The frequency ratio between the first natural frequency  $\omega_r$  and that of second  $\omega_t$  that produces zero crossing is 4.67 ( $\omega_t/\omega_r = 3706/793$ ) or smaller. This is also different from the case 1 and 2.

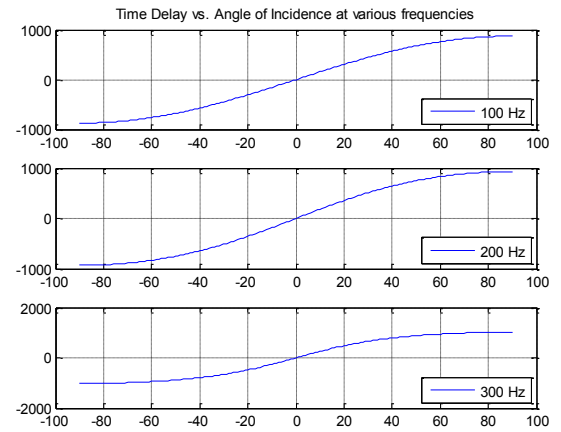
### 6.3.4 Case 4.

Similar observations have been made regarding case 4. It is added to show the relationship between the second natural frequency  $\omega_t$  and the time delay amplification throughout the bandwidth for non-zero crossing case (Figures 6.19 and 6.20) and for zero crossing case (Figures 6.21 and 6.22) which are consistent with previous observation. Zero crossing is triggered at the frequency ratio of 6.5 or smaller between the first and second natural frequencies ( $\omega_t/\omega_r = 10363/1586$ ).

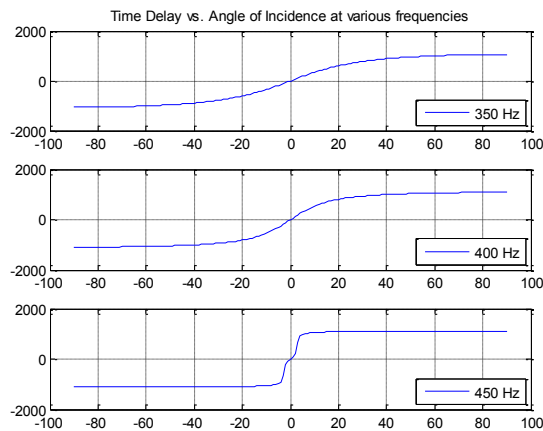
Based on four different size sensors chosen, it was shown that the sensor geometry, material selection, and spring stiffness determine the directional sensitivity and the relationship between the second natural frequency  $\omega_t$  and the first  $\omega_r$ . Due to the many design parameters it is clear that design optimization would be beneficial in the design of an effective sensor.



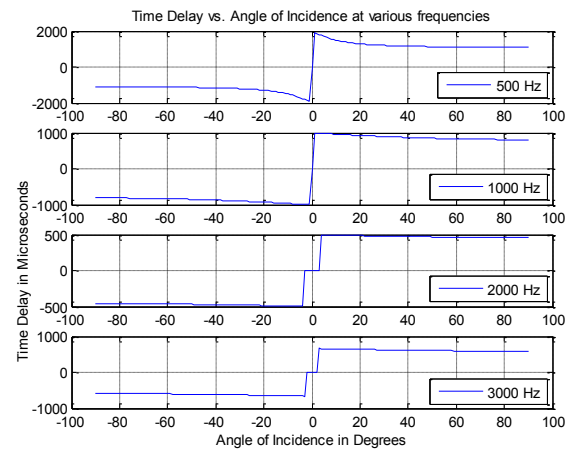
(a)



(b)

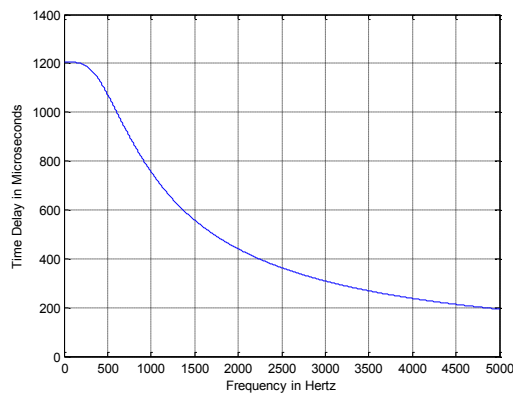


(c)

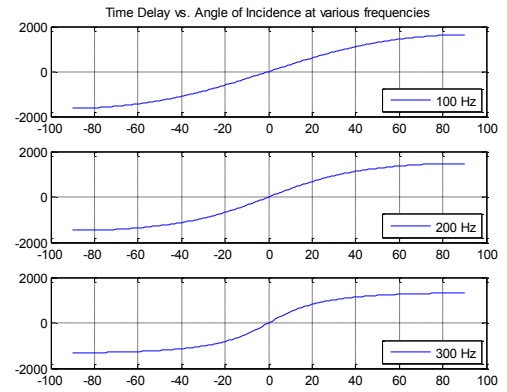


(d)

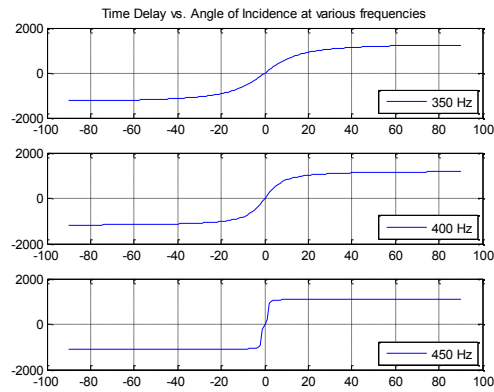
Figure 6.11: (a) Time delay vs. frequency plot of case 1 with  $k_3 = 51.8$  N/m, (b) Time delay vs. angle of incidence at 100, 200, and 300 Hz, (c) Time delay vs. angle of incidence at 350, 400, and 450 Hz (d) Time delay vs. angle of incidence at 500, 1000, 2000, and 3000 Hz.



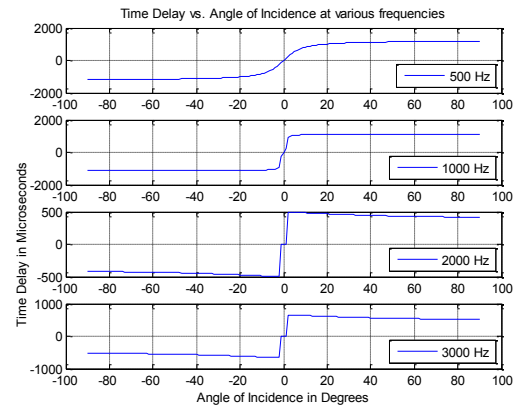
(a)



(b)



(c)



(d)

Figure 6.12: (a) Time delay vs. frequency plot of case 1 with  $k_3 = 103.6$  N/m, (b) Time delay vs. angle of incidence at 100, 200, and 300 Hz, (c) Time delay vs. angle of incidence at 350, 400, and 450 Hz (d) Time delay vs. angle of incidence at 500, 1000, 2000, and 3000 Hz.

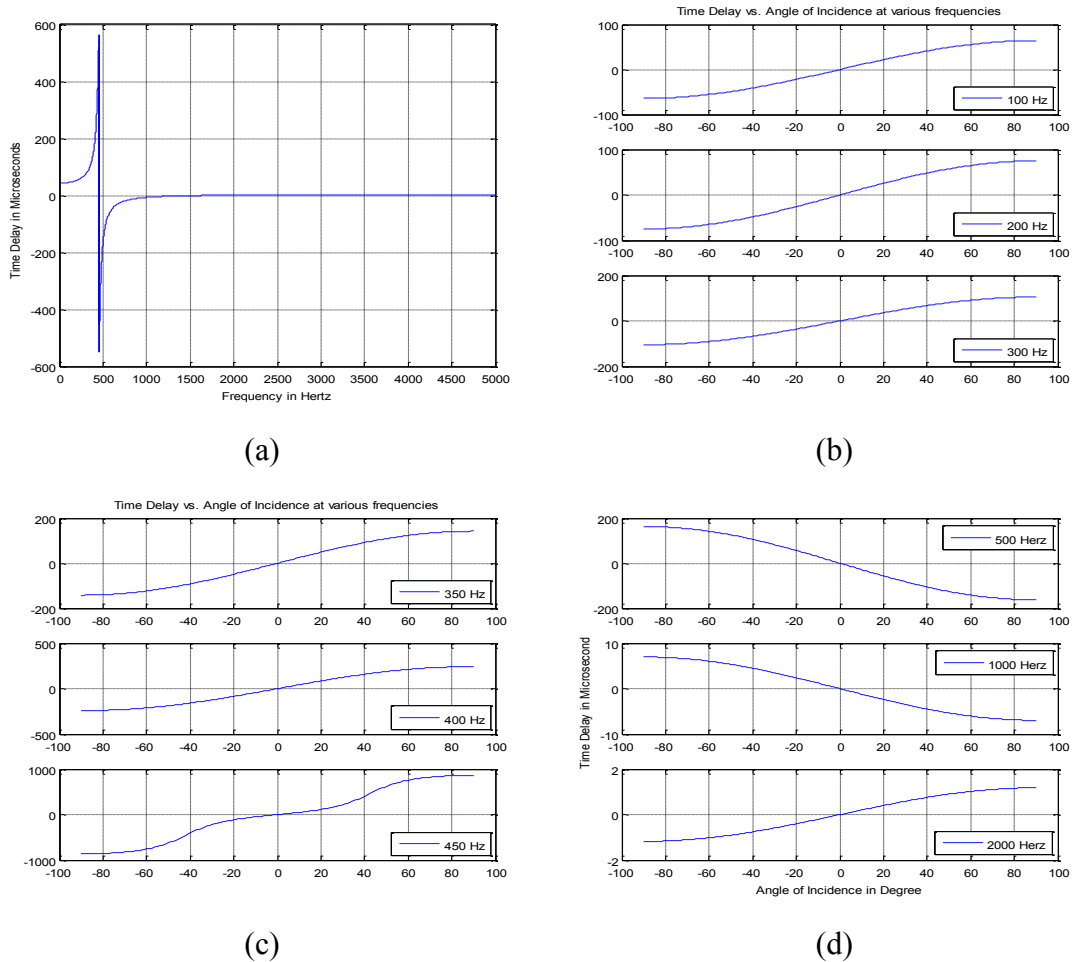


Figure 6.13: (a) Time delay vs. frequency plot of case 1 with  $k_3 = 3.45$  N/m, (b) Time delay vs. angle of incidence at 100, 200, and 300 Hz, (c) Time delay vs. angle of incidence at 350, 400, and 450 Hz (d) Time delay vs. angle of incidence at 500, 1000, and 2000 Hz.

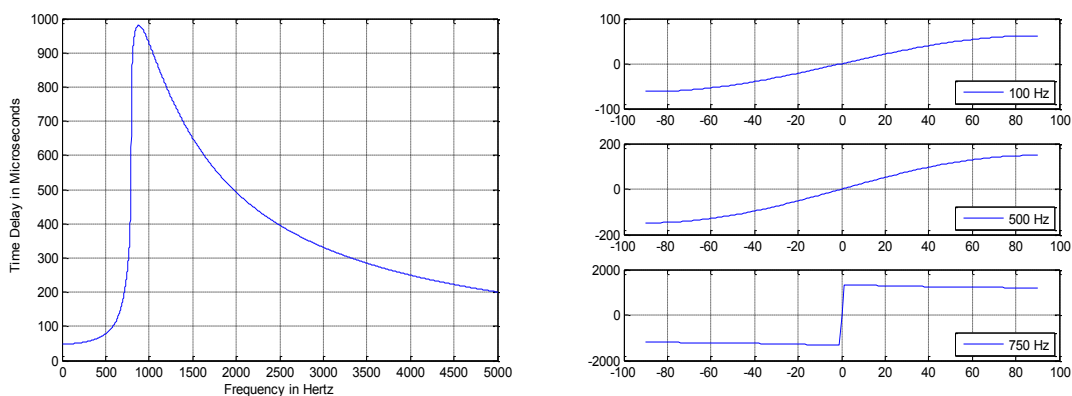


Figure 6.14: Left: Time delay vs. frequency plot of case 2 with  $k_3 = 4.9$  N/m, Right: Time delay vs. angle of incidence at 100, 500, and 750 Hz.

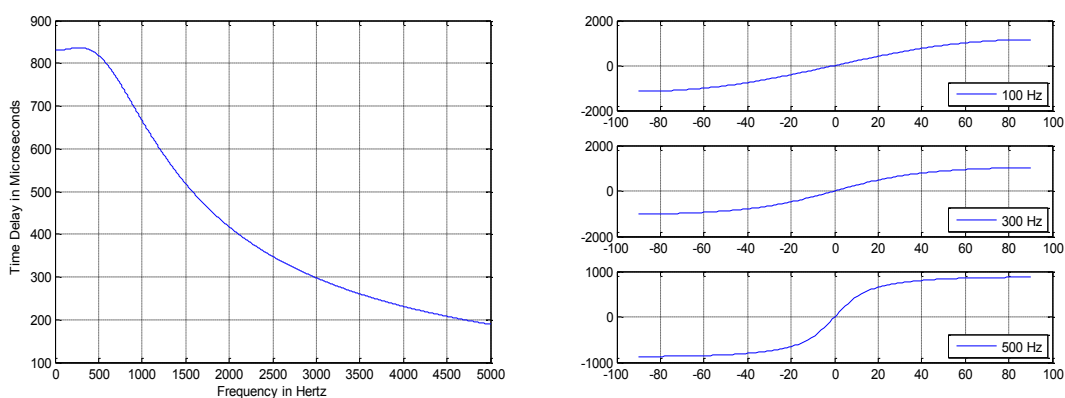


Figure 6.15: Left: Time delay vs. frequency plot of case 2 with  $k_3 = 100$  N/m, Right: Time delay vs. angle of incidence at 100, 300, and 500 Hz.

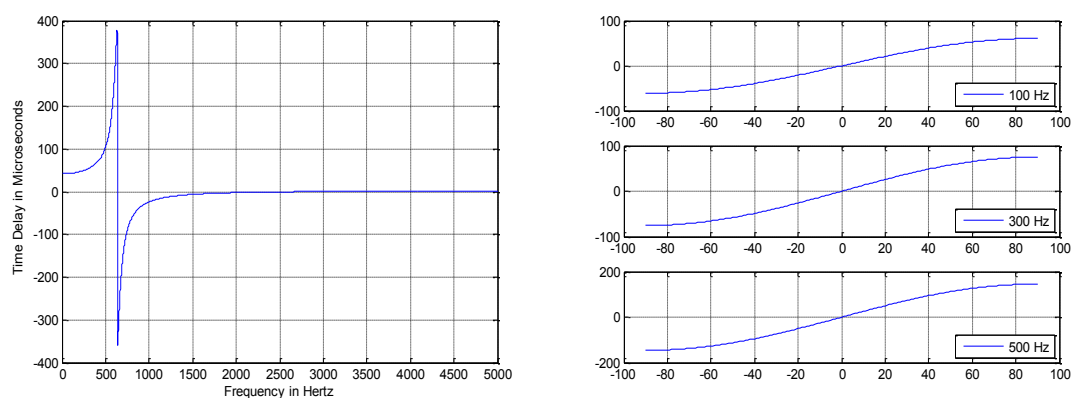


Figure 6.16: Left: Time delay vs. frequency plot of case 2 with  $k_3 = 4.8$  N/m, Right: Time delay vs. angle of incidence at 100, 300, and 500 Hz.

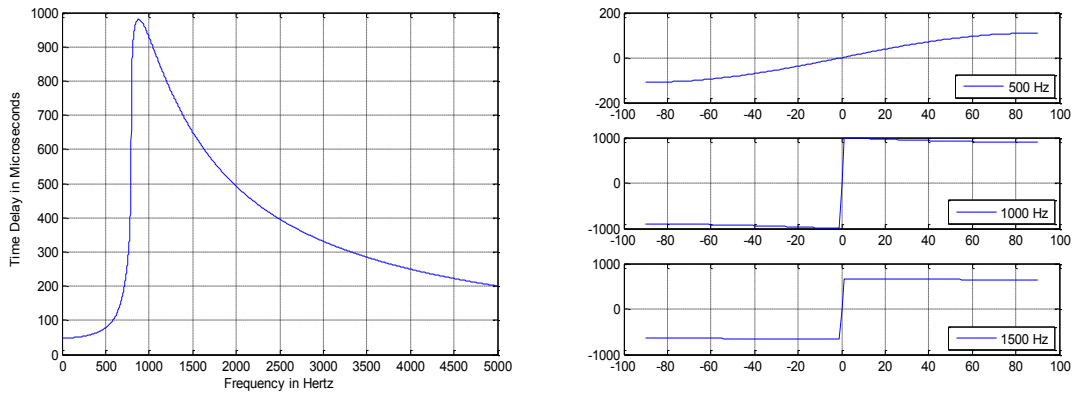


Figure 6.17: Left: Time delay vs. frequency plot of case 3 with  $k_3 = 7$  N/m, Right: Time delay vs. angle of incidence at 500, 1000, and 1500 Hz.

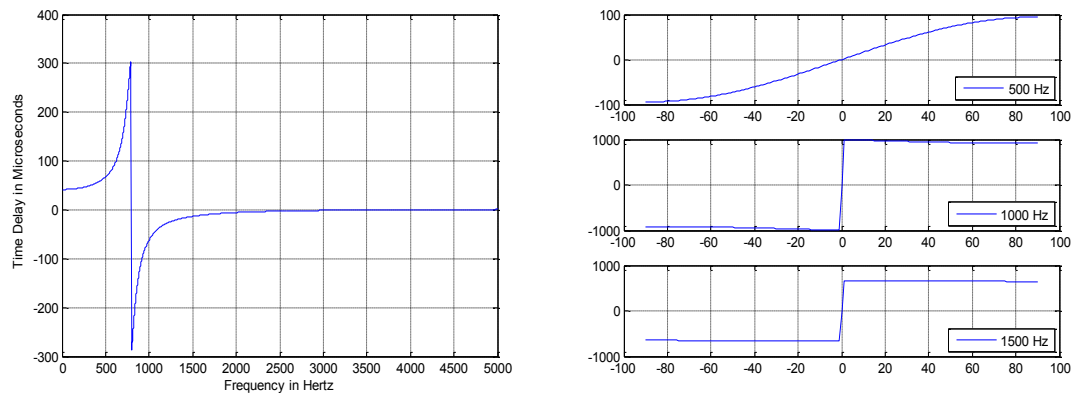


Figure 6.18: Left: Time delay vs. frequency plot of case 3 with  $k_3 = 6$  N/m, Right: Time delay vs. angle of incidence at 500, 1000, and 1500 Hz.

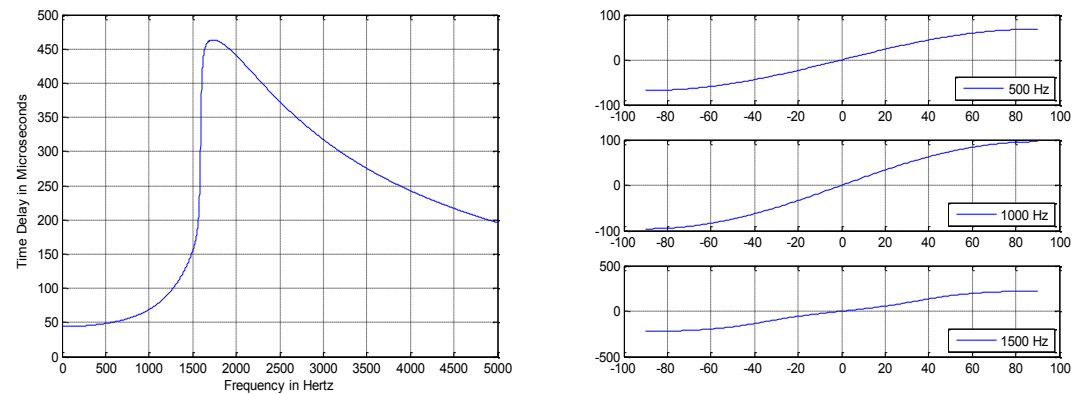


Figure 6.19: Left: Time delay vs. frequency plot of case 4 with  $k_3 = 13$  N/m, Right: Time delay vs. angle of incidence at 500, 1000, and 1500 Hz.

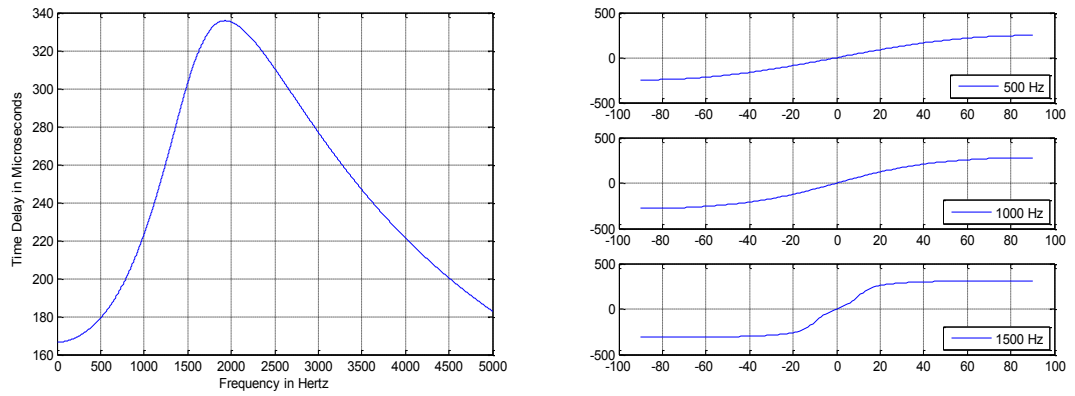


Figure 6.20: Left: Time delay vs. frequency plot of case 4 with  $k_3 = 50$  N/m, Right: Time delay vs. angle of incidence at 500, 1000, and 1500 Hz.

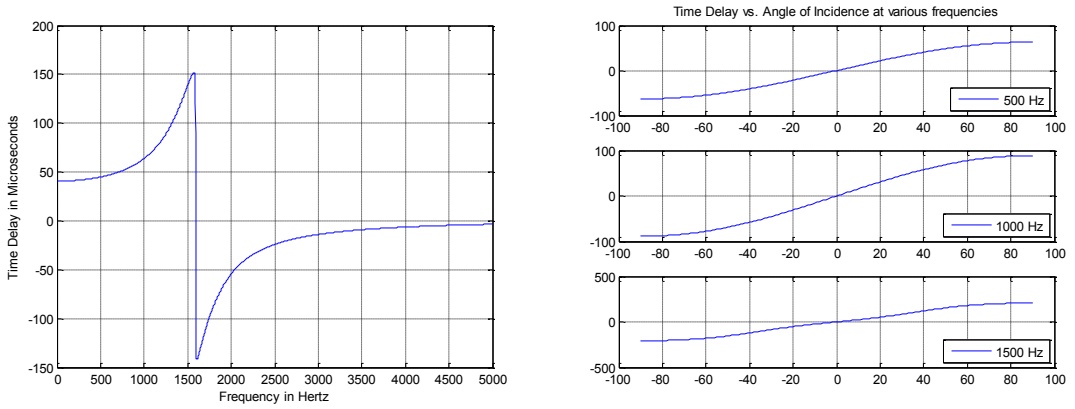


Figure 6.21: Left: Time delay vs. frequency plot of case 4 with  $k_3 = 12$  N/m, Right: Time delay vs. angle of incidence at 500, 1000, and 1500 Hz.

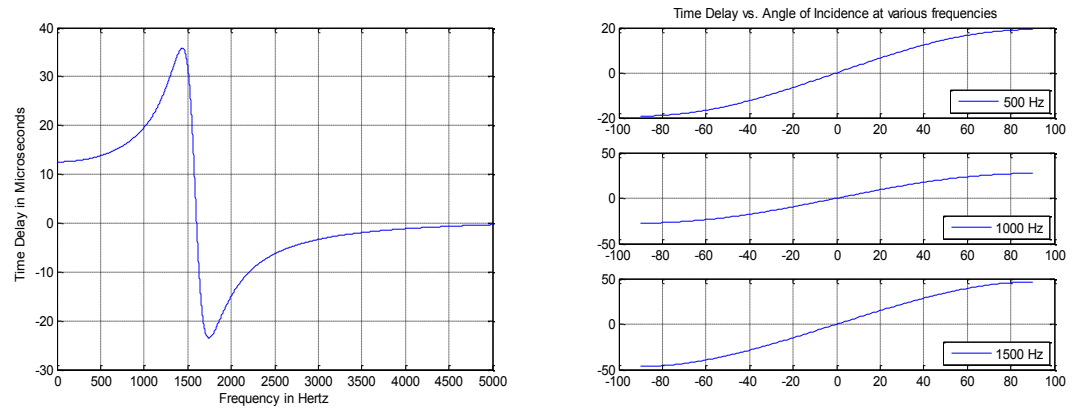


Figure 6.22: Left: Time delay vs. frequency plot of case 4 with  $k_3 = 3.5$  N/m, Right: Time delay vs. angle of incidence at 500, 1000, and 1500 Hz.

## 6.4 Design Optimization of the Sensor

Based on the 5 DOF lumped parameter model developed in chapter 2, the design optimization is performed considering the material parameters that represent the stiffness as well as mass matrices.

The purpose of the design optimization of the sensor is to amplify the output time delay  $\tau_o$  while at the same time maximizing the sensitivity of the time delay with respect to incident angle varying with respect to the incident angles. In other words, we would like to amplify the time delay while keeping the circular shape of the polar plot in Figure 6.23. The left and right plots of Figure 6.23 are two different ways to show the same information, i.e. the relationship between the time delay and the incidence angle.

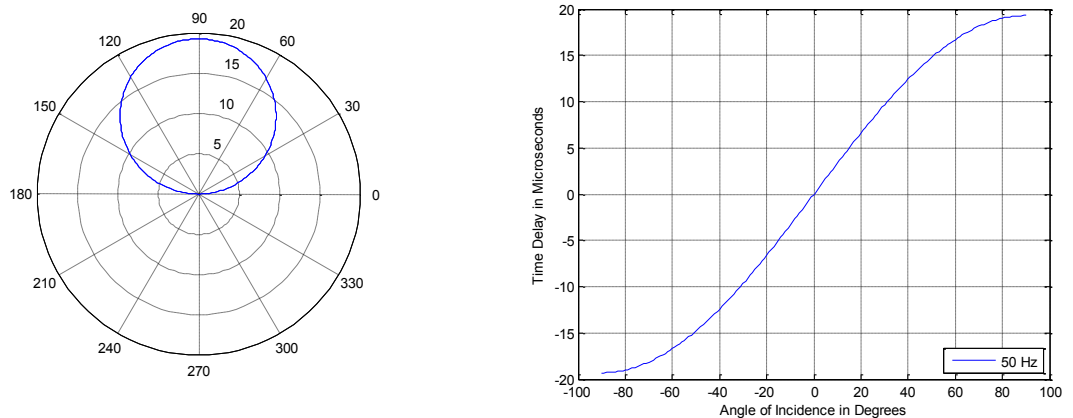


Figure 6.23: Left: Polar plot of the time delay. Right: Time delay vs. Incidence angle.

### 6.4.1 Design Optimization Problem

Since it was found previously that the second natural frequency  $\omega_t$  is related to the performance and characteristics of the sensor, it is important to determine the location of the second natural frequency  $\omega_t$  in the design optimization process. In contrast as shown in Figures 6.4a and 6.4b, the location of the first natural frequency  $\omega_r$  dictates the location of peak frequency or the time delay of the sensor to cross zero with respect to frequency.

The transfer functions  $H_{x_1 p}(\omega)$  and  $H_{x_2 p}(\omega)$ , the relationship between the sensor plate responses,  $x_1$  and  $x_2$ , and the pressure  $p$  at the pivot, are given by Eq. 2.38 and Eq. 2.39.

$$\phi_1 = \tan^{-1} \left( \frac{\text{imag} (H_{x_1,p}(\omega))}{\text{real} (H_{x_1,p}(\omega))} \right)$$

$$\phi_2 = \tan^{-1} \left( \frac{\text{imag} (H_{x_2,p}(\omega))}{\text{real} (H_{x_2,p}(\omega))} \right)$$
(6-3)

The objective in this design optimization is to maximize the phase difference between the two transfer functions, hence maximize the time delay while maximizing the sensitivity of the time delay with respect to incident angle varying with respect to the incident angles. The phase difference of the two transfer function becomes the cost function to be maximized. Based on Eq. 6.3, the cost function can be represented as  $f = \phi_1 - \phi_2$ , where  $\phi_i$  is a function of material properties and geometry information. The optimization method chosen here is the gradient-based method in Matlab, *fmincon*, which is designed to work on problems where the objective and constraint functions are both continuous and have continuous first derivatives. In Matlab, the general design model treats only minimization problems using Matlab optimization built-in function such as *fmincon*. This is not a restriction as maximization of a function  $f(E, I, L, A, b, h, \rho)$  is the same as minimization of a transformed function  $f = -f$ .

Design optimization is characterized as follows.

Maximize the *objective function*

$$f = \phi_1 - \phi_2$$
(6-4)

where  $\phi_1$  and  $\phi_2$  are the phases of transfer functions 1 and 2 respectively.

Subject to *inequality constraints* ( $c(x) \leq 0$ )

$$g_1 = \tau(90^\circ) - 100 \leq 0 \rightarrow g_1 = (\theta_1(90^\circ) - \theta_2(90^\circ))/2 \cdot \pi \cdot f - 100$$

$$g_2 = \tau(22.5^\circ) - 40 \leq 0$$

$$g_3 = -\tau(90^\circ) + \tau(67.5^\circ) \leq 0$$

$$g_4 = -\tau(67.5^\circ) + \tau(45^\circ) \leq 0$$

$$g_5 = -\tau(45^\circ) + \tau(22.5^\circ) \leq 0$$

$$g_6 = -\Delta\tau_1 + \Delta\tau_2 \leq 0$$

$$g_7 = -\Delta\tau_2 + \Delta\tau_3 \leq 0$$

$$g_8 = -\Delta\tau_3 + \Delta\tau_4 \leq 0$$

where  $\tau$  = time delay, and  $\Delta\tau_i = \tau_{i+1} - \tau_i$  ( $\tau_i$  = time delays of incidence angle at 0, 22.5, 45, 67.5, 90).

As it can be seen from Figure 6.24,  $\Delta\tau$ 's are defined as follows.

$$\Delta\tau_1 = \tau(22.5^\circ) - \tau(0^\circ)$$

$$\Delta\tau_2 = \tau(45^\circ) - \tau(22.5^\circ)$$

$$\Delta\tau_3 = \tau(67.5^\circ) - \tau(45^\circ)$$

$$\Delta\tau_4 = \tau(90^\circ) - \tau(67.5^\circ)$$

In order for the polar plot to have a circular shape, the requirements for  $\Delta\tau$ 's are

$$\Delta\tau_1 > \Delta\tau_2 > \Delta\tau_3 > \Delta\tau_4$$

where  $\Delta\tau_1 = 25.1$ ,  $\Delta\tau_2 = 21.3$ ,  $\Delta\tau_3 = 14.3$  and  $\Delta\tau_4 = 5.0$ . The reason for this inequality condition is that the time delay plot shown in Figure 6.24 is a parabolic curve with such inequality condition. Y ordinate in Figure 6.24 shows this inequality between  $\Delta\tau_1$ ,  $\Delta\tau_2$ ,  $\Delta\tau_3$ , and  $\Delta\tau_4$ . Inequality constraint can be added as  $g_9 = \min(\omega_1) - \omega_c \leq 0$  to ensure the first natural frequency  $\omega_r$  which dictates the bandwidth of the sensor does not exceed the desired maximum frequency of interest.

The objective function  $f(E, I, L, A, b, t, \rho)$  has several parameters, however, some of them are predefined such as modulus of elasticity  $E$ , the density  $\rho$ , and the moment of inertia  $I$ . Thus, we consider the width of the sensor  $L$  and thickness  $t$  as our design variables and the materials chosen for the sensor are poly-silicon and PDMS for the sensor shown in Figure 2.8. Design variables are chosen as

1.  $1e-3 \leq \text{Length}, L \leq 4e-3$  [m] and

2.  $1e-6 \leq \text{thickness}, t \leq 1e-5$  [m].

These design variables vary depending on the design objective and frequency of interest.

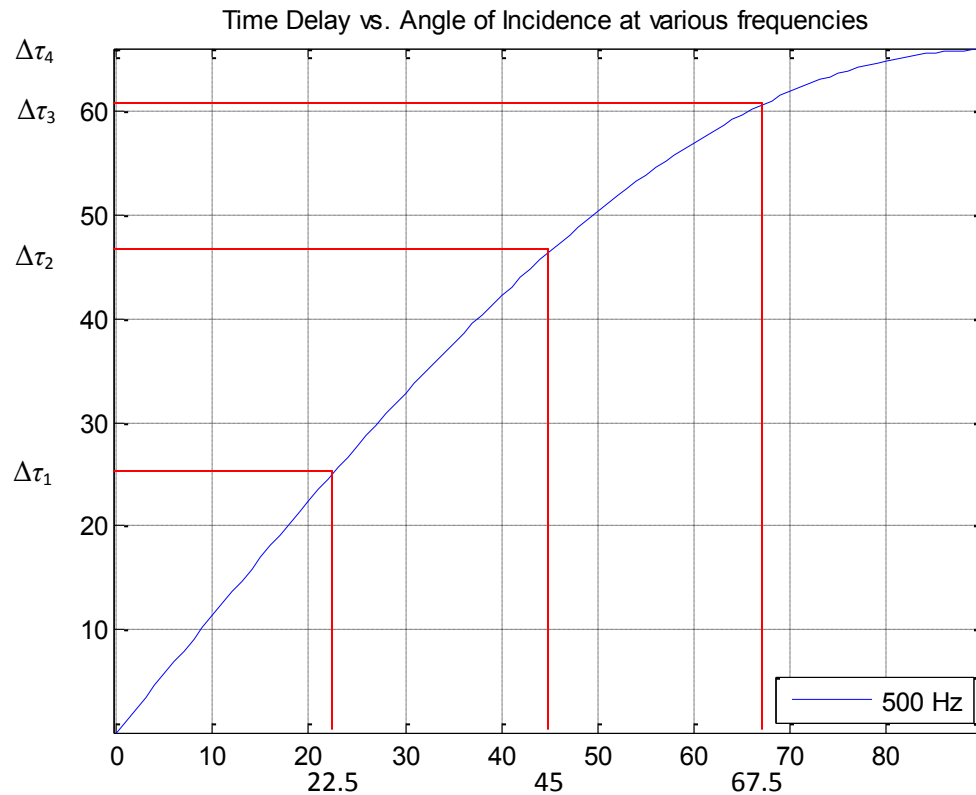


Figure 6.24: Time delay vs. Incidence angle

#### 6.4.2 Design Optimization Results

It is observed from design optimization of the sensor that as the time delay increases its amplitude near the cutoff frequency, the bandwidth of the sensor becomes narrower. This has previously been observed from our parametric design analysis. Hence, applications over the wide frequency range might require several different sensors in an array. The transfer functions (Eq. 2.38 and Eq. 2.39) incorporating the formula for the added mass due to fluid loading will be used in the design optimization. These transfer functions are derived from the 5 DOF lumped parameter discrete model developed in Chapter 2. Three different cutoff frequencies are shown as examples for 134, 315, and 1600 Hz.

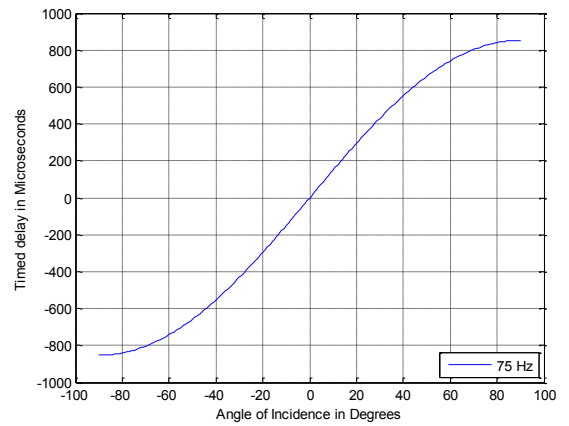
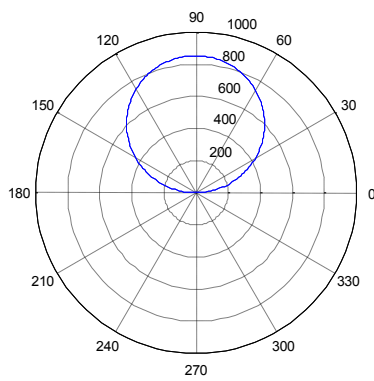


Figure 6.25: Left: Polar plot at 75 Hz. Right: Time delay vs. Incidence angle at 75 Hz.

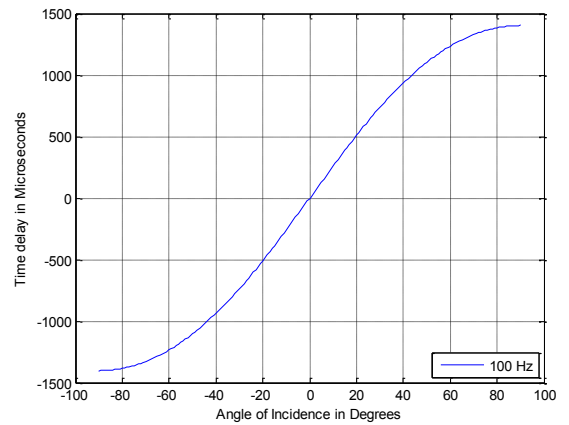
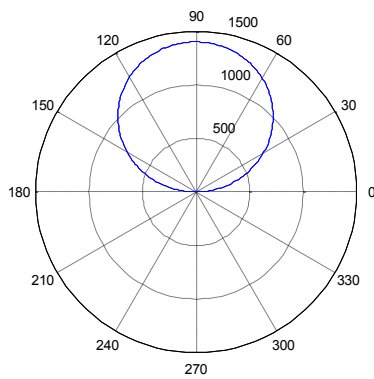


Figure 6.26: Left: Polar plot at 100 Hz. Right: Time delay vs. Incidence angle at 100 Hz.

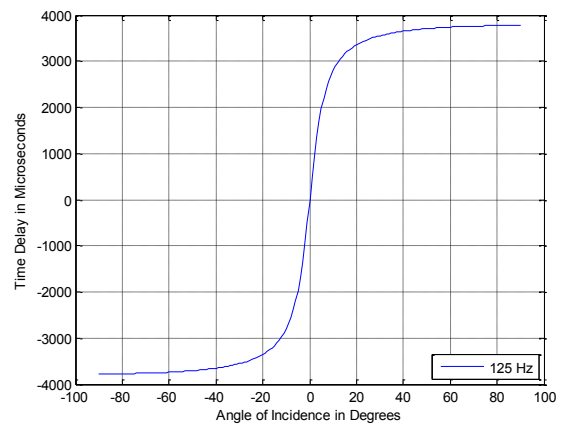
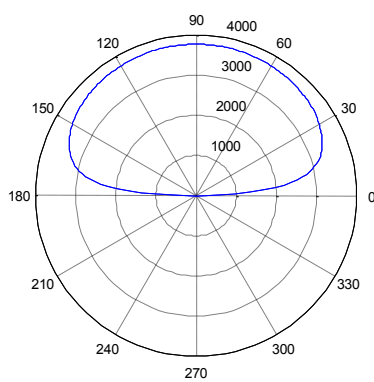


Figure 6.27: Left: Polar plot at 125 Hz. Right: Time delay vs. Incidence angle at 125 Hz.

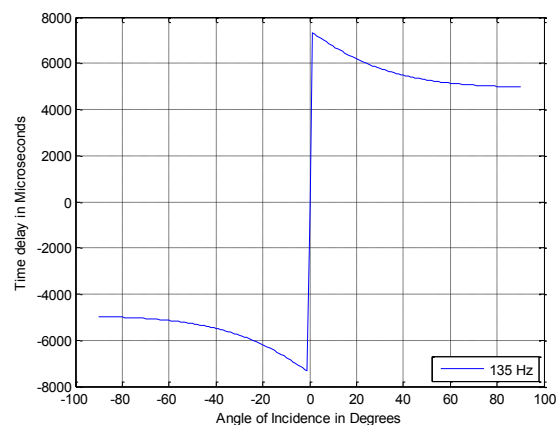
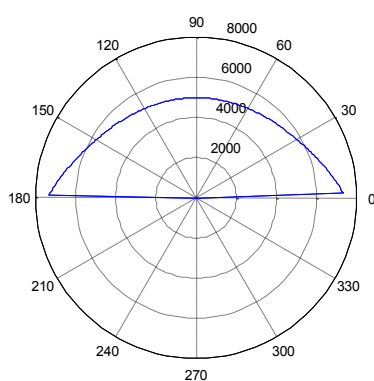


Figure 6.28: Left: Polar plot at 135 Hz. Right: Time delay vs. Incidence angle at 135 Hz

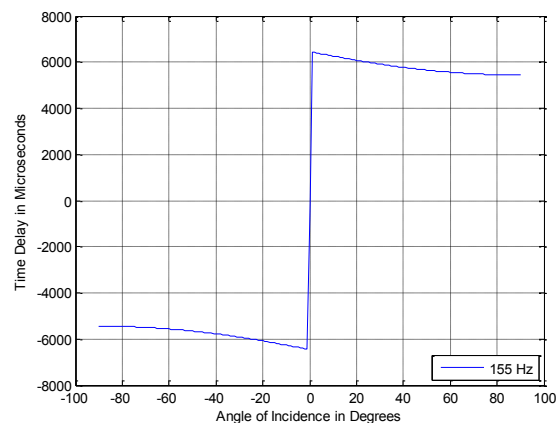
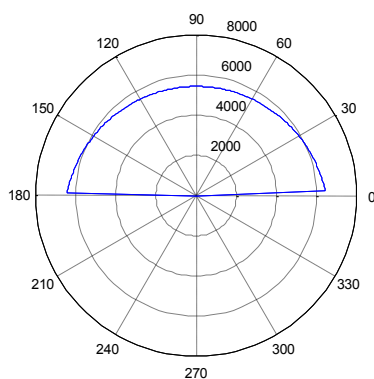


Figure 6.29: Left: Polar plot at 155 Hz. Right: Time delay vs. Incidence angle at 155 Hz

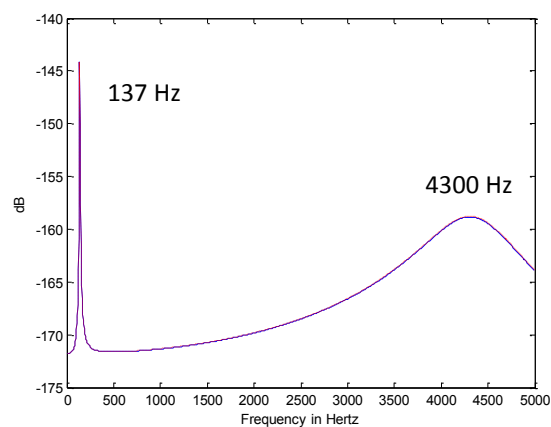
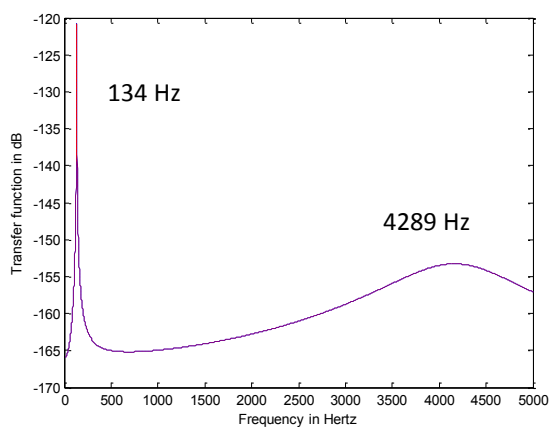


Figure 6.30: Left: Frequency response based on the 5 DOF lumped parameter model. Right: Frequency response based on FEA harmonic analysis.

For the cutoff frequency of 134 Hz, the calculated result of optimization process is  $L = 0.0012$  m and  $t = 1.932e-5$  m. Figures 6.26 through Figure 6.30 show the polar plot and the time delay vs. the angle of incidence plot based on the result at the frequencies of 75, 100, 125, 135, and 155 Hz. The useful frequency is up to around 125 Hz and as frequency reaches near the cutoff frequency, the sensor becomes incapable to detect the direction of the sound propagation.

The comparison is made between the 5 DOF lumped parameter sensor model with variable fluid loaded mass and the acoustic-structure coupled FEA model. Eq. 4.1 and Eq. 4.2 are used for the variable fluid loaded mass in the calculation of the first natural frequency and the second respectively. Figure 6.32 and Figure 6.33 show the frequency response of the lumped parameter sensor model and the harmonic FEA analysis shown in Figure 6.31, the phase difference and the output time delay  $\tau_o$  have been plotted. They show a good agreement with each other. The variable fluid loaded mass is plotted against frequency in Figure 6.31.

The reason why the second peak frequency is different in the left plot compared to the right plot in Figure 6.30 is that the 5 DOF sensor model does not include friction or damping effects either inside the rod material or at the interface between the sensor surface and the medium in which it is immersed. Figure 6.30 shows the damping effect on the sensor. Comparing the left and right plots, the first resonant frequencies have similar amplitude due to less damping on the lower frequency as shown in Figure 4.16. Due to the higher damping effect as frequency increases, the amplitude of the second resonant frequency is reduced on the damping containing model.

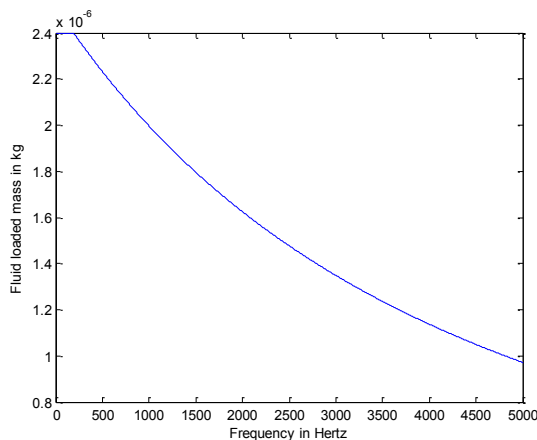


Figure 6.31: Variable fluid loaded mass.

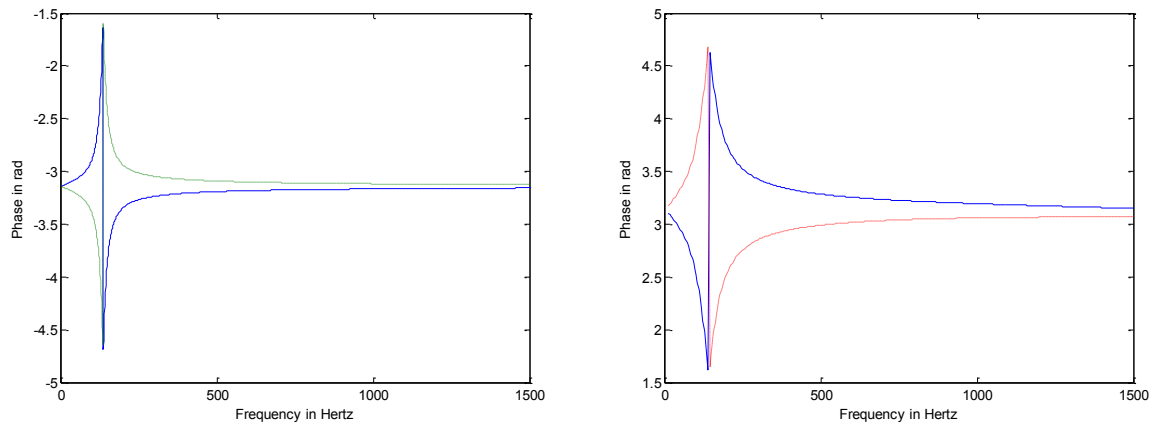


Figure 6.32: Left: Phase difference between  $x_1$  and  $x_2$  based on the 5 DOF lumped parameter model. Right: Phase difference based on FEA harmonic analysis.

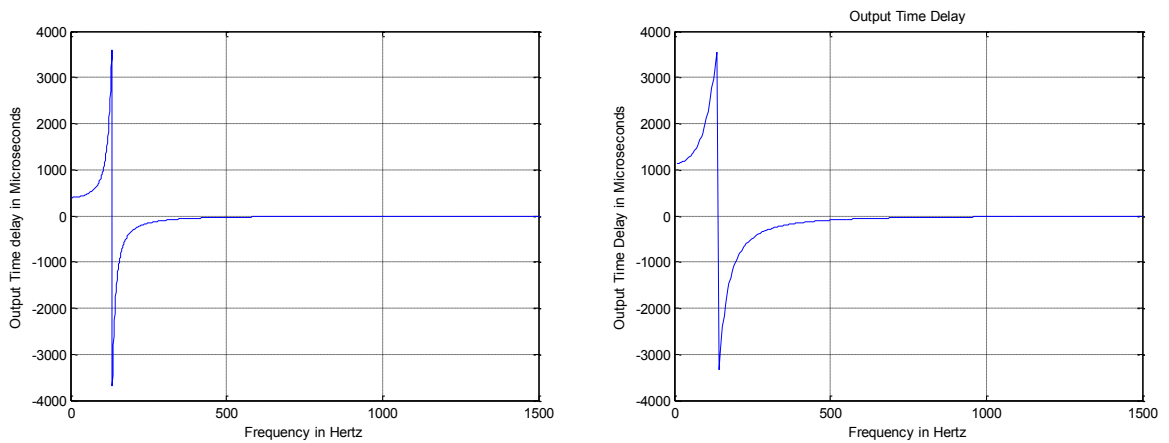


Figure 6.33: Left: Output time delay based on the 5 DOF lumped parameter model. Right: Output time delay based on FEA harmonic analysis.

For the cutoff frequency of 360 Hz, the thickness of PDMS, which acts as the linear spring  $k_1$ ,  $k_2$ , has been increased to  $4e-6$  m from  $2e-6$  m. The design optimization implementation results in  $L = 0.0013$  m and  $t = 2.94e-5$  m.

Figure 6.34 shows that the useful bandwidth of the sensor lies between near zero to the cutoff frequency of 360 Hz. As the plane wave frequency approaches the cutoff frequency, the time delay versus the angle of incidence plot becomes ill suited for detecting the directivity of the sound. This becomes obvious evident in comparing Figure 6.35 through Figure 6.39.

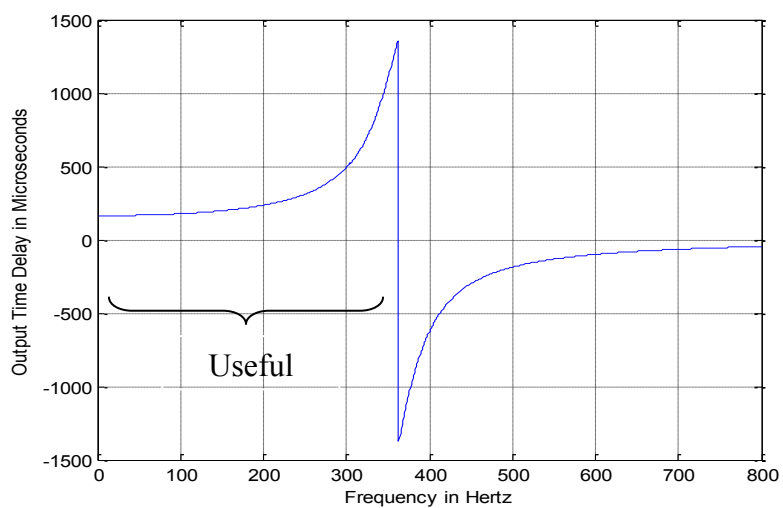


Figure 6.34: Output time delay for the cutoff frequency of 360 Hz.

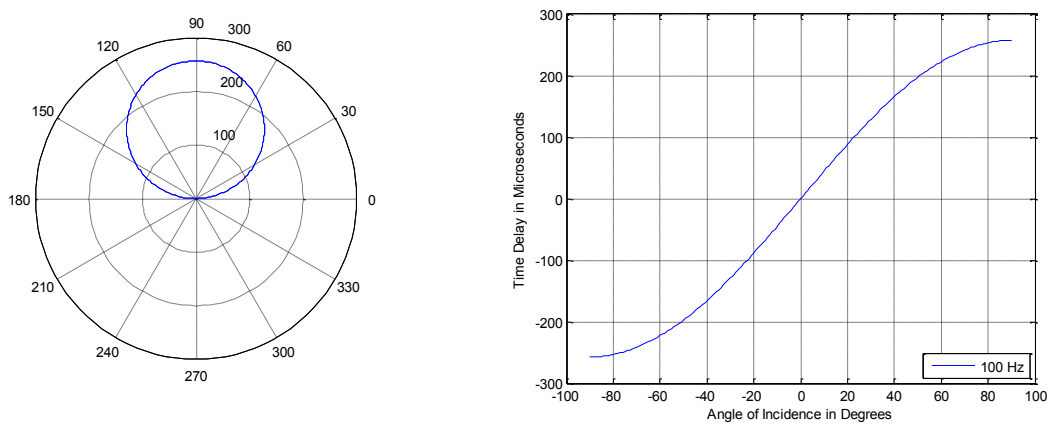


Figure 6.35: Left: Polar plot at 100 Hz. Right: Output time delay vs. angle of incidence at 100 Hz.

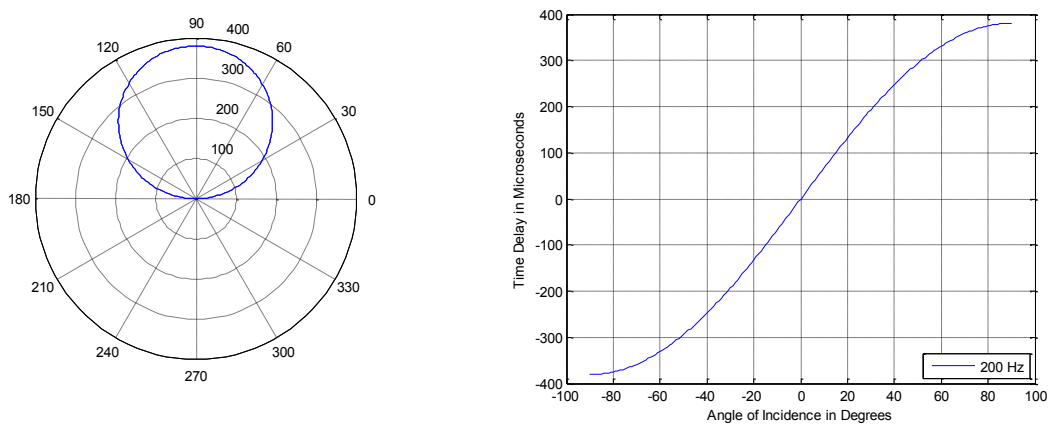


Figure 6.36: Left: Polar plot at 200 Hz. Right: Output time delay vs. angle of incidence at 200 Hz.

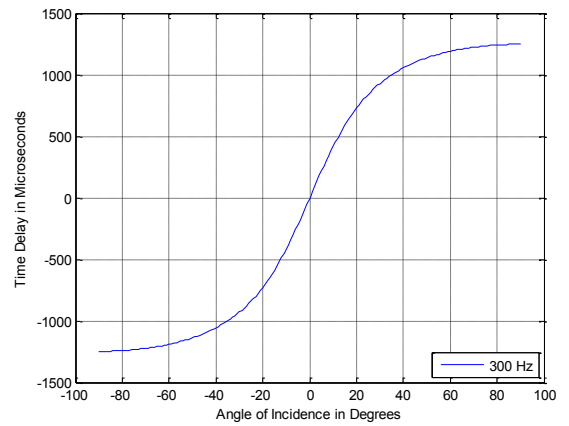
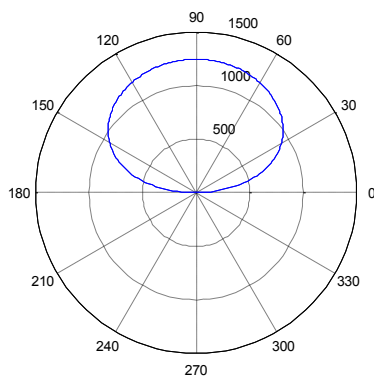


Figure 6.37: Left: Polar plot at 300 Hz. Right: Output time delay vs. angle of incidence at 300 Hz.

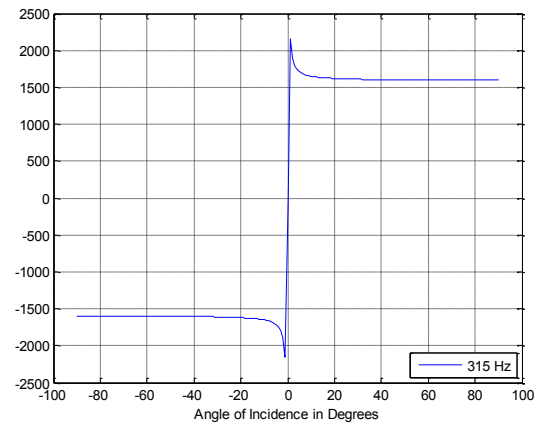
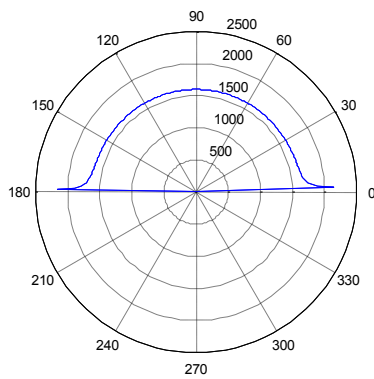


Figure 6.38: Left: Polar plot at 315 Hz. Right: Output time delay vs. angle of incidence at 315 Hz.

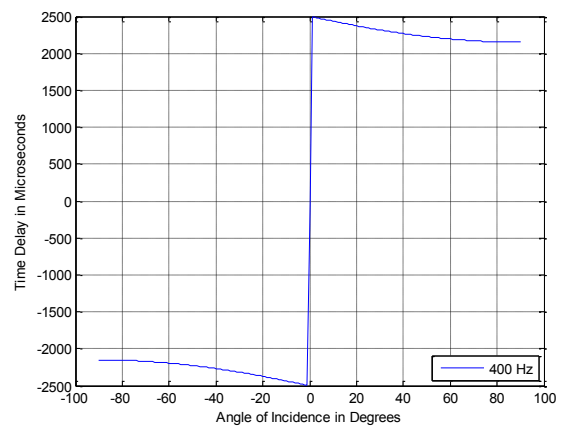
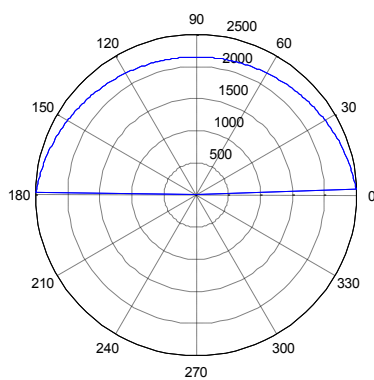


Figure 6.39: Left: Polar plot at 400 Hz. Right: Output time delay vs. angle of incidence at 400 Hz.

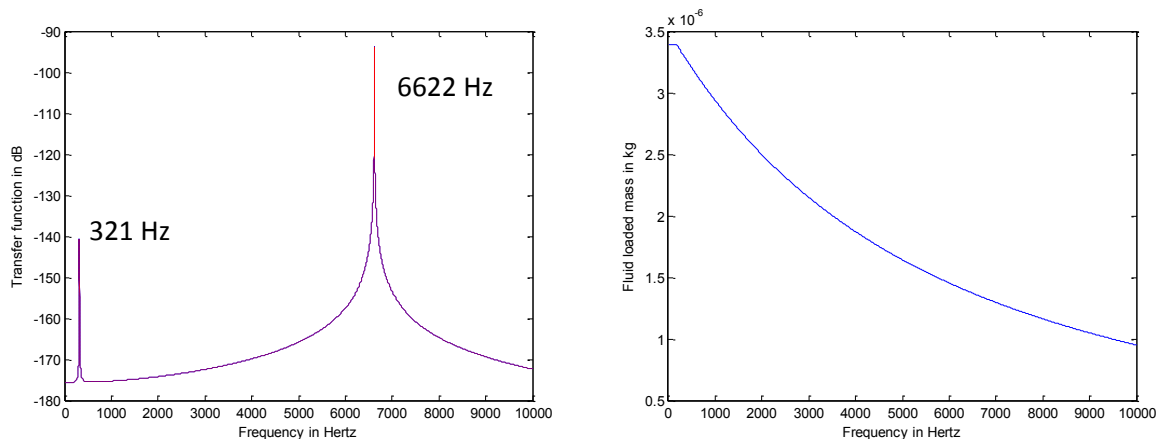


Figure 6.40: Left: Frequency response based on the 5 DOF lumped parameter model. Right: Variable fluid loaded mass.

Table 6-4 shows the first and second natural frequency as obtained via the 5 DOF lumped parameter based sensor model and FEA. Good agreement is obtained between the two models.

Table.6-2: Comparison between simulation results.

	5 DOF lumped model	FEA	% difference
1 <sup>st</sup> natural frequency	321 Hz	320 Hz	0.3
2 <sup>nd</sup> natural frequency	6622 Hz	6715 Hz	1.3

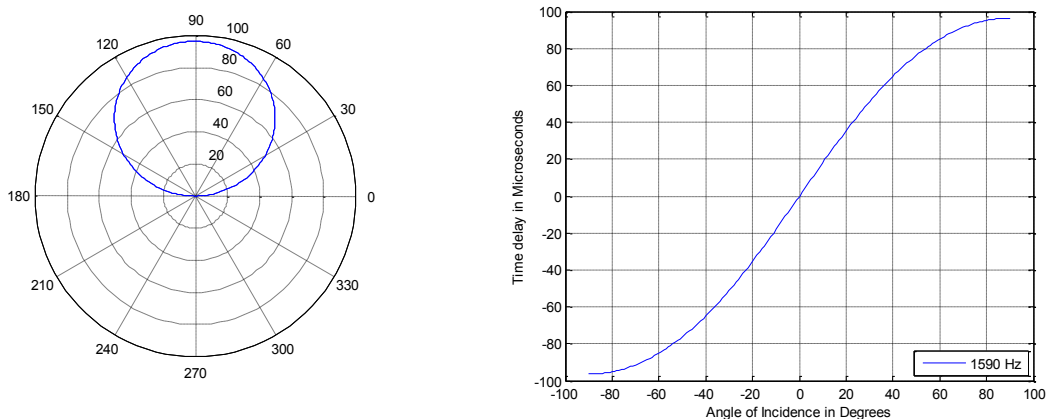


Figure 6.41: Left: Polar plot. Right: Output time delay vs. angle of incidence at 1590 Hz.

For the cutoff frequency of 1600 Hz, the thickness of the PDMS is chosen as  $1e-5$  m which helps to bring the first natural frequency  $\omega_r$  of the sensor up. According to our sensor design, there

is a tradeoff between the bandwidth of the sensor and the cutoff frequency which is as cutoff frequency goes up, bandwidth gets narrower. Figure 6.42 shows that there only exists small bandwidth where sensor is capable of detecting directivity. Comparing Figure 6.43 with Figure 6.33 and Figure 6.34, this tradeoff is evident. Hence, it is suggested to use arrays of different frequency amplification sensors for wide range sensing with maximum amplification in the output time delay  $\tau_0$  since it has been observed that as the amplification gets bigger the bandwidth gets narrower.

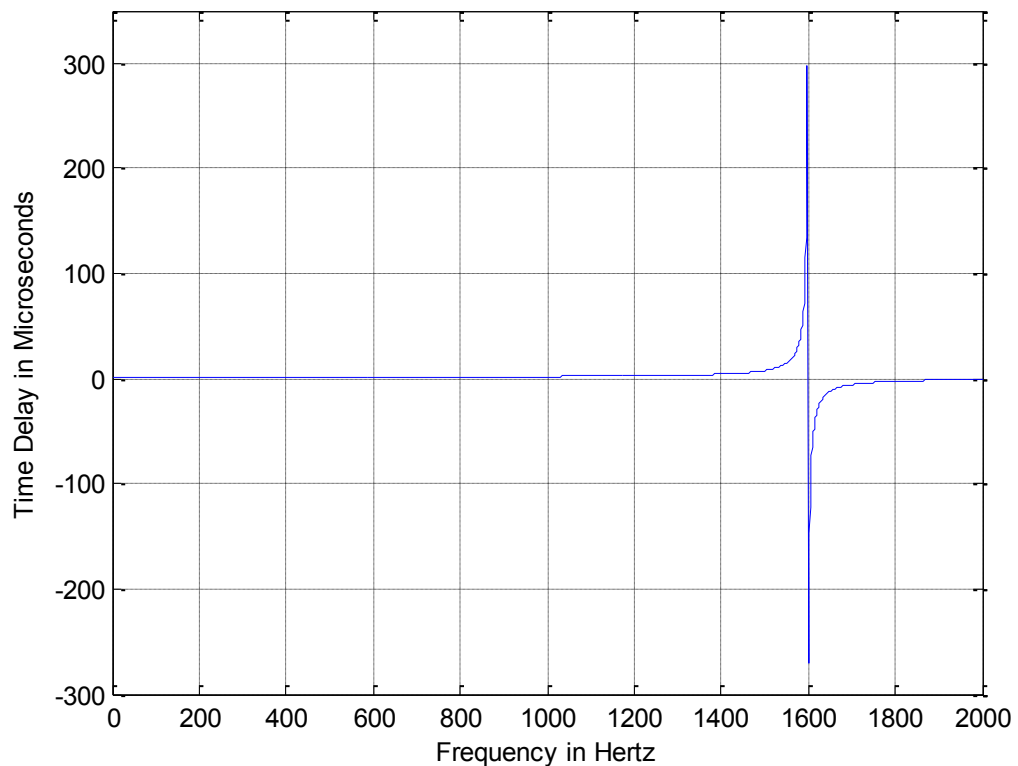


Figure.6.42: Output time delay for cutoff frequency at 1600 Hz.

### 6.4.3 Rayleigh Damping for the 5 DOF Lumped Parameter Sensor Model

The frequency response of the sensor dynamics is obtained by varying the damping based on Eq. 2.40. Damping parameter  $\beta$  ( $8.54e-6$ ) was calculated from FEA using the half power bandwidth method described in Chapter 4. For the parametric study of the damping effect, the damping parameter  $\beta$  is gradually increased from zero to the value calculated from FEA. Figures 6.43 and

6.44 show the frequency response of the sensor for the six different damping cases. The specification of the sensor was chosen based on the optimization of cutoff frequency of 134 Hz.

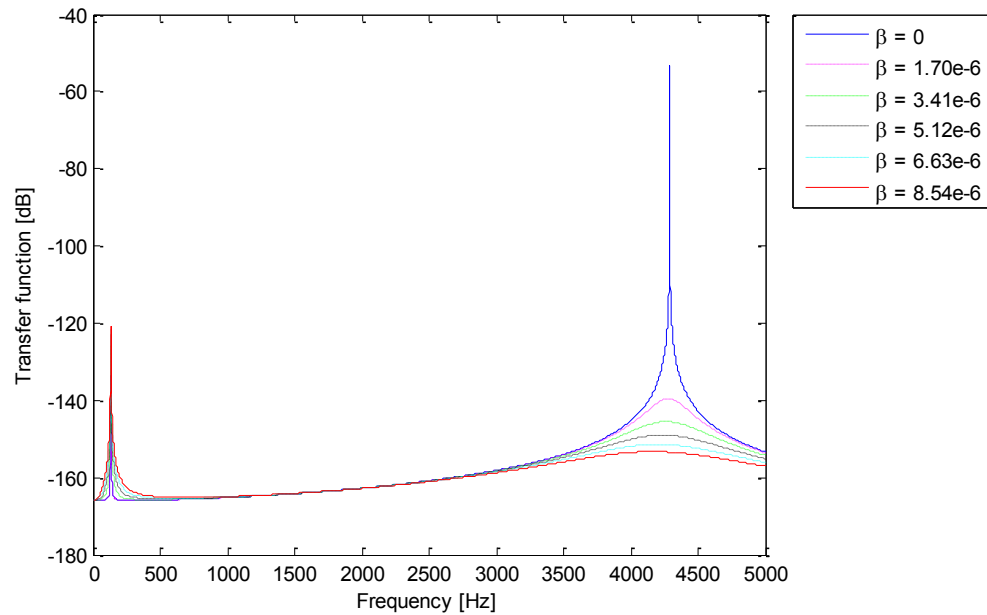


Figure 6.43: Frequency responses of the 5 DOF sensor model by varying damping coefficient.

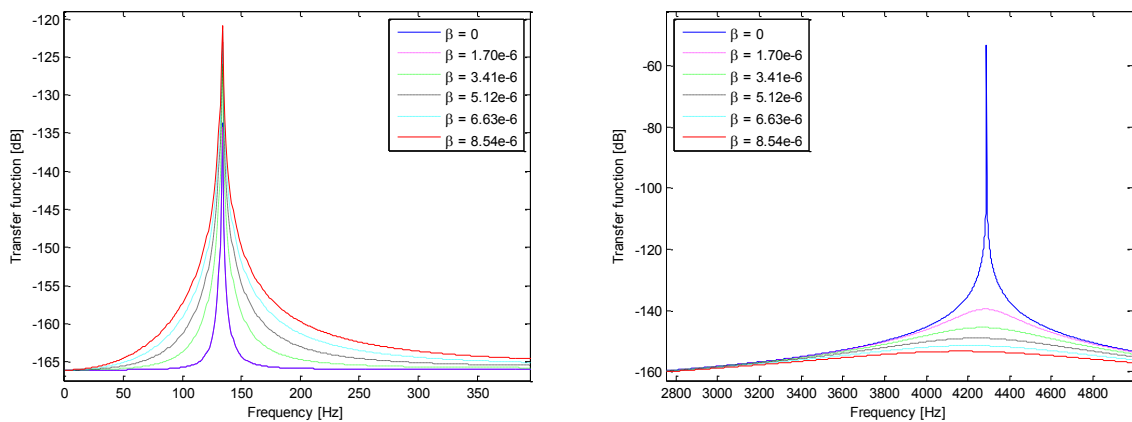


Figure 6.44: Frequency responses for the sensor when the Rayleigh damping constant  $\beta$  is varied: Left plot for the first natural frequency and Right plot for the second.

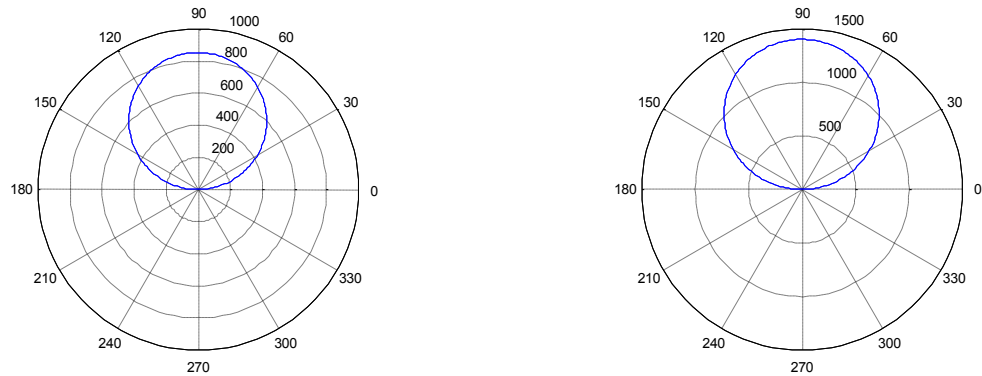


Figure 6.45: Directional sensitivity at 75 and 100 Hz from left to right plot based on the 5 DOF lumped sensor model without damping ( $\beta = 0$ ).

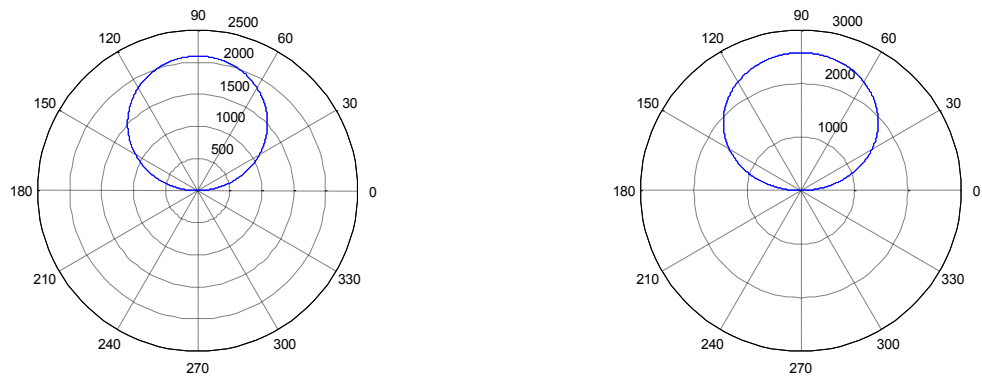


Figure 6.46: Directional sensitivity at 75 and 100 Hz from left to right plot based on the 5 DOF lumped sensor model with damping ( $\beta = 8.54e-6$ ).

Comparing the directional sensitivity via polar plot between Figures 6.45 and 6.46, it is noticeable that the damping increases the time delay within the bandwidth. This corresponds well with the time delay comparison shown in Figures 6.33; the 5 DOF lumped parameter model without damping and the FEA model. According to the simulation results of the damping effect, viscous damping (Rayleigh damping) helps to enhance the time delay. As observed with the added mass model, the damping model also needs to be a function of frequency. In Rayleigh damping, the achieved damping ratio varies as response frequency varies. The stiffness proportional term

contributes damping that is linearly proportional to response frequency and the mass proportional term contributes damping that is inversely proportional to response frequency.

Figure 6.47 illustrates how the separate mass and stiffness damping terms contribute to the overall damping ratio.

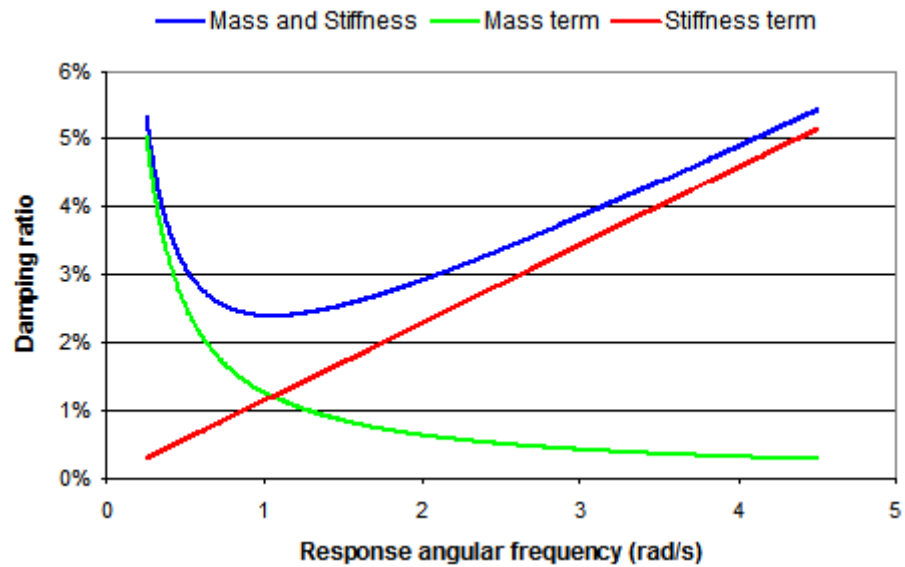


Figure 6.47: Example of Rayleigh damping ratio which varies with frequency.

## Chapter 7. Discussion

It has been shown that it is possible to use the mechanically coupled sensor inspired by the parasitoid fly, *Ormea Ochracea*, for the underwater application for the directivity search through our study. For the case of the cutoff frequency of 360 Hz from Chapter 6, the input time delay is about 2  $\mu\text{sec}$  since  $\tau_i = d\sin(\theta)/c$  where  $\tau_i$  is the input time delay,  $d$  is the length of the sensor,  $\theta$  is the incident angle of the plane sound wave, and  $c$  is the speed of sound in water. At around 350 Hz this corresponds to an output delay of 1,000  $\mu\text{sec}$  from Figure 6.34. For the cutoff frequency of 360 Hz, the input time delay can be enhanced by a factor of 500 at around 350 Hz. This is due to the strong mechanical coupling which causes the amplification of the phase difference of the sensor.

### 7.1 Signal Noise

As outlined in Chapter 3, the method for finding the directivity of the sound source should have ability to find a phase difference from  $x_1$  and  $x_2$  and this leads us to find the distance of the source. It has been shown that our sensor can be used to find the directivity of the various types of sound sources based on DSP analyses.

A basic limitation on the underwater sensors such as hydrophone performance is the electrical noise generated internally by thermal agitation in its components and in the water; this noise must not exceed the total noise for good performance. The internal noise of the hydrophone is caused by its energy dissipation mechanisms, (i.e., the electrical and mechanical dissipation factors of the transduction material, the mechanical resistance in any other moving components including mounting, and the radiation resistance). Electrical dissipation and mechanical resistance allow electrical and mechanical energy in the hydrophone to be lost as internal thermal energy, and they also allow thermal energy in the hydrophone materials to cause electrical noise. Radiation resistance differs in that it is the means by which mechanical energy in the transducer generates acoustic energy in the water, but it also allows thermal energy in the water to cause electrical noise [30]. The driving force for the thermally excited sensor is the result of collisions of surrounding fluid molecules to the hydro-acoustic sensor or the Brownian motion of the fluid. Because of the random nature of Brownian motion, it is obvious that the magnitude of this force is independent of the position along the length of the sensor. Paul and Cross (2004) showed that this force is frequency dependent and its spectral density is not white [31].

Assuming the noise in the hydro-acoustic sensor is dominated by the self-noise at the sensor, the sensitivity of the sensor in water is plotted based on FEA. Figure 7.1 shows the sensitivity plot which is obtained by two FEA simulations in water; (i) harmonic acoustically fluid-structure analysis of the sensor by shaking it, and (ii) harmonic acoustically fluid-structure analysis of the sensor by applying a plane wave. Shaking is simulated via applying acceleration to the sensor. The peak of the sensitivity appears near the resonant frequency of the sensor; hence the noise levels are lowest near this point. Base on this observation, the sensor need to be designed such that it has to be most sensitive at the resonant frequency of the sensor.

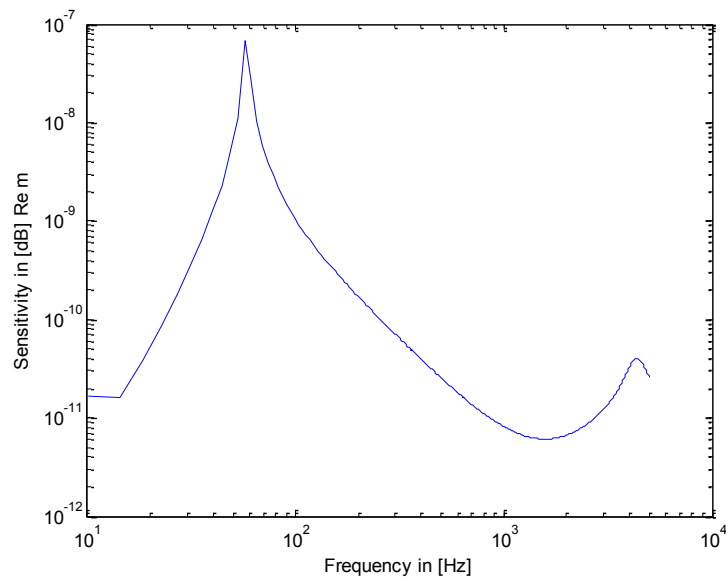


Figure 7.1: FEA Simulated Sensitivity of the Acoustic Sensor in Water.

Being the directional sensor, our sensor is sensitive to only along a specific axis while less sensitive to other axes. Our sensor can rejects more noise compared to an omni-directional sensor.

Sensor's sensitivity was analyzed in Chapter 4 in detail. Along with the acoustic sensitivity, it is important to know the lowest sound levels that can be measured with the sensor. This is usually limited by the self-noise of the sensor. Tan *et al.* (2002) observed that the predicted thermal noise floor of the *Ormia* differential microphone is 20.8 dBA while that of conventional microphone is 40.4 dBA. Tan et al. showed that the frequency response and the noise performance are substantially improved when compared to the conventional microphone due to the mechanical structure in the *Ormia* microphone [26].

### 7.1.1 Case 1: Input signal frequency is different from band-limited white noise.

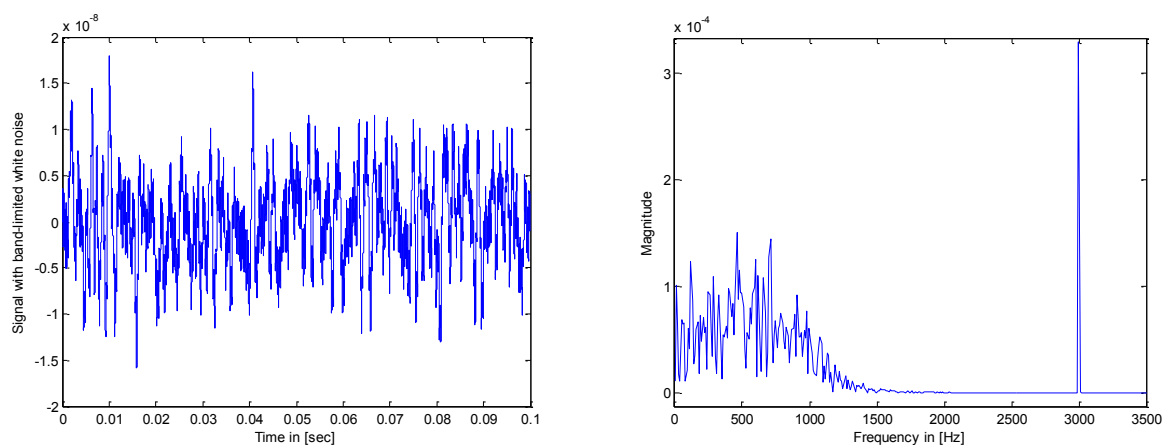


Figure 7.2: Left: Time domain representation of a modulation signal  $x_1$  with band-limited white noise. Right: Frequency domain representation of a modulation signal  $x_1$  with band-limited white noise.

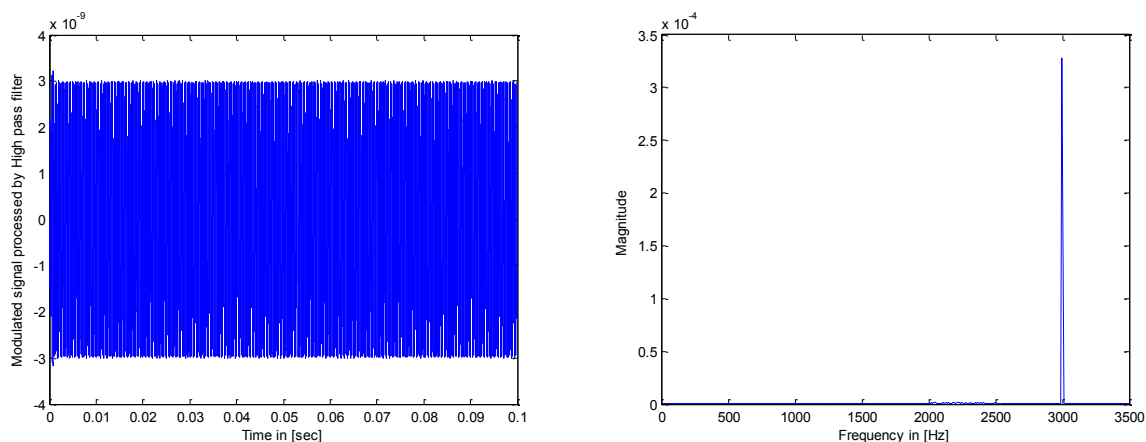


Figure 7.3: Left: Time domain representation of a signal  $x_1$  with white noise processed by high pass filter. Right: Frequency domain representation of a signal  $x_1$  with white noise processed by high pass filter.

Assuming that the data contains the band-limited white noise, we present 3 different cases to deal with the signals with noise. The output data from the sensor when a sinusoidal signal at 3000 Hz frequency is applied are shown Figure 7.2. Time representation in Figure 7.2 shows the output signal with band-limited white noise containing frequencies  $0 \sim 1000$  Hz. From this plot it looks pretty much like noise signal, however, in the frequency representation of the signal (3000 Hz) is

separated from the band-limited white noise (0 ~ 1000 Hz). The output data is then treated by high-pass filtering and the fast Fourier transform (FFT) process is applied to get Figure 7.3. Using the result of the FFT, the amplitude and phase of the displacement at the frequency of excitation is determined. High pass filtering is performed in order to remove the band-limited white noise ranging from 0 to 1000 Hz using a Butterworth filter of order 8. The cut-off frequency of this filter is set to 2000 Hz. We are then left with just the signal itself which can give us a phase difference so that the direction of the sound is decided. The output signal processed by high pass filter is shown in Figure 7.3.

### 7.1.2 Case 2: Input signal frequency is embedded in the band limited white noise.

We can also consider the case when input signal is embedded in a large amount of noise integrated within them. Usually this noise is what is called band limited white noise, i.e. a noise that affects all frequencies the same. For small amounts of noise, the signal detection is clearly not a problem. Cases 1 and 2 fall in this category. However, for large amounts of noise or low-levels of signal, Case 3, the detection becomes a nontrivial matter.

Figure 7.4 show the signal from the hydro acoustic sensor in time and frequency domains. It is seen from the figure that the sinusoidal signal of 3000 Hz is embedded in noise since the signal is of significantly bigger amplitude than the noise. The time delay for this case can easily be calculated using Eq. 3.4 as  $3.7e-5$  seconds, which corresponds to  $45^\circ$  angle of incidence.

For the signals embedded in noise, the signal-to-noise ratio (*SNR*) plays a critical. The higher the ratio, the less obtrusive the background noise is.

$$SNR = \frac{P_{signal}}{P_{noise}} = \left( \frac{A_{signal}}{A_{noise}} \right)^2 \quad (7-1)$$

where  $P$  is average power and  $A$  is root mean square (*RMS*) amplitude. Because many signals have a very wide dynamic range, *SNRs* are often expressed using the logarithmic decibel scale. In decibels, the *SNR* is defined as

$$SNR_{dB} = 10 \log_{10} \left( \frac{P_{signal}}{P_{noise}} \right) = 10 \log_{10} \left( \frac{A_{signal}}{A_{noise}} \right)^2 = 20 \log_{10} \left( \frac{A_{signal}}{A_{noise}} \right) \quad (7-2)$$

$SNR$  is usually taken to indicate an average signal-to-noise ratio, as it is possible that (near) instantaneous signal-to-noise ratios will be considerably different. The concept can be understood as normalizing the noise level to 1 (0 dB) and measuring how far the signal stands out. When the signal is constant or periodic and last long enough without changing and the noise is random, it is possible to enhance the  $SNR$  by averaging the measurement. This method is introduced for case 3.

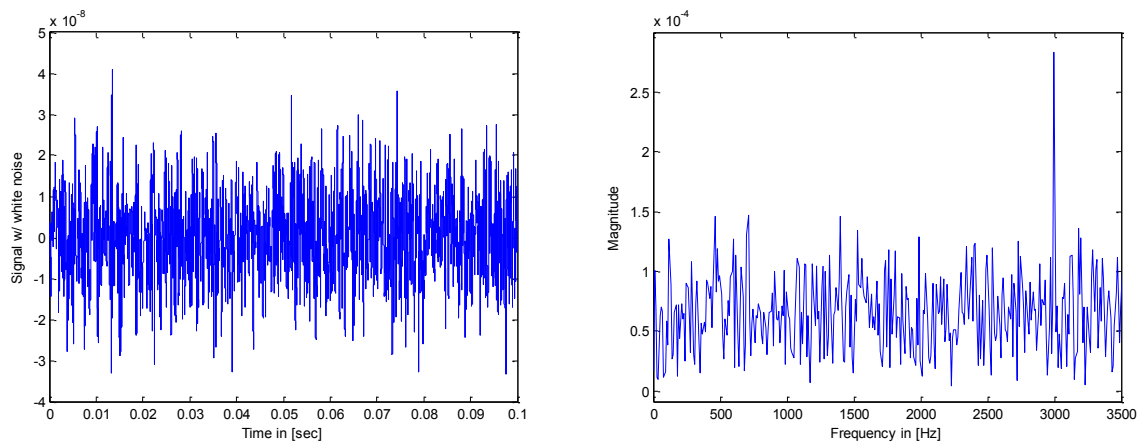


Figure 7.4: Left: Time domain representation of a signal  $x_1$  in the presence of white noise. Right: Frequency domain representation of a signal  $x_1$  in the presence of white noise.

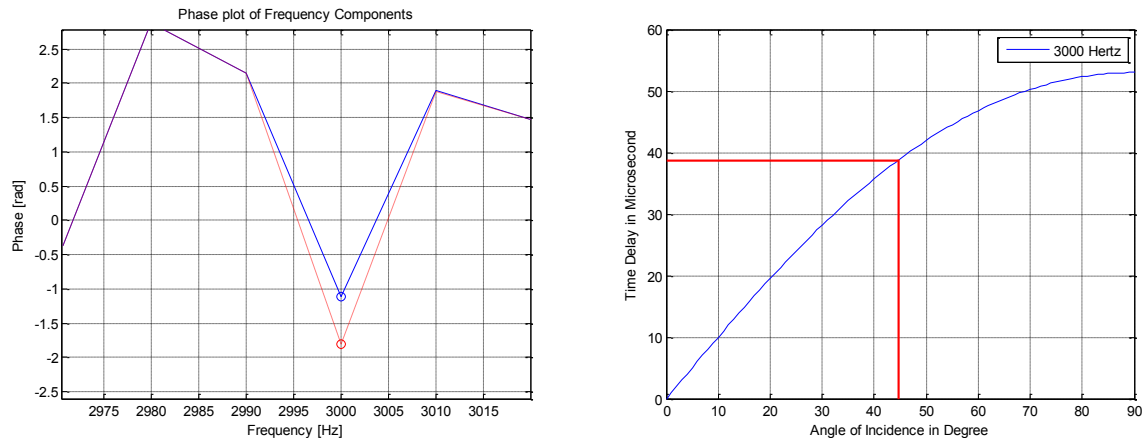


Figure 7.5: Left: Phase difference of signals  $x_1$  and  $x_2$  in the presence of white noise. Right: Time delay calculated from the phase difference at 3000 Hz.

### 7.1.3 Case 3: Input signal is smaller than white noise.

In real life, we always observe a noise in the response, the magnitude of which depends on environmental factors, such as electrical noise, thermal vibration noise of the sensor, and the surrounding sound noise. This noise limits the application of the hydro acoustic sensor.

In order to cancel the noise integrated with the signal, Active noise cancellation (ANC) can be used which creates a wave form that is the opposite of the noise so the noise is cancelled. Low frequency noise is more successfully cancelled than noise at higher frequencies, so passive noise reduction is used to reduce high frequency noise [33].

ANC method coincides with the interference-cancelling concept which is used in the communication situation. The noise integrated signal becomes not discernible. If we can pick up the correlated noise in the same environment, the noise can be cancelled by subtracting the processed correlated noise from the combined signal. This method works well for the low SNR where noise is bigger than the signal [34].

Assuming that the noise is white and the sound source continue to produce more signal data, the white-noise on the average add up to zero since the white noise is modeled as adding a normally distributed random variable with zero mean. This averaging process can ultimately extract a clean spectral signature. However, as a result, it completely removes the time domain dynamics. In other words, this would only give the averaged time domain signal [35].

The idea of spectral filtering to improve the signal detection by denoising also allows us to extract information at specific frequencies [35]. This method is similar to what has been discussed in section 3.2.3 about white noise where the frequency of interest has to be identified.

## 7.2 Effect of Rigid Body Motion of the sensor

When the sensor is placed in water to localize the source of the sound source, we also need to consider the fluid flow over the sensor or the motion of the sensor in still water. Effect of this rigid body motion of the sensor is studied as flow over immersed bodies. In this situation, the sensor is completely surrounded by the fluid and the flows are termed external flows.

Once again FEA (COMSOL) is chosen to study the effect of flow over immersed sensor since there are few known analytical solutions to the differential equation that govern the flow of Newtonian fluids. A weakly compressible Navier-Stokes module is used to solve for the pressure,  $p$ , and the velocity vector components.

The post-processing Figure 7.6 shows the velocity field, which is the absolute value of the velocity vector. In this graph notice that the flow transitions from a uniform velocity at  $x = -2.5$  and a full developed velocity profile. Arrows have been added to show the magnitude and direction of the velocity. The cross-sectional plots of the velocity along vertical lines at different positions are shown in Figure 7.7. This gives a plot in which velocity is on the  $x$ -axis and the width of the control area is on the  $y$ -axis. Each curve starting with the blue line corresponds to a given distance in the flow direction ( $x$  direction) from the left to the right direction in Figure 7.6. Notice the appearance of the vertical black lines on the original post process contour solution plot shown in Figure 7.6. These lines are the 5 cross sections and the resulting plot shows how the velocity profile develops along the main direction of the flow. Viscous effects are important inside the boundary layer whereas they are not important outside of it. The actual fluid viscosity is the same throughout; only the relative importance is different.

FEA simulation of this kind is very challenging problem due to the fact that problems involving 10,000 elements and 50,000 equations are not uncommon, COMSOL does not support frequency domain CFD simulation, time domain transient analysis requires high computing power along with the contact problem which leads to highly nonlinear problem. Besides, point-wise constraint which is used to constrain the coupling pivot in the center is not supported for transient analysis by COMSOL. For the reason, cantilever beam is used to study the effect of the rigid body motion of the sensor in water instead.

Figure 7.8 shows the  $y$ -displacement of the cantilever plate when the fluid flows over it with the normal velocity of 0.1 m/s. As shown in the figure, the end of the cantilever plate flutters which is shown as the  $y$ -displacement in time domain. For the simulation, time increment of 0.01 seconds has been used up to 10 seconds. Fluttering movement in  $y$ -direction can be regarded as unwanted noise and as long as it is smaller than the signal, our sensor can detect the directivity of the source.

The character of the flow field is a function of the shape of the body, however flows past relatively simple geometric shapes such as our sensor are expected to have less complex flow fields than flows past a complex shape objects. For the shape of our sensor, the characteristics of the flow depend strongly on parameters such as size, orientation, speed, and fluid properties. The static FEA simulation of  $5^\circ$  rotated sensor with respect to the fluid flow results in almost the identical one with  $0^\circ$  rotation model.

As a rule of thumb, flows with  $Re > 100$  are dominated by inertial effects, whereas flow with  $Re < 1$  are dominated by viscous effects. Hence flows shown in Figure 7.6 are in transition dominated by inertia and viscous effects since the calculated  $Re$  is 20 [36].

Rigid body motion of the sensor under water has been studied as flow over immersed cantilever plate. From the FEA transient analysis of the cantilever plate, the end of the cantilever plate fluttering was observed. Regarding this fluttering as unwanted noise, this becomes noise problem. As discussed in the previous section, sensor can function if the amplitude of the fluttering is smaller than the detected sound signal.

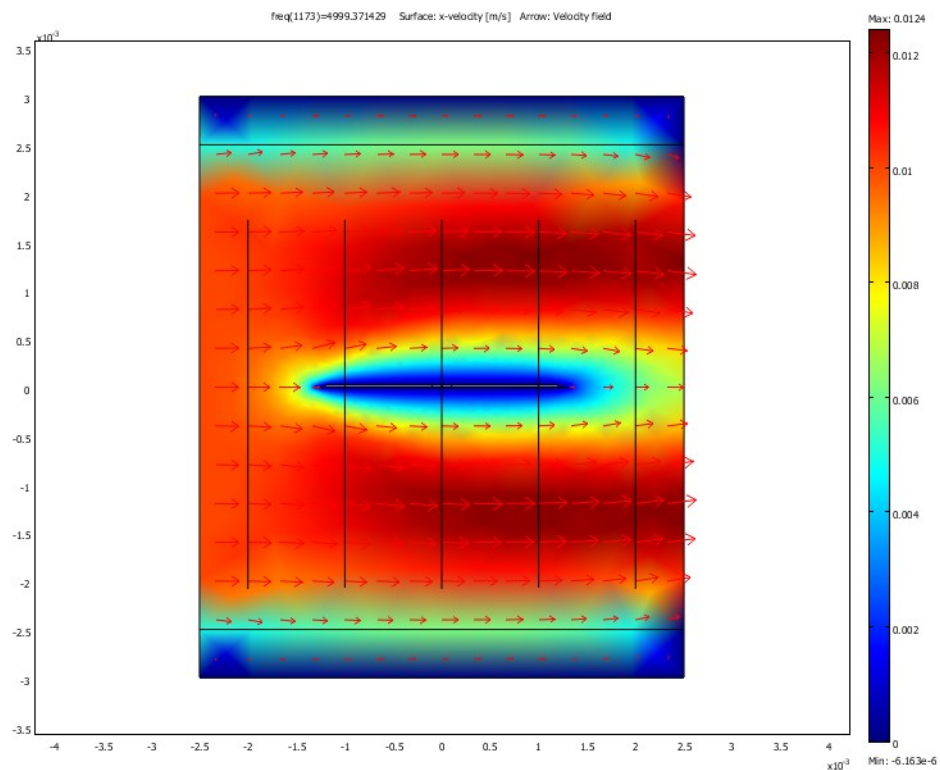


Figure 7.6: FEA simulation of the sensor in water solving weakly compressible Navier-Stokes equation.

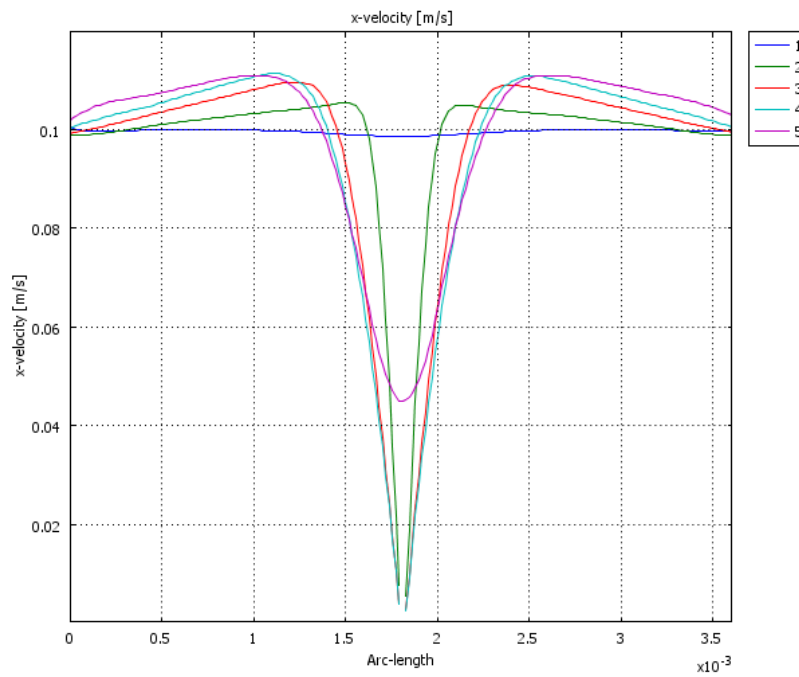


Figure 7.7:  $x$ -axis velocity at 5 vertical lines shown in Figure 7.6 from left to right order.

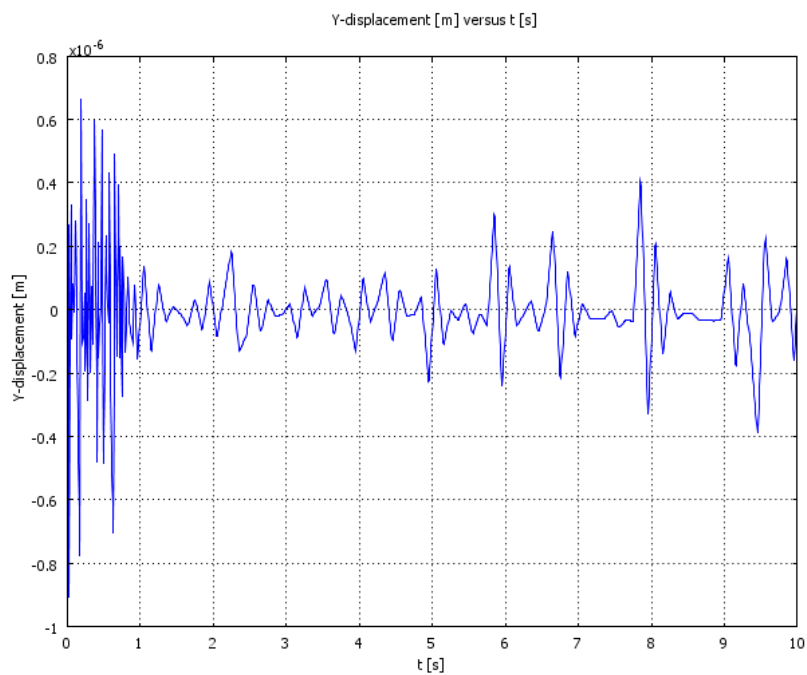


Figure 7.8: Y-displacement of the cantilever beam under normal inflow velocity of 0.1 m/s

### **7.3 Difficulties with Sound Signal Detection**

Detecting the sound signal completely to find the directivity can be a much more difficult problem than discussed in chapter 3. The difficulty arises from the inability to tell apart two identical frequency signals from different locations and when more than two noise signals are present.

### **7.4 Design Optimization (Multiple local min)**

The existence of a unique minimum for the general design error minimization problem was numerically verified by starting from different initial design values. It was seen that the final cost values converged to a single value indicating the uniqueness of the minimum. Comparing the simulation result based on the design optimization of the discrete sensor model against that of FEA result done by COMSOL proved to be agreeable each other.

It is also intrigued to take advantage of structure preservation in model reduction. Model used for the current research is rather higher order discrete model for accuracy, however if it is possible to reduce the order of the model it would be beneficial in terms of modeling and design changes. With the low order discrete model is available; it would be beneficial to implement the design optimization with more number of design parameters. In the current research, the optimization has been implemented without having the PDMS spring as design parameters. This will enhance the design optimization in the future.

When the output time delay pattern is optimized at certain frequency beginning from various initial parameter values, the final cost values do not converge to a single value, which indicates that there exist multiple local minimum points.

## Chapter 8. Conclusions and Future Research

### 8.1 Conclusion

In this research, a new design and operation methodology of a mechanically coupled hydro-acoustic sensor for directivity is presented. The sensor is designed such that there are two thin plates are coupled thus amplifies the phase difference at each end, which can be used to calculate the amplified output time delay.

For the modeling and design of the sensor, two design types are presented as well as the modeling of them based on 1. Mode-Summation, and 2. Discrete 5 DOF lumped parameter methods. Each design shares the same fundamental mechanism. Each model is used interchangeably within the scope of this research for further study since its design is flexible. FE model of the sensor is simulated and used to validate the two types of the sensor model.

The finite element method is applied to calculate the displacement of each end of the sensor impinged by plane wave due to the distance to the far field and compared to the discrete model based simulation results. This FE model is validated through the well-known published data and the fluid loading under consideration. The first and second natural frequency obtained from the discrete lumped model is validated against the FEM simulation. After validation the discrete model was implemented in a design optimization process. The obtained optimized design is then compared to the FEA model and a good agreement is shown. Our sensor can enhance the input time delay by a factor of 500, however at only low frequencies. With the current 2D design, there is a limitation to increase the coupling spring constant  $k_3$  which plays a role to increase the time delay amplification. Due to this limitation, as the frequency increases, the bandwidth of the sensor becomes narrower.

A series of analyses was performed to characterize the feasibility of the mechanically coupled sensor for underwater application in terms of parameters such as frequency range, incidence angle, underwater considerations, design parameters, and material properties.

In general there is uncertainty about the added mass due to fluid load since it is a function of many variables. However, it can be concluded that fluid loading effect is significant and varies significantly depending on many variables such as geometry, boundary conditions, and frequency. It has been shown from our FE analysis that the added mass due to fluid loading decreases the natural frequency by a factor of 50 assuming unbounded area using PML (perfectly matched layer).

Without PML, a factor of 10 reductions was observed based on the cantilever plate. At low frequencies, the added mass due to fluid loading observed to be more than high frequencies. At higher frequencies, the fluid loading appears to have less effect on the added mass which in turn has more effect on the damping. Added mass due to fluid loading decreases as frequency increases, however, damping effect on the sensor due to fluid loading increases as frequency increases. It is well known that the structure radiates acoustic damping by becoming a good vibrator at or above the critical frequency. However, our FEA study shows that the sensor adds the acoustic damping even well below the critical frequency.

It was shown that the spring constants  $k_1$ ,  $k_2$  and  $k_3$  are key factors in sensor design and performance. However, proper combination of those spring constants varies as geometry of the sensor changes. Hence the design optimization is implemented to find those parameters.

Lastly acoustic sensing via frequency-based technique shows promise in underwater sensing for directivity. Once the method of this study is proved to be valid through experimental data, this work can be used to numerically study the dynamic behavior of any underwater sensor and/or transducers in more effective way.

## 8.2 Future Research

Future research will introduce some of the features to constitute a bio-inspired low-cost hydro-acoustic sensor for directivity. First, some alternative design of the sensor will be considered for the next prototype for better performance of the sensor which can increase the bandwidth of the sensor while amplifying the high enough phase difference. At the same time, another design method will be sought after which can remove the zero crossing phenomenon. This is also related to damping control. Based on the new/alternative design of the sensor, new design optimization has to be implemented. Second, even if capacitive sensing technique has been proposed for the current work, another sensing techniques will not be overlooked which can improve the sensing capability and precision in water. Third, it is important to build and test the sensor.

Future work will concentrate on building and testing of a working model of the sensor system. Then, the modeling and optimization techniques developed in this work will be verified. These will also be used for the further improvement of the system performance.

Considering adding the torsional spring to our existing design of the sensor, the polycrystalline silicon gimbals' configuration is suggested for the part of the future work. Kudrle *et al.*, (2005)

presents a micro-mirror fabrication technique that combines the benefit of both surface and bulk micromachining to make polycrystalline silicon flexures in a gimbals' configuration [37]. By adding torsional spring at the coupling point of our 2D sensor, the coupling stiffness can be better controllable and increased, which may help to get rid of zero-crossing.

Lastly, once the sensor is built through micro-fabrication, it is possible to test the rigid body motion of the sensor by placing the sensor in flowing water as well as verify our feasibility simulation result.

## Bibliograph

- [1] Yoseph Bar-Cohen, "Biomimetics: biologically inspired technology" II ECCOMAS THEMATIC Conference on Smart Structures and Materials, Lisbon, Portugal, July 18-21, 2005.
- [2] Nima Izadi, " Bio-Inspired MEMS Aquatic Flow Sensor Arrays," Transducer Science and Technology Group of the MESA research institute, University of Twente, 2011.
- [3] M Dijkstra, and et al., "Artificial sensory hairs based on the flow sensitive receptor hairs of crickets," J. Micromech. Microeng., 2005.
- [4] "Wilcoxon Research." (<http://www.wilcoxon.com/MAST/>)
- [5] Jonas Jonsson, "Microsystems Technology for Underwater Vehicle Applications," Doctor of Philosophy Dissertation, Uppsala University, 2012.
- [6] Morse, P. M., and K. U. Ingard., "Theoretical Acoustics," McGraw Hill, New York. Pp. 418-422, 1968.
- [7] J. Clay Shipps and Bruce M. Abraham, "Vector sensors secure shore-based manufacturing plants," [www.isa.org/intech](http://www.isa.org/intech), December, 2004.
- [8] Sea Technology® Magazine Worldwide Information Leader for Marine Business, Science & Engineering, Compass Publications, Inc., 2013.
- [9] Malcolm Hawkes, "Issues in Acoustic Vector-Sensor Processing," Ph.D Dissertation, Yale University, 2000.
- [10] Robert, D., R. N. Miles, and R. R. Hoy, " Tympanal mechanics in the parasitoid fly *Ormia ochracea*: intertympanal coupling during mechanical vibration," J. Comp. Physiol. A 183: 443-452.
- [11] R. N. Miles, D. Robert, and R. R. Hoy, "Mechanically coupled ears for directional hearing in the parasitoid fly *Ormia ochracea*," J. Acoust. Soc. Am. 98 (6), December 1995.
- [12] Urick, Robert J. Principles of Underwater Sound. 3rd ed. (New York: McGraw-Hill, c1983).
- [13] S. Beeby, G. Ensell, M. Kraft, and N. White, "MEMS Mechanical Sensors," Artech House, Inc. 2004.
- [14] Walter C. Hurty, "Vibrations of Structural Systems by Component Mode Synthesis," J. Eng. Mech. Div., Proc. ASCE pp. 51-69, August 1960.

- [15] R. E. D. Bishop, "The Vibration of Frames," Proceedings of the Institution of Mechanical Engineers, 1956.
- [16] Leonard Meirovitch, "Elements of Vibration Analysis," 2<sup>nd</sup> Edition, McGraw-Hill, Inc.
- [17] R. N. Miles, "Comb Sense Microphone," United States Patent No. US 2007/0297631 A1.
- [18] Kenichi Takahata, "Advances in Micro/Nano Electromechanical Systems and Fabrication Technologies," InTech, 2013.
- [19] L. K. Baxter, "Capacitive Sensors," Copyright 6-26-00, revised 7-20-00.
- [20] Waite, A.D. Sonar for Practicing Engineers. John Wiley & Sons, 2001.
- [21] Fahy, Frank, Sound and Structural Vibration – radiation, transmission and response (Academic Press Inc., 1985).
- [22] A. Techet, "Object Impact on the Free Surface and Added Mass Effect," for 2.016 Laboratory Fall 2005 Quoted from [http://web.mit.edu/2.016/www/labs/L01\\_Added\\_Mass\\_050915.pdf](http://web.mit.edu/2.016/www/labs/L01_Added_Mass_050915.pdf).
- [23] C. E. Brennen, "A Review of Added Mass and Fluid Inertial Forces," Naval Civil Engineering Laboratory, January 1982.
- [24] M. Norton and D. Karczub, Fundamentals of Noise and Vibration Analysis for Engineers, 2nd ed. (Cambridge University Press, 2003).
- [25] Zhang, W., and Turner, K., "Frequency dependant fluid damping of micro/nano flexural resonators: Experiment, model and analysis," Sensors and Actuators, 2006.
- [26] R. N. Miles, L. Tan, S. Sundermurthy, "Design of a Biologically Inspired Directional Acoustic Sensor," Meeting of MSS Specialty Group on Battlefield Acoustic and Seismic Sensing, Magnetic and Electric Field Sensors Volume 1: Special Session Held 23 October 2001.
- [27] COMSOL® version 3.4 Acoustic User's Guide.
- [28] Andrew J. Hull, "Analysis of a Fluid-Loaded Thick Plate," NUWC-NPT Technical Report 11, 389, 1 October, 2002.
- [29] James W. M. Chon, Paul Mulvaney, and John E. Sader, "Experimental validation of theoretical models for the frequency response of atomic force microscope cantilever beams immersed in fluids," J. of Appl Phys, vol. 87, number 8, 15 April 2000.
- [30] Charles H. Sherman and John L. Butler, "Transducers and Arrays for Underwater Sound," The Underwater Acoustics Series, Springer Science+Business Media, LLC, 2007.

- [31] Paul, M. R., and M. C. Cross, "Stochastic dynamics of nanoscale mechanical oscillators immersed in a viscous fluid," *Phys. Rev. Lett.* 92, 235501, 2004.
- [33] Paul W. Zitzewitz, "The Handy Physics Answer Book," 2<sup>nd</sup> Edition, Visible Inc press, 1998.
- [34] Samuel D. Stearns, "Digital Signal Processing with Examples in MATLAB," CRC Press, 2003.
- [35] Class Notes of AMATH 582 Computational Methods for Data Analysis, University of Washington.
- [36] Bruce R. Munson, Donald F. Young, Theodore H. Okiishi, "Fundamentals of fluid mechanics," 4<sup>th</sup> Edition, John Wiley & Sons, Inc., 2002.
- [37] T.D. Kudrle, C.C. Wang, M.G. Bancu, J.C. Hsiao, A. Pareek, M. Waelti, G.A. Kirkos, T. Shone, C.D. Fung, and C.H. Mastrangelo, "Single-crystal silicon micromirror array with polysilicon flexures," *Sensors and Actuators A* 119: 559-566, 2005.
- [38] Michael R. hatch, "Vibration Simulation Using MATLAB and ANSYS," Chapman & Hall/CRC, 2001.
- [39] Fred G. Geil, "Hydrophone Techniques for Underwater Sound Pickup," *J. Audio Eng. Soc.*, Vol. 40, No. 9, 1992 September.

## Appendix A: Mathematica® File

```
(*Stiffness matrix for element 1
(15 by 15 matrix) connects nodes 1 (1,2,3) and 2 (4,5,6)*)
(*Y = 160 E9, L=0.001, b=1 e-3, h=1 e-6, A=b*h, MoI=b*h^3/12*)
theta = 0;
k1 := (Y/L) ×
{ {A × Cos[theta Degree]^2 +  $\frac{12 \times \text{MoI}}{L^2}$ ,  $\left(A - \frac{12 \times \text{MoI}}{L^2}\right) \times \text{Cos}[\text{theta Degree}] \times \text{Sin}[\text{theta Degree}]$ ,
-  $\frac{6 \times \text{MoI}}{L} \times \text{Sin}[\text{theta Degree}]$ , -  $\left(A \times \text{Cos}[\text{theta Degree}]^2 + \frac{12 \times \text{MoI}}{L^2} \times \text{Sin}[\text{theta Degree}]^2\right)$ ,
-  $\left(A - \frac{12 \times \text{MoI}}{L^2}\right) \times \text{Cos}[\text{theta Degree}] \times \text{Sin}[\text{theta Degree}]$ , -  $\frac{6 \times \text{MoI}}{L} \times \text{Sin}[\text{theta Degree}]$ ,
0, 0, 0, 0, 0, 0, 0, 0, 0, 0, 0, 0, 0, 0, 0}, {  $\left(A - \frac{12 \times \text{MoI}}{L^2}\right) \times \text{Cos}[\text{theta Degree}] \times \text{Sin}[\text{theta Degree}]$ ,
A × Sin[theta Degree]^2 +  $\frac{12 \times \text{MoI}}{L^2} \times \text{Cos}[\text{theta Degree}]^2$ ,  $\frac{6 \times \text{MoI}}{L} \times \text{Cos}[\text{theta Degree}]$ ,
-  $\left(A - \frac{12 \times \text{MoI}}{L^2}\right) \times \text{Cos}[\text{theta Degree}] \times \text{Sin}[\text{theta Degree}]$ ,
-  $\left(A \times \text{Sin}[\text{theta Degree}]^2 + \frac{12 \times \text{MoI}}{L^2} \times \text{Cos}[\text{theta Degree}]^2\right)$ ,
 $\frac{6 \times \text{MoI}}{L} \times \text{Cos}[\text{theta Degree}]$ , 0, 0, 0, 0, 0, 0, 0, 0, 0, 0, 0, 0, 0}, { -  $\frac{6 \times \text{MoI}}{L} \times \text{Sin}[\text{theta Degree}]$ ,
 $\frac{6 \times \text{MoI}}{L} \times \text{Cos}[\text{theta Degree}]$ , 4 × MoI,  $\frac{6 \times \text{MoI}}{L} \times \text{Sin}[\text{theta Degree}]$ ,
-  $\frac{6 \times \text{MoI}}{L} \times \text{Cos}[\text{theta Degree}]$ , 2 × MoI, 0, 0, 0, 0, 0, 0, 0, 0, 0, 0, 0},
{ -  $\left(A \times \text{Cos}[\text{theta Degree}]^2 + \frac{12 \times \text{MoI}}{L^2} \times \text{Sin}[\text{theta Degree}]^2\right)$ ,  $\frac{6 \times \text{MoI}}{L} \times \text{Cos}[\text{theta Degree}]$ ,
 $\frac{6 \times \text{MoI}}{L} \times \text{Sin}[\text{theta Degree}]$ , A × Cos[theta Degree]^2 +  $\frac{12 \times \text{MoI}}{L^2} \times \text{Sin}[\text{theta Degree}]^2$ ,
 $\left(A - \frac{12 \times \text{MoI}}{L^2}\right) \times \text{Cos}[\text{theta Degree}] \times \text{Sin}[\text{theta Degree}]$ ,  $\frac{6 \times \text{MoI}}{L} \times \text{Sin}[\text{theta Degree}]$ ,
0, 0, 0, 0, 0, 0, 0, 0, 0, 0, 0, 0, 0}, { -  $\left(A - \frac{12 \times \text{MoI}}{L^2}\right) \times \text{Cos}[\text{theta Degree}] \times \text{Sin}[\text{theta Degree}]$ ,
-  $\left(A \times \text{Sin}[\text{theta Degree}]^2 + \frac{12 \times \text{MoI}}{L^2} \times \text{Cos}[\text{theta Degree}]^2\right)$ ,
-  $\frac{6 \times \text{MoI}}{L} \times \text{Cos}[\text{theta Degree}]$ ,  $\left(A - \frac{12 \times \text{MoI}}{L^2}\right) \times \text{Cos}[\text{theta Degree}] \times \text{Sin}[\text{theta Degree}]$ ,
A × Sin[theta Degree]^2 +  $\frac{12 \times \text{MoI}}{L^2} \times \text{Cos}[\text{theta Degree}]^2$ , -  $\frac{6 \times \text{MoI}}{L} \times \text{Cos}[\text{theta Degree}]$ ,
0, 0, 0, 0, 0, 0, 0, 0, 0, 0, 0}, { -  $\frac{6 \times \text{MoI}}{L} \times \text{Sin}[\text{theta Degree}]$ ,
 $\frac{6 \times \text{MoI}}{L} \times \text{Cos}[\text{theta Degree}]$ , 2 × MoI,  $\frac{6 \times \text{MoI}}{L} \times \text{Sin}[\text{theta Degree}]$ ,
-  $\frac{6 \times \text{MoI}}{L} \times \text{Cos}[\text{theta Degree}]$ , 4 × MoI, 0, 0, 0, 0, 0, 0, 0, 0, 0, 0},
{0, 0, 0, 0, 0, 0, 0, 0, 0, 0, 0, 0, 0, 0, 0}, {0, 0, 0, 0, 0, 0, 0, 0, 0, 0, 0, 0, 0, 0, 0},
{0, 0, 0, 0, 0, 0, 0, 0, 0, 0, 0, 0, 0, 0, 0}, {0, 0, 0, 0, 0, 0, 0, 0, 0, 0, 0, 0, 0, 0, 0},
{0, 0, 0, 0, 0, 0, 0, 0, 0, 0, 0, 0, 0, 0, 0}, {0, 0, 0, 0, 0, 0, 0, 0, 0, 0, 0, 0, 0, 0, 0},
{0, 0, 0, 0, 0, 0, 0, 0, 0, 0, 0, 0, 0, 0, 0}} (*//MatrixForm*);
```

```

(*Stiffness matrix for element 2
(15 by 15 matrix) connect nodes 1 (1,2,3) and 3 (7,8,9)*)
thetal = 180;
k2 := (Y/L) * { {A * Cos[thetal Degree]^2 + 12 * MoI / L^2,
(A - 12 * MoI / L^2) * Cos[thetal Degree] * Sin[thetal Degree], - 6 * MoI / L * Sin[thetal Degree],
0, 0, 0, - (A * Cos[thetal Degree]^2 + 12 * MoI / L^2 * Sin[thetal Degree]^2),
- (A - 12 * MoI / L^2) * Cos[thetal Degree] * Sin[thetal Degree], - 6 * MoI / L * Sin[thetal Degree],
0, 0, 0, 0, 0, 0}, { (A - 12 * MoI / L^2) * Cos[thetal Degree] * Sin[thetal Degree],
A * Sin[thetal Degree]^2 + 12 * MoI / L^2 * Cos[thetal Degree]^2, 6 * MoI / L * Cos[thetal Degree],
0, 0, 0, - (A - 12 * MoI / L^2) * Cos[thetal Degree] * Sin[thetal Degree],
- (A * Sin[thetal Degree]^2 + 12 * MoI / L^2 * Cos[thetal Degree]^2),
6 * MoI / L * Cos[thetal Degree], 0, 0, 0, 0, 0, 0},
{- 6 * MoI / L * Sin[thetal Degree], 6 * MoI / L * Cos[thetal Degree], 4 * MoI, 0, 0, 0,
6 * MoI / L * Sin[thetal Degree], - 6 * MoI / L * Cos[thetal Degree], 2 * MoI, 0, 0, 0, 0, 0, 0},
{0, 0, 0, 0, 0, 0, 0, 0, 0, 0, 0, 0, 0, 0, 0}, {0, 0, 0, 0, 0, 0, 0, 0, 0, 0, 0, 0, 0, 0, 0},
{0, 0, 0, 0, 0, 0, 0, 0, 0, 0, 0, 0, 0, 0, 0},
{- (A * Cos[thetal Degree]^2 + 12 * MoI / L^2 * Sin[thetal Degree]^2),
6 * MoI / L * Cos[thetal Degree], 6 * MoI / L * Sin[thetal Degree], 0,
0, 0, A * Cos[thetal Degree]^2 + 12 * MoI / L^2 * Sin[thetal Degree]^2,
(A - 12 * MoI / L^2) * Cos[thetal Degree] * Sin[thetal Degree], 6 * MoI / L * Sin[thetal Degree],
0, 0, 0, 0, 0, 0}, {- (A - 12 * MoI / L^2) * Cos[thetal Degree] * Sin[thetal Degree],
- (A * Sin[thetal Degree]^2 + 12 * MoI / L^2 * Cos[thetal Degree]^2),
- 6 * MoI / L * Cos[thetal Degree], 0, 0, 0,
(A - 12 * MoI / L^2) * Cos[thetal Degree] * Sin[thetal Degree], A * Sin[thetal Degree]^2 +
12 * MoI / L^2 * Cos[thetal Degree]^2, - 6 * MoI / L * Cos[thetal Degree], 0, 0, 0, 0, 0, 0},
{- 6 * MoI / L * Sin[thetal Degree], 6 * MoI / L * Cos[thetal Degree], 2 * MoI, 0, 0, 0,
6 * MoI / L * Sin[thetal Degree], - 6 * MoI / L * Cos[thetal Degree], 4 * MoI, 0, 0, 0, 0, 0, 0},
{0, 0, 0, 0, 0, 0, 0, 0, 0, 0, 0, 0, 0, 0, 0}, {0, 0, 0, 0, 0, 0, 0, 0, 0, 0, 0, 0, 0, 0, 0},

```

```

{0, 0, 0, 0, 0, 0, 0, 0, 0, 0, 0, 0, 0, 0, 0},
{0, 0, 0, 0, 0, 0, 0, 0, 0, 0, 0, 0, 0, 0, 0}, {0, 0, 0, 0, 0, 0, 0, 0, 0, 0, 0, 0, 0, 0, 0},
{0, 0, 0, 0, 0, 0, 0, 0, 0, 0, 0, 0, 0, 0, 0} (//MatrixForm*);

(*Stiffness matrix for element 3
(15 by 15 matrix) connects nodes 2 (4, 5, 6) and 4 (10, 11, 12)*)
(*Yp = 8.7 E6, Lp=1 e-4, bp=1 e-3, hp=2 e-6, Ap=bp*hp, MoIp=bp*hp^3/12*)
theta = 0;
k3 := (Yp / Lp) ×
{ {0, 0, 0, 0, 0, 0, 0, 0, 0, 0, 0, 0, 0, 0, 0}, {0, 0, 0, 0, 0, 0, 0, 0, 0, 0, 0, 0, 0, 0, 0},
{0, 0, 0, 0, 0, 0, 0, 0, 0, 0, 0, 0, 0, 0, 0}, {0, 0, 0, Ap × Cos[theta Degree]^2 +  $\frac{12 \times \text{MoIp}}{\text{Lp}^2}$ ,
 $\left(\text{Ap} - \frac{12 \times \text{MoIp}}{\text{Lp}^2}\right) \times \text{Cos}[\text{theta Degree}] \times \text{Sin}[\text{theta Degree}]$ ,  $-\frac{6 \times \text{MoIp}}{\text{Lp}} \times \text{Sin}[\text{theta Degree}]$ ,
0, 0, 0,  $-\left(\text{Ap} \times \text{Cos}[\text{theta Degree}]^2 + \frac{12 \times \text{MoIp}}{\text{Lp}^2} \times \text{Sin}[\text{theta Degree}]^2\right)$ ,
 $-\left(\text{Ap} - \frac{12 \times \text{MoIp}}{\text{Lp}^2}\right) \times \text{Cos}[\text{theta Degree}] \times \text{Sin}[\text{theta Degree}]$ ,  $-\frac{6 \times \text{MoIp}}{\text{Lp}} \times \text{Sin}[\text{theta Degree}]$ ,
0, 0, 0}, {0, 0, 0,  $\left(\text{Ap} - \frac{12 \times \text{MoIp}}{\text{Lp}^2}\right) \times \text{Cos}[\text{theta Degree}] \times \text{Sin}[\text{theta Degree}]$ ,
Ap × Sin[theta Degree]^2 +  $\frac{12 \times \text{MoIp}}{\text{Lp}^2} \times \text{Cos}[\text{theta Degree}]^2$ ,  $\frac{6 \times \text{MoIp}}{\text{Lp}} \times \text{Cos}[\text{theta Degree}]$ ,
0, 0, 0,  $-\left(\text{Ap} - \frac{12 \times \text{MoIp}}{\text{Lp}^2}\right) \times \text{Cos}[\text{theta Degree}] \times \text{Sin}[\text{theta Degree}]$ ,
 $-\left(\text{Ap} \times \text{Sin}[\text{theta Degree}]^2 + \frac{12 \times \text{MoIp}}{\text{Lp}^2} \times \text{Cos}[\text{theta Degree}]^2\right)$ ,  $\frac{6 \times \text{MoIp}}{\text{Lp}} \times \text{Cos}[\text{theta Degree}]$ ,
0, 0, 0}, {0, 0, 0,  $-\frac{6 \times \text{MoIp}}{\text{Lp}} \times \text{Sin}[\text{theta Degree}]$ ,  $\frac{6 \times \text{MoIp}}{\text{Lp}} \times \text{Cos}[\text{theta Degree}]$ , 4 × MoIp,
 $\frac{6 \times \text{MoIp}}{\text{Lp}} \times \text{Sin}[\text{theta Degree}]$ , 0, 0, 0,  $-\frac{6 \times \text{MoIp}}{\text{Lp}} \times \text{Cos}[\text{theta Degree}]$ , 2 × MoIp, 0, 0, 0},
{0, 0, 0, 0, 0, 0, 0, 0, 0, 0, 0, 0, 0, 0, 0}, {0, 0, 0, 0, 0, 0, 0, 0, 0, 0, 0, 0, 0, 0, 0},
{0, 0, 0, 0, 0, 0, 0, 0, 0, 0, 0, 0, 0, 0, 0},
{0, 0, 0,  $-\left(\text{Ap} \times \text{Cos}[\text{theta Degree}]^2 + \frac{12 \times \text{MoIp}}{\text{Lp}^2} \times \text{Sin}[\text{theta Degree}]^2\right)$ ,
 $\frac{6 \times \text{MoIp}}{\text{Lp}} \times \text{Cos}[\text{theta Degree}]$ ,  $\frac{6 \times \text{MoIp}}{\text{Lp}} \times \text{Sin}[\text{theta Degree}]$ , 0, 0, 0,
Ap × Cos[theta Degree]^2 +  $\frac{12 \times \text{MoIp}}{\text{Lp}^2} \times \text{Sin}[\text{theta Degree}]^2$ ,  $\left(\text{Ap} - \frac{12 \times \text{MoIp}}{\text{Lp}^2}\right) \times$ 
Cos[theta Degree] × Sin[theta Degree],  $\frac{6 \times \text{MoIp}}{\text{Lp}} \times \text{Sin}[\text{theta Degree}]$ , 0, 0, 0},
{0, 0, 0,  $-\left(\text{Ap} - \frac{12 \times \text{MoIp}}{\text{Lp}^2}\right) \times \text{Cos}[\text{theta Degree}] \times \text{Sin}[\text{theta Degree}]$ ,
 $-\left(\text{Ap} \times \text{Sin}[\text{theta Degree}]^2 + \frac{12 \times \text{MoIp}}{\text{Lp}^2} \times \text{Cos}[\text{theta Degree}]^2\right)$ ,  $-\frac{6 \times \text{MoIp}}{\text{Lp}} \times$ 
Cos[theta Degree], 0, 0, 0,  $\left(\text{Ap} - \frac{12 \times \text{MoIp}}{\text{Lp}^2}\right) \times \text{Cos}[\text{theta Degree}] \times \text{Sin}[\text{theta Degree}]$ ,
Ap × Sin[theta Degree]^2 +  $\frac{12 \times \text{MoIp}}{\text{Lp}^2} \times \text{Cos}[\text{theta Degree}]^2$ ,  $-\frac{6 \times \text{MoIp}}{\text{Lp}} \times \text{Cos}[\text{theta Degree}]$ ,

```

```

0, 0, 0}, {0, 0, 0, -\frac{6 \times \text{MoIp}}{\text{Lp}} \times \text{Sin}[\text{theta Degree}], \frac{6 \times \text{MoIp}}{\text{Lp}} \times \text{Cos}[\text{theta Degree}], 2 \times \text{MoIp},
\frac{6 \times \text{MoIp}}{\text{Lp}} \times \text{Sin}[\text{theta Degree}], 0, 0, 0, -\frac{6 \times \text{MoIp}}{\text{Lp}} \times \text{Cos}[\text{theta Degree}], 4 \times \text{MoIp}, 0, 0, 0},
{0, 0, 0, 0, 0, 0, 0, 0, 0, 0, 0, 0, 0, 0, 0}, {0, 0, 0, 0, 0, 0, 0, 0, 0, 0, 0, 0, 0, 0, 0},
{0, 0, 0, 0, 0, 0, 0, 0, 0, 0, 0, 0, 0, 0, 0}>(*//MatrixForm*);

```

(\*Stiffness matrix for element 4

(15 by 15 matrix) connect nodes 3 (7,8,9) and 5 (13,14,15)\*)

thetal = 180;

k<sub>4</sub> := (Yp / Lp) ×

```

{0, 0, 0, 0, 0, 0, 0, 0, 0, 0, 0, 0, 0, 0, 0}, {0, 0, 0, 0, 0, 0, 0, 0, 0, 0, 0, 0, 0, 0, 0},
{0, 0, 0, 0, 0, 0, 0, 0, 0, 0, 0, 0, 0, 0, 0}, {0, 0, 0, 0, 0, 0, 0, 0, 0, 0, 0, 0, 0, 0, 0},
{0, 0, 0, 0, 0, 0, 0, 0, 0, 0, 0, 0, 0, 0, 0}, {0, 0, 0, 0, 0, 0, 0, 0, 0, 0, 0, 0, 0, 0, 0},
{0, 0, 0, 0, 0, 0, Ap \times \text{Cos}[\text{thetal Degree}]^2 + \frac{12 \times \text{MoIp}}{\text{Lp}^2}, \left( \text{Ap} - \frac{12 \times \text{MoIp}}{\text{Lp}^2} \right) \times
\text{Cos}[\text{thetal Degree}] \times \text{Sin}[\text{thetal Degree}], -\frac{6 \times \text{MoIp}}{\text{Lp}} \times \text{Sin}[\text{thetal Degree}], 0, 0, 0,
-\left( \text{Ap} \times \text{Cos}[\text{thetal Degree}]^2 + \frac{12 \times \text{MoIp}}{\text{Lp}^2} \times \text{Sin}[\text{thetal Degree}]^2 \right), -\left( \text{Ap} - \frac{12 \times \text{MoIp}}{\text{Lp}^2} \right) \times
\text{Cos}[\text{thetal Degree}] \times \text{Sin}[\text{thetal Degree}], -\frac{6 \times \text{MoIp}}{\text{Lp}} \times \text{Sin}[\text{thetal Degree}]},
{0, 0, 0, 0, 0, 0, \left( \text{Ap} - \frac{12 \times \text{MoIp}}{\text{Lp}^2} \right) \times \text{Cos}[\text{thetal Degree}] \times \text{Sin}[\text{thetal Degree}],
\text{Ap} \times \text{Sin}[\text{thetal Degree}]^2 + \frac{12 \times \text{MoIp}}{\text{Lp}^2} \times \text{Cos}[\text{thetal Degree}]^2, \frac{6 \times \text{MoIp}}{\text{Lp}} \times \text{Cos}[\text{thetal Degree}],
0, 0, 0, 0 - \left( \text{Ap} - \frac{12 \times \text{MoIp}}{\text{Lp}^2} \right) \times \text{Cos}[\text{thetal Degree}] \times \text{Sin}[\text{thetal Degree}],
-\left( \text{Ap} \times \text{Sin}[\text{thetal Degree}]^2 + \frac{12 \times \text{MoIp}}{\text{Lp}^2} \times \text{Cos}[\text{thetal Degree}]^2 \right),
\frac{6 \times \text{MoIp}}{\text{Lp}} \times \text{Cos}[\text{thetal Degree}]}, {0, 0, 0, 0, 0, 0, -\frac{6 \times \text{MoIp}}{\text{Lp}} \times \text{Sin}[\text{thetal Degree}],
\frac{6 \times \text{MoIp}}{\text{Lp}} \times \text{Cos}[\text{thetal Degree}], 4 \times \text{MoIp}, 0, 0, 0, \frac{6 \times \text{MoIp}}{\text{Lp}} \times \text{Sin}[\text{thetal Degree}],
-\frac{6 \times \text{MoIp}}{\text{Lp}} \times \text{Cos}[\text{thetal Degree}], 2 \times \text{MoIp}}, {0, 0, 0, 0, 0, 0, 0, 0, 0, 0, 0, 0, 0, 0, 0},
{0, 0, 0, 0, 0, 0, 0, 0, 0, 0, 0, 0, 0, 0, 0}, {0, 0, 0, 0, 0, 0, 0, 0, 0, 0, 0, 0, 0, 0, 0},
{0, 0, 0, 0, 0, 0, -\left( \text{Ap} \times \text{Cos}[\text{thetal Degree}]^2 + \frac{12 \times \text{MoIp}}{\text{Lp}^2} \times \text{Sin}[\text{thetal Degree}]^2 \right),
\frac{6 \times \text{MoIp}}{\text{Lp}} \times \text{Cos}[\text{thetal Degree}], \frac{6 \times \text{MoIp}}{\text{Lp}} \times \text{Sin}[\text{thetal Degree}], 0, 0, 0,
\text{Ap} \times \text{Cos}[\text{thetal Degree}]^2 + \frac{12 \times \text{MoIp}}{\text{Lp}^2} \times \text{Sin}[\text{thetal Degree}]^2, \left( \text{Ap} - \frac{12 \times \text{MoIp}}{\text{Lp}^2} \right) \times
\text{Cos}[\text{thetal Degree}] \times \text{Sin}[\text{thetal Degree}], \frac{6 \times \text{MoIp}}{\text{Lp}} \times \text{Sin}[\text{thetal Degree}]},
{0, 0, 0, 0, 0, 0, -\left( \text{Ap} - \frac{12 \times \text{MoIp}}{\text{Lp}^2} \right) \times \text{Cos}[\text{thetal Degree}] \times \text{Sin}[\text{thetal Degree}],

```

$$\begin{aligned}
& - \left( A_p \times \sin[\text{theta1 Degree}]^2 + \frac{12 \times \text{MoIp}}{L_p^2} \times \cos[\text{theta1 Degree}]^2 \right), \\
& - \frac{6 \times \text{MoIp}}{L_p} \times \cos[\text{theta1 Degree}], 0, 0, 0, \left( A_p - \frac{12 \times \text{MoIp}}{L_p^2} \right) \times \cos[\text{theta1 Degree}] \times \\
& \sin[\text{theta1 Degree}], A_p \times \sin[\text{theta1 Degree}]^2 + \frac{12 \times \text{MoIp}}{L_p^2} \times \cos[\text{theta1 Degree}]^2, \\
& - \frac{6 \times \text{MoIp}}{L_p} \times \cos[\text{theta1 Degree}], \{0, 0, 0, 0, 0, 0, -\frac{6 \times \text{MoIp}}{L_p} \times \sin[\text{theta1 Degree}], \\
& \frac{6 \times \text{MoIp}}{L_p} \times \cos[\text{theta1 Degree}], 2 \times \text{MoIp}, 0, 0, 0, \frac{6 \times \text{MoIp}}{L_p} \times \sin[\text{theta1 Degree}], \\
& - \frac{6 \times \text{MoIp}}{L_p} \times \cos[\text{theta1 Degree}], 4 \times \text{MoIp}\} \text{//MatrixForm*};
\end{aligned}$$

(\*Mass matrix for element 1 (15 by 15 matrix) connects nodes 1 (1,2,3) and 2 (4,5,6)\*)  
(\*rho=2320, Y = 160 E9, L=0.001, b=1e-3, h=1e-6, A=b\*h, MoI=b\*h^3/12\*)  
theta = 0;

$$\begin{aligned}
m_1 & := (\text{rho} \times A \times L / 6) \times \left\{ \{2, 0, 0, 1, 0, 0\}, \left\{0, \frac{156}{70}, \frac{22 \times L}{70}, 0, \frac{54}{70}, -\frac{13 \times L}{70}\right\}, \right. \\
& \left\{0, \frac{22 \times L}{70}, \frac{4 \times L^2}{70}, 0, \frac{13 \times L}{70}, -\frac{3 \times L^2}{70}\right\}, \{1, 0, 0, 2, 0, 0\}, \left\{0, \frac{54}{70}, \frac{13 \times L}{70}, 0, \right. \\
& \left. \frac{156}{70}, -\frac{22 \times L}{70}\right\}, \left\{0, -\frac{13 \times L}{70}, -\frac{3 \times L^2}{70}, 0, -\frac{22 \times L}{70}, \frac{4 \times L^2}{70}\right\} \text{//MatrixForm*}; \\
m_t & := \{\{\cos[\text{theta Degree}], \sin[\text{theta Degree}], 0, 0, 0, 0\}, \\
& \{-\sin[\text{theta Degree}], \cos[\text{theta Degree}], 0, 0, 0, 0\}, \\
& \{0, 0, 1, 0, 0, 0\}, \{0, 0, 0, \cos[\text{theta Degree}], \sin[\text{theta Degree}], 0\}, \\
& \{0, 0, 0, -\sin[\text{theta Degree}], \cos[\text{theta Degree}], 0\}, \{0, 0, 0, 0, 0, 1\} \text{//MatrixForm*} \\
m_{t1} & := \text{Transpose}[\{\{\cos[\text{theta Degree}], \sin[\text{theta Degree}], 0, 0, 0, 0\}, \\
& \{-\sin[\text{theta Degree}], \cos[\text{theta Degree}], 0, 0, 0, 0\}, \{0, 0, 1, 0, 0, 0\}, \\
& \{0, 0, 0, \cos[\text{theta Degree}], \sin[\text{theta Degree}], 0\}, \{0, 0, 0, -\sin[\text{theta Degree}], \\
& \cos[\text{theta Degree}], 0\}, \{0, 0, 0, 0, 0, 1\} \} \text{//MatrixForm*} \\
M_1 & = m_{t1} \cdot m_1 \cdot m_t \text{//MatrixForm*}; \\
GM_1 & := \left\{ \left\{ \frac{A L \text{rho}}{3}, 0, 0, \frac{A L \text{rho}}{6}, 0, 0, 0, 0, 0, 0, 0, 0, 0, 0, 0, 0 \right\}, \right. \\
& \left\{ 0, \frac{13 A L \text{rho}}{35}, \frac{11}{210} A L^2 \text{rho}, 0, \frac{9 A L \text{rho}}{70}, -\frac{13}{420} A L^2 \text{rho}, 0, 0, 0, 0, 0, 0, 0, 0, 0, 0 \right\}, \\
& \left\{ 0, \frac{11}{210} A L^2 \text{rho}, \frac{1}{105} A L^3 \text{rho}, 0, \frac{13}{420} A L^2 \text{rho}, -\frac{1}{140} A L^3 \text{rho}, 0, 0, 0, 0, 0, 0, 0, 0, 0, 0 \right\}, \\
& \left\{ \frac{A L \text{rho}}{6}, 0, 0, \frac{A L \text{rho}}{3}, 0, 0, 0, 0, 0, 0, 0, 0, 0, 0, 0, 0 \right\}, \\
& \left\{ 0, \frac{9 A L \text{rho}}{70}, \frac{13}{420} A L^2 \text{rho}, 0, \frac{13 A L \text{rho}}{35}, -\frac{11}{210} A L^2 \text{rho}, 0, 0, 0, 0, 0, 0, 0, 0, 0, 0 \right\}, \left\{ 0, \right. \\
& \left. -\frac{13}{420} A L^2 \text{rho}, -\frac{1}{140} A L^3 \text{rho}, 0, -\frac{11}{210} A L^2 \text{rho}, \frac{1}{105} A L^3 \text{rho}, 0, 0, 0, 0, 0, 0, 0, 0, 0, 0 \right\}, \\
& \{0, 0, 0, 0, 0, 0, 0, 0, 0, 0, 0, 0, 0, 0, 0, 0\}, \{0, 0, 0, 0, 0, 0, 0, 0, 0, 0, 0, 0, 0, 0, 0, 0\}, \\
& \{0, 0, 0, 0, 0, 0, 0, 0, 0, 0, 0, 0, 0, 0, 0, 0\}, \{0, 0, 0, 0, 0, 0, 0, 0, 0, 0, 0, 0, 0, 0, 0, 0\}, \\
& \{0, 0, 0, 0, 0, 0, 0, 0, 0, 0, 0, 0, 0, 0, 0, 0\}, \{0, 0, 0, 0, 0, 0, 0, 0, 0, 0, 0, 0, 0, 0, 0, 0\}, \\
& \{0, 0, 0, 0, 0, 0, 0, 0, 0, 0, 0, 0, 0, 0, 0, 0\} \text{//MatrixForm*};
\end{aligned}$$





```

(*Mass matrix for element 4
(15 by 15 matrix) connects nodes 3 (7,8,9) and 5 (13,14,15)*)
(*rhop=483.1081, Yp = 8.7E6, Lp=1e-4, bp=1e-3, hp=2e-6, Ap=bp*hp, MoIp=bp*hp^3/12*)
theta1 = 180;
m4 := (rhop*Ap*Lp/6) * {{2, 0, 0, 1, 0, 0},
  {0, 156/70, 22*Lp/70, 0, 54/70, -13*Lp/70}, {0, 22*Lp/70, 4*Lp^2/70, 0, 13*Lp/70, -3*Lp^2/70},
  {1, 0, 0, 2, 0, 0}, {0, 54/70, 13*Lp/70, 0, 156/70, -22*Lp/70},
  {0, -13*Lp/70, -3*Lp^2/70, 0, -22*Lp/70, 4*Lp^2/70}} (*//MatrixForm*)
mt2 := {{Cos[theta1 Degree], Sin[theta1 Degree], 0, 0, 0, 0},
  {-Sin[theta1 Degree], Cos[theta1 Degree], 0, 0, 0, 0},
  {0, 0, 1, 0, 0, 0}, {0, 0, 0, Cos[theta1 Degree], Sin[theta1 Degree], 0},
  {0, 0, 0, -Sin[theta1 Degree], Cos[theta1 Degree], 0},
  {0, 0, 0, 0, 0, 1}} (*//MatrixForm*)
tmt2 := Transpose[{{Cos[theta1 Degree], Sin[theta1 Degree], 0, 0, 0, 0},
  {-Sin[theta1 Degree], Cos[theta1 Degree], 0, 0, 0, 0}, {0, 0, 1, 0, 0, 0},
  {0, 0, 0, Cos[theta1 Degree], Sin[theta1 Degree], 0}, {0, 0, 0,
  -Sin[theta1 Degree], Cos[theta1 Degree], 0}, {0, 0, 0, 0, 0, 1}}] (*//MatrixForm*)
M4 = tmt2.m4.mt2 (*//MatrixForm*);

GM4 :=
{{0, 0, 0, 0, 0, 0, 0, 0, 0, 0, 0, 0, 0, 0, 0}, {0, 0, 0, 0, 0, 0, 0, 0, 0, 0, 0, 0, 0, 0, 0},
  {0, 0, 0, 0, 0, 0, 0, 0, 0, 0, 0, 0, 0, 0, 0}, {0, 0, 0, 0, 0, 0, 0, 0, 0, 0, 0, 0, 0, 0, 0},
  {0, 0, 0, 0, 0, 0, Ap*Lp*rhop/3, 0, 0, 0, 0, 0, Ap*Lp*rhop/6, 0, 0}, {0, 0, 0, 0, 0, 0,
  0, 13*Ap*Lp*rhop/35, -11/210*Ap*Lp^2*rhop, 0, 0, 0, 0, 9*Ap*Lp*rhop/70, 13/420*Ap*Lp^2*rhop},
  {0, 0, 0, 0, 0, 0, 0, -11/210*Ap*Lp^2*rhop, 1/105*Ap*Lp^3*rhop, 0, 0, 0, 0, 0, 0},
  {-13/420*Ap*Lp^2*rhop, -1/140*Ap*Lp^3*rhop}, {0, 0, 0, 0, 0, 0, 0, 0, 0, 0, 0, 0, 0, 0, 0},
  {0, 0, 0, 0, 0, 0, 0, 0, 0, 0, 0, 0, 0, 0, 0}, {0, 0, 0, 0, 0, 0, 0, 0, 0, 0, 0, 0, 0, 0, 0},
  {0, 0, 0, 0, 0, 0, Ap*Lp*rhop/6, 0, 0, 0, 0, 0, Ap*Lp*rhop/3, 0, 0},
  {0, 0, 0, 0, 0, 0, 0, 9*Ap*Lp*rhop/70, -13/420*Ap*Lp^2*rhop, 0, 0, 0, 0, 13*Ap*Lp*rhop/35,
  11/210*Ap*Lp^2*rhop}, {0, 0, 0, 0, 0, 0, 0, 13/420*Ap*Lp^2*rhop, -1/140*Ap*Lp^3*rhop,
  0, 0, 0, 0, 11/210*Ap*Lp^2*rhop, 1/105*Ap*Lp^3*rhop}} (*//MatrixForm*);

K = k1 + k2 + k3 + k4 (*//MatrixForm*);

M = GM1 + GM2 + GM3 + GM4 (*//MatrixForm*);

```



$$\text{num} = \text{Det} \left[ \begin{array}{cccc} \frac{2}{105} A L^3 \rho \times D^2 + \frac{8 Mo I Y}{L} & 0 & -\frac{1}{140} A L^3 \rho \times D^2 + \frac{2 Mo I Y}{L} & \\ \frac{13}{420} A L^2 \rho \times D^2 - \frac{6 Mo I Y}{L^2} & -s \times e^{i \times \omega \times \tau / 2} & -\frac{11}{210} A L^2 \rho \times D^2 + \frac{11}{210} A p L p^2 \rho h o p \times D^2 - \frac{6 Mo I Y}{L^2} + \frac{6 Mo I p}{L p^2} & \\ -\frac{1}{140} A L^3 \rho \times D^2 + \frac{2 Mo I Y}{L} & 0 & \frac{1}{105} A L^3 \rho \times D^2 + \frac{1}{105} A p L p^3 \rho h o p \times D^2 + \frac{4 Mo I Y}{L} + \frac{4 Mo I p}{L p} & \\ -\frac{13}{420} A L^2 \rho \times D^2 + \frac{6 Mo I Y}{L^2} & -s \times e^{-i \times \omega \times \tau / 2} & 0 & \\ -\frac{1}{140} A L^3 \rho \times D^2 + \frac{2 Mo I Y}{L} & 0 & 0 & 0 \end{array} \right] (* /. D \rightarrow i \times \omega *) ;$$

$$\text{t num} = \text{num} /. D \rightarrow i \times \omega ;$$

t num // Simplify;

$$\text{num1} = \text{Det} \left[ \begin{array}{cccc} \frac{2}{105} A L^3 \rho \times D^2 + \frac{8 Mo I Y}{L} & \frac{13}{420} A L^2 \rho \times D^2 - \frac{6 Mo I Y}{L^2} & & \\ \frac{13}{420} A L^2 \rho \times D^2 - \frac{6 Mo I Y}{L^2} & \frac{13 A L \rho h o \times D^2}{35} + \frac{13 A p L p \rho h o p \times D^2}{35} + \frac{12 Mo I Y}{L^3} + \frac{12 Mo I p Y p}{L p^3} & -\frac{11}{210} A L^2 & \\ -\frac{1}{140} A L^3 \rho \times D^2 + \frac{2 Mo I Y}{L} & -\frac{11}{210} A L^2 \rho \times D^2 + \frac{11}{210} A p L p^2 \rho h o p \times D^2 - \frac{6 Mo I Y}{L^2} + \frac{6 Mo I p Y p}{L p^2} & \frac{1}{105} A L^3 & \\ -\frac{13}{420} A L^2 \rho \times D^2 + \frac{6 Mo I Y}{L^2} & 0 & & \\ -\frac{1}{140} A L^3 \rho \times D^2 + \frac{2 Mo I Y}{L} & 0 & & \end{array} \right] (* /. D \rightarrow i \times \omega *) ;$$

$$\text{temp1} = \text{num1} /. D \rightarrow i \times \omega ;$$

temp1 // Simplify;

(\*Modal Analysis\*)

$$\begin{aligned}
 \text{mat} = & -\left\{ \left\{ \frac{2}{105} A L^3 \text{rho}, \frac{13}{420} A L^2 \text{rho}, -\frac{1}{140} A L^3 \text{rho}, -\frac{13}{420} A L^2 \text{rho}, -\frac{1}{140} A L^3 \text{rho} \right\}, \right. \\
 & \left\{ -\frac{13}{420} A L^2 \text{rho}, \frac{13 A L \text{rho}}{35} + \frac{13 A p L p \text{rhop}}{35}, -\frac{11}{210} A L^2 \text{rho} + \frac{11}{210} A p L p^2 \text{rhop}, 0, 0 \right\}, \\
 & \left\{ -\frac{1}{140} A L^3 \text{rho}, -\frac{11}{210} A L^2 \text{rho} + \frac{11}{210} A p L p^2 \text{rhop}, \frac{1}{105} A L^3 \text{rho} + \frac{1}{105} A p L p^3 \text{rhop}, 0, 0 \right\}, \\
 & \left\{ -\frac{13}{420} A L^2 \text{rho}, 0, 0, \frac{13 A L \text{rho}}{35} + \frac{13 A p L p \text{rhop}}{35}, \frac{11}{210} A L^2 \text{rho} - \frac{11}{210} A p L p^2 \text{rhop} \right\}, \\
 & \left. \left\{ -\frac{1}{140} A L^3 \text{rho}, 0, 0, \frac{11}{210} A L^2 \text{rho} - \frac{11}{210} A p L p^2 \text{rhop}, \frac{1}{105} A L^3 \text{rho} + \frac{1}{105} A p L p^3 \text{rhop} \right\} \right\} + \\
 \text{lambda} * & \left\{ \left\{ \frac{8 M o I Y}{L}, -\frac{6 M o I Y}{L^2}, \frac{2 M o I Y}{L}, \frac{6 M o I Y}{L^2}, \frac{2 M o I Y}{L} \right\}, \right. \\
 & \left\{ -\frac{6 M o I Y}{L^2}, \frac{12 M o I Y}{L^3} + \frac{12 M o I p Y p}{L p^3}, -\frac{6 M o I Y}{L^2} + \frac{6 M o I p Y p}{L p^2}, 0, 0 \right\}, \\
 & \left\{ \frac{2 M o I Y}{L}, -\frac{6 M o I Y}{L^2} + \frac{6 M o I p Y p}{L p^2}, \frac{4 M o I Y}{L} + \frac{4 M o I p Y p}{L p}, 0, 0 \right\}, \\
 & \left\{ \frac{6 M o I Y}{L^2}, 0, 0, \frac{12 M o I Y}{L^3} + \frac{12 M o I p Y p}{L p^3}, \frac{6 M o I Y}{L^2} - \frac{6 M o I p Y p}{L p^2} \right\}, \\
 & \left. \left\{ \frac{2 M o I Y}{L}, 0, 0, \frac{6 M o I Y}{L^2} - \frac{6 M o I p Y p}{L p^2}, \frac{4 M o I Y}{L} + \frac{4 M o I p Y p}{L p} \right\} \right\} (*//MatrixForm*) \\
 & \left\{ \left\{ -\frac{2}{105} A L^3 \text{rho} + \frac{8 \text{lambda} M o I Y}{L}, -\frac{13}{420} A L^2 \text{rho} - \frac{6 \text{lambda} M o I Y}{L^2}, \right. \right. \\
 & \left. \frac{1}{140} A L^3 \text{rho} + \frac{2 \text{lambda} M o I Y}{L}, \frac{13}{420} A L^2 \text{rho} + \frac{6 \text{lambda} M o I Y}{L^2}, \frac{1}{140} A L^3 \text{rho} + \frac{2 \text{lambda} M o I Y}{L} \right\}, \\
 & \left\{ -\frac{13}{420} A L^2 \text{rho} - \frac{6 \text{lambda} M o I Y}{L^2}, -\frac{13}{35} A L \text{rho} - \frac{13 A p L p \text{rhop}}{35} + \text{lambda} \left( \frac{12 M o I Y}{L^3} + \frac{12 M o I p Y p}{L p^3} \right), \right. \\
 & \left. \frac{11}{210} A L^2 \text{rho} - \frac{11}{210} A p L p^2 \text{rhop} + \text{lambda} \left( -\frac{6 M o I Y}{L^2} + \frac{6 M o I p Y p}{L p^2} \right), 0, 0 \right\}, \\
 & \left\{ \frac{1}{140} A L^3 \text{rho} + \frac{2 \text{lambda} M o I Y}{L}, \right. \\
 & \left. \frac{11}{210} A L^2 \text{rho} - \frac{11}{210} A p L p^2 \text{rhop} + \text{lambda} \left( -\frac{6 M o I Y}{L^2} + \frac{6 M o I p Y p}{L p^2} \right), \right. \\
 & \left. -\frac{1}{105} A L^3 \text{rho} - \frac{1}{105} A p L p^3 \text{rhop} + \text{lambda} \left( \frac{4 M o I Y}{L} + \frac{4 M o I p Y p}{L p} \right), 0, 0 \right\}, \\
 & \left\{ \frac{13}{420} A L^2 \text{rho} + \frac{6 \text{lambda} M o I Y}{L^2}, 0, 0, \right. \\
 & \left. -\frac{13}{35} A L \text{rho} - \frac{13 A p L p \text{rhop}}{35} + \text{lambda} \left( \frac{12 M o I Y}{L^3} + \frac{12 M o I p Y p}{L p^3} \right), \right. \\
 & \left. -\frac{11}{210} A L^2 \text{rho} + \frac{11}{210} A p L p^2 \text{rhop} + \text{lambda} \left( \frac{6 M o I Y}{L^2} - \frac{6 M o I p Y p}{L p^2} \right) \right\}, \\
 & \left\{ \frac{1}{140} A L^3 \text{rho} + \frac{2 \text{lambda} M o I Y}{L}, 0, 0, \right. \\
 & \left. -\frac{11}{210} A L^2 \text{rho} + \frac{11}{210} A p L p^2 \text{rhop} + \text{lambda} \left( \frac{6 M o I Y}{L^2} - \frac{6 M o I p Y p}{L p^2} \right), \right. \\
 & \left. -\frac{1}{105} A L^3 \text{rho} - \frac{1}{105} A p L p^3 \text{rhop} + \text{lambda} \left( \frac{4 M o I Y}{L} + \frac{4 M o I p Y p}{L p} \right) \right\} \}
 \end{aligned}$$

Eigenvalues[mat];

poly = Det[mat];

Solve[poly == 0, lambda];

## Appendix B: Sensitivity Analysis

1. Rigid body consideration: the coupling spring  $k_3$  is infinitely large.

It is always good to check either a system's rigid body or spring-like low frequency nature by hand according to [38]. This way we could see how the mechanical structure enhances internal differences. As the values of the coupling spring constant  $k_3$  and the damping constant  $c_3$  become large, the expressions become strongly dependent on the difference between Eq. 2.2  $H_{x_1,p}(\omega)$  and  $H_{x_2,p}(\omega)$ . This means that the displacement at each end of the sensor  $x_1(t)$  and  $x_2(t)$  become dependent on the difference between the applied forces of the far field sound wave at each end of the sensor  $f_1(t)$  and  $f_2(t)$ . The rigidly coupled pivot system would provide no level difference. Considering two identical diaphragm as a rigid diaphragm which means there is no mechanical coupling between them, the response of one end, say  $x_1$ , is equal to that of the other, say  $x_2$  but with different sign. For this reason, only the equation of motion for the response  $x_1$  is derived and analyzed below.

The equation of motion for the rigid body system becomes

$$m \ddot{x}_1 + c \dot{x}_1 + kx_1 = f_1 \quad (\text{A.1})$$

Taking the Laplace transform of a general second order differential equation with initial conditions and solving for the transfer function gives

$$\frac{X_1(s)}{F_1(s)} = \frac{1}{ms^2 + cs + k} = \frac{1/m}{s^2 + \frac{c}{m}s + \frac{k}{m}} \quad (\text{A.2})$$

We can simplify the Eq. A.2 by applying the following definitions:

- 1)  $\omega_n^2 = \frac{k}{m}$ , where  $\omega_n$  is the undamped natural frequency [rad/sec]
- 2)  $c_{cr} = 2\sqrt{km}$ , where  $c_{cr}$  is the "critical" damping value

3)  $\zeta$  is the amount of proportional damping, typically stated as a percentage of critical damping

4)  $2\zeta\omega_n$  is the multiplier of the velocity term, so that  $\frac{c}{m} = 2\zeta\omega_n$

Rewriting, using the above substitutions and substituting “ $j\omega$ ” for “ $s$ ” to calculate the frequency response, where “ $j$ ” is the imaginary operator:

$$\frac{X_1(s)}{F_1(s)} = \frac{1/m}{s^2 + 2\zeta\omega_n s + \omega_n^2} \rightarrow \frac{X_1(s)}{P_1(s)} = \frac{s \cdot e^{j\omega\tau/2} / m}{s^2 + 2\zeta\omega_n s + \omega_n^2} \quad (\text{A.3})$$

where “ $s$ ” in the numerator represents the surface area as indicated in Chapter 2.

$$\frac{X_1(j\omega)}{P_1(j\omega)} = \frac{s \cdot e^{j\omega\tau/2} / m}{(j\omega)^2 + 2\zeta\omega_n(j\omega) + \omega_n^2} \quad (\text{A.4a})$$

$$= \frac{s \cdot e^{j\omega\tau/2} / m}{-\omega^2 + 2 \cdot \zeta \cdot \omega \cdot \omega_n \cdot j + \omega_n^2} \quad (\text{A.4b})$$

$$= \frac{s \cdot e^{j\omega\tau/2} / (m \cdot \omega^2)}{-1 + \frac{2 \cdot \zeta \cdot \omega_n \cdot j}{\omega} + \frac{\omega_n^2}{\omega^2}} \quad (\text{A.4c})$$

$$= \frac{s \cdot e^{j\omega\tau/2} / (m \cdot \omega^2)}{\left(\frac{\omega_n^2}{\omega^2} - 1\right) + \frac{2 \cdot \zeta \cdot \omega_n \cdot j}{\omega}} \quad (\text{A.4d})$$

The frequency response equation above shows how the ratio ( $X_1/P_1$ ) varies as a function of frequency  $\omega$ . The ratio is a complex number that has some interesting properties at different values of the ratio ( $\omega_n/\omega$ ).

At low frequencies relative to the resonant frequency,  $\omega_n^2 \gg \omega\omega_n \gg \omega^2$ , and the transfer function in Eq. A.4b is given by:

$$\frac{X_1(j\omega)}{P_1(j\omega)} = \frac{s \cdot e^{j\omega\tau/2} / m}{-\omega^2 + 2 \cdot \zeta \cdot \omega \cdot \omega_n \cdot j + \omega_n^2}$$

$$\cong \frac{s \cdot e^{j\omega\tau/2} / m}{\omega_n^2} = \frac{s \cdot e^{j\omega\tau/2}}{m \cdot \omega_n^2} = \frac{s \cdot e^{j\omega\tau/2}}{m \cdot \left(\frac{k}{m}\right)} = \frac{s \cdot e^{j\omega\tau/2}}{k} \quad (\text{A.5})$$

Since the frequency response value at any frequency is a complex number, we can take the magnitude and phase.

$$\left| \frac{X_1(j\omega)}{P_1(j\omega)} \right| = \frac{s \cdot e^{j\omega\tau/2}}{k} \quad (\text{A.6a})$$

$$\angle \frac{X_1(j\omega)}{P_1(j\omega)} = 0 \quad (\text{A.6b})$$

Thus, the gain at low frequencies is a constant. Phase is  $0^\circ$  because the sign is positive.

At high frequencies,  $\omega^2 \gg \omega\omega_n \gg \omega_n^2$ , the transfer function is given by:

$$\begin{aligned} \frac{X_1(j\omega)}{P_1(j\omega)} &= \frac{s \cdot e^{j\omega\tau/2} / m}{-\omega^2 + 2 \cdot \zeta \cdot \omega \cdot \omega_n \cdot j + \omega_n^2} \\ &\cong \frac{s \cdot e^{j\omega\tau/2} / m}{-\omega^2} = \frac{-s \cdot e^{j\omega\tau/2}}{m \cdot \omega^2} \end{aligned} \quad (\text{A.7})$$

Once again, taking the magnitude and phase:

$$\left| \frac{X_1(j\omega)}{P_1(j\omega)} \right| = \left| \frac{-s \cdot e^{j\omega\tau/2}}{m \cdot \omega^2} \right| = \frac{s \cdot e^{j\omega\tau/2}}{m \cdot \omega^2} \quad (\text{A.8a})$$

$$\angle \frac{X_1(j\omega)}{P_1(j\omega)} = -180^\circ \quad (\text{A.8b})$$

At high frequencies, the gain is given by Eq. A.8a and the phase is  $-180^\circ$  because the sign is negative.

At resonance,  $\omega = \omega_n$ , the transfer function is given by:

$$\begin{aligned}
\frac{X_1(j\omega)}{P_1(j\omega)} &= \frac{s \cdot e^{j\omega\tau/2} / m}{-\omega^2 + 2 \cdot \zeta \cdot \omega \cdot \omega_n \cdot j + \omega_n^2} \\
&\cong \frac{s \cdot e^{j\omega\tau/2} / m}{2 \cdot \zeta \cdot \omega \cdot \omega_n \cdot j} = \frac{s \cdot e^{j\omega\tau/2}}{2 \cdot \zeta \cdot \omega_n^2 \cdot m \cdot j} = \frac{s \cdot e^{j\omega\tau/2}}{2 \cdot \zeta \cdot k \cdot m \cdot j} = \frac{s \cdot e^{j\omega\tau/2}}{2 \cdot \zeta \cdot k \cdot j} \\
&= \frac{-j \cdot s \cdot e^{j\omega\tau/2} / k}{2 \cdot \zeta}
\end{aligned} \tag{A.9}$$

Taking magnitude and phase at resonance:

$$\left| \frac{X_1(j\omega)}{P_1(j\omega)} \right| = \left| \frac{-j \cdot s \cdot e^{j\omega\tau/2} / k}{2 \cdot \zeta} \right| = \frac{s \cdot e^{j\omega\tau/2} / k}{2 \cdot \zeta} \tag{A.10a}$$

$$\angle \frac{X_1(j\omega)}{P_1(j\omega)} = -90^\circ \tag{A.10b}$$

The magnitude at resonance is seen to be the gain at low frequency in Eq. 6a divided by  $2\zeta$ . Since  $\zeta$  is typically a small number, for example 1% of critical damping or 0.01, the magnitude at resonance is seen to be amplified. At resonance the phase angle is  $-90^\circ$ . This also can be seen physically by first imagining that the coupling terms  $k_3$  and  $c_3$  take on infinite values since in this case the mechanically coupled diaphragm now becomes a single rigid bar [11].

2. Non-rigid body system consideration: the coupling spring  $k_3$  is finite instead of infinitely large. Now suppose that the mechanical coupling due to  $k_3$  and  $c_3$  in our model system is finite instead of completely rigid. This allows the two responses,  $x_1(t)$  and  $x_2(t)$ , with different amplitudes and, with the appropriate choice of  $k_3$  and  $c_3$ , provides the enhancement in time delay. The system thus provides a very simple means of greatly expanding both time delays and level difference. The relatively large (but finite) stiffness of the connection at the pivot point is an important feature of the dynamic model [11].

The transfer function shown in Eq. 2.2 which was obtained by a direct approach can further be expressed as Eq. A.11 using a modal approach. In this method, the motion is decomposed into two “natural” modes of vibration. There are only two modes of motion in this system because the model contain two response coordinates,  $x_1(t)$  and  $x_2(t)$ , and hence has two degrees of freedom.

$$\begin{aligned}
H_{x_1p}(\omega) &= \frac{(H_{f_1p}(\omega) - H_{f_2p}(\omega))/(2m)}{\omega_r^2 - \omega^2 + 2\omega_r \xi_r \hat{i} \omega} + \frac{(H_{f_1p}(\omega) + H_{f_2p}(\omega))/(2m)}{\omega_t^2 - \omega^2 + 2\omega_t \xi_t \hat{i} \omega} \\
H_{x_2p}(\omega) &= \frac{(H_{f_1p}(\omega) + H_{f_2p}(\omega))/(2m)}{\omega_t^2 - \omega^2 + 2\omega_t \xi_t \hat{i} \omega} - \frac{(H_{f_1p}(\omega) - H_{f_2p}(\omega))/(2m)}{\omega_r^2 - \omega^2 + 2\omega_r \xi_r \hat{i} \omega}
\end{aligned} \tag{A.11}$$

where

$$\left. \begin{aligned}
\omega_r &= \sqrt{k/m} \\
\omega_t &= \sqrt{(k + 2k_3)/m}
\end{aligned} \right\} \text{natural frequencies}$$

$$\left. \begin{aligned}
\xi_r &= c/(\omega_r m) \\
\xi_t &= (c + 2c_3)/(\omega_t m)
\end{aligned} \right\} \text{damping ratios of the two resonant modes}$$

Eq. A.11 becomes Eq. A.12 if we substitute with expressions given in Eq. 2.2 for  $H_{f_1p}(\omega)$  and  $H_{f_2p}(\omega)$  and express the complex exponential functions in terms of sines and cosines.

$$\begin{aligned}
H_{x_1p}(\omega) &= \frac{s \hat{i} \sin(\omega\tau/2)/m}{\omega_r^2 - \omega^2 + 2\omega_r \xi_r \hat{i} \omega} + \frac{s \cos(\omega\tau/2)/m}{\omega_t^2 - \omega^2 + 2\omega_t \xi_t \hat{i} \omega} \\
H_{x_2p}(\omega) &= \frac{s \cos(\omega\tau/2)/m}{\omega_t^2 - \omega^2 + 2\omega_t \xi_t \hat{i} \omega} - \frac{s \hat{i} \sin(\omega\tau/2)/m}{\omega_r^2 - \omega^2 + 2\omega_r \xi_r \hat{i} \omega}
\end{aligned} \tag{A.12}$$

At very low frequencies, near  $\omega \approx 0$ ,  $\sin(\omega\tau/2) \approx 0$  and  $\cos(\omega\tau/2) \approx 1$ . Eq. A.12 then becomes

$$H_{x_1p}(\omega) \approx H_{x_2p}(\omega) \approx \frac{s/m}{\omega_t^2} \tag{A.13}$$

We thus expect both sides,  $x_1(t)$  and  $x_2(t)$ , to move together at very low frequencies.

At somewhat higher frequencies, where  $\omega \approx \omega_r < \omega_t$ , the terms that are proportional to  $\sin(\omega\tau/2)$  become more significant contributors to the total response.

$$\begin{aligned}
H_{x_1p}(\omega) &= \frac{s \hat{i} \sin(\omega\tau/2)/m}{2\omega_r \xi_r \hat{i} \omega} + \frac{s \cos(\omega\tau/2)/m}{\omega_t^2 - \omega^2 + 2\omega_t \xi_t \hat{i} \omega} \\
H_{x_2p}(\omega) &= \frac{s \cos(\omega\tau/2)/m}{\omega_t^2 - \omega^2 + 2\omega_t \xi_t \hat{i} \omega} - \frac{s \hat{i} \sin(\omega\tau/2)/m}{2\omega_r \xi_r \hat{i} \omega}
\end{aligned} \tag{A.14a}$$

Since the second term of  $H_{f_1p}(\omega)$  is the same as the first term of  $H_{f_2p}(\omega)$ , Eq. 14a can be reduced to Eq. 14b by setting the term as  $A$ .

$$\begin{aligned} H_{x_1p}(\omega) &= \frac{s\hat{i} \sin(\omega\tau/2)/m}{2\omega_r \xi_r \hat{i} \omega} + A \\ H_{x_2p}(\omega) &= A - \frac{s\hat{i} \sin(\omega\tau/2)/m}{2\omega_r \xi_r \hat{i} \omega} \end{aligned} \quad (\text{A.14b})$$

In this case, the two responses,  $x_1(t)$  and  $x_2(t)$ , move in nearly opposite phase at frequencies near  $\omega \approx \omega_r$ .

At still higher frequencies, where  $\omega_r < \omega < \omega_t$ , all terms in Eq. A.14 will be significant since there is no cancellation. However, those terms for  $H_{f_1p}(\omega)$  add together while those for  $H_{f_2p}(\omega)$  subtract.

At high frequencies, where  $\omega \approx \omega_t > \omega_r$ , the terms that are proportional to  $\cos(\omega\tau/2)$  become more significant contributors to the total response.

$$\begin{aligned} H_{x_1p}(\omega) &= \frac{s\hat{i} \sin(\omega\tau/2)/m}{\omega_r^2 - \omega^2 + 2\omega_r \xi_r \hat{i} \omega} + \frac{s \cos(\omega\tau/2)/m}{2\omega_t \xi_t \hat{i} \omega} \\ H_{x_2p}(\omega) &= \frac{s \cos(\omega\tau/2)/m}{2\omega_t \xi_t \hat{i} \omega} - \frac{s\hat{i} \sin(\omega\tau/2)/m}{\omega_r^2 - \omega^2 + 2\omega_r \xi_r \hat{i} \omega} \end{aligned} \quad (\text{A.15a})$$

Since the first term of  $H_{f_1p}(\omega)$  is the same as the second term of  $H_{f_2p}(\omega)$  with the opposite sign, Eq. A.15a can be reduced to Eq. A.15b by setting the term as  $B$ .

$$\begin{aligned} H_{x_1p}(\omega) &= B + \frac{s \cos(\omega\tau/2)/m}{2\omega_t \xi_t \hat{i} \omega} \\ H_{x_2p}(\omega) &= \frac{s \cos(\omega\tau/2)/m}{2\omega_t \xi_t \hat{i} \omega} - B \end{aligned} \quad (\text{A.15b})$$

In this case, the two responses,  $x_1(t)$  and  $x_2(t)$ , move together with magnitude difference of  $2B$  at frequencies near  $\omega \approx \omega_t$ .

## Appendix C: Sensor Size Selection

$f$ $d$ [m]	Input Time Delay	500 Hz	Amp ratio	1000 Hz	Amp ratio	2000 Hz	Amp ratio	3000 Hz	Amp ratio	4000 Hz	Amp ratio	5000 Hz	Amp ratio
0.002	9.54E-07	1.42E-04	1.49E+02	-4.04E-05	4.24E+01	-2.93E-05	3.07E+01	-1.40E-05	1.47E+01	-7.76E-06	8.14E+00	-4.71E-06	4.94E+00
0.003	1.43E-06	-3.96E-04	2.77E+02	-1.28E-04	8.93E+01	-3.44E-05	2.41E+01	-1.49E-05	1.04E+01	-7.82E-06	5.47E+00	-4.51E-06	3.15E+00
0.004	1.91E-06	-4.77E-04	2.50E+02	-1.36E-04	7.14E+01	-3.48E-05	1.83E+01	-1.46E-05	7.68E+00	-7.45E-06	3.91E+00	-4.10E-06	2.15E+00
0.005	2.38E-06	-4.82E-04	2.02E+02	-1.38E-04	5.78E+01	-3.46E-05	1.45E+01	-1.43E-05	5.98E+00	-7.01E-06	2.94E+00	-3.64E-06	1.53E+00
0.006	2.86E-06	-4.82E-04	1.68E+02	-1.38E-04	4.83E+01	-3.43E-05	1.20E+01	-1.38E-05	4.83E+00	-6.55E-06	2.29E+00	-3.17E-06	1.11E+00
0.007	3.34E-06	-4.82E-04	1.44E+02	-1.38E-04	4.13E+01	-3.39E-05	1.01E+01	-1.34E-05	4.00E+00	-6.09E-06	1.82E+00	-2.70E-06	-8.09E-01
0.01	4.77E-06	-4.81E-04	1.01E+02	-1.37E-04	2.87E+01	-3.25E-05	6.82E+00	-1.20E-05	2.51E+00	-4.67E-06	-9.80E-01	-1.28E-06	-2.68E-01
0.02	9.54E-06	-4.78E-04	5.02E+01	-1.33E-04	1.40E+01	-2.80E-05	2.93E+00	-7.26E-06	-7.61E-01	9.35E-08	9.80E-03	-1.96E-04	2.06E+01
0.03	1.43E-05	-4.76E-04	3.33E+01	-1.29E-04	9.04E+00	-2.34E-05	1.63E+00	-2.50E-06	-1.75E-01	-2.45E-04	1.71E+01	-1.92E-04	1.34E+01
0.04	1.91E-05	-4.73E-04	2.48E+01	-1.25E-04	6.57E+00	-1.87E-05	-9.81E-01	2.31E-06	1.21E-01	-2.40E-04	1.26E+01	-1.87E-04	9.79E+00
0.05	2.38E-05	-4.71E-04	1.97E+01	-1.21E-04	5.09E+00	-1.40E-05	-5.87E-01	-3.26E-04	1.37E+01	-2.35E-04	9.87E+00	-1.82E-04	7.63E+00
0.06	2.86E-05	-4.68E-04	1.64E+01	-1.17E-04	4.10E+00	-9.25E-06	-3.23E-01	-3.21E-04	1.12E+01	-2.30E-04	8.05E+00	-1.77E-04	6.18E+00
0.07	3.34E-05	-4.66E-04	1.40E+01	-1.13E-04	3.39E+00	-4.46E-06	-1.34E-01	-3.16E-04	9.48E+00	-2.25E-04	6.75E+00	-1.72E-04	5.15E+00
0.1	4.77E-05	-4.58E-04	9.61E+00	-1.01E-04	2.11E+00	-4.90E-06	1.03E+01	-3.01E-04	6.32E+00	-2.10E-04	4.41E+00	-1.57E-04	3.28E+00
0.2	9.54E-05	-2.19E-04	2.30E+00	-9.85E-05	1.03E+01	-4.21E-06	4.42E+00	-2.43E-04	2.55E+00	-1.56E-04	1.64E+00	-1.05E-04	1.10E+00

Table A-1: Various  $\tau_{out}$  at frequencies of interests under 5000 Hz w/ various sized diaphragm (*Red*: highest amplified  $\tau_{out}$ ; *Blue*: highest amplification ratio)

# Curriculum Vitae

## Jin-Hyuk Lee

### EDUCATION

THE UNIVERSITY OF WASHINGTON, SEATTLE, WA

*Ph.D. in Mechanical Engineering, Summer 2013 (Advisor: Dr. Per G. Reinhall)*

- “Bio-Inspired Hydro-Acoustic Sensor for Sensing Directivity of Sound – Design and Optimization”
- Finite Element Analysis (Structural, Dynamics & Vibration, Fluid-Structure Interaction and Multi-Physics)
- DSP (Digital Signal Processing)
- MEMS (Micro Electro Mechanical System)
- Design Optimization (Linear and Nonlinear System)
- System Modeling, Simulation and Estimation

THE OHIO STATE UNIVERSITY, Columbus, OH

*M.S. in Mechanical Engineering, Autumn 2004 (Advisor: Dr. Stephen Yurkovich)*

- Dynamic Modeling & Control of Torque Converter System (Multi-Disciplinary)
- Recipient of LuK Inc. GATE Fellowship.
- Graduate Research Associate at the Center for Automotive Research.

THE GEORGE WASHINGTON UNIVERSITY, Washington D.C.

*M.S. in Mechanical Engineering, December 1993 (Advisor: Dr. James D. Lee)*

- Mechatronics, Robotics & CIM (Computer Integrated Manufacturing)
- Recipient of University Fellowship from the George Washington University, 1992

THE GEORGE WASHINGTON UNIVERSITY, Washington D.C.

*B.S. in Mechanical Engineering, December 1991, (Advisor: Dr. Douglas L. Jones)*

- Named to a member of Kappa Mu Epsilon, a national mathematics honor organization – New York Alpha Chapter, 1990

### EXPERIENCES

SHORELINE COMMUNITY COLLEGE, SHORELINE, WA

*Full time faculty for Engineering Department (September 2012 ~ June 2013)*

- Engr 225: Mechanics of Materials
- Engr 215: Dynamics
- Engr 214: Statics
- Engr 115: Intro to Statics and Engineering Problems
- Engr 114: Engineering Graphics
- Engr 100: Intro to Engineering
- Engr 205: Solid Works and Parametric Modeling
- Engr 206: Advanced Solid Works

THE UNIVERSITY OF WASHINGTON, SEATTLE, WA

*Predocctoral Lecturer (Instructor) for Mechanical Engineering (Summer2009~Summer 2013)*

- ME 230: Dynamics
- ME 478: Finite Element Analysis
  - : Received student evaluation of 4.5/5.0 for Summer 2010 \* 2012 Qtr
  - : EDGE (Education at a Distance for Growth and Excellence) class for online students including Boeing employees

*Graduate Teaching Assistant for Physics & Mechanical Engineering (Winter 2006 ~ September 2012 only Winter Qtrs)*

- ME 565: Mechanical Engineering Analysis
- ME 230: Kinematics and Dynamics

- ME 469: Applications of Dynamics in Engineering
- Phys 121: Introductory to Physics

*Facilitator for Teaching Assistant/Research Assistant Conference (September 2010, 2011 & 2012)*

SHORELINE COMMUNITY COLLEGE, SHORELINE, WA

*Instructor (Part time faculty) for Engineering Department (Winter2010)*

- Engr 215: Dynamics

*Guest Speaker for Engineering Department (Autumn2009)*

- Engr 100: Introduction to Engineering and Design

INTELLECTUAL VENTURES, BELLEVUE, WA

*Technical Analyst (June 2008 ~ August 2009)*

- Research patents for technical contents, coverage, and market value
- Judging relevance of technology to current industry use & ease of discovery and ways to work around
- Researching and gathering evidence of use

THE OHIO STATE UNIVERSITY, COLUMBUS, OH

*Graduate Teaching Assistant for Department of Mechanical Engineering (Winter 2000 ~ Autumn 2004)*

- EE 753.01: Powertrain Control (Graduate Course)
- ME 571: Principles of Automatic Control (Undergraduate Course)
- ME 570: Mechanical Engineering Measurements (Undergraduate Course)
- ME 481& 482: System Dynamics and Vibrations/Electromechanics (Undergraduate Course)

LUK INC. WOOSTER, OH

*Research Engineer: Design and Testing Engineer in Advanced Technologies Department (Jul 2002-Oct 2002)*

- Testing and Analyzing Multi Function Torque Converter on the Dynamometer and on Board.

THE OHIO STATE UNIVERSITY, COLUMBUS, OH

*Research Engineer at CAR (Center for Automotive Research) and LuK Inc. (Jan 2000 ~ Dec 2003)*

- Specialization in Nonlinear Dynamic Control Oriented Modeling of Torque Converter.
- Research on Nonlinear Control Strategy for Torque Converter Clutch Minimal Slip Control.
- Research on Real-Time Model-Based Turbine Torque Estimation for Powertrain Control and Diagnostics Purpose.
- Developing a Nonlinear Model-Based Torque Estimation Algorithm Using Matlab/Simulink™.

SAMSUNG SDS, SEOUL, KOREA

*Assistant Engineer, PDM Business Team, CAD/CAM Business Operations (Nov 1997-Jun 1999)*

- CE/PDM Business and Services including CE/PDM/EDM Consulting/Implementation.
- CAD/CAM/CAE and Information Infrastructure Consulting Services.
- Provide Consulting Service on Engineering – CIM Process Innovation based on Concurrent Engineering.
- TRIZ/TIPS (Theory of Inventive Problem Solving) Implementation Proposal to SDD (Samsung Display Devices).

KIA MOTORS CO., LTD. (R&D CENTER), SEOUL, KOREA

*CAE(Computer Aided Engineering) Research Engineer for Crashworthiness & Safety Department (Sept 1995-Oct 1997)*

- Analyzing on Vehicle's Performance regarding Crashworthiness and Safety using LS-Dyna3D.
- Conducting Field Tests: Credos I & II (Frontal-FMVSS208 & 40% European Offset, Side FMVSS204 & European).
  - Conducting Elan Frontal Impact Test at Millbrook Proving Ground in UK as a part of Elan Project.

*Development Engineer for Powertrain Development Department (May 1995-Sept 1995)*

- Participated KAT (Kia Automatic Transmission) Project: Kia Motors' first own A/T.

*Test Engineer for Powertrain Test Department (Jan 1995-Jun 1995)*

- Performing N.V.H (Noise, Vibration & Harshness) Tests on Transmission using Accelerometer and FFT Analyzer (Rattle, Whistle Noise of T/M Gear on the Vehicles: Sportage, Aspire, Potentia).
- Performing various N.V.H related Tests such as Modal and Field Test.

*Design Engineer for Powertrain Design Department (Jan 1994-Dec 1994)*

- Design Transmission (Manual): Sportage (4WD).

## EXPERIENCES

- J. Lee, and H. Lee, “Dynamic Simulation of Nonlinear Model-Based Observer for Hydrodynamic Torque Converter System”, SAE Technical Paper No. 04CONG-4, Proc. 2004 SAE International Congress, Detroit, March 2004.
- J. Lee, “Dynamic Simulation for Torque Converter Clutch Slip System Using Sliding Mode Control”, FISITA Technical Paper Number F2004F061, World Automotive Congress, Barcelona, Spain, May 2004.
- J. Lee, “Modeling and Simulation of Dynamic Torque Converter using Matlab and Simulink®”, 2003 ASME IMECE: Symposium on Design-Oriented Modeling, Nov 16-21, 2003, Washington, D.C., USA (Draft)

## SKILLS

- Experimental Data Acquisition and Computation, Including Experimental Design/Setup and Operation of Accelerometer, Measurement, and Data Analysis Systems Using FFT and Oscilloscope and Data Acquisition Systems (DSP).
- Digital Signal Processing (FFT, Wavelet)
- On-Board Torque Estimation for Real-Time Torque Converter Control.
- Nonlinear Dynamic Modeling and Control Simulation for Torque Converter in System Dynamic and Fluid Dynamic Levels.
- Computer Languages: FORTRAN, Turbo-Pascal, VP-Expert, HTML, Maple, Mathematica and Matlab/Simulink™.
- Application Software Includes:  
CAD/CAM Packages: I-DEAS, NASTRAN, CATIA, AutoCAD, CADkey, CADAM, LS-Dyna3D, HyperMesh, ANSYS, COMSOL 3.5a  
PDM Packages: SDRC Metaphase